Particle Collider Probes of Dark Energy, Dark Matter and Generic Beyond Standard Model Signatures in Events With an Energetic Jet and Large Missing Transverse Momentum Using the ATLAS Detector at the LHC

J. Lindon

Thesis submitted for the degree of
Doctor of Philosophy

Particle Physics Group,
School of Physics and Astronomy,
University of Birmingham.

November 29, 2020

Particle colliders don't probe dark energy

Sabine Hossenfelder

ABSTRACT

Various Beyond Standard Model signatures are probed using a monojet analysis with the ATLAS experiment using $\sqrt{s} = 13$ TeV proton-proton collision data, and model-independent limits on generic Beyond Standard Model signatures are set. Three specific Beyond Standard Model signatures are highlighted: Horndeski dark energy and axial-vector and pseudoscalar WIMP candidates. Limits are reported at 95% confidence level observed(expected). For the WIMP candidates limits extend to $m_{Z_A} \geq 2060(2175)$ GeV and $m_{Z_P} \geq 368(404)$ GeV for the dark matter mass of axial-vector and psedudoscalar cases respectively, with a mediator mass of 1 GeV. This extends the reach of the axial-vector WIMP limits by 500(400) GeV from previous monojet searches, while this is the first time this channel in ATLAS is sensitive to the pseudoscalar WIMP. For the Horndeski dark energy model, limits are set at a cross section of $\sigma \leq 0.0433(0.0366)$ fb and mass scale of $M_2 \geq 1558(1591)$ GeV, an improvement of 400(300) GeV over using only the 2015+2016 data, which is the first time a dark energy model has been probed in a particle collider based search. Numerous improvements were made to the previous monojet analysis to perform these measurements and increase the model independent reach.

In addition this thesis presents preliminary results in developing a realtime beam monitor for the Birmingham MC40 cyclotron, the aim being to allow more precise irradiations of components which will be used in the High Luminosity-LHC upgrade. This precise irradiation will enable measurements of their radiation hardness, a vital property of components which will need to survive the high radiation levels near the interaction points in the High Luminosity-LHC.

DECLARATION OF AUTHOR'S CONTRIBUTION

The ATLAS experiment at CERN is a large international collaboration, hence there is content within this thesis that is reliant upon the work of other members of the collaboration.

Chapter 4 outlines the monojet analysis of which I am a part. The work into justifying and lowering the $P_{\mathrm{T}}^{\mathrm{recoil}}$ and leading jet p_{T} threshold is entirely my work, as are the consequences that doing so had in having to adjust Monte Carlo simulations, as well as the bug fix required to fix the old samples found during this work. The results in the signal region, and each control region, involved the work of everyone in the group. My contribution to this was not limited to, but mainly consisted of, estimates of the $t\bar{t}$ + single-t background, in addition to being the EXOT5 derivation contact, responsible for the EXOT5 derivation format, which due to the large volume of data in ATLAS was required to store the data and monte carlo that was needed while storing as little as was strictly necessary to reduce both storage and processing requirements. I also performed some work towards showing that merging the CR1mu0b and CR1e0b regions is better for the top control region than treating them separately, but work towards this was also done by others in the group.

In Chapter 5, everything other than the initial motivation for the study into L1_XE50, which came from the unexpected inefficiency in Figure 5.1, and the plot showing the 'batman ears' effect, Figure 5.4, was my own work.

In Chapter 6, of the background systematic uncertainties, the matching uncertainties on W + $jets$, Z + $jets$ backgrounds, and showing why they are not needed in the final results, was wholly my work. In addition the $t\bar{t}$ + single-t background systematic as well as treating them separately to improve precision rather than having a single systematic for both was exclusively my work.

Of the signal systematic uncertainties, all theoretical signal systematic uncertainties on the WIMP candidates and the dark energy model were entirely my work.

The post-fit signal region plots and model-independent results were a collaborative effort I took part in, as mentioned in my contributions to chapter 4.

I contributed towards the final result of the two WIMP models, as did many others in the group. In particular, I contributed towards the decision of which signal points to generate, while others helped to interpolate these to produce the final phase plot.

The final result of the dark energy model in the monojet channel is exclusively my work; though of course it is reliant upon others in the group for work mentioned earlier such as the background prediction. However Figure 6.27 is not from the monojet analysis and I did not directly contribute towards this, albeit I was involved in many discussions which worked towards the production of it.

I did not directly contribute towards the comparison plots with direct detection of the axial-vector WIMP nor the reinterpretation as a vector mediator, though both of these of course requires the WIMP results discussed earlier which I did contribute towards.

In chapter 7, everything was my own work, however, the integrator board and pixel sensor used were equipment kindly lent from colleagues in University of Liverpool. As well as this, assistance in producing the ionisation chamber was given by the workshop at the University of Birmingham, and of course help in performing these studies within the cyclotron was given by the cyclotron operators at the University of Birmingham.

ACKNOWLEDGEMENTS

I've spent the past week trying to figure out how to write my acknowledgements and haven't managed to even begin, so perhaps it will be best to start from the beginning and just ramble until the end, after mentioning STFC, which I have been told I have to acknowledge, so there we go (I think they used to give me money, never really understood where that came from, except for I would probably never get it if it wasn't for Maria who was always incredibly friendly and helpful).

So starting from the beginning, apologies Rob I'll get you a new bag someday, and thank you for being a great friend (even if you make the rest of us look bad). Thank you to Russell (double-checked the spelling) for putting up with living with me for a year and managing to make sure I got home (though I think when George, George's mum and I had to clean your bathroom probably made up for it).

Thank you to everyone for setting the bar especially high at Liverpool ATLAS UK, especially Jimmy for what probably shouldn't be written down. And thank you to Phil for the next day asking me to help in the cleanroom for some VIPs on the condition that I don't make a mess (and thank you to presumably Alan for telling him).

Thank you to everyone I've shared an office with, though especially the first year office who I probably learnt more about physics with through the various contraptions built than I did in my PhD. Particular thanks to Andy for helping me throughout my first year, who I wouldn't acknowledge to get back at for not acknowledging me, but you did cycle to my house a couple days ago so you get a sentence at least. And, as is always the case, with Andy has to be Jamés, so thank you Jamés for not being like Andy described you and for the great times, particularly with Point Break.

The first year office wouldn't have been complete without Matt Baca's sea shanties,

batarangs (and various other things that probably will be best unmentioned), I still expect that 3D model of my head someday. And naturally if mentioning the sea shanties, Alasdair's karaoke sessions, especially Escape couldn't go unmentioned. Thanks as well to Rhys for the Dilshad sessions and the helpful tips. And, needless to say, I couldn't have done it without John's flips, or Elliot's friendship, help, good times and 'expert' poker ability, or Tim's stories (you'd get a longer acknowledgement if you fixed the trains though). Thank you as well to Mark for managing to take some time away from WWE to provide me with a huge amount of help. Also thanks to Simon and Juergen for the company in the cleanroom. And thanks to Chaw who seems to somehow have everything, I feel like the time he offered me shoelaces they had to be his own..

I was debating whether to include Tony in the section for my office or my supervisors. I think with how often he forgot his keys he was in the office as much as anyone else, so I'll include him here. Thank you Tony for both being a great laugh and a great mentor. In the same vein, thank you to Laura for teaching me to work in the cyclotron (despite the radiation scares).

Talking about radiation scares, it would be impossible to miss off outdoorsy Briglin, thank you for the help teaching me hardware (even if we both had as little a clue about what we were doing as each other), and for teaching me to snowboard (even if the most I managed to do was go a few feet while getting over took by 5 year olds doing flips). Thanks as well for living with me and for the great times.

Thank you to Robbie, Nandish, Michael Gove, Dan, Pat and Pat for not talking to us for a few weeks. Unfortunately you started eventually, though thank you for some of my best times of my PhD while I was sharing an office with Nandish, Gove and Dan at CERN, Robbie's various games and especially the great trips we took, hopefully there will be many more ouais to come, and on the same line thank you to Chisholm for generally being a good laugh but especially his great going away party (and for distracting Elliot sometimes), as well as thank you to Ryan for a great time living together and always making sure I wasn't the most annoying drunk.

Living away from Nandos for so long wouldn't have been possible without PizzaFast, CFDK and the chicken man, so thank you very much especially for the copious free food and camaraderie at CFDK.

Unfortunately I didn't get to spend much time with the lower years due to being away at CERN until close to when the apocalypse started, though thanks for a good time at my final ATLAS UK.

Thank you to Chris for the huge amount of help putting together this thesis (though luckily he has not yet seen these acknowledgements). And thank you to Steve for having a great time with me and always having my back, especially with the various conferences and similar you somehow managed to get me to go on, for which I am very grateful and without which my PhD would have been a lot less fulfilling. Though of course I made sure to help you out as well, I'm sure the LHC Minecraft

project would have took a lot longer if I didn't teach you how to run... Thank you as well for being patient especially with the equipment I broke (though, after reading your thesis and the things you broke I can see why). On a similar note, thank you to ATLAS for the shout-out when I broke the FTK on run control.

Thank you of course to Giuliano for the huge amount of help with my analysis, without which I would probably still just be trying to start compiling.

On a similar note thank you to Juraj and Hillier for the help on my trigger work, and thank you to Dave, Chisholm, Miriam, Paul and Kostas for the advice throughout.

Thank you to Tim, James and Adam for sticking with me, though not managing to visit me in 8 years. And thank you to Louis for the free dentistry, I expect you to prescribe me some lucozade for mentioning you. Thanks as well to Max for tricking me for a full day that you were visiting me. Thank you to Rob, Dipto, Pritpal, Matt, Shelf, Alex and George for the good times.

Thank you to John Wilson, Paul and Nigel for the help and motivation throughout my undergrad, without which I certainly would not be here today, and thank you to Mr Hall and Mr Gunawardena for starting my love for physics. As well, thank you to Andreas for the invaluable opportunity to work over the summer with outreach for LIGO, and for Evgueni for the great help in my master's project, my first real experience of research (I promise I'm not just acknowledging you since you're my examiner).

Thank you for Mike for giving me the opportunity to help out with tours, and of course for taking the time to give my parents a great tour. They got you a bottle of wine to thank you, but you were away and I ended up drinking it.. I'll get you another if I come back to CERN someday. Similarly, thank you to Dwayne for the good times and helping me with the virtual visits.

There is of course much more people to thank, but I'm already beyond the trend of 1-2 pages of acknowledgements, so I will just mention thank you to everyone else in the department and otherwise that helped to make the past few years a great time.

Finally thank you to my mum, dad, nan, Grandad Colin and Grandad Les.

Dedicated to my Grandad Les

Contents

List of Tables

List of Figures

DEFINITIONS OF ACRONYMS

SM Standard Model

DM Dark Matter

DE Dark Energy

ATLAS A Toroidal Large hadron collider ApparatuS

LHC Large Hadron Collider

ISR Initial-State Radiation

FSR Final-State Radiation

p_{T} Transverse Momentum

LJPT Leading Jet p_{T}

$p_{\mathrm{T}}^{\mathrm{recoil}}$ Recoil Transverse Momentum
'missing' momentum required to conserve momentum

$E_{\mathrm{T}}^{\mathrm{miss}}$ Recoil Transverse Momentum

XE Recoil Transverse Momentum

MET Recoil Transverse Momentum

eV ElectronVolt

HL-LHC High-Luminosity LHC

CMS Compact Muon Solenoid

q Quark

l Lepton

ν neutrino

g Gluon

γ Photon

$W^{+/-}$ W boson

Z Z boson

H Higgs boson

u, d, s, c, t, b up,down,strange,charm,top,bottom quark

e, μ, τ electron,muon,tau lepton

WIMP Weakly Interacting Massive Particles

χ WIMP

DMA Dark Matter Axial-vector

DMP Dark Matter Pseudo-scalar

ϕ Scalar Dark Energy field

$\mathcal{L}$ Lagrangian

H_0 Hubble constant

Q_{tr} Momentum transfer in hard parton scatter

MC Monte Carlo

LEP Large Electron-Positron collider

LUCID LUminosity measurement using Cerenkov Integrating Detector

ALFA Absolute Luminosity For ATLAS

SCT SemiConductor Tracker

LAr Liquid Argon (calorimeter)

FCal Forward Calorimeter

L1 Level 1

HLT Higher Level Trigger

CR Control Region

SR Signal Region

CR1e0b CR 1 electron 0 b-jets

CR1mu0b CR 1 muon 0 b-jets

CR1e1b CR 1 electron 1 b-jets

CR1mu1b CR 1 muon 1 b-jets

CR1l1b CR 1 lepton 1 b-jets

CR2e CR 2 electrons

CR2mu CR 2 muons

NCB Non-Collision Background

bornkt transverse momentum of the interacting partons

RECO Reconstructed

CKKW Matching Catani, Krauss, Kuhn, Webber Matching

PTV Transverse Momentum of Vector boson

UP Up variation

DOWN Down variation

PDF Parton Density Function

MPI MultiParton Interaction

JES Jet Energy Scale

VH No energy deposited in hadronic calorimeter

ivar isolated from other particles

nod0 no transverse impact parameter cuts

CHAPTER 1

Introduction

Despite the success of the Standard Model (SM) of particle physics, there are a number of measurements, particularly in the astrophysical and cosmological sectors, that indicate the existence of Beyond the Standard Model physics. Two of the largest indications of beyond the Standard Model physics in these sectors are called Dark Matter (DM) and Dark Energy (DE).

The rotational speed of stars in galaxies and gravitational lensing imply beyond the Standard Model physics [1–3]. These observations require either changes to the standard r^{-2} scaling of gravitational force or more unseen non-luminous matter than regular matter, dubbed dark matter. Recent observations of galaxy cluster collisions [4], cannot be explained by any non-standard gravitational force that scales with the observed mass, demonstrating the observation of dark matter.

The observation of the accelerated expansion of the universe (dubbed dark energy) requires beyond the Standard Model physics. The first observation of dark energy

came from measurements of supernovae [5,6]. Recent observations come in the form of precision measurements of the cosmic microwave background [7] and the large scale structure of the universe [8].

The "A Toroidal Large hadron collider ApparatuS" (ATLAS) experiment, described in Chapter 3, has been collecting particle collision data at the Large Hadron Collider (LHC) since 2010. Dark matter interacts with Standard Model matter with only low cross sections, prohibiting direct detection with ATLAS. However, dark matter production can be constrained by its influence on Standard Model particles produced in association with it at the LHC. One approach used by the monojet search (explained in detail in Chapter 4) vetos particles other than jets, measures all final state particles from a selected collision and calculates the vector sum of the transverse momentum (p_{T}). As the initial protons that collide have $p_{\mathrm{T}} \approx 0$, a large total p_{T} in the final state indicates the production of undetected particles carrying missing transverse momentum ($p_{\mathrm{T}}^{\mathrm{recoil}}$, defined in Section 4.2.6), allowing constraints to be placed on dark matter models that involve the production of undetected particles.

A Feynman diagram of a typical monojet event produced in association with dark matter is shown in Figure 1.1. In this diagram the jet arises from Initial State Radiation (ISR) (similarly the jet could arise from Final State Radiation (FSR)), allowing probing of generic beyond the Standard Model physics as it does not require that the jet directly interacts with beyond the Standard Model particles, only that they interact with at least one Standard Model particle. In comparison to other $P_{\mathrm{T}}^{\mathrm{recoil}} + X$ searches, the monojet search has a large number of events from initial state radiation since $\alpha_S \gg \alpha_{EW}$ [9].

An event display of the highest $P_{\mathrm{T}}^{\mathrm{recoil}}$ monojet event detected with the ATLAS detector is shown in Figure 1.2.

By the end of Run 2 (the end of 2018, after 8 years of data taking, including shutdowns), ATLAS had recorded 147 fb^{-1} of $\sqrt{s} = 13$ TeV (tera electronVolts) proton-

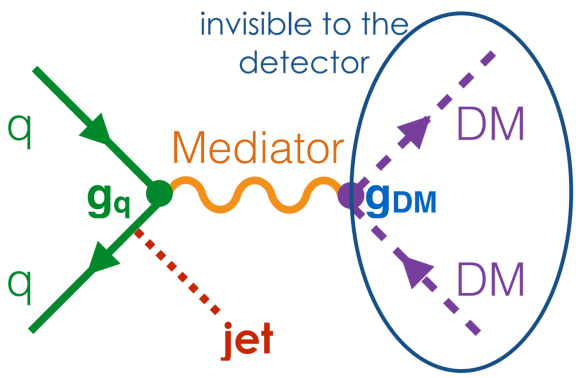

Figure 1.1: A typical monojet signature arising from initial state radiation from a quark that collides with another quark, forming a mediator that decays to dark matter candidates. The jet is detected and influenced via recoiling off the dark matter which is undetected. No coupling between the jet and dark matter is required, allowing probing of generic dark matter models.

proton collision data, an average of ≈ 18 fb^{-1} per year. It is aimed to record over 3000 fb^{-1} by 2037, requiring $\gtrapprox 160$ fb^{-1} per year, which will greatly increase sensitivity to many dark matter models due to their low production cross sections requiring a large amount of statistics to distinguish them from background. Part of this increased rate of data taking is expected to be reached by having shorter periods of shutdown, however this alone will not allow recording the desired amount of data. In addition, the LHC will be upgraded to the High-Luminosity LHC (HL-LHC), increasing the peak luminosity and time spent at peak luminosity.

The increased luminosity at the HL-LHC results in a large increase in the radiation dose the ATLAS detector receives, in particular the sub-detectors near the collision point. In addition, due to the desire for shorter periods of shutdown, there will not be time to replace large sections of the detector during the HL-LHC period of operation. Therefore, it is required for the inner detectors to be made much more radiation hard so that they may survive the increased radiation without requiring replacement.

The closest sub-detector of ATLAS to the collision point is the inner detector, which currently consists of the pixel detector, the semiconductor tracker and the transition radiation tracker. For the HL-LHC upgrade the transition radiation tracker will be removed and the inner detector will be fully based on silicon trackers. It is important

to test the radiation hardness of the new silicon tracker before it is added to ATLAS. To do this, the MC40 proton cyclotron beamline in the University of Birmingham is used which can deliver in hours doses equivalent to that which will be experienced over the full HL-LHC lifetime, at proton energies of up to 36 MeV.

To reliably determine the radiation hardness of the new inner detector components, it is necessary to know the fluence they have been irradiated with accurately and precisely, hence a beam monitoring system has been developed for the MC40 cyclotron as detailed in Chapter 7.

Throughout this thesis, the monojet search performed at the ATLAS detector will be described, along with some of its recent achievements and improvements that have been made to it in recent years. In particular, a new dark energy model is investigated using the monojet search, the first time dark energy has been investigated with a collider based experiment. Relevant theory behind the monojet search will be discussed in Chapter 2 and the ATLAS detector and LHC which is used for these studies described in Chapter 3. Then in Chapters 4 and 5 the monojet analysis and recent improvements to it are outlined, finally with the recent results shown in Chapter 6.

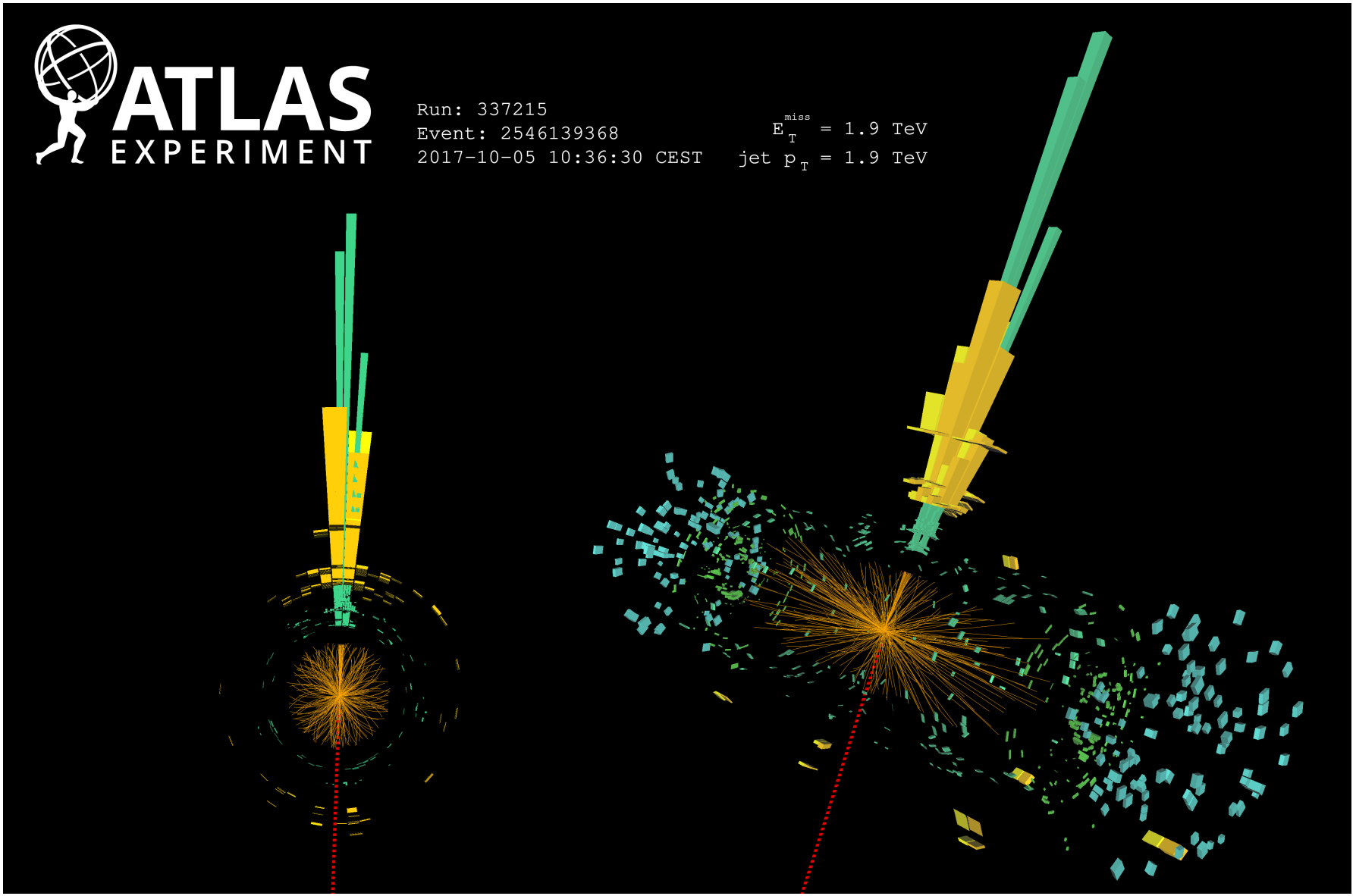

Figure 1.2: A monojet event with lead jet $p_{\mathrm{T}} = 1924$ GeV, $P_{\mathrm{T}}^{\mathrm{recoil}} = 1913$ GeV, the highest $P_{\mathrm{T}}^{\mathrm{recoil}}$ monojet event detected by ATLAS. No other jets with $p_{\mathrm{T}} > 30$ GeV are found in this event. Green and yellow bars correspond to the energy depositions in the electromagnetic and hadronic calorimeters, respectively, discussed in Section 3.2.4. The $P_{\mathrm{T}}^{\mathrm{recoil}}$ is shown as the red dashed line on the opposite side of the detector [10].

CHAPTER 2

Theory

The Standard Model of particle physics is a quantum field theory and it is currently the most successful description of the interactions under all of the known fundamental forces other than gravity (i.e. the electromagnetic force, weak force and color force). The Standard Model has arguably been tested to a higher level of precision than any other theory in physics; for example the measurement of the electron magnetic moment, $g/2$, is in agreement with the Standard Model prediction to a precision of greater than one part in a trillion [11]. In addition, the Standard Model predicted the existence of many particles before their discovery. The final fundamental particle predicted by the Standard Model was the Higgs Boson, the discovery of which the ATLAS and the Compact Muon Solenoid (CMS) experiments announced in 2012 at global significances of 5.1σ and 4.6σ respectively [12, 13], completing the Standard Model.

2.1 Feynman diagrams

Particles within a quantum field theory are described as excitations of a quantum field, and hence interactions of particles are due to the interaction of fields. An interaction term in a quantum field theory for n fields ϕ_i is given in general by Equation 2.1, where g is a dimensionless coupling constant that determines the amplitude of the interaction:

$$\mathcal{L} = g \prod_{i=1}^{n} \phi_i. \tag{2.1}$$

This can be represented graphically as a vertex in a Feynman diagram with n lines. For example the case of $n = 4$ is shown by Figure 2.1. It may be thought that this leads to an infinite number of possible vertices in any quantum field theory, since n can be arbitrarily high; however the number of fields in a vertex is constrained by the requirements that the theory is renormalizable. For a renormalizable theory the sum of the dimensions of all fields at a vertex must be less than four [14].

In four spacetime dimensions fermionic fields have a dimension of $E^{\frac{3}{2}}$ while bosonic fields have a dimension of E^1 [15], constraining the largest number of fields to a vertex to 4 bosonic fields.

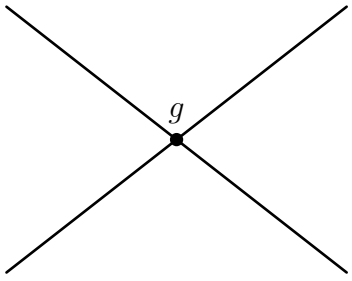

Figure 2.1: Four fields interacting at a vertex with coupling g.

Furthermore, the constraint on the dimension of the fields at a vertex prevents direct interaction between fermions without a bosonic mediator, other than the trivial case of 1 fermion going into a vertex and 1 fermion coming out (i.e. simple prop-

agation of the field). Three or more fermionic fields to a vertex are not possible, but two fermionic fields + one bosonic field is possible, allowing vertices such as Figures 2.2 & 2.3, which respectively represent two incoming fermionic fields annihilating to produce an outgoing bosonic field, and an incoming fermionic field scattering off a bosonic field to produce an outgoing fermionic field (which depending on the interaction may or may not be the same fermionic field). Importantly, while these two Feynman diagrams represent different interactions, they have the same amplitude. In Figure 2.2 the arrow representing one of the fermionic fields is reversed. This arrow does not represent the direction of the fermion's momentum, but the fermionic flow, which must be continuous. The fermionic flow pointing backwards represents an antifermion particle, which has all quantum numbers reversed and hence a reversed fermionic flow.

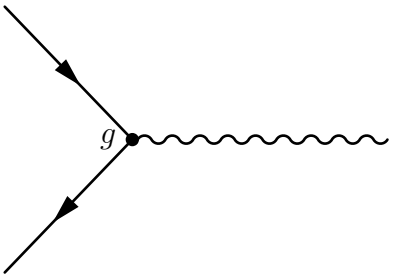

Figure 2.2: Two incoming fermionic fields annihilating into a bosonic field. The arrow for one of the fermions is reversed, representing an antifermion particle.

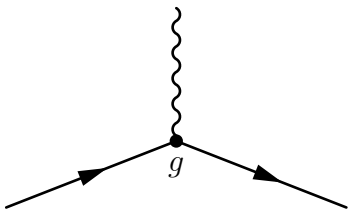

Figure 2.3: One incoming fermionic field scattering off a bosonic field into an outgoing fermionic field.

After constructing the vertices for a quantum field theory, a Feynman diagram can be constructed with multiple vertices allowing more complicated interactions. In fact, an infinite number of vertices may be added, and any particular transformation from initial state to final state will have an infinite number of possible Feynman diagrams that can describe it. The more vertices a Feynman diagram has, the higher order it is said to be.

The total amplitude of any initial state to final state transition can be calculated by summing up the contributions to the amplitude from the infinite number of Feyn-

man diagrams that describe the transition. This might at first make it seem that every total amplitude is divergent, however thanks to Wick's Theorem when g is small (which is true for all interactions in the Standard Model at energy scales corresponding to proton collisions at the LHC), the quantum field theory is perturbative, which results in the more vertices in a diagram, the smaller its amplitude. This allows the total amplitude to be predicted by just considering low order diagrams, and the precision of the prediction can be increased to whatever is desired by including more higher order diagrams.

With all this in mind, the amplitude for the transition from two incoming fermionic fields to two outgoing fermionic fields (ignoring the trivial case where there is no interaction) can be calculated as shown in Figure 2.4. Each time a new fermionic or bosonic line is produced this line may be an entirely new field and hence each vertex may have its own independent coupling factor which has not been labelled for simplicity.

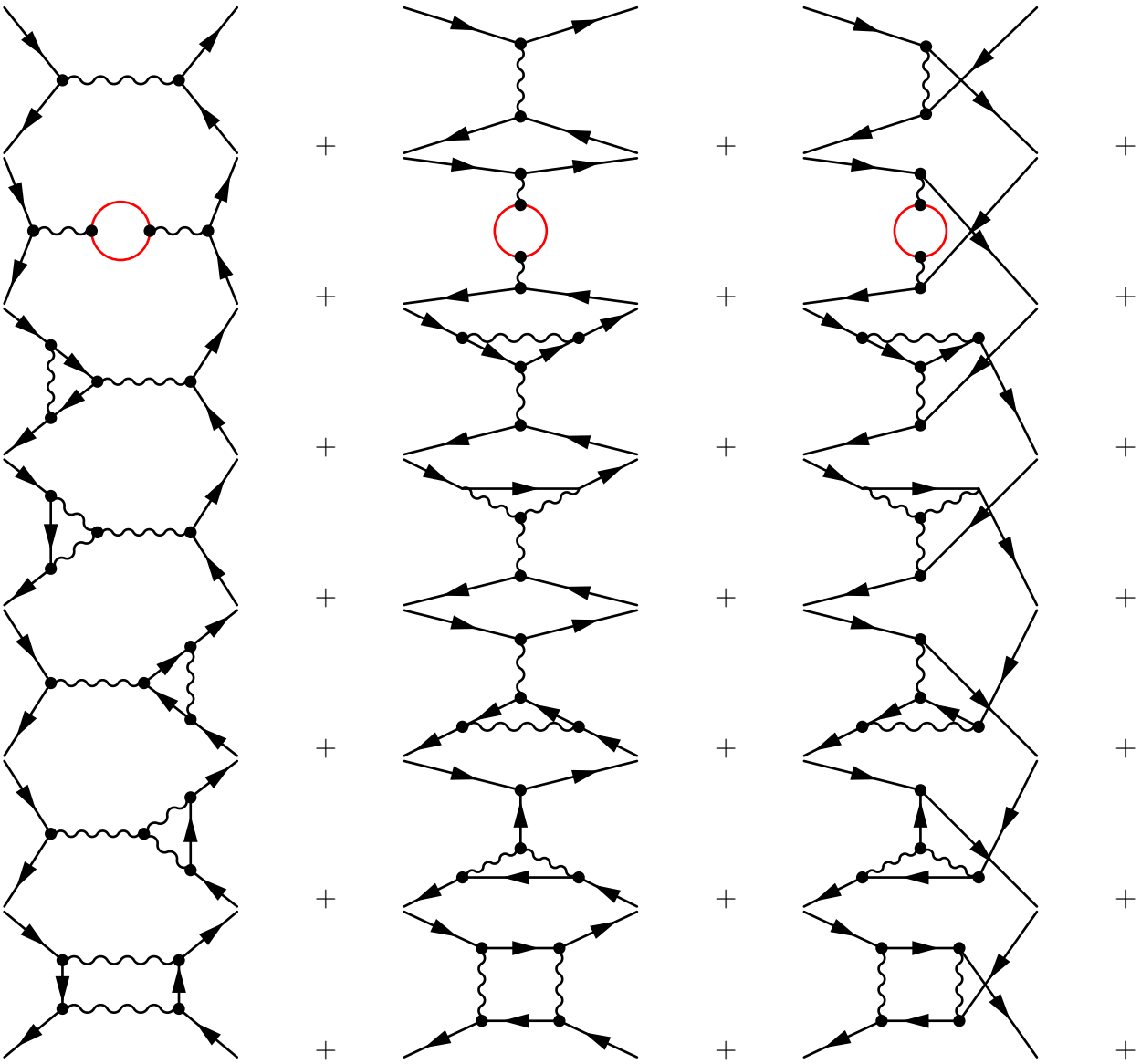

. . . (Diagrams with more than 4 vertices)

Figure 2.4: Two incoming fermionic fields interacting and producing two outgoing fermionic fields; all Feynman diagrams at leading (two vertices) and next-to-leading order (four vertices). The first, second and third columns represent s-channel, t-channel and u-channel processes respectively. u-channel diagrams are only involved where the 2 final state fields are indistinguishable (e.g. in the case of $e^-e^- \to e^-e^-$). Vertices are represented by a dot; importantly the crossing of the outgoing fermionic fields in the u-channel does not involve a vertex. Diagrams with two plain red lines in them represent the sum of two Feynman diagrams, one where both red lines are bosonic fields and one where both red lines are fermionic fields.

2.2 Standard Model

As mentioned in the previous section, each vertex in a Feynman diagram involves a coupling constant, and incoming and outgoing fields. The Standard Model outlines the fundamental fields and the coupling constants of their interactions.

The field content of the Standard Model is shown in Figure 2.5. There are three generations of each fermionic field. Each generation is identical to the previous generation except for having a higher mass, i.e. the coupling constant at each vertex is identical if any fermionic field is replaced with one of the same type but from another generation, except for interactions with the Higgs field, which depend on mass. This is with the potential exception of the neutrinos, for which it is not known if the mass increases as the generation is increased, nor is it known how or whether they couple to the Higgs field. In this case generation refers to the neutrino mass eigenstates, conventionally notated as ν_1, ν_2, ν_3, where it is known that the mass of $\nu_2 >$ the mass of ν_1, but it is not known whether ν_3 is the most massive or least massive.

The gluon field mediates the color force and has a non-zero coupling constant with any field that has color charge, i.e. the quark field and the gluon field itself, allowing a pure self interaction.

The photon field mediates the electromagnetic force and has a non-zero coupling constant with any field that has electric charge, i.e. the W fields and all the fermionic fields in the Standard Model other than the neutrinos.

The Z and W fields mediate the weak force, with a non-zero coupling with all the Standard Model fermionic fields and with each other.

The Higgs field couples to the mass of the other fundamental fields and itself, with the potential exception of the neutrino fields.

These rules for the coupling constants of the various fields allow the Feynman dia-

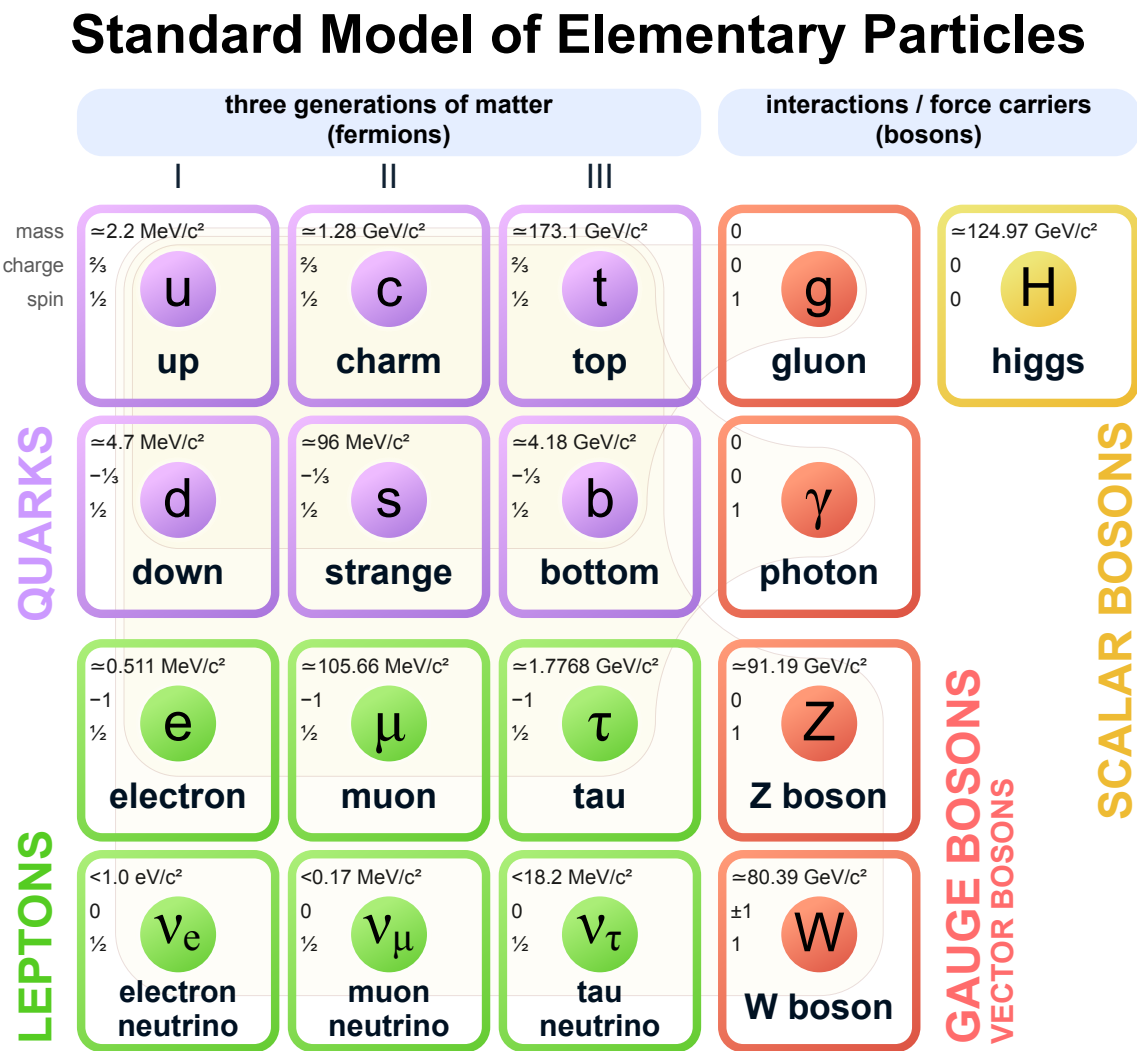

Figure 2.5: Field content of the Standard Model [16].

gram vertices in Figure 2.6.

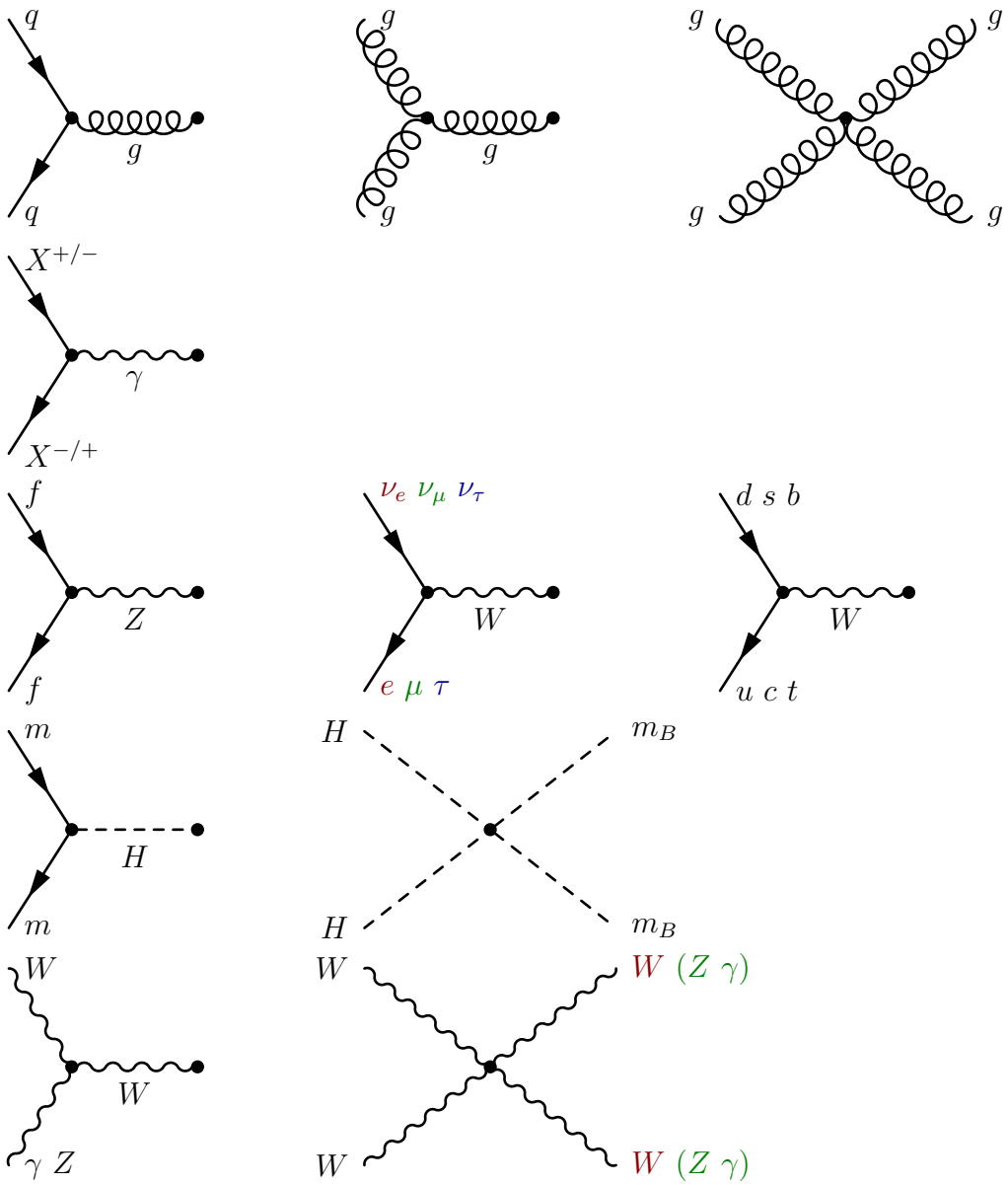

Figure 2.6: All vertices allowed in the Standard Model: q is any quark, $X^{+/-}$ is any charged particle, γ is a photon, f is any fermion, m is any particle with mass (with the possible exception of the neutrinos), m_B is any boson with mass. For diagrams with multiple particle labels on one line, one particle label is chosen. For diagrams with coloured particle labels the particles must be chosen so there is two of one colour in the diagram. i.e. for the four electroweak boson case the valid diagrams are $WWWW$,$WWZZ$,$WW\gamma\gamma$,$WWZ\gamma$. Every interaction in the Standard Model is made up of combinations of these vertices.

2.2.1 Quantum chromodynamics running

As mentioned in Section 2.1 the magnitude of the coupling constant at a vertex in a Feynman diagram is important to the amplitude of the Feynman diagram. In general these coupling constants need not be constant. Particularly relevant for the monojet analysis, which will be discussed later in this thesis, the coupling constant in quantum chromodynamics, α_S which governs the coupling between objects with color charge, varies depending on the momentum transfer.

This variation is largely due to a charge screening mechanism. A color charged particle can emit virtual $q\bar{q}$ pairs and then reabsorb them. A similar effect occurs with e^-e^+ pairs in electromagnetism, which causes the coupling constant to increase with higher momentum transfers. However, in quantum chromodynamics as the mediator particle, the gluon, is charged itself pairs of virtual gluons can also be emitted and reabsorbed. This has the effect of causing the coupling constant to increase at lower momentum transfers, and is a larger effect than the $q\bar{q}$ case.

This effect allows color charged particles at high energy to appear free, referred to as asymptotic freedom, while at low energy color charged particles are confined, which allows hadronization to occur which is discussed in the next section.

2.2.2 Standard Model collision processes at the LHC

In this thesis, only high energy ($\sqrt{s} = 13$ TeV) proton-proton collisions in the LHC are considered. At this high energy, collisions occur between individual partons (fundamental particles within protons or other composite particles), with most 'hard' collisions (collisions with large momentum transfers, which are predominantly what is considered in this thesis) having negligible effect from the overall structure of the proton and other partons.

Due to this, the LHC can be considered a quark/gluon collider, at least for the hard collisions considered here. The vertices in Figure 2.6 can be used to construct

Feynman diagrams showing the possible ways for these to collide. Six common Feynman diagrams for these collisions are shown in Figure 2.7. This is not an exhaustive list of all possible collisions, and the relative probability of these, and other, collisions depends upon the final state searched for.

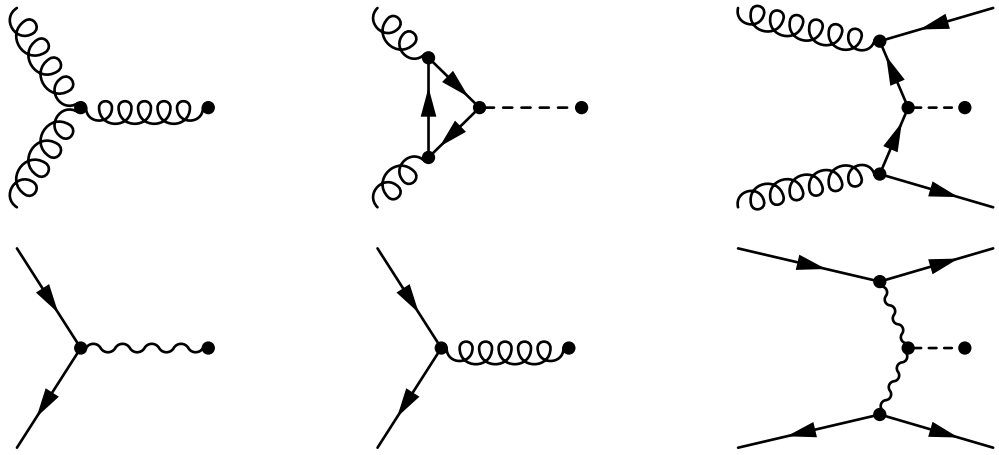

Figure 2.7: Common LHC collision Feynman diagrams, without the final state included. The full Feynman diagram can be produced by adding the final state particles desired to the unfinished vertices, following the possible vertices in Figure 2.6 (if following the Standard Model). The top row shows gluon-gluon interactions from left to right: direct gluon fusion, gluon fusion mediated by a fermion (quark in the Standard Model) loop, and fermionic fusion (quark in the Standard Model). The second row shows quark-antiquark interactions, from left to right: quark annihilation to an electroweak boson, quark annihilation to a gluon, vector boson fusion.

2.2.3 Jets

As shown in the top row of Figure 2.6, the gluon can couple with both itself and the quarks. As a result of this as a high energy quark or gluon propagates over a distance of order femtometres within the detector volume, it can radiate gluons from itself, or in the case of a gluon convert to $q\bar{q}$, producing more as it continues, lowering its energy. Eventually, as the energy is reduced enough, hadronization occurs; the quarks and gluons that have been formed produce a large number of hadrons all travelling in approximately the same direction as the quark/gluon that was originally produced in the primary collision. These particles travelling together are referred to as a jet. An example showing a particle collision with many jets produced is shown in Figure 2.8. As the LHC is a hadron collider, involving collisions of quarks/gluons,

most collisions produce a large number of jets, both from the colliding partons and from the remnants of the protons. Therefore to extract information about the collision from jets, a large amount of background reduction is required to distinguish between the jets that are involved in the collision being investigated and additional unwanted jets.

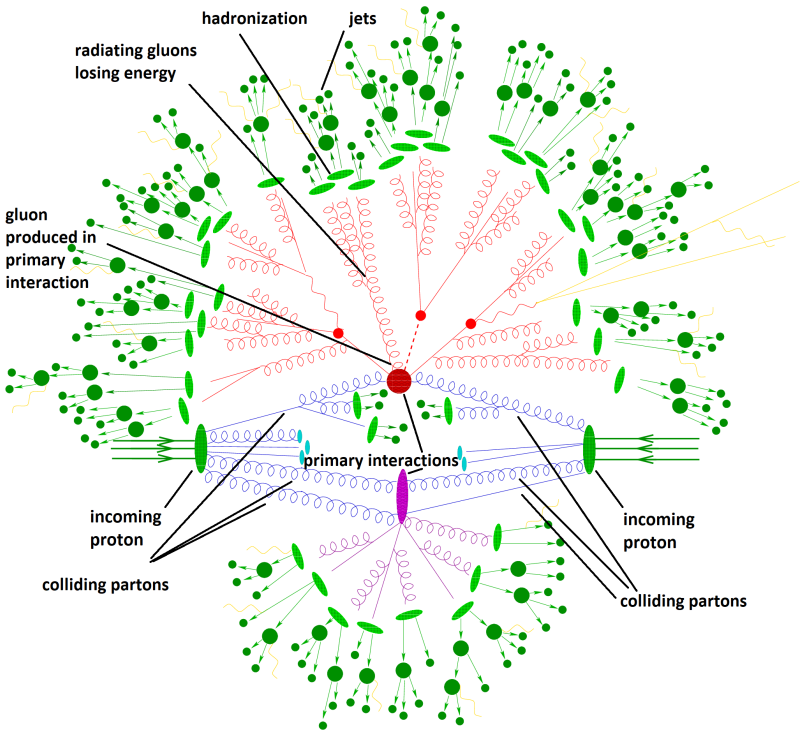

Figure 2.8: A typical proton-proton collision at the LHC, producing a large number of jets from various sources. There are two primary interactions in this example, shown as the purple and dark red shaded ellipses, from colliding partons, that then produce many quarks and gluons shown in the same colour as the primary interaction that go on to radiate, lose energy and hadronize to form jets [17].

2.2.4 Initial/final state radiation

As the LHC is a quark/gluon collider, and there exist Standard Model vertices of $q \rightarrow qg$ and $g \rightarrow gg$, as shown on the top row of Figure 2.6, any incoming quark/gluon can radiate a gluon, which could go on to form a jet of particles that could be detected. Radiation from an incoming particle is referred to as initial-state radiation, and the same process from outgoing particles is referred to as final-

state radiation. Every Feynman diagram representing an event that occurs in the LHC can be modified to include initial state radiation; this allows very generic probing of different models by detecting initial state radiation, see Figure 2.9. This effect is independent of any new particles produced, as the initial state radiation couples purely with the incoming quarks/gluons. This initial state radiation can be measured and, via momentum conservation, the properties of any other particles produced in the collision can then be inferred. It can be seen from Figure 2.6 that there are also other forms of initial state radiation possible (e.g. photons), however the coupling strength between quarks and gluons is much larger than any other coupling in the Standard Model and hence there is a much larger amount of jet initial state radiation than other forms of initial state radiation.

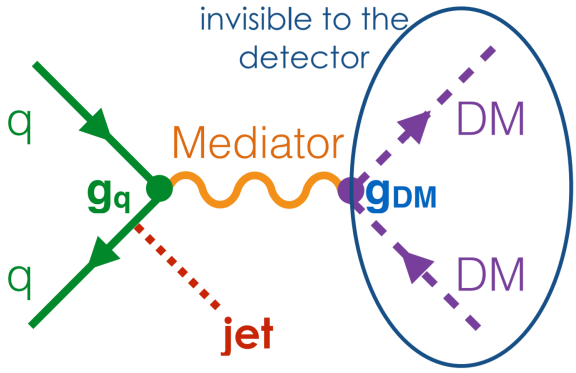

Figure 2.9: A typical monojet signature arising from initial state radiation from a quark that collides with another quark, forming a mediator that decays to dark matter candidates. The jet is detected and influenced via recoiling off the dark matter, which is undetected. No coupling between the jet and dark matter is required, allowing generic probing of dark matter models.

2.3 Beyond the Standard Model

While the Standard Model is a very successful theory, as mentioned in Chapter 1, there is strong evidence for physics beyond the Standard Model. The simplest way to extend the Standard Model is via a quantum field theory with additional fields and coupling constants than those that exist in the Standard Model, and hence additional vertices. These new fields can potentially interact with each other

producing a sector rich with new interactions, referred to as the dark sector. It is possible to produce beyond the Standard Model theories that either do or do not involve any couplings to Standard Model fields. However, only those that do couple to Standard Model fields are considered at the LHC, as it is possible to probe them only if they interact with Standard Model particles.

As the monojet search technique is able to probe a large range of beyond the Standard Model theories, a variety are investigated here.

2.3.1 Weakly Interacting Massive Particles (WIMPs)

WIMPs are one of the simplest possible additions to the Standard Model. WIMPs are described analogously to the three Standard Model vertices involving fermions and weak bosons on the third row of Figure 2.6. The Standard Model fermion fields are replaced with new fermion fields, χ, beyond the Standard Model, that have different couplings to the weak bosons. In addition, WIMP models may replace the weak bosons in these vertices with a new bosonic field from beyond the Standard Model, M. While direct and indirect detection experiments look for the scattering of a WIMP from nuclei and for its annihilation into Standard Model particles, respectively, the LHC experiments search for evidence of the production of WIMPs in pp interactions. An example production of a WIMP candidate in pp interactions via a $q\bar{q}$ collision is shown in Figure 2.10.

Complementary sensitivities are achieved in this way, with collider experiments providing a unique discovery potential in the mass region 1 GeV $\lesssim m_\chi \lesssim$ 100 GeV. Models in which M is exchanged in the s-channel and is a spin-0 pseudoscalar mediator (DMP) or a spin-1 axial-vector mediator (DMA), with negative or positive parity respectively, or in which M is exchanged in the t-channel, are investigated using simplified models, which depend only on the spin and $(g_q, g_\chi, M_{mass}, \chi_{mass})$ [18–20].

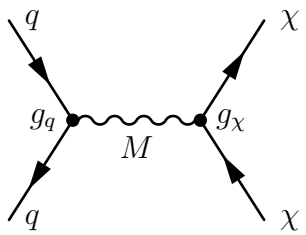

Figure 2.10: A representative leading order WIMP production Feynman diagram. An incoming quark and anti-quark colliding, interacting with a virtual mediator M (which may be a Standard Model weak boson or a beyond the Standard Model boson) with a coupling g_q (that may be different from the usual coupling at a vertex between two quarks and a weak boson if M is beyond the Standard Model). This mediator then interacts with a coupling g_χ to produce two χ (WIMP) particles.

2.3.2 Dark energy

The following discussion on the theory of dark energy and the validity of the dark energy effective field theory is largely taken from the paper [21], of which I am a significant author. Dark energy is a term that refers to the accelerating expansion of the universe. Its existence has been corroborated by precision measurements of the cosmic microwave background radiation [22] and the large scale structure of the universe [8]. It has become a very active field with many experiments currently under construction or planned [23,24]. In order to provide a theoretical description of dark energy, a plethora of models have been proposed ranging from modifications of Einstein's gravity theory to the addition of new particles beyond the Standard Model [25, 26]. Despite the wide array of models that are consistent with observations, no prevalent theory exists and it has also been shown that cosmological observations alone are unable to distinguish modified gravity models from those with additional fundamental fields [27, 28]. Input from particle physics experiments is therefore necessary to elucidate the microscopic nature of dark energy.

The detection of dark energy at colliders relies on the assumption of a non-zero interaction between the dark energy and Standard Model fields. An effective field theory framework provides the most conservative way to search for dark energy, since it integrates out the microscopic dynamics of the dark energy interactions, which

are completely unknown. Such a model has been developed in [29], following the framework of the Horndeski theories [30], which provides the most general framework for describing dark energy theories with one scalar field and second order equations of motion.

A representative Feynman diagram of a dark energy production event is shown in Figure 2.11. This model introduces a new scalar field, ϕ, in an attempt to explain observations of dark energy cosmologically. The lagrangian can be represented by an operator product expansion such as

$$\mathcal{L} = \mathcal{L}_{SM} + \sum_i C_i \mathcal{L}_i + \frac{1}{2} m_\phi^2 \phi^2, \tag{2.2}$$

where C_i are called Wilson coefficients, and m_ϕ is the mass of the new scalar field.

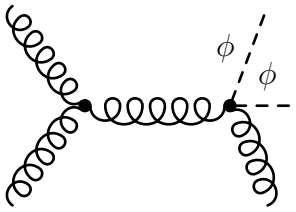

Figure 2.11: Diagram showing monojet production in association with a pair of dark energy scalar particles ϕ in the $\mathcal{L}_2$ interaction.

We focus on the case where $m_\phi = 0.1$ GeV, which is light in comparison to typical collider scales, and hence we consider $\frac{1}{2} m_\phi^2 \phi^2 \approx 0$. This value of m_ϕ is much larger ($\approx 10^{41}$ times larger) than the value required to correctly reproduce the equation of state that dark energy is observed to follow over cosmological scales ($m_\phi = \mathcal{O}(H_0) \approx 10^{-42}$ GeV, where H_0 is the Hubble constant) [31], however in collider experiments all m_ϕ low enough such that $\frac{1}{2} m_\phi^2 \phi^2 \approx 0$ behave identically and $m_\phi = 0.1$ GeV is easier to simulate.

There are two classes of operators in this model: operators that are invariant under a shift symmetry $\phi \to \phi + c$ and operators that break this symmetry. Operators that break this symmetry contain direct interactions with Standard Model particles and so result in ϕ being unstable on collider length scales; these are not considered

in this study.

There are nine shift symmetric operators of this model allowing Equation 2.2 to be written as

$$\mathcal{L} = \mathcal{L}_{SM} + \sum_{i}^{9} \frac{C_i}{M_i^{(d-4)}} \mathcal{O}_i^{(d)}, \tag{2.3}$$

where M_i is the mass scale of the theory. The lowest order interactions between the new scalar particle and the Standard Model fields are through the operators $\mathcal{O}_1$ and $\mathcal{O}_2$:

$$\mathcal{L}_1 = \frac{\partial_\mu \phi \partial^\mu \phi}{M^4} T^\nu_\nu, \tag{2.4}$$

$$\mathcal{L}_2 = \frac{\partial_\mu \phi \partial_\nu \phi}{M^4} T^{\mu\nu}, \tag{2.5}$$

where $T^{\mu\nu}$ is the stress-energy tensor. As the ϕ field is considered to be stable, the dark energy particles escape the detector and produce a $p_{\mathrm{T}}^{\mathrm{recoil}}$ signature.

The factor $T^{\mu\nu}$ in $\mathcal{L}_2$, Equation 2.5, causes this term to couple more strongly in high four-momentum transfers. The monojet search technique has good statistics in high $P_{\mathrm{T}}^{\mathrm{recoil}}$ signal regions which involve high four-momentum transfers, and hence this search can probe the $\mathcal{L}_2$ coupling well.

However, the factor T^ν_ν in $\mathcal{L}_1$ Equation 2.4, causes this term to couple to all mass terms in the Standard Model. Since the monojet search includes a large contribution to the hadronic cross section coming from massless gluons and low mass quarks in the final states, the $\mathcal{L}_1$ coupling is suppressed significantly. To probe this coupling, and hence set constraints on the leading order terms for this model, therefore requires combination with other search strategies that involve a larger contribution from higher mass objects. The $t\bar{t}$+$P_{\mathrm{T}}^{\mathrm{recoil}}$ search has been investigated due to the large mass of the top quark; an example Feynman diagram for this is shown in Figure 2.12.

Along with the $\mathcal{L}_1$ and $\mathcal{L}_2$ operators investigated, the seven other shift-symmetric operators are: $\mathcal{L}_3$-$\mathcal{L}_5$ correspond to higher-order versions of $\mathcal{L}_1$ and $\mathcal{L}_2$; $\mathcal{L}_6$ corresponds to a (generalised) kinetic term for the dark energy scalar, and operators

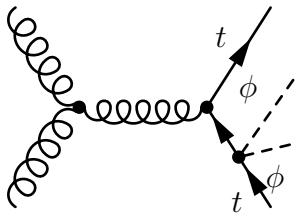

Figure 2.12: Diagram showing $t\bar{t}$ production in association with a pair of dark energy scalar particles ϕ in the $\mathcal{L}_1$ interaction.

$\mathcal{L}_7$-$\mathcal{L}_9$ correspond to the non-trivial galileon terms, where galileons are particles which obey the symmetry $\phi \rightarrow \phi + b_\mu x^\mu + c$ where b_μ and c are constants, referred to as galileons as this symmetry is similar to the symmetry in galilean relativity.

2.3.2.1 Validity of the effective field theory approximation and truncation procedure

The operators that describe the interactions of the dark energy scalar field are obtained by an expansion in the suppression scale M and are therefore valid only in the regime where the momentum transfer is $Q_{tr} << M$, where Q_{tr} is the momentum transfer in the hard parton scattering process. In practice, it is assumed that the effective field theory approximation is valid for events where $Q_{tr} < g_* M$, where g_* is a number that depends on the details of the ultraviolet completion of the model and should satisfy $g_* < 4\pi$, in order for the couplings to be in the perturbative regime [32]. Since the ultraviolet completion (behaviour at arbitrarily high energies) of the dark energy effective field theory model is unknown, a conservative approach for the evaluation of the momentum transfer amounts to using the partonic centre-of-mass energy. This gives

$$Q_{tr} = \sqrt{\hat{s}} = \sqrt{\left(\sum_i p_i\right)^2} < g_* M$$

where i runs over all the partons in the final state, as a condition which should be fulfilled in order for the effective field theory to be valid. For events that do not satisfy this, the iterative rescaling procedure developed in [33] is applied in order to

rescale the effective field theory limits. The procedure amounts to iteratively estimating the fraction of events that satisfy the effective field theory validity criterion and then rescaling the limit as described in [33] until the fraction of valid events reaches 0 or 1.

The evaluation of the rescaled limit relies on the Q_{tr} distribution, which is evaluated at truth level after applying the relevant analysis selection criteria, which for the $j\phi\phi$ case will be described in Chapter 4. The Q_{tr} distributions for the $t\bar{t}\phi\phi$ and $j\phi\phi$ final states are shown in Figure 2.13.

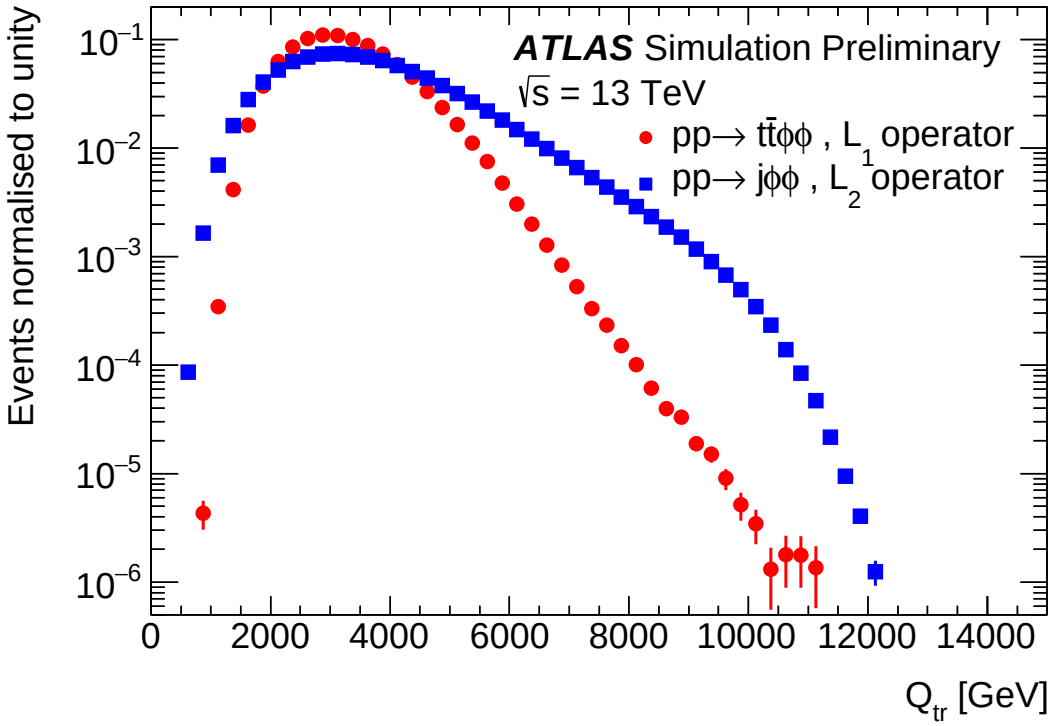

Figure 2.13: Q_{tr} distributions for the $t\bar{t}\phi\phi$ final state involving the $\mathcal{L}_1$ operator and for the $j\phi\phi$ final state involving the $\mathcal{L}_2$ operator, after applying the respective event selection criteria [21].

Some recent constraints both on this dark energy model and WIMP models discussed in Section 2.3.1 are summarised in [34].

2.4 Monte Carlo (MC) simulations

To determine whether measured data better fits the Standard Model or another particular beyond the Standard Model model, it is important to know precisely both the distribution of the Standard Model for whichever property is being measured, and the distribution of the new beyond the Standard Model model being investigated.

To do this, Monte Carlo (MC) simulations are used. Within the monojet analysis, a large number of tools to produce MC are used, including MadGraph [35], Sherpa [36], PYTHIA [37] and POWHEG BOX [38].

There are two main classes of MC simulations, matrix-element generators and parton shower generators. MadGraph is a matrix-element generator, PYTHIA a parton shower generator, while Sherpa and POWHEG BOX includes both.

Matrix-element generators simulate the event using the full quantum mechanical matrix element at any specific jet multiplicity. This method struggles to accurately reproduce jets that involve a large number of emissions producing low energy partons (such as in parton showers shown in Figure 2.8), largely due to these events being very high order, which is computationally expensive, and because quantum chromodynamics becomes non-perturbative at low energy, as discussed in Section 2.2.1.

Parton shower generators instead use a method called Markov chain evolution [17], producing successive emissions, allowing an arbitrarily high number of emissions down to arbitrarily low energy partons. Unlike matrix element generators, which are largely determined by theory, parton shower generators are easily tunable to measured data and hence they are more useful in the low energy regime where quantum chromodynamics theory is not well understood, effectively behaving as an approximation to a very high order diagram.

Usually a matrix-element generator is used to simulate up to the parton shower, and then the results of this are passed to a parton shower generator, which simulates the parton shower.

For the models discussed in this chapter, the WIMPs are generated with POWHEG and showered with PYTHIA8, while the dark energy model is generated in MadGraph and showered with PYTHIA8. For most background samples, they are produced and showered in sherpa.

The output of this is referred to as TRUTH. This TRUTH is then passed to other programs that simulate how this event would affect the detector, primarily GEANT4 [39], producing an output referred to as RECO. For the ATLAS detector, which is discussed in Chapter 3, this is detailed further in [40].

CHAPTER 3

The ATLAS Experiment at the Large Hadron Collider

To find evidence of a particle in a collision that we cannot directly detect requires a good understanding of the collisions and high precision measurements of the particles that we do detect. To do this, the ATLAS detector is used, which sits within the LHC.

3.1 The Large Hadron Collider

The LHC is the world's largest particle accelerator and collider, with a circumference of 26,658.883 m, made up of 8 octants.

The hadrons that the LHC primarily, but not only, accelerates are individual protons in two beams that travel in opposite directions. In this thesis, only proton collisions will be considered.

3.1.1 LHC layout

Each octant of the LHC contains a 528m straight section, an arc section, that itself contains 23 106.9m cells, and two sections to connect arc and straight sections. The sections are arranged such that each octant starts with the end half of an arc, then a straight section, and then beginning half of the next arc with the ending half of this arc being the start of the next octant [41].

The straight sections contain radiofrequency cavities which increase the energy of each proton within the proton beams that pass through it by 485 keV per orbit (from now on I will use 'energy per beam' to mean 'energy per proton per beam' rather than the total energy of the beam), until reaching the desired energy. As of 2018 and for all of the data used in this thesis, the energy is 6.5 TeV per beam, which was achieved in the second run of the LHC (Run 2), while the highest designed energy (which the LHC has not yet reached at the time of writing) is 7 TeV per beam.

As well as the radiofrequency cavities, the straight sections also contain interaction points which are where the protons collide. There are four such interaction points, each of which is encompassed by a particle detector. One of these detectors is the ATLAS experiment, which is the focus of this thesis and will be detailed further in Section 3.2.

Each cell in the arc sections contains 6 dipole magnets, which bend the proton beam's path to follow the path of the LHC. As the beams gain energy, the force required to bend the beams to follow the same path increases, and hence the magnetic field strength is increased over time to maintain the beam orbit. However, magnets used in the LHC which are designed for high magnetic field strengths are not stable at very low magnetic field strengths, hence before reaching the LHC the proton beams are accelerated to 450 GeV by a successive chain of previous accelerators shown in Figure 3.1, and then injected into the LHC.

At a beam energy of 450 GeV the dipole magnets have a magnetic field strength of 0.54 T, while at the maximum designed energy of 7 TeV the dipole magnet's

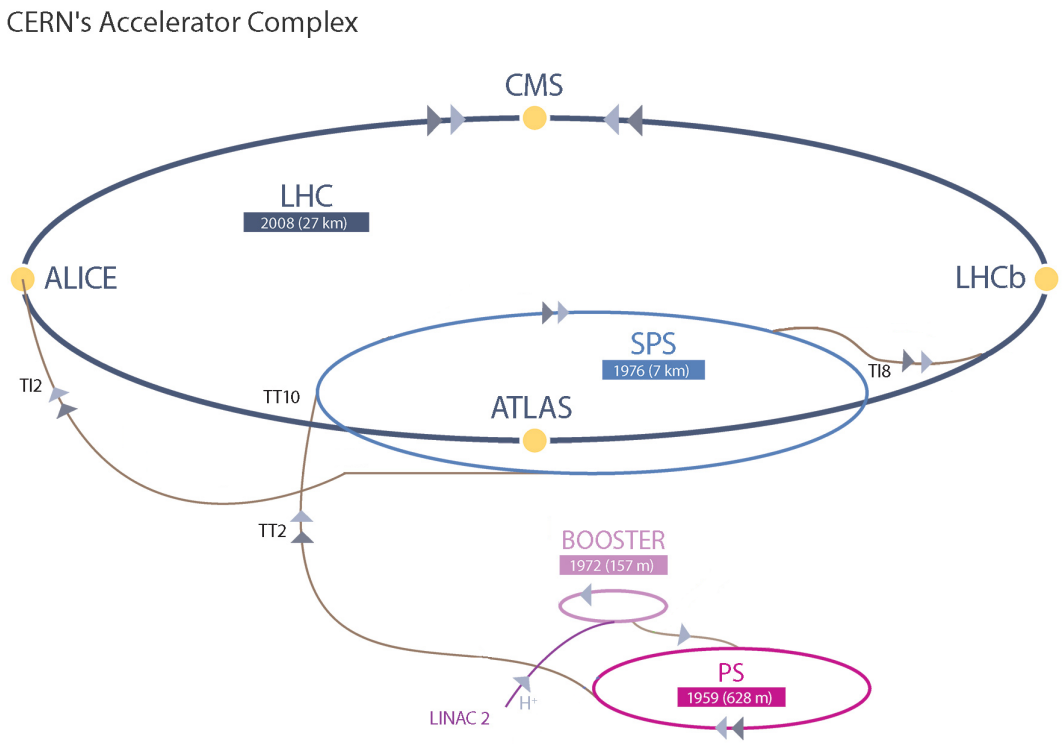

Figure 3.1: The LHC and its preaccelerators [42].

magnetic field strength is 8.33 T.

The long length of the straight sections is not ideal for a hadron accelerator, which would ideally have shorter straight sections and longer arcs. The energy per beam in the LHC is limited not by how much energy can be given to the beams by the radiofrequency cavities but by how much the dipole magnets can bend the beam.

However the tunnel the LHC is built in was originally designed for the Large Electron-Positron collider (LEP) which required the long straight sections for long radiofrequency cavities to replace energy lost due to synchrotron radiation, a problem that hadron colliders have to a much lower degree due to the increased mass of hadrons compared to electrons.

Along with the dipole magnets and radiofrequency cavities, there are many other pieces of instrumentation designed for steering the beam. These are quadrupole magnets which focus the beam, and sextupole magnets which reduce the dispersion of the beam caused by a small spread of momentum among different protons in the

same beam, which results in them taking slightly different paths in the dipole and quadrupole fields.

3.1.2 Filling scheme

The proton beams of the LHC are not continuous beams, but are split into lengths called 'buckets', the size of which are determined by the frequency of the radiofrequency cavities. The LHC has 3564 buckets, which are 24.95 ns apart, of which 2808 are occupied by proton bunches. The distribution of occupied bunches to empty bunches is given by the filling scheme which is non-trivial and occasionally changed in an attempt to optimise the number of collisions while ensuring the beam can be safely dumped if required. An example of a nominal filling scheme is shown in Figure 3.2.

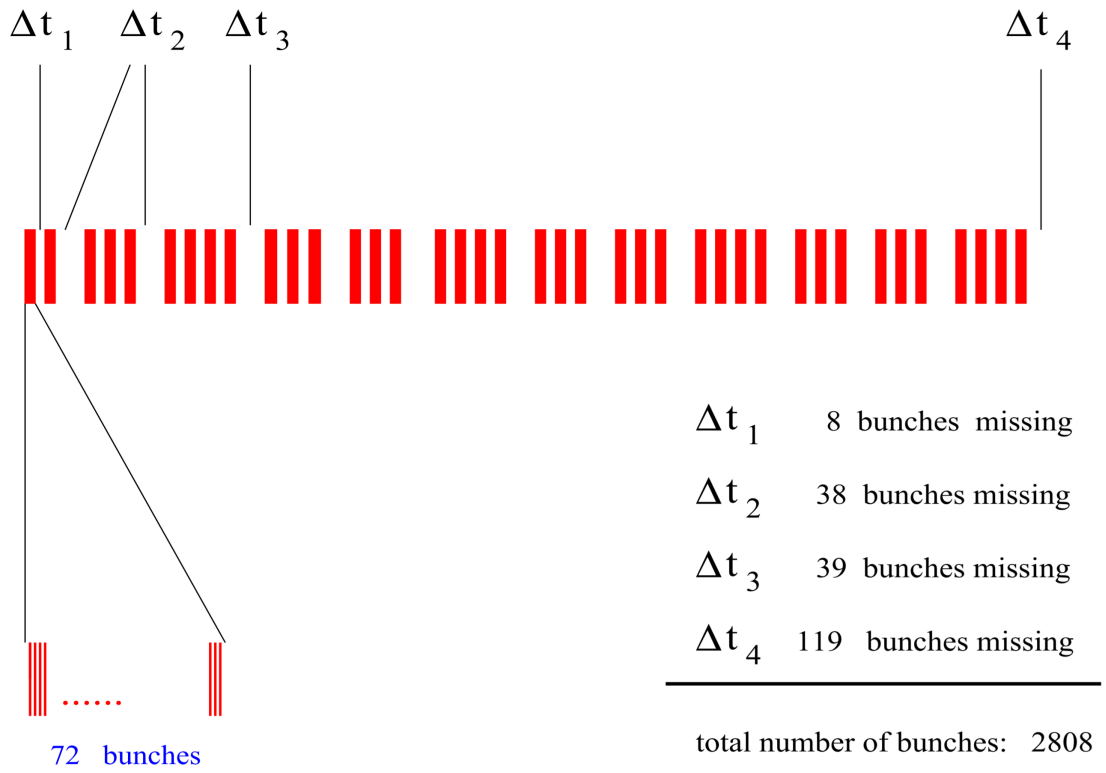

Figure 3.2: An example filling scheme, showing all the buckets in a fill, buckets which are filled with proton bunches are shown in red. There is a long gap (Δt_4) after the final filled bunch before repeating to help with beamdumps. [43].

3.1.3 Luminosity

The LHC was originally designed to operate at a peak luminosity (a measure related to the number of collisions per second, $\mathcal{L} = \frac{1}{\sigma}\frac{dN}{dt}$) of $\mathcal{L} = 10^{34}$ cm^{-2}s^{-1} in each fill (where a single fill is the duration of time between protons being injected into the LHC until they are dumped), corresponding to 1.15×10^{11} protons per bunch. However, improvements to the LHC over its lifetime have increased the peak luminosity by over double, up to a peak luminosity, measured by the "LUminosity measurement using Cerenkov Integrating Detector" (LUCID) and the "Absolute Luminosity For ATLAS" (ALFA) detectors which detect small angle inelastic p-p scattering events to measure luminosity, of $\mathcal{L} = 2.1\times10^{34}$ cm^{-2}s^{-1}, as shown in Figure 3.3.

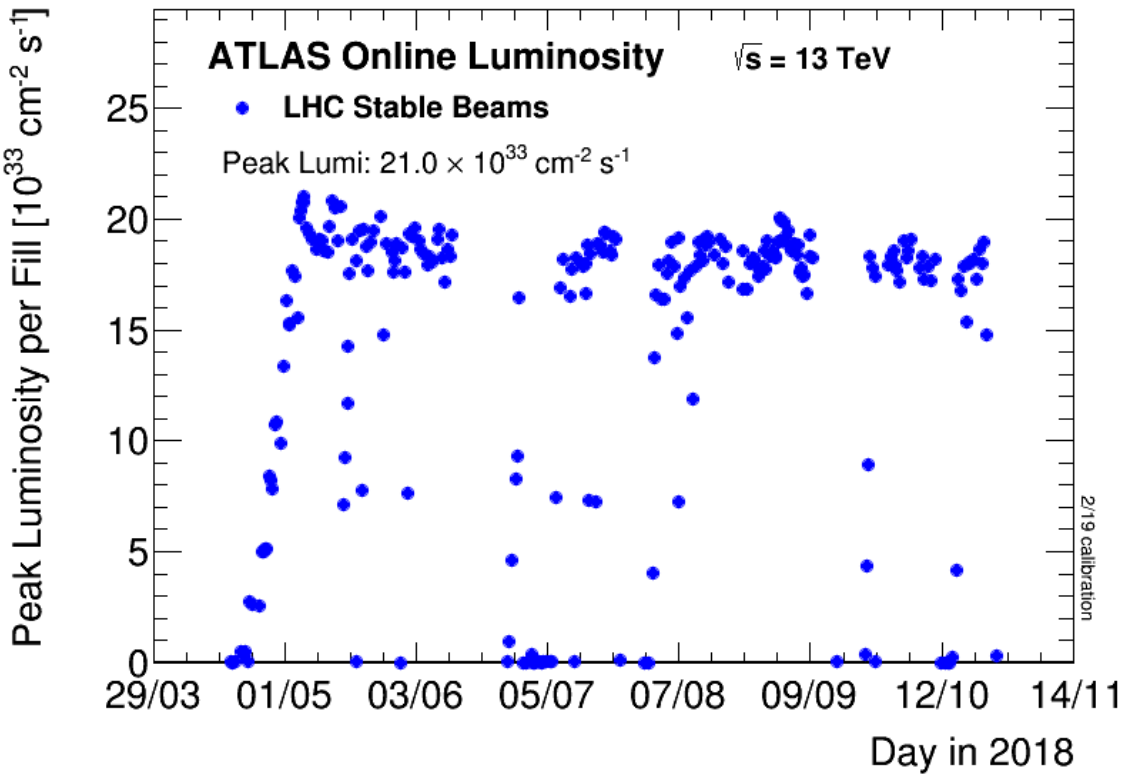

Figure 3.3: Peak luminosity over all 2018 fills [44].

This high luminosity is very useful for the number of events it produces, allowing detection of rare signatures. However, it also brings with it additional challenges, the two most important ones being increased pile-up and increased data-taking requirements.

Pile-up is the number of collisions per bunch crossing, the average of which is as high as 70 in some fills of the LHC as shown in Figure 3.4. A large pile-up increases the difficulty in distinguishing separate collisions. For an example if two collisions occur very close to each other, and both of them produce two muons, it can be difficult or impossible to tell which collision each muon comes from, as when propagating their paths back to the original vertex all of the muons will propagate back to the same location. This could even make this look like a single collision producing four muons instead of two collisions producing two each. Fortunately, the monojet analysis which is considered in this thesis is approximately pile-up independent.

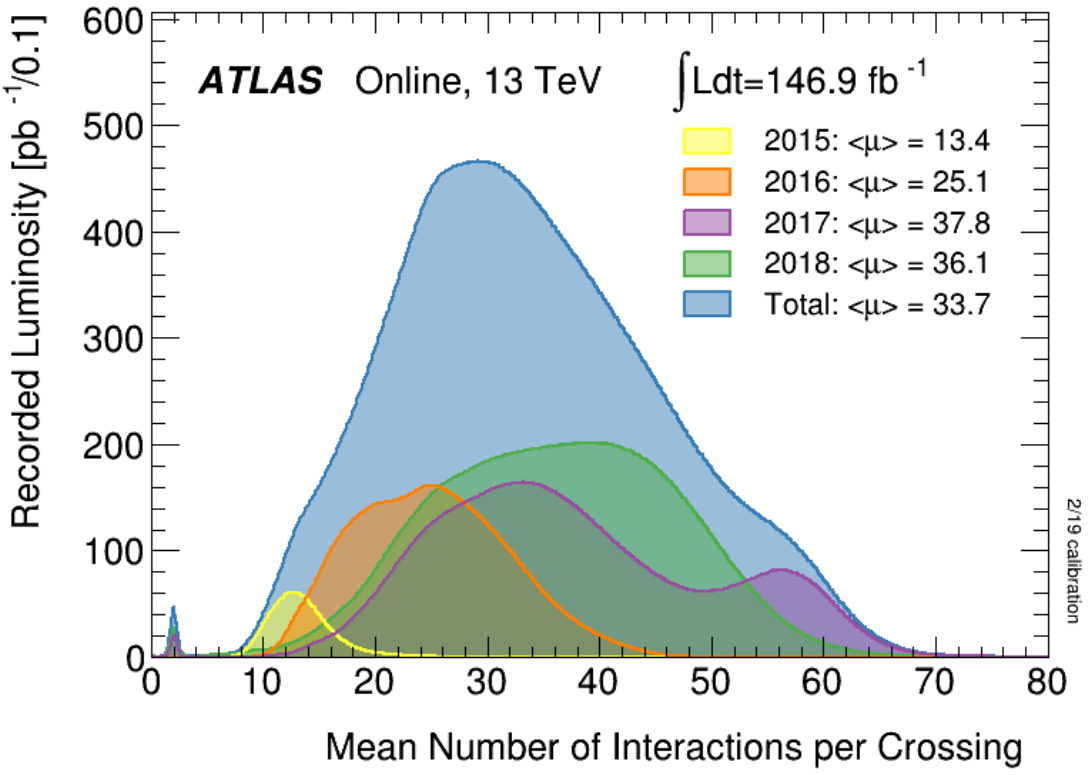

Figure 3.4: Mean number of collisions per bunch crossing in the ATLAS detector for all of Run 2 of the LHC [44]. The peak at approximately 2 collisions per bunch crossing is due to special low luminosity fills, which are not considered in this thesis.

The increased data-taking requirements result in some data having to be discarded, as there is only so much data that can be both processed and stored. This will be discussed further in Section 3.2.6.

Despite the increased peak luminosity compared to design, the total integrated luminosity per year is significantly below the design of 80 to 120 fb^{-1} a year, with the most actually achieved in a year being 63 fb^{-1} in 2018, as shown in Figure 3.5. This deficit is largely due to a greater turnaround time between fills than expected.

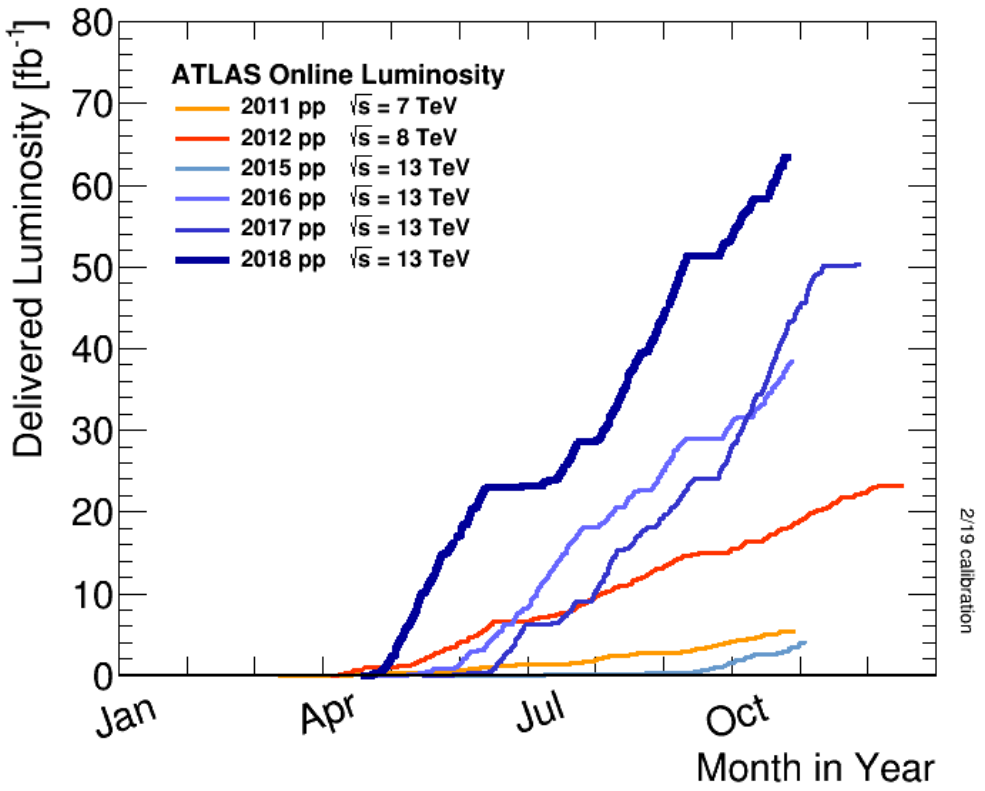

Figure 3.5: Total integrated luminosity in the ATLAS detector per year [44].

3.1.4 LHC schedule

The LHC schedule is split between multi-year running sessions, referred to as 'Runs' (typically approximately 3 years long) where data is collected and multi-year shutdowns, referred to as 'Long Shutdowns' (typically approximately 2 years long) where the LHC and experiments within it are upgraded. In addition there are short shutdowns at the end of each year, referred to as 'Year end technical stops' (typically around 3 months). At the time of writing (2020) the LHC has finished Run 2 and is currently in Long Shutdown 2. Due to the present global pandemic the immediate

schedule is not currently completely clear, however Run 3 is tentatively expected to begin within a year.

After Run 3 finishes, it is currently planned for the Long Shutdown 3 to be spent upgrading the LHC into its HL-LHC phase, which will begin in Run 4. Work towards upgrades of the ATLAS inner tracker which is required for the HL-LHC phase will be discussed in Chapter 7.

In addition, each Run is divided into multiple smaller sections, referred to in order of increasing size as: luminosity blocks, runs (not the same as the Runs referred to earlier) and periods. A luminosity block is all of the data taken in a small period of time, by default one minute. These luminosity blocks are then collected into runs, each of which is a longer period of time over which one data taking session is performed, typically around approximately 12 hours, but there is a lot of variation in the length of runs. Usually one LHC fill, as discussed in Section 3.1.3, will be associated with one run, but there are also other runs such as calibration runs which are not associated with a fill, and in some cases a fill may have multiple runs or a run may not last for the full length of the fill or may last longer than a fill. After this runs are collected into periods that have similar data taking conditions.

Luminosity blocks and runs are notated simply by luminosity block (x) and run (x), where x is a number. All run numbers are unique, while all luminosity block numbers within a single run are unique, but they are not unique across multiple runs. The first luminosity block within a run is luminosity block 1, and then each subsequent luminosity block increases the number by 1. Periods are denoted slightly differently, as period xy, where x is a letter and y is a number, e.g. period C4. Each period contains multiple runs as mentioned earlier, and runs within the exact same period have very similar data taking conditions. Runs within other periods that have the same letter but not the same number also have similar data taking conditions, but less similar than runs within the exact same period.

3.2 The ATLAS detector

ATLAS (Figure 3.6) is the largest detector at the LHC, a cylindrical detector 44 m in length and 25 m in diameter, split into a cylindrical 'barrel' section with an end-cap at either end slightly displaced from the barrel. The average collision point is at the interaction point discussed earlier and is at the centre of ATLAS, with the general purpose ATLAS detector being forward-backward symmetric and axially symmetric about this point and covering almost the whole solid angle. This allows a high acceptance of events due to few events missing the detector [45].

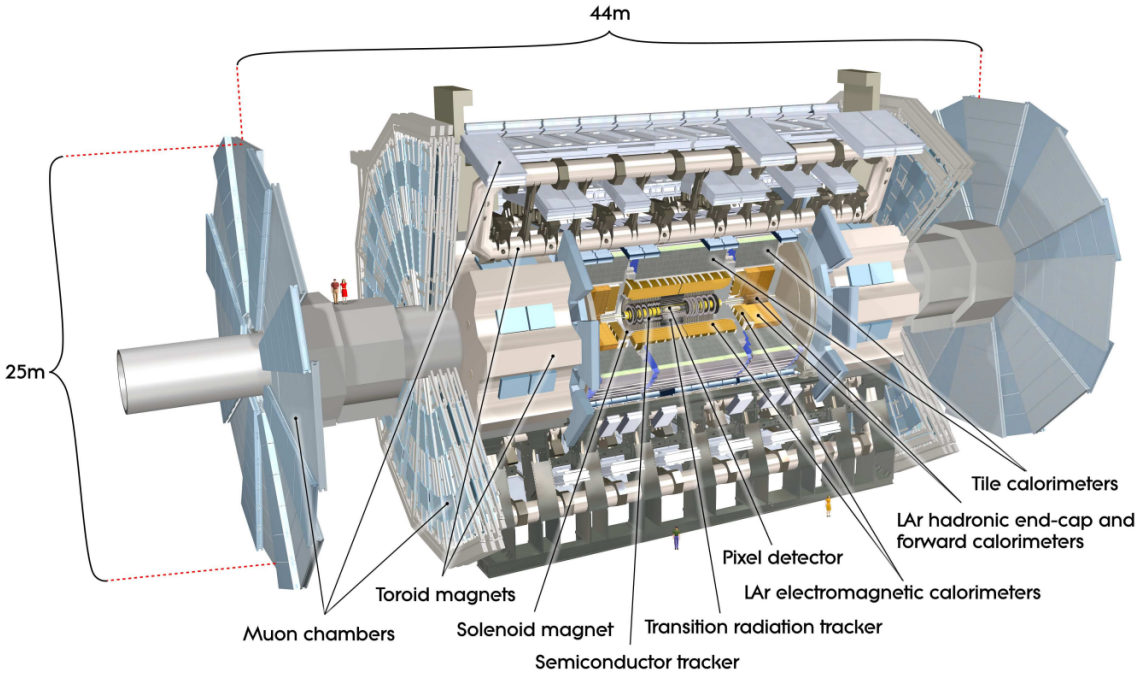

Figure 3.6: The ATLAS detector [45].

3.2.1 Common co-ordinate systems

As the collision point is at the centre of ATLAS, and we are interested in the collisions, a useful co-ordinate system has the collision point at the origin. In euclidean co-ordinates, this is defined as:

- x axis points from the interaction point to the centre of the LHC.

- z axis points from the interaction point along the beam direction heading to the north-east.
- y axis points perpendicular to the x-z plane from the interaction point, which is at an angle of 0.704° from vertical, due to the tilt of the LHC tunnel [46].
- the interaction point is at (0,0,0).

This co-ordinate system is shown graphically in Figure 3.7.

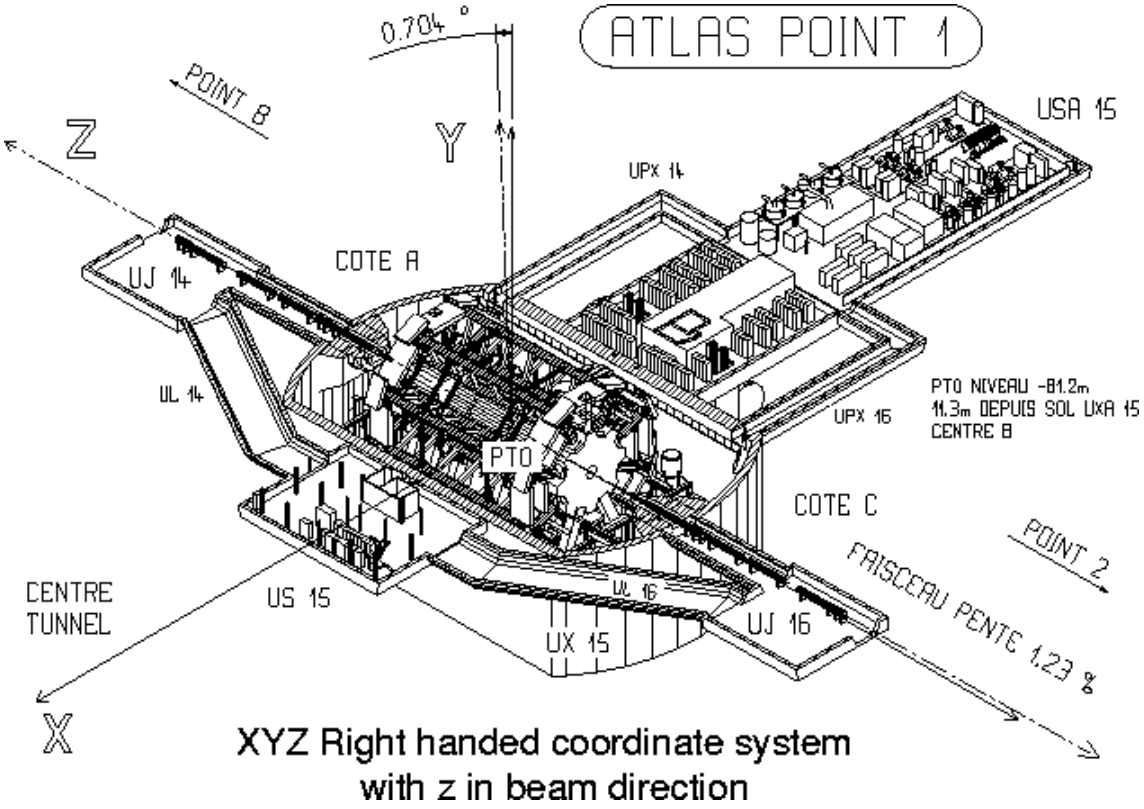

Figure 3.7: The ATLAS detector euclidean co-ordinate system [46].

As the ATLAS detector is axially symmetric, it is often more useful to use an angular based co-ordinate system. However rather than using cylindrical co-ordinates, as might initially be thought to be the best description, the following is usually used:

- ϕ is the azimuthal angle around the beam axis in the x-y plane.
- $\eta = -ln\left(tan\left(\frac{\theta}{2}\right)\right)$ where θ is the polar angle from the beam axis.

- For (ϕ, η), (ϕ,inf) points from the interaction point along the beam axis, and (ϕ,0) points from the interaction point perpendicular to the beam axis.

The quantity η is called the pseudorapidity. This is used rather than simply θ for two reasons. One is that the number of any certain events that are produced uniformly across phase space should be constant as a function of pseudorapidity (for example if x muons are produced between $\eta = 1$ and $\eta = 2$, then x muons should also be produced between $\eta = 2$ and $\eta = 3$). The other reason is that for highly relativistic particles (which almost all particles detected by ATLAS are), pseudorapidity differences are Lorentz invariant with respect to boosts along the beam axis, whereas θ differences are frame dependent.

In addition, a quantity is defined $\Delta R(a, b) = \sqrt{\Delta\phi(a, b)^2 + \Delta\eta(a, b)^2}$, which is a measure of the magnitude of separation between two particles a and b.

3.2.2 Magnet system

ATLAS has two types of superconducting magnets, a single solenoid producing a uniform 1.998 T axial magnetic field along the beam axis, and three large toroidal magnet systems, after which the ATLAS detector is named, one along the beam axis and two at the end-caps. These produce toroidal magnetic fields of 0.5 T around the central muon detectors and 1 T around the end-cap muon detectors.

The stronger 1.998 T axial field is across the inner detectors close to the collision point. This allows the transverse momentum of charged particles to be determined precisely, via the measurement of their radius of curvature in the magnetic field.

The weaker toroidal magnetic field covers a larger volume, extending out to the muon detectors, allowing measurement of the momentum of muons. The layout of the magnet windings is shown in Figure 3.8.

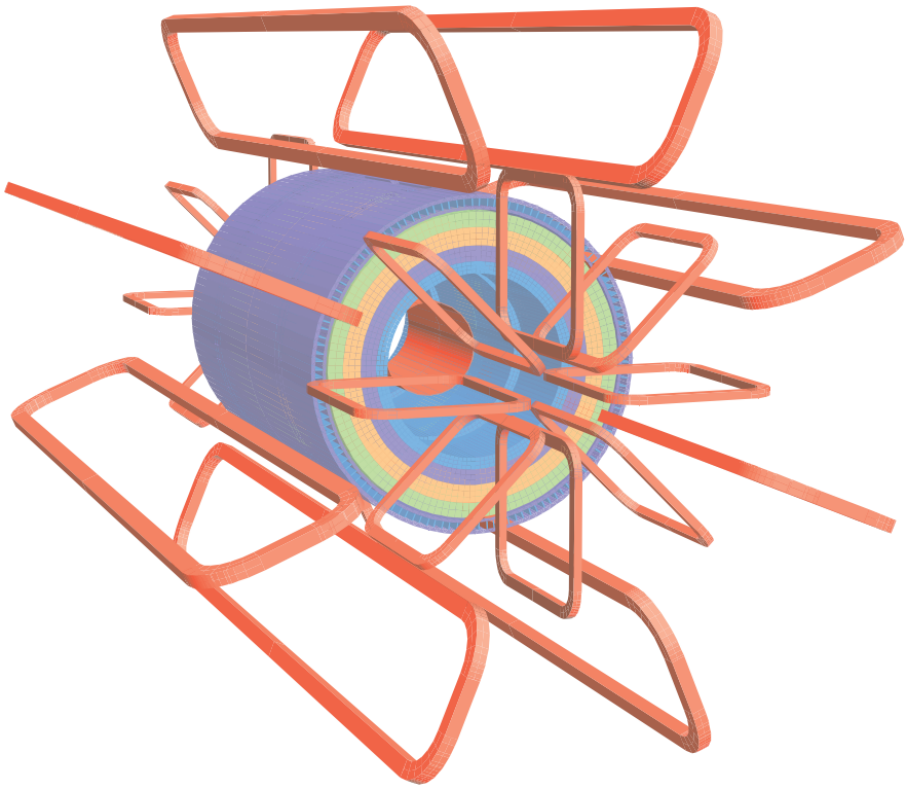

Figure 3.8: The ATLAS magnet windings, shown with the tile calorimeter. The solenoidal magnet lies within the calorimeter volume [45].

3.2.3 Inner detector

The three main design goals of the inner detector are to make precise measurements of charged particle momentum, determine the primary vertex of any collision and determine the secondary vertices from particle decays. Due to this the inner detector is chosen to be the closest detector to the interaction point, within the precisely uniform axially symmetric magnetic field of the solenoid.

These three goals all require accurate tracking of the trajectory of charged particles passing through the inner detector (Figure 3.9 and Figure 3.10). In addition to this, the trajectories of multiple events must be distinguishable, due to the pileup discussed in Section 3.1.3.

The inner detector consists of three main components aligned along the beam axis

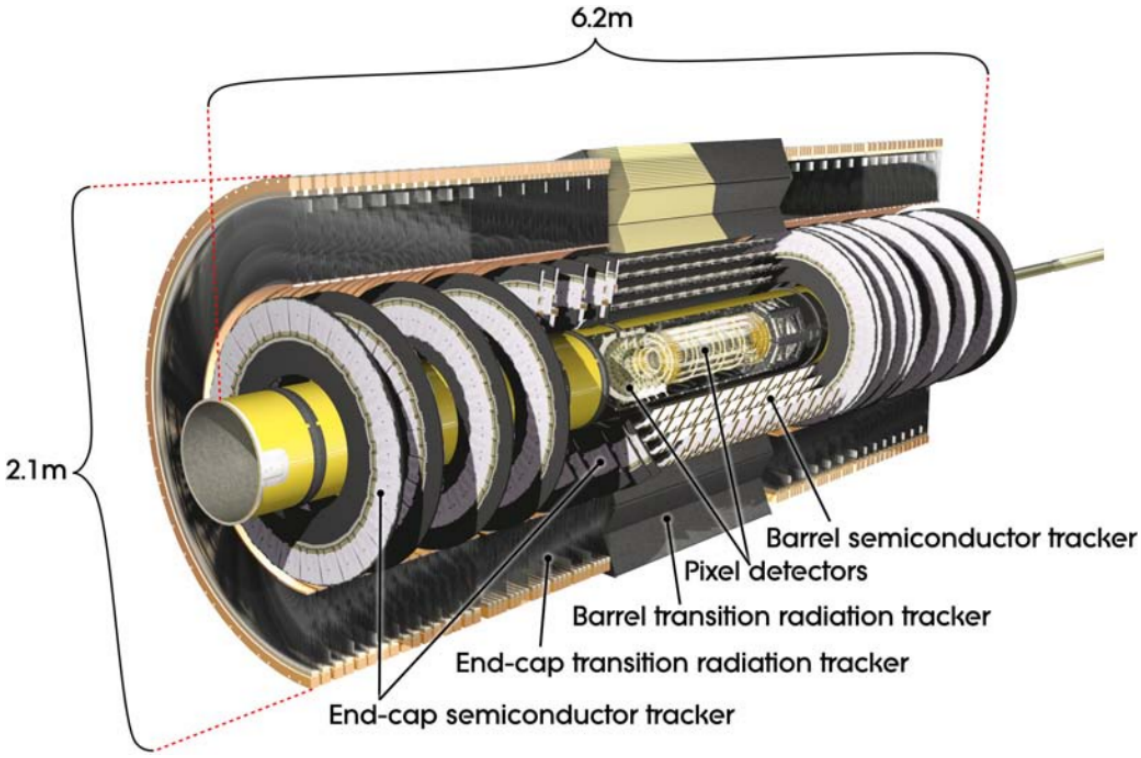

Figure 3.9: Cut-away view of the ATLAS Inner Detector [47].

and in the endcaps. These are described below in order of their distance from the collision point.

3.2.3.1 Pixel detector

The pixel detector is silicon-based and extends from a radius of $(45.5 < R < 242)$ mm. The pixel layer produces the best spatial resolution out of all the tracking detectors, however it is costly and is hence minimised via being the closest detector to the interaction point. There are 1744 pixel sensors, of 250 μm thickness and area 19x63 mm^2. These sensors consist of oxygenated n-type wafers with n^+ implants which are bump bonded to a readout chip. All of the sensors are identical with 47232 pixels on each.

The size of the pixels on the sensor is largely dictated by the pitch of the read-out. Approximately 90% of pixels have dimensions 50x400 μm^2. The remaining pixels have a larger area of 50x600 μm^2. Due to physical space constraints, some pixels

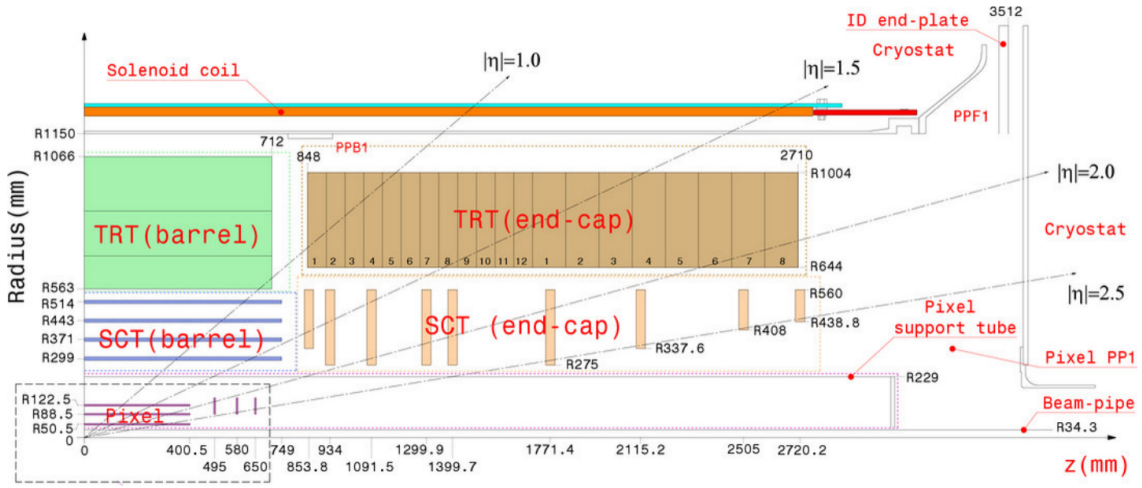

Figure 3.10: Schematic of a quarter section of the ATLAS Inner Detector [47].

are ganged together leading to only 46080 readout channels per sensor; ≈ 80 million over all the sensors [45].

In the barrel there are three cylindrical pixel layers, and in each endcap there are three disks. This allows tracking resolution in the barrel of 10 μm (R-ϕ), 115 μm (z), and 10 μm (R-ϕ), 115 μm (R) in the end-caps.

The choice of oxygenated material and n^+ implants was made due to the high radiation damage that was encountered as a consequence of being the closest detector to the collision point. After a neutron equivalent fluence of $\approx 2\text{x}10^{13}$ cm^{-2}, the n-type bulk undergoes type inversion becoming p-type, lowering the depletion voltage while it does. It has been shown experimentally that oxygenated material is resistant to radiation damage from charged hadrons and has improved charge collection after type inversion. In addition n^+ implants continue to have good charge-collection efficiency when operating below depletion voltage [47].

In 2014 the pixel detector was upgraded via the installation of the Insertable B-layer, a layer of pixel detector that was inserted closer to the interaction point than the rest of the pixel detector. This has enabled an improvement to vertex reconstruction and b-tagging (identifying jets that arise from b quarks) which was particularly important due to the increasing pileup in later years results in a decrease in vertex reconstruction efficiency. The active area of 75% of the pixels in the B-layer

is 16.8x40.9 mm^2 while the final 25% is 16.8x20.0 mm^2 and consist of an n-in-n Si wafers [48].

3.2.3.2 Semiconductor tracker

The SemiConductor Tracker (SCT) is silicon-based and extends from $255 < R < 549$ mm in the barrel and $251 < R < 610$ mm in the end-caps.

The semiconductor tracker is a set of 15912 p-in-n type reverse-biased diode strips of 6.4 mm length and 80 μm pitch and 285 ± 15 μm thickness with a stereo-angle of 40 mrads to enable measurement of both co-ordinates, that initially operated at a bias voltage $\approx$ 150 V. However radiation damage means that after 10 years of operation the bias voltage will rise to $\approx$ 250-350 V to continue good charge collection efficiency [45]. When a charge above a certain threshold is deposited in the strips, a hit is registered.

In the barrel there are 4 cylindrical semiconductor tracker layers, and in each endcap there are 9 disks. This allows tracking resolutions in the barrel of 17 μm (R-ϕ), 580 μm (z) and 17 μm (R-ϕ), 580 μm (R) in the end-caps.

3.2.3.3 Transition radiation tracker

Unlike the other two detectors in the inner detector, the transition radiation tracker is not silicon based, but instead consists of gaseous proportional drift tubes. These extend from $554 < R < 1082$ mm in the barrel and $617 < R < 1106$ mm in the end-caps.

The drift tube walls are made of two 35 μm multi-layer polyimide films, producing a tube of 4 mm diameter, which is mechanically stabilized using carbon fibres. Their length is 144 cm in the barrel, and 37 cm in the end-caps. Each is typically filled with 70% Xe, 27% CO_2 and 3% O_2; however a mixture of $Ar/CO_2/CF_4$ is used on occasion to clean silicon-based deposits from the anode wire. This is because

a relative concentration of organo-silicone impurities above 10^{-11} is harmful to the transition radiation tracker's operation and cannot be prevented over the lifetime of the transition radiation tracker.

The transition radiation tracker allows tracking resolutions of 130 μm in both the barrel and end-caps [45].

3.2.4 Calorimeters

Further from the interaction point, after the inner detector and solenoidal magnet are the calorimeters (Figure 3.11) that measure particles' energy. As well as measuring the particle's energy, they also provide position measurements. To do this, the calorimeters are made out of high density material and measure the shape of the particle shower that is formed when particles collide with it. To accurately measure the particle shower, the calorimeters must be deep enough to contain the shower. This also ensures the essential property of preventing particles other than muons from reaching the muon spectrometer.

In ATLAS there are multiple electromagnetic calorimeters, designed to measure the energy of particles that interact electromagnetically, and multiple hadronic calorimeters designed to measure the energy of hadrons.

These calorimeters provide coverage from $|\eta| = 0$ to $|\eta| = 4.9$. Below $|\eta| = 2.5$ (the η range covered by the inner detector) the calorimeters have finer granularity than above this range, allowing precision physics.

Other than the hadronic tile calorimeter, all calorimeters use liquid argon (LAr) as the active layer, due to its linear behaviour, stability over time and radiation hardness [45].

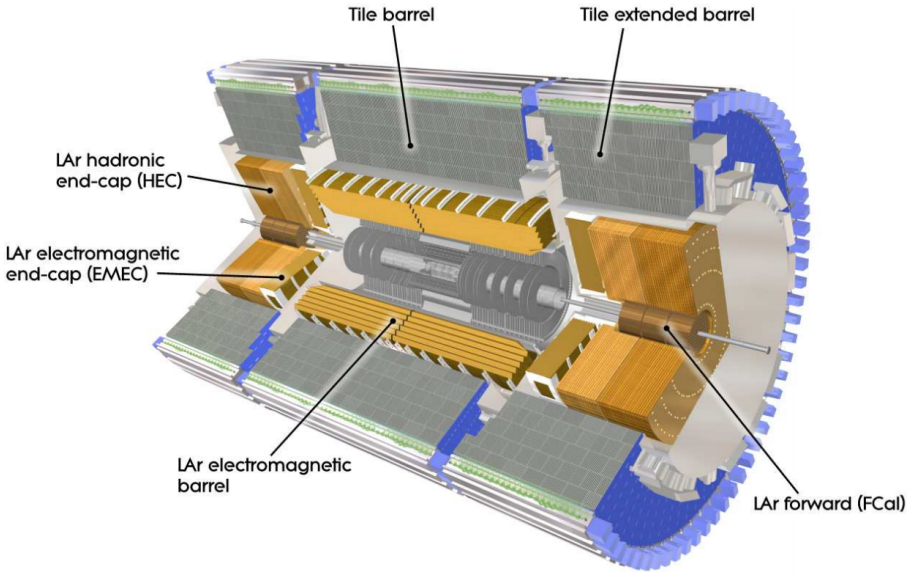

Figure 3.11: ATLAS calorimeters schematic [45].

3.2.4.1 Electromagnetic calorimeter

The electromagnetic calorimeters consist of the liquid argon calorimeter and the forward electromagnetic liquid argon calorimeter. The liquid argon calorimeter covers the barrel region up to $|\eta| < 1.475$ and both end-caps between $1.375 < |\eta| < 3.2$ (slightly overlapping with the barrel region), while the forward electromagnetic liquid argon calorimeter covers the region $3.1 < |\eta| < 4.9$.

The liquid argon calorimeter has three layers below $|\eta| = 2.5$, and two layers above. These consist of alternating layers of lead plates, the high density material used to initiate the particle shower with thin layers of liquid argon being the active layer, which is ionized by this particle shower to produce a readout through electrodes in the argon. These alternating layers are in an accordion geometry to ensure azimuthal uniformity, preventing gaps in coverage. The three layers have various granularity, and the granularity of each layer varies as a function of $|\eta|$. The first layer, which is only present below $|\eta| = 2.5$ has a very fine granularity, then the second and third layer have a coarser and coarser still granularity, as shown in Figure 3.12.

To contain the shower, the thickness of the calorimeter is > 22 radiation lengths, which varies as a function of η, ranging from 22 to 30 from $|\eta| = 0$ to $|\eta| = 0.8$ and

from 24 to 33 from $|\eta| = 0.8$ to $|\eta| = 1.3$.

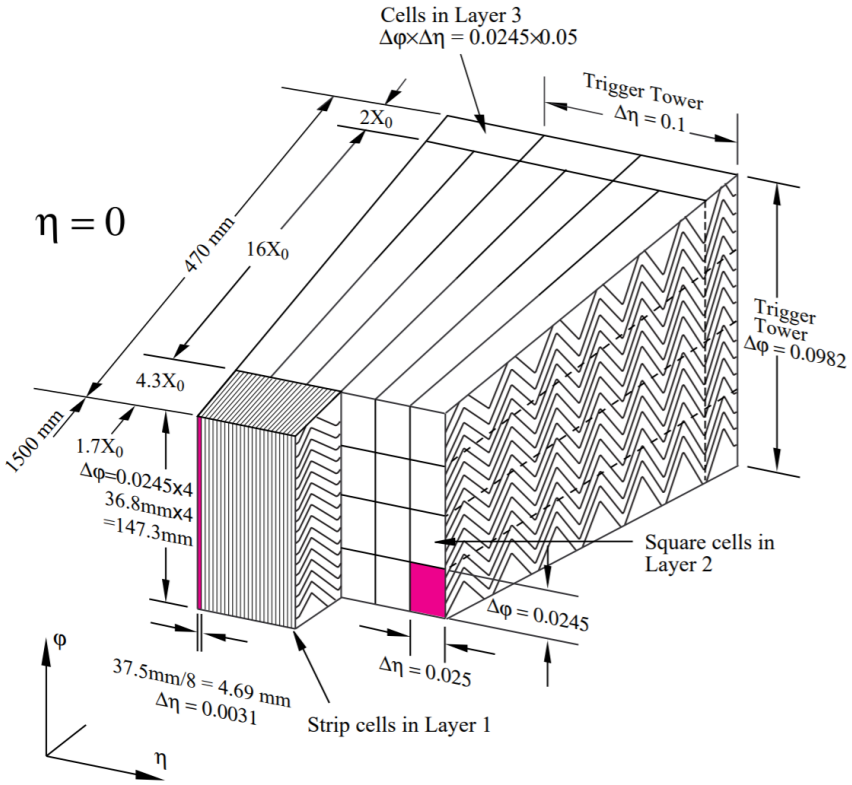

Figure 3.12: The electromagnetic calorimeter accordion geometry, showing all three layers. Only layer 2 and layer 3 are present above $|\eta| = 2.5$. An individual section, highlighted in pink, is called a cell [45].

The forward electromagnetic liquid argon calorimeter consists of alternating layers of copper, the high density material used to initiate the particle shower with liquid argon as the active layer, with a thickness of 27.6 radiation lengths.

3.2.4.2 Hadronic calorimeter

ATLAS has three hadronic calorimeters, the tile calorimeter along the beam axis, liquid argon hadronic end-cap and liquid argon forward calorimeter. The tile calorimeter covers the range $|\eta| < 1.7$, whereas the liquid argon hadronic end-cap covers the range from $|\eta| = 1.5$ to $|\eta| = 3.2$, and the liquid argon forward calorimeter covers the range from $|\eta| = 3.1$ to $|\eta| = 4.9$.

The tile calorimeter consists of alternating layers of steel plates, the high density

material used to initiate the particle shower with scintillators being the active layer. The reason for this choice rather than liquid argon as for the other calorimeters is due to this providing maximum radial depth for minimum cost. The radial depth provided by the tile calorimeter is 7.4 nuclear interaction lengths.

The liquid argon hadronic end-cap consists of alternating layers of copper, the high density material used to initiate the particle shower with liquid argon as the active layer, while the hadronic liquid argon forward calorimeter is similar but substitutes tungsten for copper.

The hadronic liquid argon forward calorimeter is split into two modules, Forward Calorimeter 2 (FCal2) and FCal3, which are situated with FCal3 behind FCal2 relative to the interaction point. FCal2 is situated behind the electromagnetic forward calorimeter relative to the interaction point, The hadronic liquid argon forward calorimeter has a much larger thickness in nuclear interaction lengths (3.68 and 3.60 for FCal2 and FCal3 respectively) compared to the electromagnetic liquid argon forward calorimeter (2.66) allowing it to function as a hadronic calorimeter.

3.2.4.3 Jets

As discussed in Section 2.2.3, jets consisting of many particles are formed in hadron collisions. However, due to both pileup and other particles produced in the same event, it can be difficult to determine exactly which particles measured are part of a jet. There are many algorithms used to determine from measurements which particles are part of a particular jet, and which are not. In this thesis the only algorithm used will be the anti-k_t algorithm [49].

The cells in the calorimeters have a significance, ζ, associated with them given by $\zeta = \frac{E}{\sigma}$ where E is the energy measured by the cell and σ is the noise of the cell, which is a combination of electronic noise and pile-up noise.

Cells with a $\zeta > 4$ are referred to as seeds, which start a topological clustering

algorithm around them. This algorithm counts the seed as a cluster, and if a cell connected to the cluster has $\zeta > 2$ it is added to the cluster. This then continues until no cell is connected to the cluster with $\zeta > 2$. It is then repeated for other cells with $\zeta > 4$ that are not connected to already formed clusters [50]. Note, it does not matter which order the seed cells are chosen, as any cluster forming from one seed that overlaps another seed would be overlapped in the same way if the other seed was chosen first.

These clusters are then grouped with the anti-k_t algorithm which introduces two distance measures, one between entities (clusters) within the jet, $d_{ij} = min\left(k_{ti}^{-2}, k_{tj}^{-2}\right)\frac{\Delta_{ij}^2}{R^2}$ and one between the jet and the beam $d_{iB} = k_{ti}^{-2}$, where k_{ti} is the transverse momentum of entity i, $\Delta_{ij} = (\eta_i - \eta_j)^2 - (\phi_i - \phi_j)^2$ and R is an arbitrary parameter that determines the size of the jets.

The anti-k_t algorithm uses an entity, i, and finds both d_{iB} and d_{ij} for all other entities, j. if d_{iB} is smaller than any d_{ij} then the entity i is considered a jet and the algorithm stops. If there is a d_{ij} smaller than d_{iB}, the entity j with the smallest d_{ij} is grouped with entity i and is treated as a new single entity, i. This is then repeated until d_{iB} is smaller than all d_{ij} and then the entity i (which is now multiple combined initial entities) is considered a jet and the algorithm stops.

An example showing the jets formed by this clustering with anti-k_t, and other algorithms not discussed here, is shown in Figure 3.13.

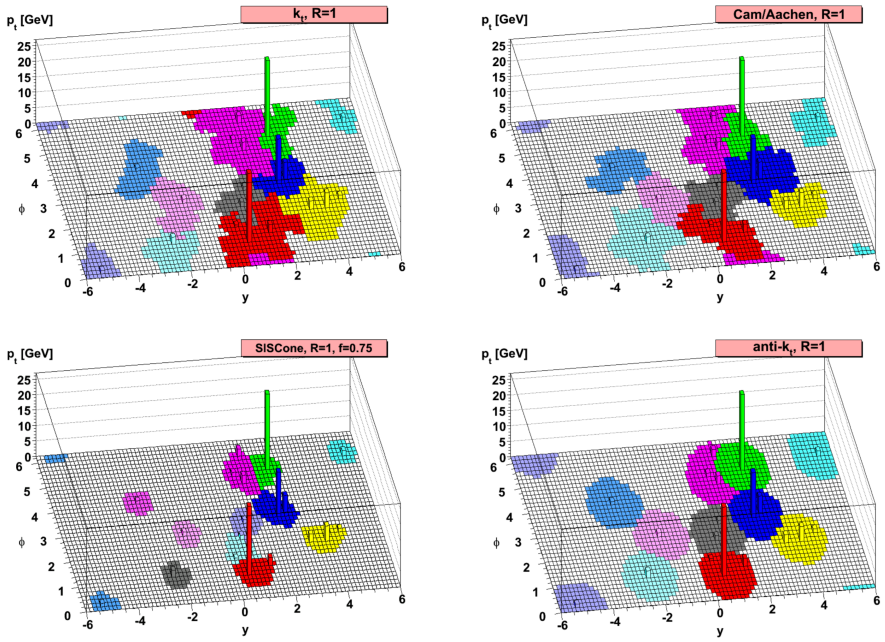

Figure 3.13: Jets formed for an example event with the anti-k_t algorithm, and other jet clustering algorithms [49].

3.2.5 Muon spectrometer

The muon spectrometers are at the outer regions of the ATLAS detector. This is because most muons produced in the LHC are minimally ionizing and hence pass through the rest of the ATLAS detector with minimal energy loss, allowing them to reach the outer detectors. Putting the muon spectrometers in the outer regions reduces noise (and radiation damage) from other particles that are stopped by the detectors before the muon spectrometers, while reducing the signal from muons by a much smaller fraction. This ensures at high probability that particles detected in the muon spectrometers are muons.

There are 4 technologies used for the muon spectrometer, two of which, the resitive plate chambers and thin gap chambers, are used primarily for triggering below $|\eta| = 2.4$ (triggering will be discussed in Section 3.2.6) and two of which, monitored drift tubes and cathode strip chambers, are used primairly for tracking below $|\eta| = 2.7$.

The muon spectrometer sits within the toroidal magnetic field which is designed to produce a magnetic field perpendicular to the paths of the muons. Below $|\eta| = 2.7$ the tracks of the muons in this field are measured by the monitored drift tubes, which provide precise tracking. In the region $|\eta| = 2.0$ to $|\eta| = 2.7$ the cathode strip chambers are used in conjunction with the monitored drift tubes as they provide superior time resolution and a higher rate capability which is useful due to the higher background at high $|\eta|$.

Using this along with the inner detectors it is possible to measure the muons' momenta precisely and provide good track reconstruction for them.

3.2.6 Trigger system

Due to the very high rate of collisions at the LHC, of the order of 1-2 GHz collisions arising from 40 MHz bunch crossings, it is not feasible to record data from every collision, or fully reconstruct every collision. Instead, many distinguishing characteristics of each collision are estimated by the trigger system, which is used to determine in real time whether or not to record this collision for further analysis. If a trigger decides to keep an event it is said the trigger passes the event and otherwise the trigger fails the event.

There are two levels of triggers, Level 1 (L1) and Higher Level Trigger (HLT). The L1 triggers are faster than HLT triggers and run on every collision, but they are not as accurate or precise as the slower HLT triggers, which run only on events that pass an L1 trigger. The L1 trigger records at a rate of approximately 100 kHz events which the HLT then reads and records at approximately 1000 Hz [51].

3.2.6.1 Prescale

Some triggers select events with a low enough rate and/or are interesting enough that the trigger passes all events it identifies. However, some triggers look for events

that have too high a rate (and/or are deemed not as interesting) to feasibly record all the events it selects and hence the trigger will randomly fail a proportion of events, even if they match the requirements to pass. This is called trigger prescaling, and the proportion of events that fail, despite reaching the requirements to pass, is called the "prescale".

The prescale, and even the triggers used, may vary on a fill-to-fill basis. The value of each trigger's prescale and the triggers used are described by the trigger menu.

3.2.7 Data

After an event passes the triggers it is saved for offline analysis. However, due to the very large quantities of data it is not feasible due to computing power resources available for every analysis to run over the entire ATLAS dataset each time they wish to analyse data. Instead, 'derivations' are produced. These derivations are designed by derivation contacts in each analysis group to select events that are required for their analysis (called skimming), and only to save information that is useful for their analysis (called pruning). The derivation primarily used by the monojet analysis is the EXOT5 derivation, which is also used by the MET+X ($P_{\mathrm{T}}^{\mathrm{recoil}}$ + any object) group and VBF-Hinv (Vector Boson Fusion Higgs→invisible) group. The reason for multiple groups using this same derivation is that it has been determined that the three groups have a large overlap in the events they need, and require similar information for their analyses. Merging their derivations into one allows a smaller overall storage requirement without increasing computing power requirements by a large amount. However, it does cause a problem that the slightly different skimming each uses can cause biases in each analysis. To prevent this, each analysis' pre-selection cuts are designed to remove this bias, by ensuring the analysis' pre-selection cuts only allow events that have passed the skimming designed for their own analysis.

CHAPTER 4

Monojet Analysis Definition

4.1 Introduction

As mentioned in Chapter 1 the monojet analysis is primarily used to search for beyond Standard Model physics. To do this requires a good knowledge of the Standard Model to precisely predict the expected background. Then it is determined how well measurements from data are described by this background prediction, and also how well they are described by various beyond Standard Model predictions.

A large portion of the following discussion on the monojet analysis is also detailed in the ATLAS internal note and ATLAS CONF-NOTE [10, 52], both of which I am a significant author of.

The monojet analysis employs a number of Control Regions (CRs) used to estimate the backgrounds in the Signal Region (SR). These CRs are targeted at processes in-

cluding one or two muons/electrons, possibly with b-jets. All regions are orthogonal with each other by construction. All of these regions are based on a common set of preselection cuts as described in Section 4.5.1. Each individual CR and the SR will be described in the following sections.

4.2 Object definition

The analysis selection is based on physics objects: jets measured with the calorimeter discussed in Section 3.2.4.3, b-jets, muons, electrons, photons and $P_{\mathrm{T}}^{\mathrm{recoil}}$. These objects are defined in the sections below. Two categories are introduced for each object: *baseline* objects are used for preselection and vetoes, while *signal* objects are part of the actual analysis selection, defining the event topology in the signal and control regions.

4.2.1 Jets

Jets are reconstructed using the anti-k_t clustering algorithm [49], with a distance parameter of $R = 0.4$.

Baseline jets are selected for offline analysis if they satisfy the following criteria:

- $p_{\mathrm{T}} > 30$ GeV and $|\eta| < 2.8$;
- an additional requirement of Jet Vertex Tagger, $JVT > 0.59$, is applied if both $p_{\mathrm{T}} < 60$ GeV and $|\eta| < 2.4$. This condition reduces the contribution from pileup jets, while keeping the jet efficiency almost constant as a function of p_{T} . The value of $JVT > 0.59$ is a fairly loose cut that removes less than 1% of non-pile-up jets and more than 99% of pile-up jets for jets with $20 < p_{\mathrm{T}} < 30$ GeV. No study has been performed for jets with the specific cuts mentioned here, however studies have been done that indicate there is no significant dependence on the sample used. This is explained in detail in [53].

In order to suppress contributions from calorimeter noise and non-collision background, events are discarded when any jet passes the overlap removal described in Section 4.3 and fails the *Loose* jet cleaning criteria [54] (where the cleaning criteria, in order of weakest cuts to strongest, are: loose, medium, tight and very tight).

Further rejection of non-collision background events, due to losses from the LHC collimators or beam-gas interactions, is obtained by imposing the *Tight* jet cleaning criterion on the leading jet.

Signal jets are defined in the same way as the baseline jets.

The H_{T} variable, which is used for example in the definition of `CR1e0b` and `CR1e1b` (described in Section 4.5.5 and Section 4.5.6.1 respectively), is defined as the scalar sum of the transverse momenta of signal jets.

4.2.1.1 *b*-jets

b-jets, produced by the hadronisation of bottom quarks, are identified using the `MV2c10` discriminant, which is the output of a boosted decision tree, trained to discriminate *b*-like jets from a mixture of charm and light-flavour jets, largely based upon the long lifetime of b-hadrons in comparison, explained in more detail in [55]. If a jet passes the pileup cleaning, and if it is inside the *b*-tag acceptance, i.e. it has $p_{\mathrm{T}} > 30$ GeV and $|\eta| < 2.5$, then its relative `MV2c10` discriminant value is evaluated. The jet is identified as a *b*-jet by applying a cut on this discriminant, which yields an efficiency of ∼60%.

4.2.2 Electrons

Electrons are reconstructed from an electromagnetic cluster, with a sliding window algorithm [56], that is matched to an inner detector track refitted with a Gaussian Sum Filter [57] to account for bremsstrahlung energy losses. The detailed perfor-

mance of this likelihood identification can be found in [58].

Baseline electrons are required to have a transverse energy E_{T} above 7 GeV and $|\eta|$, defined by the calorimeter cluster position, < 2.47. In addition, the baseline electrons must satisfy the *LooseAndBLayerLLH* electron likelihood identification criteria, which take tracking information from the insertable B-layer into account [59]. A cut of $|z_0 \sin\theta| < 0.5$ mm is applied, where z_0 is the longitudinal impact parameter, ensuring the lepton tracks point to a primary vertex. The baseline electron definition also requires that the calorimeter cluster satisfies certain quality criteria to prevent, for instance, the presence of dead electromagnetic calorimeter front-end boards or dead high-voltage channels. Finally the baseline electrons are required to survive the overlap removal described in Section 4.3. These baseline electron criteria are used to veto the presence of electrons.

Signal electrons are a subset of the baseline electrons satisfying the *TightLLH* electron likelihood identification criteria [59]. The electron track's d_0/σ_{d_0} (where d_0 and σ_{d_0} are the transverse impact parameter and its uncertainty respectively) is required to be < 5 and the p_{T} threshold is increased to 30 GeV. Signal electrons are used in the electron control regions (Section 4.5.5, Section 4.5.6 and Section 4.5.6.1).

4.2.3 Muons

Muon candidates are reconstructed using a combination of the tracking information from the inner detector and the muon spectrometer. They are required to pass the *Medium* identification criteria defined in references [60, 61]. This choice allows the systematic uncertainties associated with muon reconstruction and calibration to be minimized.

Baseline muons are required to have $p_{\mathrm{T}} > 7$ GeV and $|\eta| < 2.5$. They are used in the overlap removal described in Section 4.3, in the $P_{\mathrm{T}}^{\mathrm{recoil}}$ definition and in the muon veto used to define the signal region and the control regions. Cosmic ray muons and 'bad muons' are not used as baseline muons and therefore vetoed.

Signal muons have the same definition as the baseline muons with some additional criteria. Cuts are applied on the impact parameter variables, requiring d_0/σ_{d_0} and $|z_0 \sin\theta|$ smaller than 3 and 0.5 mm, respectively, and the p_{T} threshold is increased to 10 GeV. These muons are used to define the muon control regions described in Sections 4.5.3, 4.5.4 and 4.5.6.1.

4.2.4 Taus

Tau candidates are reconstructed according to reference [62].

Baseline taus are required to pass the baseline selections of $p_{\mathrm{T}} > 20$ GeV, $|\eta| < 2.5$ (excluding the overlap region between the barrel and endcap from $1.37 < |\eta| < 1.52$), and to have 1 or 3 charged tracks. The standard tau identification is then performed by requiring the tau candidate to pass the *Loose* working point of a Boosted Decision Tree discriminant that combines both tracking and calorimeter based information [62].

Signal taus: No signal taus are defined in this analysis since they are used only in the veto selection.

4.2.5 Photons

Photons are reconstructed from clusters of energy deposits in the electromagnetic calorimeters. Clusters without a matching track or reconstructed conversion vertex in the inner detector are classified as being unconverted photons [63].

Baseline photons are required to pass the *Tight* identification requirement, $p_{\mathrm{T}} > 10$ GeV and $|\eta| < 2.37$.

4.2.6 Missing transverse momentum

$P_{\mathrm{T}}^{\mathrm{recoil}}$ is defined as the negative vector sum of the momenta reconstructed in the transverse plane, associated to baseline candidate electrons, jets, taus, photons and muons, as well as to particle tracks reconstructed in the inner detector (*track-based soft term*) [64].

4.3 Overlap removal

An overlap removal is applied to jet, electron, muon and photon candidates of baseline quality, before applying the signal definitions mentioned in the previous sections[1]. Hadronically-decaying tau leptons are not considered. The recommendations detailed in the harmonization note [65] have been followed to ensure consistency and allow easy combination within the overall ATLAS analysis space.

- electron-muon: if they share the same track, remove the electron and keep the muon.
- b-jet -muon/electron: keep the jet and remove the electron or muon (since the lepton is likely to come from a semileptonic b decay).
- jet-electron:
  - if $\Delta R(j,e) < 0.2$ and the p_{T} ratio $p_{\mathrm{T}}^{e}/p_{\mathrm{T}}^{\mathrm{jet}} > 0.8$, remove the jet and keep the electron.
  - if $0.2 < \Delta R(j,e) < 0.4$ keep the jet and discard the electron.
- jet-muon:
  - if $\Delta R(j,\mu) < 0.2$ and jet has high track multiplicity (≥ 3 associated inner-detector tracks) and p_{T} ratio $p_{\mathrm{T}}^{\mu}/p_{\mathrm{T}}^{\mathrm{jet}} < 0.5$ or $p_{\mathrm{T}}^{\mu}/\sum p_{\mathrm{T}}^{\mathrm{track}} < 0.7$, remove the muon and keep the jet.

[1]The JVT selection, described in Section 4.2.1, is applied to the jets considered for overlap removal.

  - if $\Delta R(j,\mu) < 0.2$ and jet has < 3 tracks or with p_{T} ratio $p_{\mathrm{T}}^{\mu}/p_{\mathrm{T}}^{\mathrm{jet}} > 0.5$ and $p_{\mathrm{T}}^{\mu}/\sum p_{\mathrm{T}}^{\mathrm{track}} > 0.7$, keep the muon and discard the jet.
  - if $0.2 < \Delta R(j,\mu) < 0.4$ keep the jet and discard the muon.

- $\Delta R(\gamma, e) < 0.4$: remove the photon and keep the electron.
- $\Delta R(\gamma,\mu) < 0.4$: remove the photon and keep the muon.
- $\Delta R(\gamma, j) < 0.4$: keep the photon and remove the jet.

4.4 Anti scale factors

Mismodelling of the Monte Carlo simulation reconstruction and identification efficiencies of leptons and photons is corrected by scale factors. The overall effect on an MC sample is then to scale the number of events where (e.g.) leptons are reconstructed and identified. This implies that a similar scaling should be applied to samples with a lepton or photon *veto*. In order to account for this effect, the analysis applies channel-level anti–scale factors to correct the number of events falling into any veto region. These anti–scale factors function as event–level weights.

4.5 Event selection

4.5.1 Pre-selection - triggers

The monojet analysis is based upon searching for invisible particles that carry a large transverse momentum, and hence the collisions relevant for the monojet analysis involve a large $P_{\mathrm{T}}^{\mathrm{recoil}}$. Therefore, the triggers employed for the selection of SR events, and for most of the control regions, are calorimeter based $P_{\mathrm{T}}^{\mathrm{recoil}}$ -triggers. This means that the muon spectrometer information is not used in the evaluation of $P_{\mathrm{T}}^{\mathrm{recoil}}$ at trigger level, i.e. that muons are considered as invisible particles. Con-

trol regions that do not include muons or genuine $P_{\mathrm{T}}^{\mathrm{recoil}}$ utilize non-$P_{\mathrm{T}}^{\mathrm{recoil}}$ triggers. Different trigger strategies are used to analyse data collected in 2015, 2016, 2017 and 2018 to reflect the corresponding differences in trigger menus. In the signal and muon control regions (`SR`, `CR1mu0b`, `CR2mu`) the lowest unprescaled $P_{\mathrm{T}}^{\mathrm{recoil}}$ trigger is used (Table 4.1).

In the electron control regions (`CR1e0b`, `CR2e`) the lowest unprescaled single electron trigger is used (Table 4.2).

In the 1 lepton (e/μ) + 1 or more b-jets CR (`CR1l1b`), the lowest unprescaled single electron or $P_{\mathrm{T}}^{\mathrm{recoil}}$ trigger is used, depending on the detected lepton (Table 4.1 / Table 4.2).

The preselection cuts for all regions are listed in Table 4.3.

Data period	Trigger
2015	
all runs	HLT_xe70_mht
2016	
$296939 \leq$ run ≤ 302872	HLT_xe90_mht_L1XE50
$302919 \leq$ run ≤ 303892	HLT_xe100_mht_L1XE50
$303943 \leq$ run ≤ 311481	HLT_xe110_mht_L1XE50
2017	
$325713 \leq$ run ≤ 331975	HLT_xe110_pufit_L1XE55
$332303 \leq$ run ≤ 341649	HLT_xe110_pufit_L1XE50
2018	
$348197 \leq$ run ≤ 350066	HLT_xe110_pufit_xe70_L1XE50
$350067 \leq$ run ≤ 363400	HLT_xe110_pufit_xe65_L1XE50

Table 4.1: Triggers used in the signal region and muon control regions. How to read these is explained in Appendix A.1.

Data period	Trigger
2015 data	(HLT_e24_lhmedium_L1EM20VH — HLT_e60_lhmedium — HLT_e120_lhloose)
2016, 2017, 2018 data	(HLT_e26_lhtight_nod0_ivarloose — HLT_e60_lhmedium_nod0 — HLT_e140_lhloose_nod0)

Table 4.2: Triggers used in the electron control regions. The lowest unprescaled trigger is always the one used which varies throughout the year. How to read these is explained in Appendix A.2.

Category	Selection Criteria
Trigger	Logic defined for the specific region
GRL	`PHYS_StandardGRL_all_Good_25ns`
Vertex	$\geq$1 vertex with $N_{\text{trk}} \geq 2$
No detector issues	SCTGood, TileGood, LArGood, CoreFlags
Jet cleaning	Jet Loose cleaning criteria (after overlap removal)
	$p_{\text{T}} > 150$ GeV
Leading jet	$\lvert\eta\rvert < 2.4$
	Tight jet cleaning criteria
Jet multiplicity	$N_{\text{jets}} \leq 4$ (signal jets)
Multijet suppression	$\lvert\Delta\phi(p_{\text{T}}(V), \text{any jet})\rvert > (0.6)0.4$
$P_{\text{T}}^{\text{recoil}}$	$P_{\text{T}}^{\text{recoil}} > 200$ GeV

Table 4.3: Preselection cuts for the signal region and all control regions. "SCTGood", "TileGood", "LArGood" and "CoreFlags" indicate the requirements that, in the event, there are no SemiConductor Tracker, Tile and Liquid Argon calorimeter problems and that there are no lost detector fragments in the detector readout, respectively. The cut aimed to suppress the multijet background is tightened to 0.6 in the first $P_{\text{T}}^{\text{recoil}}$ bin and kept at 0.4 in the rest of the distribution, as the multijet background is greatly enhanced in the first $P_{\text{T}}^{\text{recoil}}$ bin. The Good Run List (GRL) is a list of luminosity blocks (by default 1 minute periods of each run) that are considered 'good' by the data quality team.

4.5.2 SR: signal region

Events are assigned to the signal region, SR, if:

- They pass the pre-selection cuts
- No baseline lepton or photon, as defined in Section 4.2, is reconstructed

The dominant background in SR is $Z(\nu\nu) + \text{jets}$ events. The second largest contribution arises from $W(\tau\nu) + \text{jets}$ events, as discussed further in Section 4.7.

Figure 4.1 shows the expected kinematic distributions where the background prediction is obtained directly from MC simulation, which is adjusted later after the fit mentioned in Section 4.7, corresponding to the full Run 2 data sample.

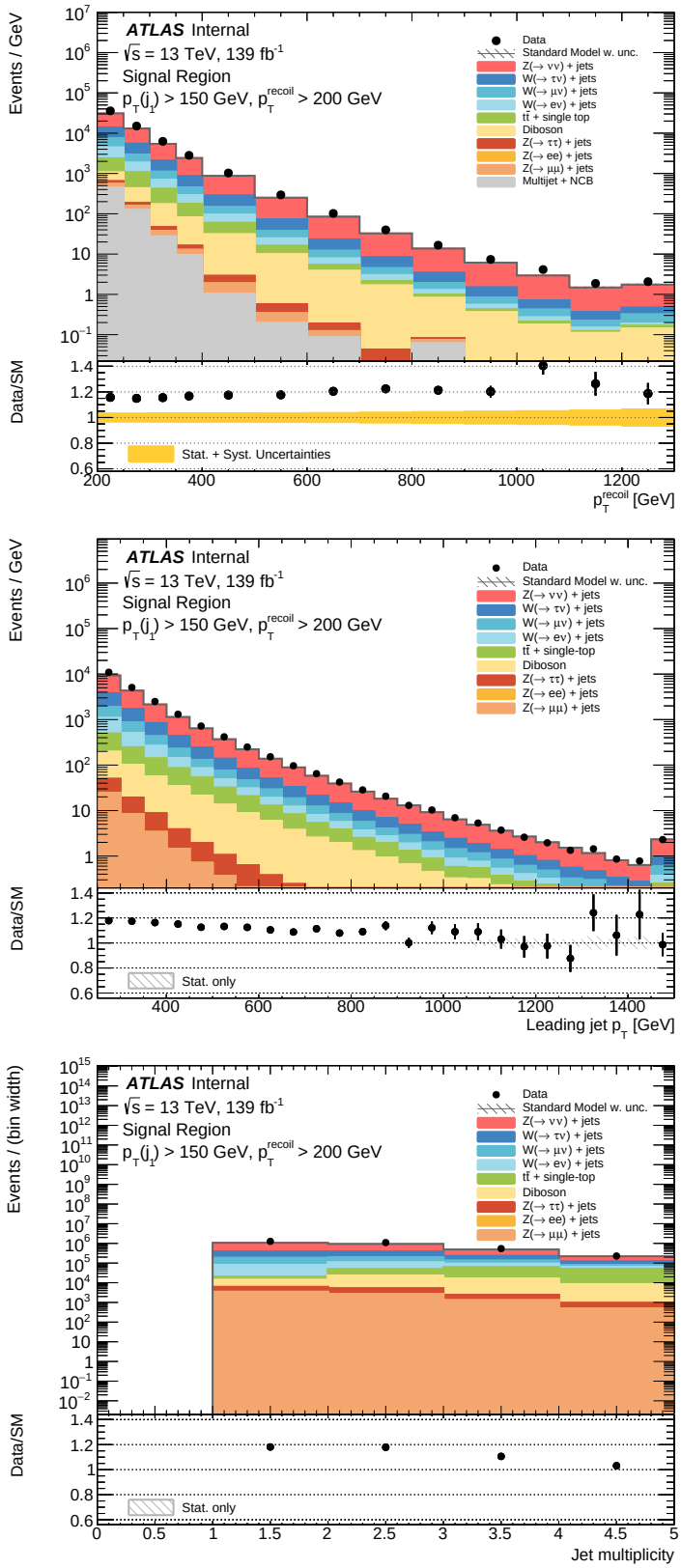

Figure 4.1: SR distributions in $P_{\mathrm{T}}^{\mathrm{recoil}}$ and leading jet p_{T} based on the full Run 2 dataset. The uncertainty band in the ratio includes only the statistical uncertainties except for in the $p_{\mathrm{T}}^{\mathrm{recoil}}$ distribution in which the statistical + systematic uncertainty is shown. The last bin includes overflow events. The deviation between Data and MC prediction is largely due to the MC normalization of the V+jets background which is corrected by the fit mentioned in Section 4.7.

4.5.3 CR1mu0b: one-muon + 0 b-jets control region

The CR1mu0b region is enriched in the background process $W(\mu\nu)$ + jets, and is defined in such a way as to be orthogonal to a region enriched in events with $t\bar{t}$ and single-t backgrounds, CR1l1b. Events are assigned to CR1mu0b region if:

- they pass the pre-selection cuts
- $p_{\mathrm{T}}(W) > 200$ GeV[2]
- no baseline electron, tau or photon, as defined in Section 4.2, is reconstructed
- exactly one baseline muon is reconstructed
- the baseline muon also passes the signal muon selection criteria
- the transverse mass ($m_{\mathrm{T}}^2 = E_{\mathrm{T}}^2 - p_{\mathrm{T}}^2$, $E_{\mathrm{T}} = E\frac{p_{\mathrm{T}}}{|p|}$) of the $(P_{\mathrm{T}}^{\mathrm{recoil}}, \mu)$ system satisfies 30 GeV $< m_{\mathrm{T}} <$ 100 GeV
- b-jets are vetoed (as defined in Section 4.2)

The p_{T}(W) distribution can be exploited to model the boson p_{T} of the $Z(\nu\nu)$ + jets background in the SR using data (see Section 4.7)

Figure 4.2 shows kinematic distributions for events in this region for the full Run 2 data samples, where the background normalization is obtained directly from MC simulation, which is adjusted later after the fit mentioned in Section 4.7.

[2]Here and in the following the boson-p_{T} , p_{T}(W) or p_{T}(Z), is defined as the vectorial sum of $P_{\mathrm{T}}^{\mathrm{recoil}}$ and the p_{T} of the leptons selected in the event.

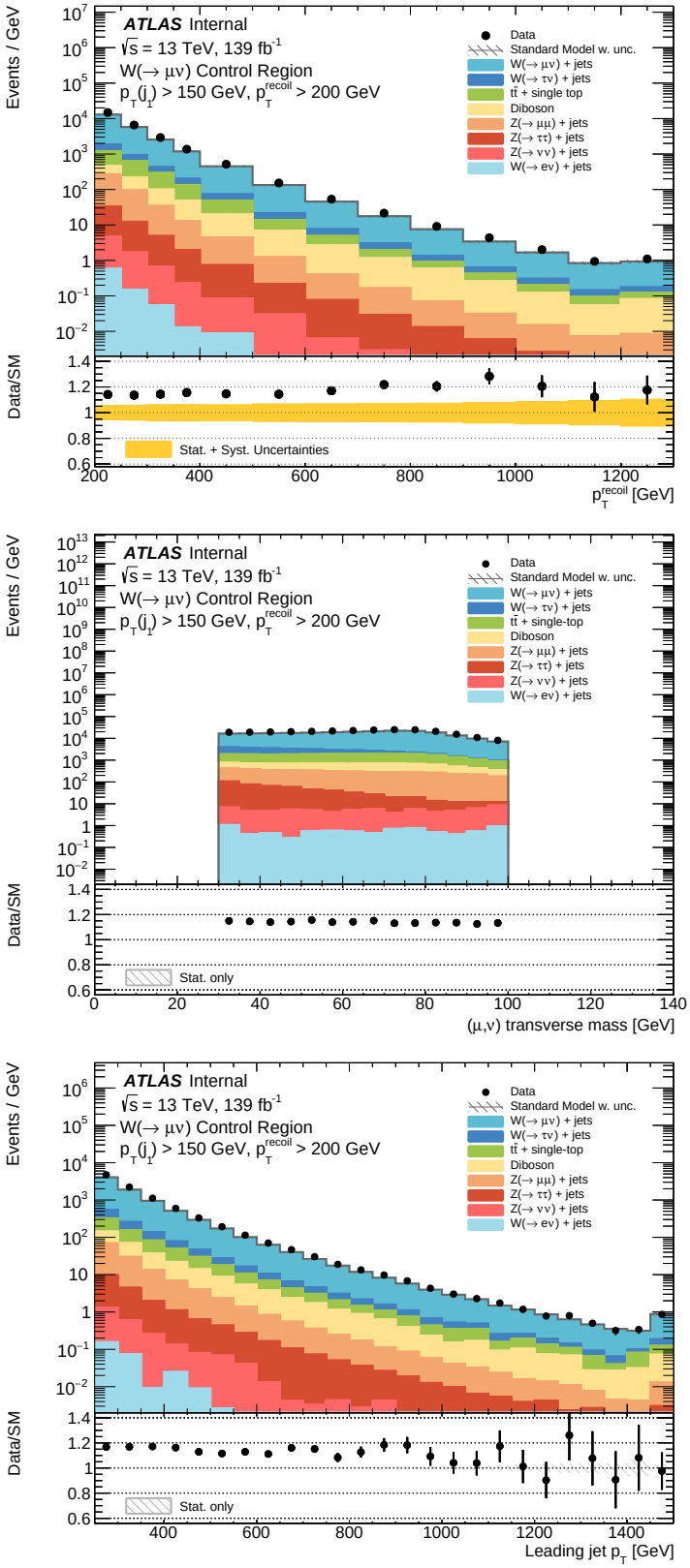

Figure 4.2: `CR1mu0b` distributions in $P_{\mathrm{T}}^{\mathrm{recoil}}$ and leading jet p_{T} based on the full Run 2 dataset. The uncertainty band in the ratio includes only the statistical uncertainties except for in the $P_{\mathrm{T}}^{\mathrm{recoil}}$ distribution in which the statistical + systematic uncertainty is shown. The last bin includes overflow events.

4.5.4 CR2mu: dimuon control region

The CR2mu region is enriched in the background process $Z(\mu\mu)$ + jets. Events are assigned to this region if:

- they pass the pre-selection cuts
- $p_{\mathrm{T}}(Z) > 200$ GeV
- no baseline electron, tau or photon as defined in Sec.4.2, is reconstructed
- exactly two baseline muons are reconstructed.
- both the baseline muons also pass the signal muon selection criteria
- the invariant mass of the dimuon system satisfies 66 GeV $< m_{\mu\mu} <$ 116 GeV

Also in this case the $p_{\mathrm{T}}(Z)$ can be exploited to constrain the $Z(\nu\nu)$+jets background in the SR using data (see Section 4.7).

Figure 4.3 shows kinematic distributions for events in this region for the full Run 2 data samples, where the background normalization is obtained directly from MC simulation, which is adjusted later after the fit mentioned in Section 4.7.

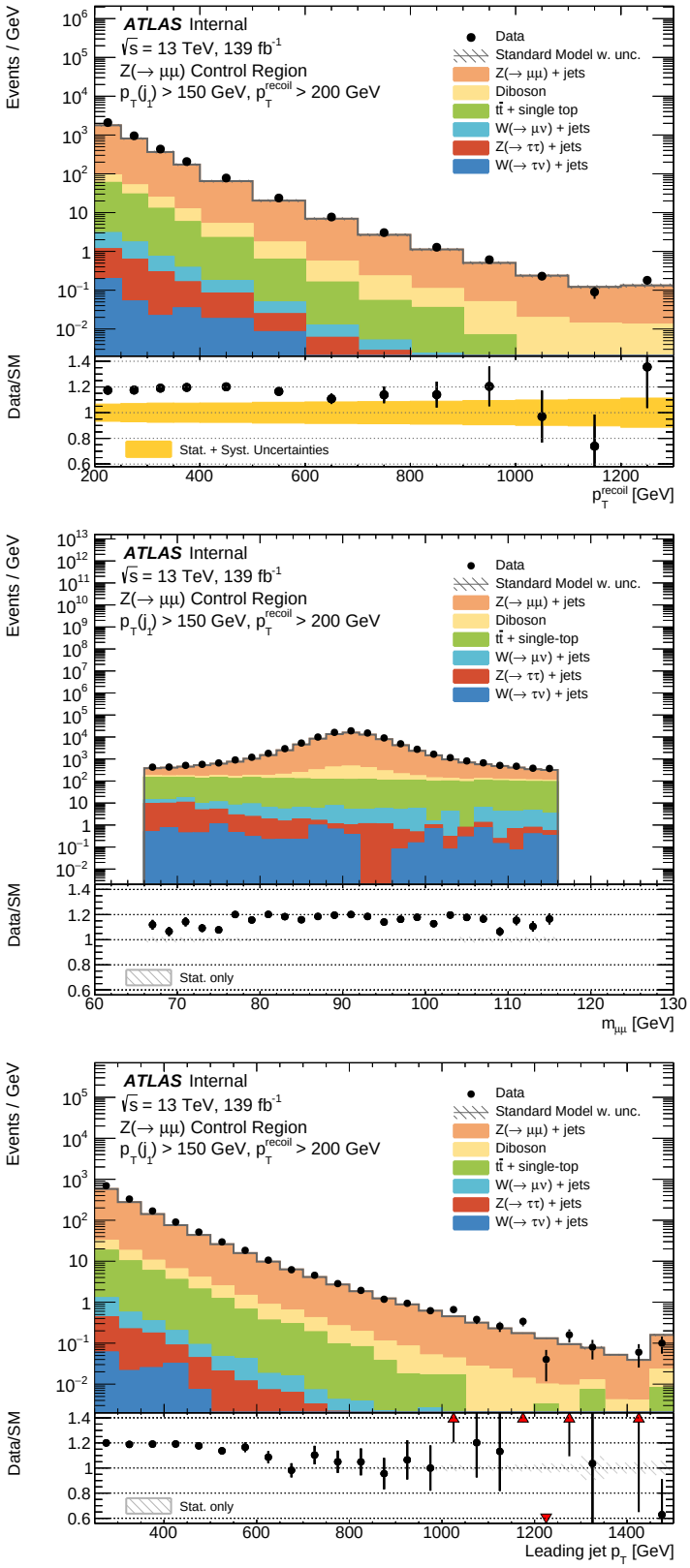

Figure 4.3: `CR2mu` distributions in $P_{\mathrm{T}}^{\mathrm{recoil}}$ and leading jet p_{T} based on the full Run 2 dataset. The uncertainty band in the ratio includes only the statistical uncertainties except for in the $P_{\mathrm{T}}^{\mathrm{recoil}}$ distribution in which the statistical + systematic uncertainty is shown. The last bin includes overflow events.

4.5.5 CR1e0b: one-electron control region

The CR1e0b region is enriched in the background processes $W(e\nu)$ + jets. Events are assigned to this region if:

- they pass the pre-selection cuts
- $p_{\mathrm{T}}(W) > 200$ GeV
- no baseline muon, tau or photon, as defined in Sec.4.2, is reconstructed
- exactly one baseline electron is reconstructed with $p_{\mathrm{T}} > 30$ GeV and $|\eta| > 1.52$ or $|\eta| < 1.37$ (to exclude the overlap region)
- the baseline electron also passes the signal electron selection criteria, and passes the FixedCutTight isolation criteria
- the transverse mass of the $P_{\mathrm{T}}^{\mathrm{recoil}}$ -e system satisfies: 30 GeV $< m_{\mathrm{T}} <$ 100 GeV
- $P_{\mathrm{T}}^{\mathrm{recoil}} > 70$ GeV and $P_{\mathrm{T}}^{\mathrm{recoil}} / \sqrt{H_{\mathrm{T}}} > 5$ GeV$^{1/2}$ to further suppress multijet background (see Appendix P of Ref. [66])
- b-jets are vetoed (as defined in Section 4.2)

This region is defined in a similar way as CR1mu0b, with the difference of the usage of single electron triggers, the introduction of a veto of electrons in the overlap region and of tight isolation criteria, and a few additional cuts in order to avoid contamination from the multijet background.

Figure 4.4 shows kinematic distributions for events in this region for the full Run 2 data samples, where the background normalization is obtained directly from MC simulation, which is adjusted later after the fit mentioned in Section 4.7.

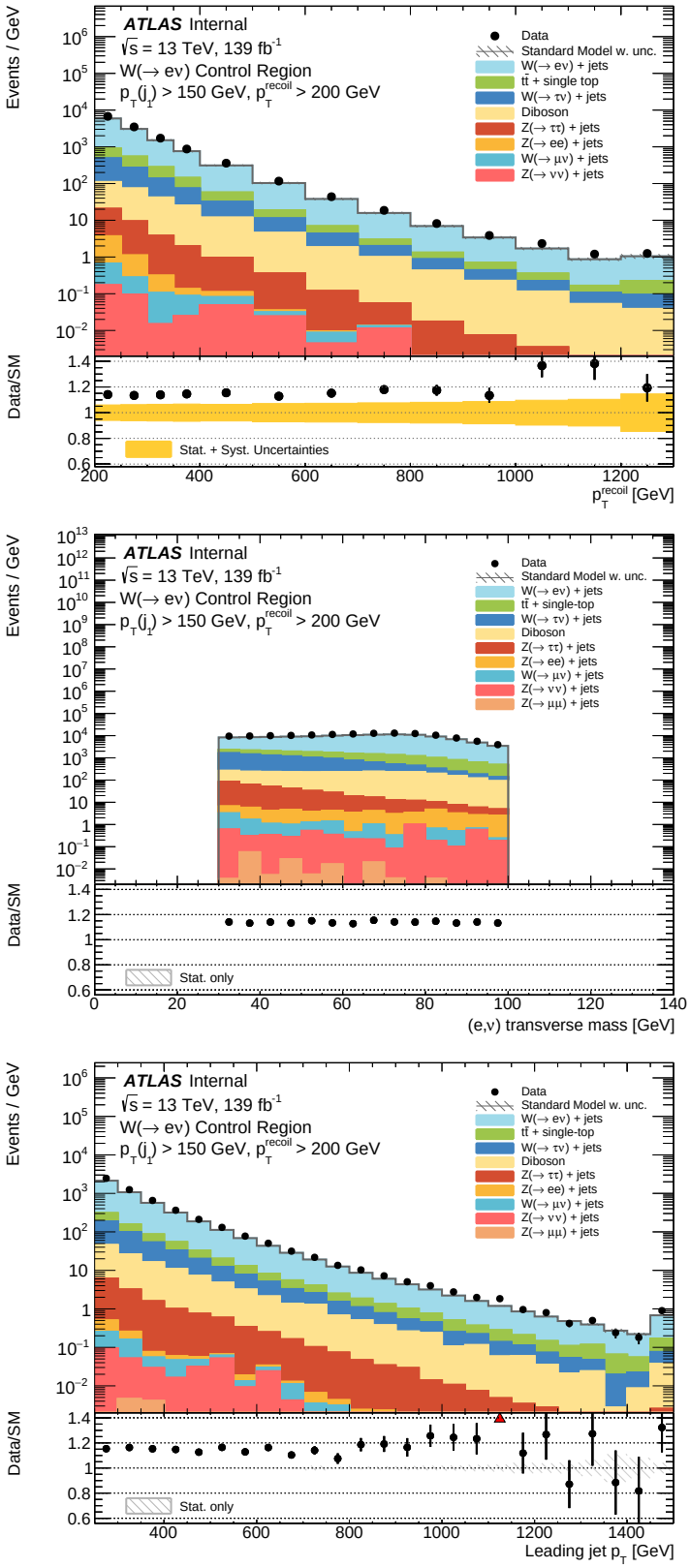

Figure 4.4: `CR1e0b` distributions in $P_{\mathrm{T}}^{\mathrm{recoil}}$ and leading jet p_{T} based on the full Run 2 dataset. The uncertainty band in the ratio includes only the statistical uncertainties except for in the $p_{\mathrm{T}}^{\mathrm{recoil}}$ distribution in which the statistical + systematic uncertainty is shown. The last bin includes overflow events.

4.5.6 CR2e: dielectron control region

The CR2e region is enriched in the background process $Z(ee)$ + jets. Events are assigned to this region if:

- they pass the pre-selection cuts
- $p_{\mathrm{T}}(Z) > 200$ GeV
- no baseline muon, tau or photon, as defined in Sec.4.2, is reconstructed
- exactly two baseline electrons are reconstructed.
- both the baseline electrons also pass the signal electron selection criteria
- the invariant mass of the dielectron system satisfies 66 GeV $< m_{ee} <$ 116 GeV

In section 4.7 it will be shown how the dominant $Z(ee)$ + jets process in this CR can be exploited to constrain the $Z(\nu\nu)$ + jets background in the SR using data.

Figure 4.5 shows kinematic distributions for events in this region for the full Run 2 data samples, where the background normalization is obtained directly from MC simulation, which is adjusted later after the fit mentioned in Section 4.7.

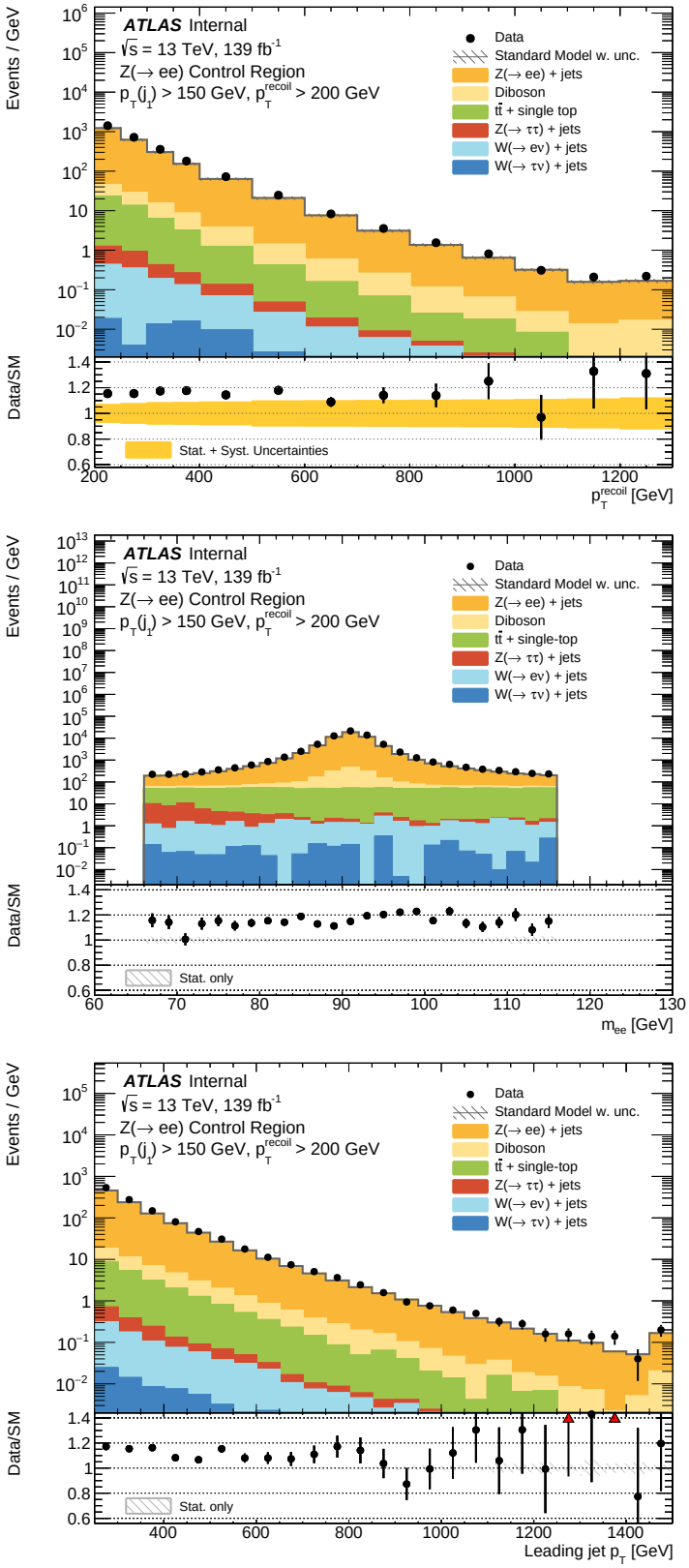

Figure 4.5: CR2e distributions in $P_{\mathrm{T}}^{\mathrm{recoil}}$ and leading jet p_{T} based on the full Run 2 dataset. The uncertainty band in the ratio includes only the statistical uncertainties except for in the $p_{\mathrm{T}}^{\mathrm{recoil}}$ distribution in which the statistical + systematic uncertainty is shown. The last bin includes overflow events.

4.5.6.1 CR1l1b: one-lepton + at least 1 b-jet control region

This control region is designed to be enriched in the $t\bar{t}$ and single-t backgrounds. It is constructed starting from the same conditions as required for the CR1mu0b and CR1e0b regions, except that now at least one b-jet is required instead of being vetoed, identified as explained in Section 4.2. The events selected from both these conditions are then merged to define the CR1l1b region. As the CR1mu0b and CR1e0b regions are orthogonal by construction, no method is required to prevent double counting in the merging.

Figure 4.6 shows kinematic distributions for events in this region for the full Run 2 data samples, where the background normalization is obtained directly from MC simulation, which is adjusted later after the fit mentioned in Section 4.7.

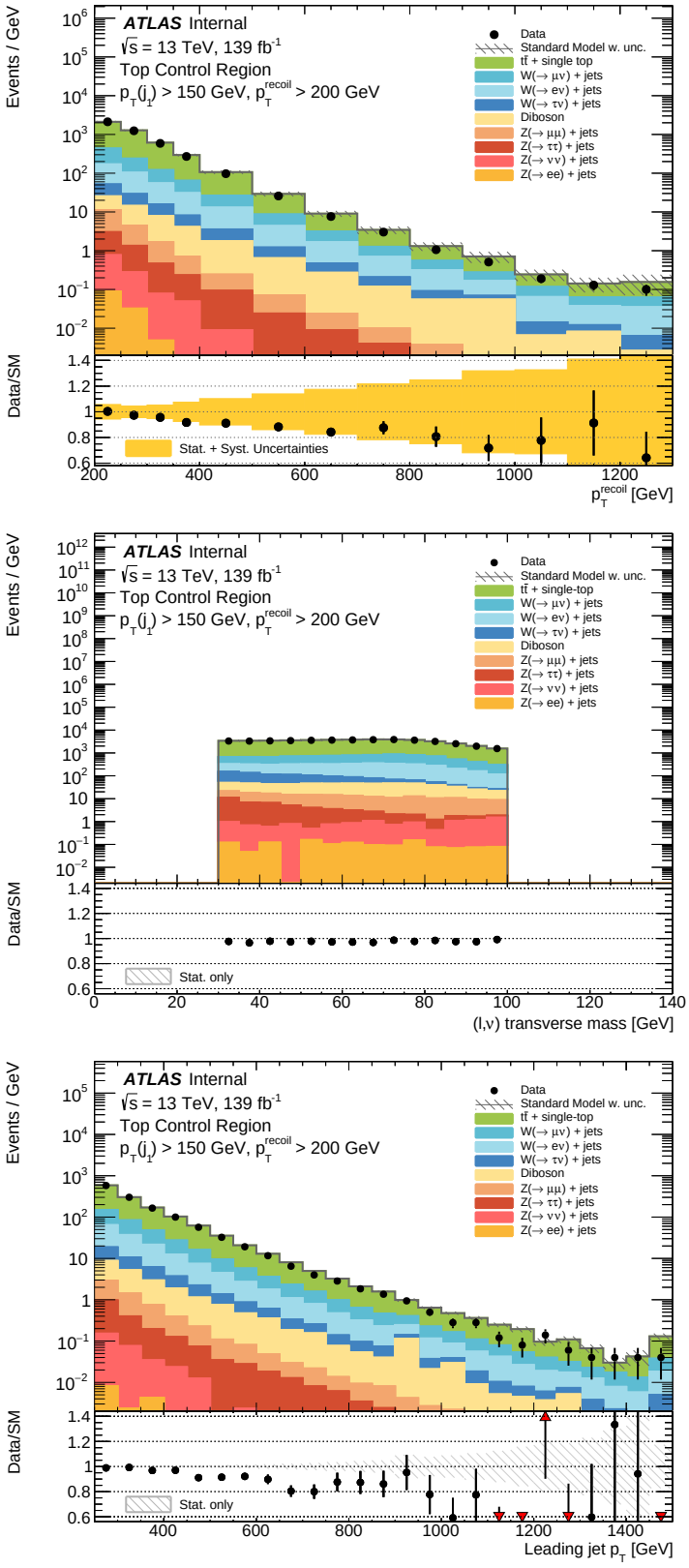

Figure 4.6: `CR1l1b` distributions in $P_{\mathrm{T}}^{\mathrm{recoil}}$ and leading jet p_{T} based on the full Run 2 dataset. The uncertainty band in the ratio includes only the statistical uncertainties except for in the $p_{\mathrm{T}}^{\mathrm{recoil}}$ distribution in which the statistical + systematic uncertainty is shown. The last bin includes overflow events. No offset between data and MC predictions is observed here since the region is dominated by $t\bar{t}$ events and the data is compatible with the MC predictions within the uncertainties.

4.6 Lowering $P_{\mathrm{T}}^{\mathrm{recoil}}$ threshold and leading jet p_{T} threshold

In the previous version of the monojet analysis, a $P_{\mathrm{T}}^{\mathrm{recoil}}$ threshold and leading jet p_{T} threshold of 250 GeV were chosen, largely due to constraints on available computing power and that which is required for simulations increasing rapidly as the $P_{\mathrm{T}}^{\mathrm{recoil}}$ and leading jet p_{T} thresholds are decreased. It was decided at the time that as most signals looked for in the monojet analysis are 'hard' (i.e. their $P_{\mathrm{T}}^{\mathrm{recoil}}$ distribution falls more slowly at high $P_{\mathrm{T}}^{\mathrm{recoil}}$ than the Standard Model and hence deviations from the Standard Model are more visible in data at high $P_{\mathrm{T}}^{\mathrm{recoil}}$) the sensitivity gain from lowering the $P_{\mathrm{T}}^{\mathrm{recoil}}$ and leading jet p_{T} thresholds for these signals would be negligible and not worth the additional computing power required.

However, as the monojet analysis has moved more into the precision regime and also now explores more signals and aims to explore even more, many of which are quite soft, it was decided to study the $P_{\mathrm{T}}^{\mathrm{recoil}}$ and leading jet p_{T} thresholds again to determine whether lowering them could gain significant sensitivity. Lowering the thresholds as far as $P_{\mathrm{T}}^{\mathrm{recoil}} = 200$ GeV and leading jet $p_{\mathrm{T}} = 150$ GeV were considered, as our current method of estimating the multijet background is not valid below this region.

Two such soft signals that are now being investigated by the monojet analysis but were not in the previous version are the Higgs→invisible search and the pseudoscalar WIMP search, which hence were used in this study.

As this study was performed largely to determine whether it was worthwhile to simulate samples for use with a low $P_{\mathrm{T}}^{\mathrm{recoil}}$ threshold, at the time the study was performed there were few simulation samples to compare with. However, Higgs→invisible is a signal common to many analyses and hence MC data was already available at RECO level. For the pseudoscalar WIMPs, many small samples were generated at TRUTH level.

In addition, as this study was performed quite early in the monojet analysis devel-

opment many parts of the monojet analysis were not yet finalised. An important part of this was that the Non-Collision Background (NCB) had not been estimated yet, which rises quite rapidly at low $P_{\mathrm{T}}^{\mathrm{recoil}}$ and hence including this would adjust the results of the following study slightly. However, it is known that NCB is subdominant to the multijet background everywhere in the monojet analysis, so it would not change the results of the study by a large amount.

The number of signal events was evaluated for each $P_{\mathrm{T}}^{\mathrm{recoil}}$ bin and divided by the uncertainty on the background to estimate the signal sensitivity in each bin, the value from this in each bin is then summed over the full $P_{\mathrm{T}}^{\mathrm{recoil}}$ range to produce an estimate of the total sensitivity to the signal. An estimate of the sensitivity, by comparing the number of signal events to uncertainty in background events, in each $P_{\mathrm{T}}^{\mathrm{recoil}}$ bin at varying leading jet p_{T} thresholds for Higgs→invisible and three example pseudoscalar WIMP signals with mediator mass = 300 GeV is shown in Figure 4.7.

These results were then combined into an estimate of the global sensitivity gained compared to the previous monojet thresholds of $P_{\mathrm{T}}^{\mathrm{recoil}} = 250$ GeV and leading jet $p_{\mathrm{T}} = 250$ GeV, shown in Figure 4.8. From this it is clear that significant improvements can be made for soft signals by lowering the $P_{\mathrm{T}}^{\mathrm{recoil}}$ and leading jet p_{T} thresholds to $P_{\mathrm{T}}^{\mathrm{recoil}} = 200$ GeV leading jet $p_{\mathrm{T}} = 150$ GeV. However, as expected these gains are much smaller for hard signals. Shown in Figure 4.9 is the sensitivity gained at this threshold for the axial-vector WIMP model we consider, which is a much harder signal, showing much smaller gains in sensitivity.

As a result of this study the thresholds were lowered to $P_{\mathrm{T}}^{\mathrm{recoil}} = 200$ GeV and leading jet $p_{\mathrm{T}} = 150$ GeV. This also requires calculating scale factors for our $P_{\mathrm{T}}^{\mathrm{recoil}}$ triggers in this lower $P_{\mathrm{T}}^{\mathrm{recoil}}$ region, which is discussed further in Section 5.2.

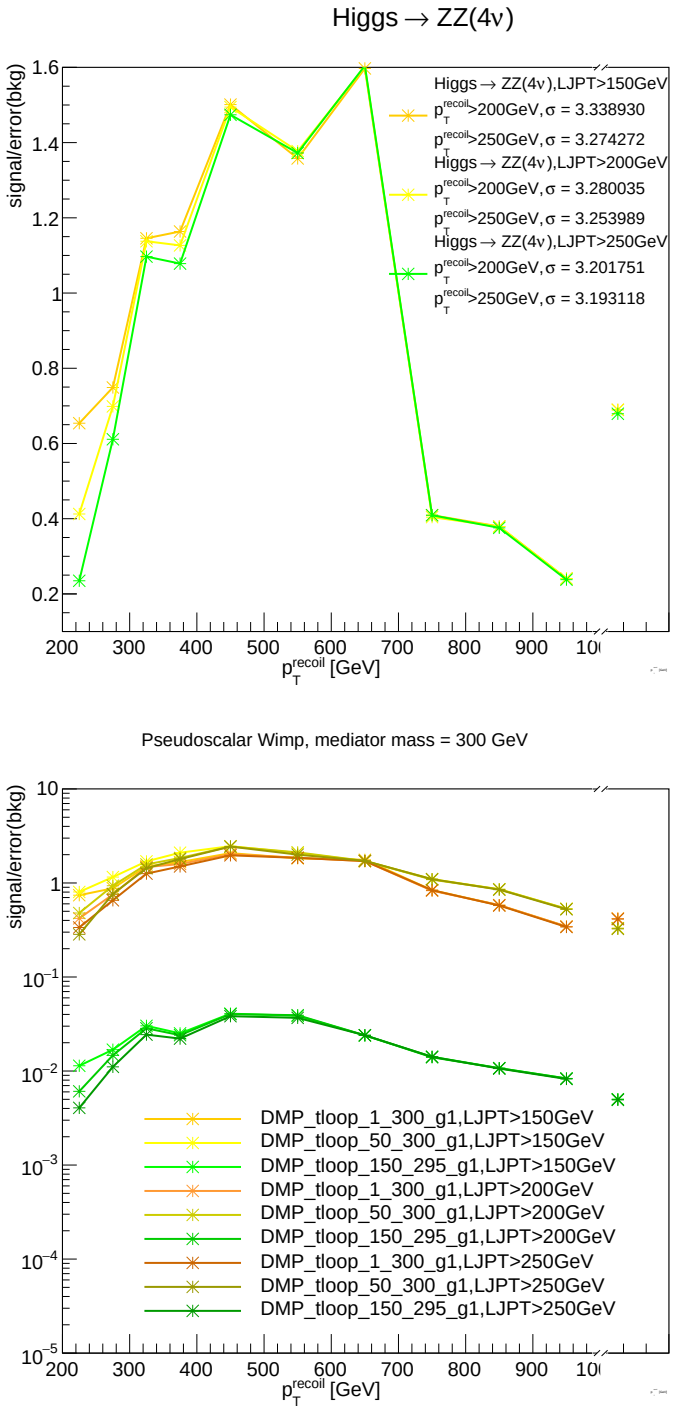

Figure 4.7: Sensitivity estimate per bin when lowering $P_{\mathrm{T}}^{\mathrm{recoil}}$ and leading jet p_{T} thresholds for Higgs→invisible (top) and three example pseudoscalar WIMP models (bottom) (DMP_tloop_x_y_g1 = pseudoscalar WIMP with a WIMP mass = x GeV and mediator mass = y GeV). The sensitivity in the new $P_{\mathrm{T}}^{\mathrm{recoil}}$ = 200-250 GeV bin can be seen to be comparable to the 250-300 GeV bin when also lowering the leading jet p_{T} threshold for many samples.

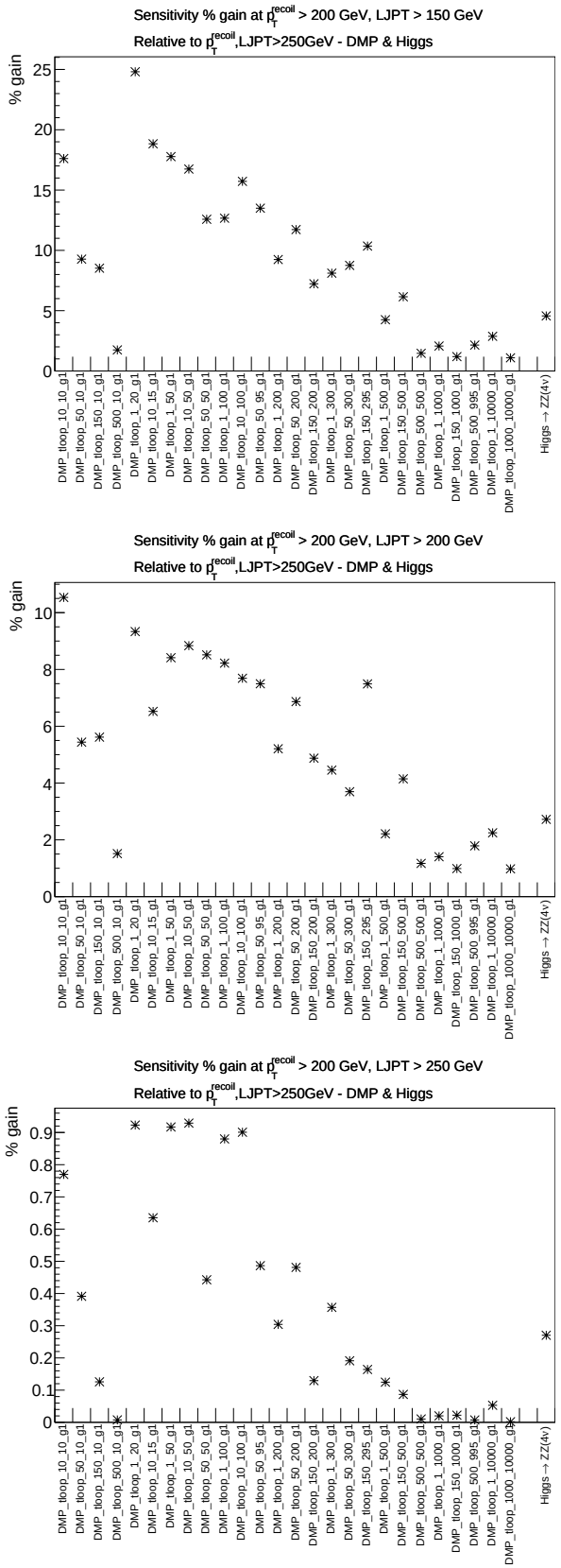

Figure 4.8: Global sensitivity gain estimate when lowering $P_{\mathrm{T}}^{\mathrm{recoil}}$ and leading jet p_{T} thresholds for Higgs→invisible and pseudoscalar WIMP models (DMP_tloop_x_y_g1 = pseudoscalar WIMP with a WIMP mass = x GeV and mediator mass = y GeV). A significant increase compared to the previous analysis thresholds, up to 25% for some with the $P_{\mathrm{T}}^{\mathrm{recoil}}$ threshold = 200 GeV, and leading jet p_{T} threshold = 150 GeV.

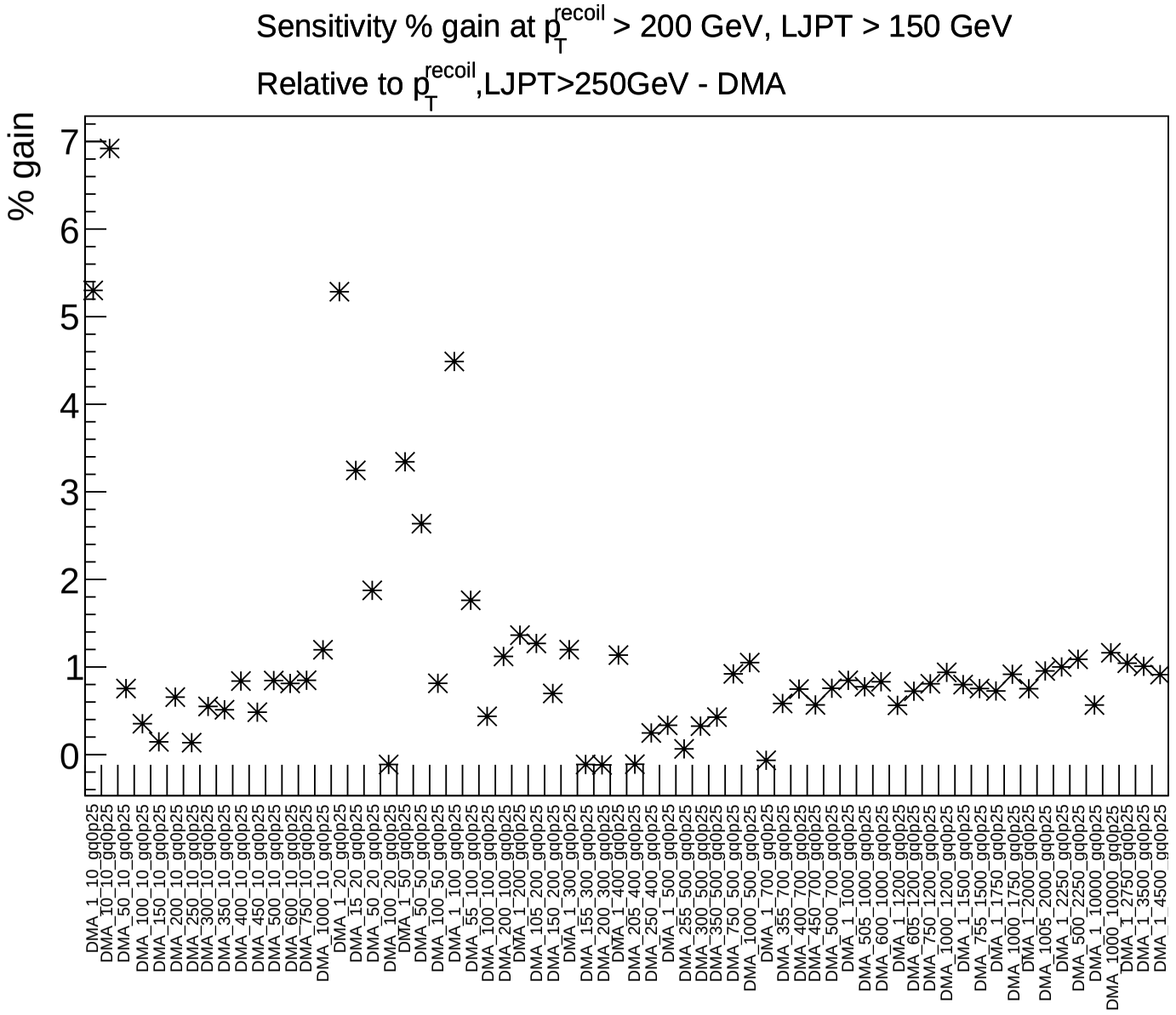

Figure 4.9: Global sensitivity gain estimate when lowering $P_{\mathrm{T}}^{\mathrm{recoil}}$ and leading jet p_{T} thresholds for axial-vector WIMP models (DMA_x_y_gq0p25 = an axial-vector WIMP with a WIMP mass = x GeV and mediator mass = y GeV). A much smaller sensitivity gain is achieved than in the pseudoscalar WIMP case, due to the relative hardness of the axial-vector WIMP.

4.6.1 WIMP MC filter

The simulations used in the previous monojet analysis were designed to be fully efficient above the $P_{\mathrm{T}}^{\mathrm{recoil}}$ and leading jet p_{T} thresholds used at the time. As the thresholds have now been lowered, the simulations need to be adjusted to include statistics in the lower $P_{\mathrm{T}}^{\mathrm{recoil}}$ and leading jet p_{T} regions. It was originally planned to generate a small number of events in just the lower $P_{\mathrm{T}}^{\mathrm{recoil}}$ and leading jet p_{T} region and use the previous simulations for the more boosted region, however a bug was discovered in the old simulations that affected jet vetoing in PYTHIA for emissions.

The effect of this bug on the leading jet p_{T} is shown in Figure 4.10, comparing samples with the bug to samples with this bug fixed. From this it can be seen that this bug significantly affects the leading jet p_{T} distribution. The affected samples have a deficit of leading jets at low p_{T} and an excess at high p_{T}. This can be understood as with vetoing included for emissions, high p_{T} jets should lose some p_{T} as they radiate emissions, shifting the distribution to lower p_{T}.

It can be seen however, that after pre-selection has been applied and baseline leptons have been vetoed ('monojet cuts'), there is no significant difference between the affected samples and the fixed samples. It was still decided to regenerate over the full region, since the monojet analysis is heavily dependent upon jet distributions and it was believed that the incorrect underlying jet distribution could cause other unnoticed subtle problems. In addition to this, in the future the monojet analysis will be changed further and after these changes it may no longer be the case that the leading jet p_{T} distribution after monojet cuts is not affected by this bug.

To ensure sufficient statistics were available, it was decided to generate the same number of events per MC campaign in the region $P_{\mathrm{T}}^{\mathrm{recoil}} > 400$ GeV (chosen as this is far enough from the threshold that lowering the leading jet p_{T} threshold has no effect) as had been generated in the previous version, while also generating events in the new lower threshold region.

To do this, a filter that is applied on the WIMP samples was lowered. The filter

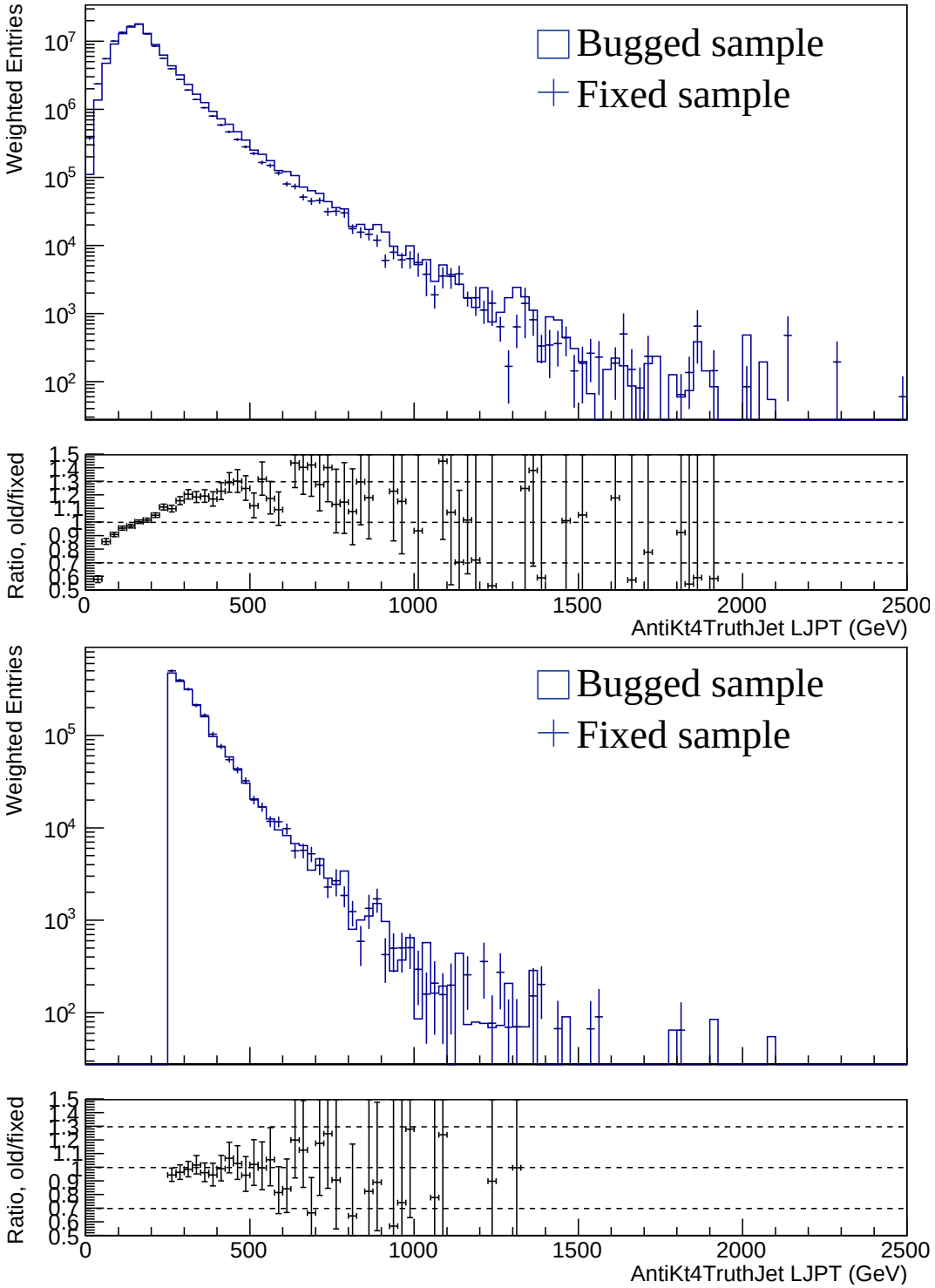

Figure 4.10: Comparison of WIMP TRUTH leading jet p_{T} (AntiKt4TruthJet LJPT) distribution with PYTHIA vetoing bug (histogram) and without (markers), both without and with monojet cuts (top and bottom respectively).

bornktmin = x GeV applies a cut on the transverse momentum of the interacting partons (*bornkt*) at generation level, rejecting events with *bornkt* < x GeV. This is very strongly correlated in the monojet analysis with the transverse momentum of the observed jets.

Hence, this filter cut was lowered until the full region that was desired was covered. Care had to be taken to ensure that this was valid, as the cross section is divergent at very low *bornkt*. By generating small test samples at varying *bornktmin* it was determined that for *bornkt* $\geq$ 20 GeV, the WIMP models used were valid, which is significantly lower than the filter needed to be.

As the WIMP samples were available at this time only at TRUTH level, while we desire the results at RECO level, the difference between RECO $P_{\mathrm{T}}^{\mathrm{recoil}}$ and TRUTH $P_{\mathrm{T}}^{\mathrm{recoil}}$ was measured, and it was found that less than 0.01% of events have a difference of more than 100 GeV. Hence, it was decided to set *bornktmin* such that the TRUTH $P_{\mathrm{T}}^{\mathrm{recoil}}$ distribution was 100% efficient above 100 GeV, as this would ensure it was > 99.99% efficient above the new 200 GeV RECO $P_{\mathrm{T}}^{\mathrm{recoil}}$ threshold.

Shown in Figure 4.11 is the highest value of *bornktmin* possible while being 100% efficient above TRUTH $P_{\mathrm{T}}^{\mathrm{recoil}}$ = 100 GeV, both without and with monojet cuts. From this, it can be seen that the values of *bornktmin* required without and with monojet cuts are 60 GeV and 100 GeV respectively.

While it would be ideal to have the samples valid down to the $P_{\mathrm{T}}^{\mathrm{recoil}}$ threshold without monojet cuts, so that other aspects of the monojet analysis can be adjusted in the future without possibly needing to generate new samples, unfortunately the computing power required scales with *bornktmin* too rapidly to feasibly generate at *bornktmin* = 60 GeV. Compared to *bornktmin* = 150 GeV (the value used in the previous analysis before lowering the thresholds), *bornktmin* = 60 GeV and *bornktmin* = 100 GeV take four times and two times as much computing power respectively. For the number of samples required and the computing resources used, *bornktmin* = 150 GeV would take approximately 20 days to generate. Hence it

was decided to generate at $bornktmin = 100$ GeV, as this would allow us to lower the threshold as far as currently desired without requiring an unfeasible amount of computing resources, although a lower threshold will likely be needed in a future analysis.

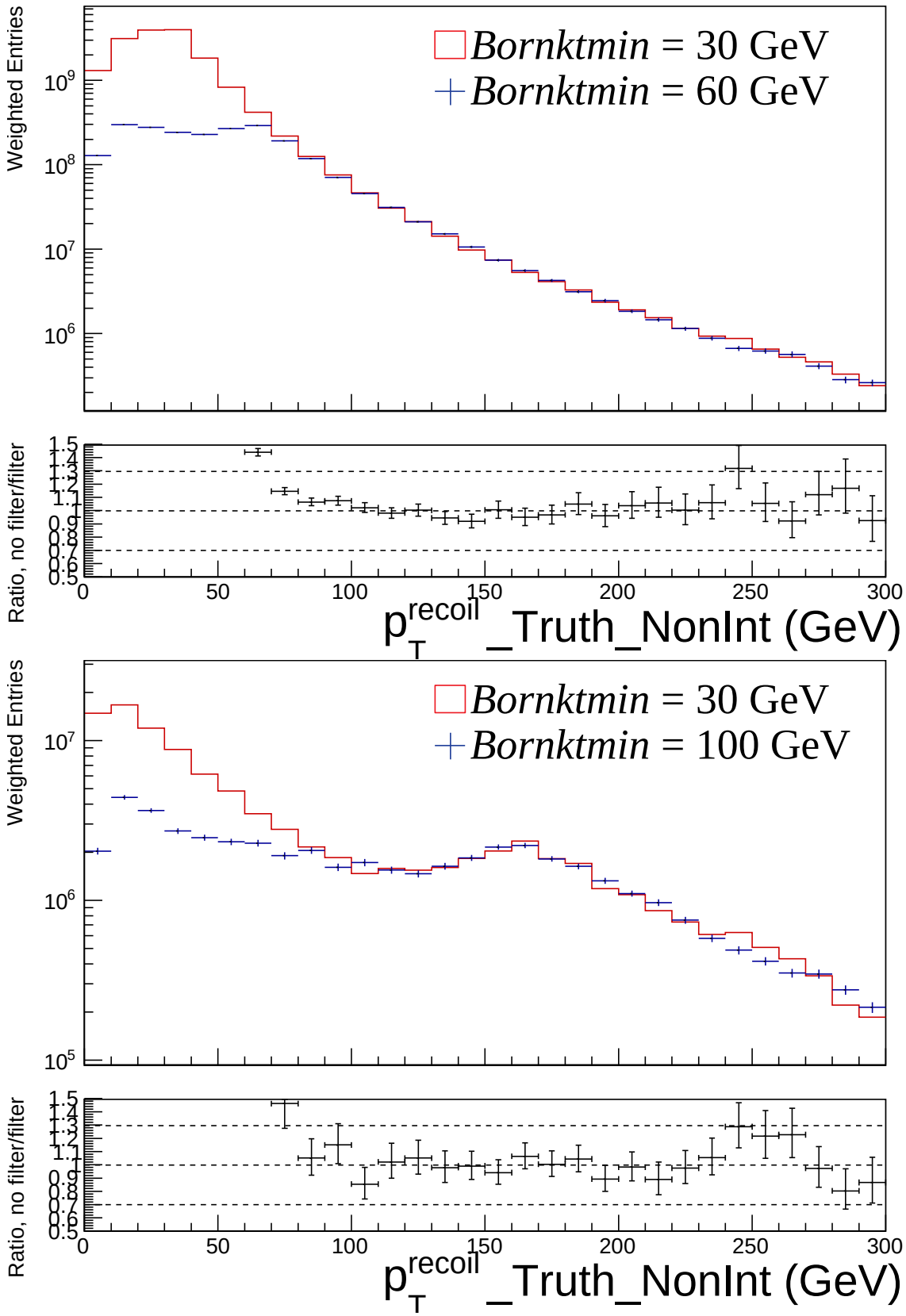

Figure 4.11: $P_{\mathrm{T}}^{\mathrm{recoil}}$ (MET) distribution comparing low *bornktmin* filters both without (above) and with (below) monojet cuts, *bornktmin* set such that the $P_{\mathrm{T}}^{\mathrm{recoil}}$ TRUTH ($P_{\mathrm{T}}^{\mathrm{recoil}}$ _TRUTH_NonInt) distribution is 100% efficient above 100 GeV.

4.7 Standard Model background

As discussed in Section 4.5, all events assigned to any of the control regions and the signal region involve at least one energetic jet and $P_{\mathrm{T}}^{\mathrm{recoil}} > 200$ GeV. This can be achieved in Standard Model processes either by production of jets in association with high p_{T} neutrinos, as neutrinos are not detected by the ATLAS detector and hence their p_{T} appears as $P_{\mathrm{T}}^{\mathrm{recoil}}$, or by production of jets in association with other objects, for example a lepton, that are missed by ATLAS.

The main sources of background to this search are:

- $Z(\nu\nu) +$ jets production (irreducible)
- $W(\tau\nu)+$jets with the tau decaying hadronically or into an unidentified charged lepton and neutrinos
- $W(\mu\nu) +$ jets where the muon is not reconstructed or is not identified
- $W(e\nu) +$ jets where the electron is not reconstructed or is not identified
- $Z(\tau\tau) +$jets with the tau leptons decaying hadronically or into an unidentified charged lepton and neutrinos
- $Z(\mu\mu) +$ jets where both muons are not reconstructed or not identified
- $Z(ee) +$ jets where both electrons are not reconstructed or not identified
- diboson (WW, ZZ or WZ) production with unreconstructed or unidentified leptons in the final state
- $t\bar{t}$ or single-t production with unreconstructed or unidentified leptons in the final state
- multi-jet background, with $P_{\mathrm{T}}^{\mathrm{recoil}}$ originating from the misreconstruction of one jet

- non-collision background (NCB) originating, for example, from beam-halo interactions producing a muon which travels parallel to the beam axis and emits radiation identified as a jet, or from calorimeter noise (in this case, $P_{\mathrm{T}}^{\mathrm{recoil}}$ originates from the kinematic inbalance in the transverse plane)

Of these, the $Z(\nu\nu)+\mathrm{jets}$ process is dominant over the full $P_{\mathrm{T}}^{\mathrm{recoil}}$ range followed by $W+\mathrm{jets}$, multi-jet and NCB are only relevant in the low $P_{\mathrm{T}}^{\mathrm{recoil}}$ region, diboson and top are relevant from low to medium $P_{\mathrm{T}}^{\mathrm{recoil}}$, and $Z+\mathrm{jets}$ are relevant over the full $P_{\mathrm{T}}^{\mathrm{recoil}}$ range.

The contributions of the $Z+\mathrm{jets}$, $W+\mathrm{jets}$ and $t\bar{t}$ processes in the signal region are evaluated using a semi-data-driven technique based on:

- the predictions obtained with MC simulation
- the observations in the data control regions, enriched in the different $Z+\mathrm{jets}$, $W+\mathrm{jets}$ and $t\bar{t}$ backgrounds, described in Section 4.5

In particular, the $Z(\nu\nu)+\mathrm{jets}$ contribution, which would otherwise be indistinguishable from signal, is inferred from the measured $W+\mathrm{jets}$ and $Z+\mathrm{jets}$ contributions in the control regions. More details on the estimation technique used for each of the backgrounds are given in Table 4.4. Systematic uncertainties resulting from this assumption are taken into account as described in Section 6.1.

The contribution of the diboson processes in the signal region is evaluated directly from MC simulation, rather than a fit to control regions as done for Z/W + jets and the top background. This is largely due to it being a non-dominant background in all regions.

The multi-jet background needs to be estimated from a fully data-driven method because of failure of MC simulation to reproduce the non-Gaussian detector effects of the jet measurement in data, which prevent the possibility of a simple rescaling of MC. Due to its low acceptance in the signal region, this method is sufficient to

model it. The jet smearing method is performed as follows to evaluate the multi-jet background and is described in more detail in Ref. [66]:

- Select 'seed events' from data with low $P_{\mathrm{T}}^{\mathrm{recoil}}$, which will be used in the next two steps.
- Measure the jet response function for b-jets and separately for b-veto jets to estimate the fluctuation in the measured jet transverse momenta. The response functions are initially measured in MC simulated data by comparing the generator truth level jet p_{T} to the reconstructed p_{T} . These are then modified so that pseudo data, generated by smearing the seed events from step 1, agree with data in specific control regions. The control regions are defined to be sensitive to the jet response function. For example the di-jets control region constrains the Gaussian core of the jet response, whereas the three-jets control region constrains the non-Gaussian response tail of a signal jet. The modified jet response function is named as the data-constrained jet response function and will be used in step 3.
- The data-constrained jet response function obtained from step 2 is used to smear the seed events from step 1, in order to get the estimated distributions of key variables in the control and signal regions within the main analysis.

4.7.1 Simultaneous fit

The control regions and the signal region described in Section 4.5 are used with a simultaneous fitting technique based upon a binned likelihood to obtain the normalization for the backgrounds as listed in Table 4.4.

This fit uses the shapes of the $P_{\mathrm{T}}^{\mathrm{recoil}}$ distributions in each region; for the control regions the $P_{\mathrm{T}}^{\mathrm{recoil}}$ is calculated while treating the charged leptons as invisible (which causes $P_{\mathrm{T}}^{\mathrm{recoil}}$ to act as a measure of the momentum of the electroweak boson produc-

Process	Background estimation method
$Z(\nu\nu)+$jets	simultaneous fit
$W(\mu\nu)+$jets	simultaneous fit
$W(e\nu)+$jets	simultaneous fit
$W(\tau\nu)+$jets	simultaneous fit
$Z(\mu\mu)+$jets	simultaneous fit
$Z(\tau\tau)+$jets	simultaneous fit
$Z(ee)$ + jets	simultaneous fit
diboson	from MC
$t\bar{t}$ and single-t	simultaneous fit
multi-jet	jet smearing
non-collision background	tagger

Table 4.4: Background estimation techniques used for the different processes contributing to the signal region.

ing the charged leptons). This shape information is used to attempt to distinguish Standard Model background processes from signal processes.

The control regions are each dominated, by design, by either a single or two background processes, which can be seen from the pre-fit plots shown in the various regions in Section 4.5, listed in Table 4.5.

Region	Dominant Process(es)
`SR`	$Z(\nu\nu)+$jets, $W(l\nu)$ + jets
`CR1e0b`	$W(e\nu)+$jets, $W(\tau\nu)+$jets
`CR1mu0b`	$W(\mu\nu)+$jets
`CR2e`	$Z(ee)+$jets
`CR2mu`	$Z(\mu\mu)+$jets
`CR1l1b`	$t\bar{t}$, single-t

Table 4.5: Dominant processes in the signal region and each control region.

Three normalization factors are used, one for all V+jets processes (κ^{V}), one for $t\bar{t}$ ($\kappa^{t\bar{t}}$) and one for single-t ($\kappa^{\text{single-}t}$). The reason that both Z+jets and W+jets are given the same normalization factor, is that their kinematics are very similar so this allows $W(l\nu)$+jets which has large statistics in comparison to $Z(ee)+$jets and $Z(\mu\mu)+$jets, to constrain the normalization of $Z(\nu\nu)+$jets, which otherwise would be dependent on low statistics.

These normalization factors are allowed to vary in the fit, based on the measurements in control regions dominated by their relevant backgrounds. In addition, a fourth parameter is fitted, μ, which is the signal strength.

For model-dependent limits the $P_{\mathrm{T}}^{\mathrm{recoil}}$ distribution in each region is binned as shown in the previous plots in Section 4.5. For model-independent limits the same process is used however the $P_{\mathrm{T}}^{\mathrm{recoil}}$ distribution is instead binned inclusively, where each bin only has a lower limit (which is the same lower limit as the bins in the model-dependent case) and extends indefinitely. This inclusive binning is used for the model-independent case to remove shape information, which is very model-dependent. In addition, for model-independent limits a single normalization factor for both $t\bar{t}$ and single-t is used, as the shape information in `CR1l1b` is lost which makes the two separate normalization factors redundant.

The definition of the likelihood is taken from [52] and is as follows:

- i, with $1 \leq i \leq N_{\mathrm{bins}}$, is the i-th $p_{\mathrm{T}}^{\mathrm{recoil}}$ bin considered in the fit.
- r runs over the signal or control regions.
- N_{ri}^{obs} is the observed total yield in the i-th $p_{\mathrm{T}}^{\mathrm{recoil}}$ bin of region r.
- $N_{ri}^{X} = N_{ri}^{X}(\theta)$ is the expected yield of process X in the i-th $p_{\mathrm{T}}^{\mathrm{recoil}}$ bin of region r.
- θ is the vector of nuisance parameters describing systematic uncertainties on the predicted yield of each background in each region and $p_{\mathrm{T}}^{\mathrm{recoil}}$ bin.
- $\mu \geq 0$ is the scale factor associated to the normalisation of the considered signal (*signal strength*).
- κ is the vector of κ-factors, $\kappa = \left(\kappa^{V}, \kappa^{t\bar{t}}, \kappa^{t}\right)$, where these κ-factors are normalisation factors for V+jets, $t\bar{t}$ and single-t respectively.

Then, the likelihood $\mathcal{L}$ is defined as

$$\mathcal{L}(\mu, \kappa, \theta) = \prod_{r} \prod_{i} \mathrm{Poisson}\left(N_{ri}^{\mathrm{obs}} \mid \mu N_{ri}^{\mathrm{sig}}(\theta) + N_{ri}^{\mathrm{bkg}}(\kappa, \theta)\right) f_{\mathrm{constr}}(\theta), \tag{4.1}$$

where

$$
\begin{aligned}
N_{ri}^{\text{bkg}} = \kappa^{V}(&N_{ri}^{Z(\nu\nu)+\text{jets}} \\
&+ N_{ri}^{W(\mu\nu)+\text{jets}} + N_{ri}^{W(e\nu)+\text{jets}} + N_{ri}^{W(\tau\nu)+\text{jets}} \\
&+ N_{ri}^{Z(\tau\tau)+\text{jets}} + N_{ri}^{Z(\mu\mu)+\text{jets}} + N_{ri}^{Z(ee)+\text{jets}}) \\
&+ \kappa^{t\bar{t}}(N_{ri}^{t\bar{t}}) + \kappa^{t}(N_{ri}^{\text{single-}t}) \\
&+ N_{ri}^{\text{diboson}} + N_{ri}^{\text{multi-jet+NCB}}.
\end{aligned}
\tag{4.2}
$$

The dependence of N_{ri}^{X} on the nuisance parameters θ (which allow for fluctuations with respect to the nominal prediction of the yield of each process) is omitted to simplify the notation. The term f_{constr} represents the product of the gaussian constraints applied to each of the nuisance parameters.

More details on the technical implementation are provided in Section 2.2 of [67].

In order to take into account the MC statistical uncertainties, an additional gaussian constraint in a certain bin is applied if $\sqrt{N_{ri}^{data}}/\sigma_{MC,ri}^{stat} < 10$, where $\sigma_{MC,ri}^{stat}$ is the sum in quadrature of the MC statistical uncertainties of the several background processes in the ri-bin. In addition to this requirement, the total background uncertainty in a specific bin has to be greater than 0.5% to be included.

The results of the fit within the signal region are shown in Section 6.1.6.1, after the following Chapter 5 which details improvements to the trigger system which were essential for the data taking needed to feed into the fit, and a discussion on systematic uncertainties which are used in the fit at the start of Chapter 6.

CHAPTER 5

Monojet Triggers

5.1 L1 $P_{\mathrm{T}}^{\mathrm{recoil}}$ trigger validity studies & improvements/fixes

Each trigger has a threshold beyond which it is designed to accept events. However due to the trigger's lower precision and accuracy compared to offline analysis, the triggers are not 100% efficient at these thresholds when measured offline and typically have a turn-on curve which describes how the efficiency of the trigger increases as the property of the event being measured increases above the threshold.

To measure this turn-on curve a control region with a W($\rightarrow \mu\nu$)+jets selection was used. It might be thought that this control sample is not analogous in terms of $P_{\mathrm{T}}^{\mathrm{recoil}}$ to our search for dark matter + jets, as the p_{T}^{μ} could balance the p_{T}^{jets} if the p_{T}^{ν} is low. However the L1 $P_{\mathrm{T}}^{\mathrm{recoil}}$ trigger used does not include muon information which causes them to appear invisible to it, allowing us to use the same trigger for both the signal region and this control region.

A good understanding of the triggers is needed to allow the precise measurement of the background that is required. However, there were unexplained properties of the turn-on curve for the L1_XE50 online trigger, which is designed to select events with L1 $P_{\mathrm{T}}^{\mathrm{recoil}} > 50$ GeV, as shown in Figure 5.1 [68].

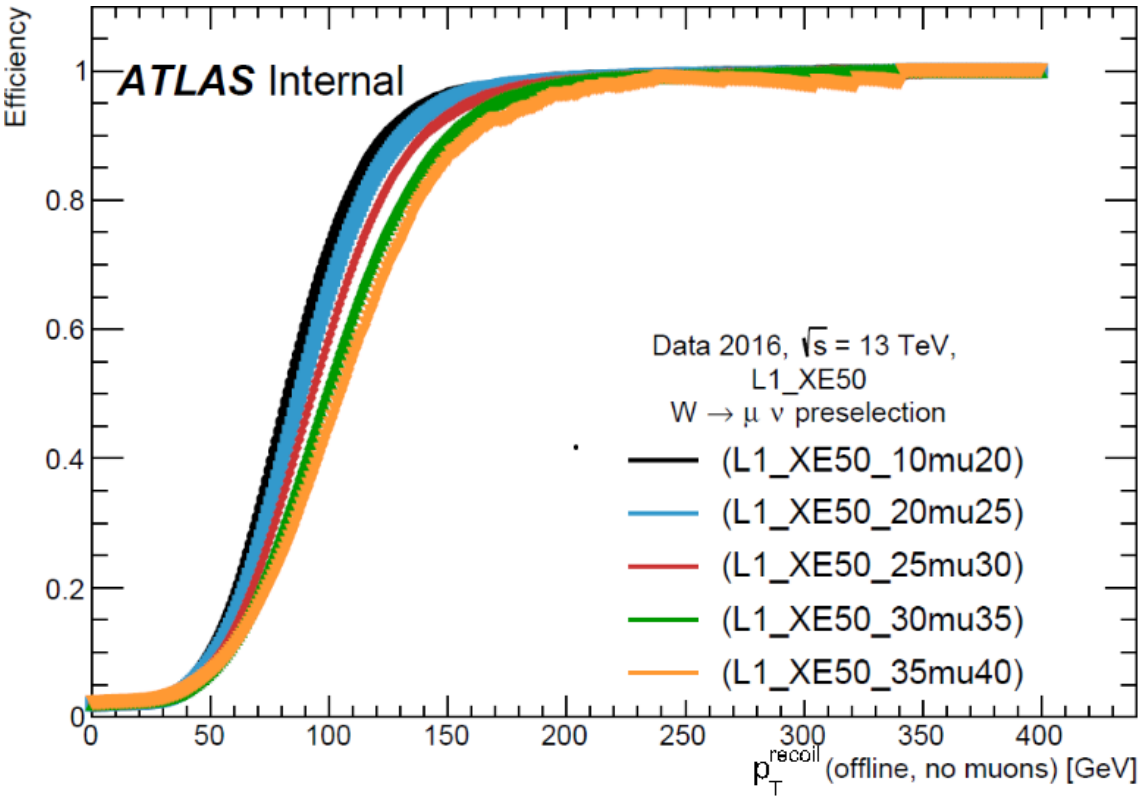

Figure 5.1: L1_XE50 turn-on curve for a variety of muon triggers. **x**mu**y** is a trigger designed to accept events that contain a muon of energy between **x**-**y** GeV. The efficiency is evaluated as $\frac{\text{passes L1\_XE50 AND passes L1\_10mu20}}{\text{passes L1\_10mu20}}$. The muon trigger is used in addition to the L1_XE50 trigger to prevent biasing the selected samples, as just $\frac{\text{passes L1\_XE50}}{\text{all events recorded}}$ would be biased by events only being recorded if they pass another trigger, which is much more likely to occur for events that pass L1_XE50 (Events that pass L1_XE50 are more 'interesting' than a typical event and hence are likely to have other 'interesting' properties that separate triggers may trigger on) [68].

The shift in turn-on curves for different muon momentum triggers does not concern the monojet analysis, as monojet events require high offline $P_{\mathrm{T}}^{\mathrm{recoil}}$ where the triggers should be $\approx 100\%$ efficient. However, as can be seen in Figure 5.1 all the way up to $P_{\mathrm{T}}^{\mathrm{recoil}} \approx 350$ GeV the efficiency is below 100%. This curve was hence reproduced using the cuts used in the monojet analysis (Figure 5.2) and it was found that there were 136 events (0.07% of total) with $P_{\mathrm{T}}^{\mathrm{recoil}} > 250$ GeV that did not trigger L1_XE50

(Figure 5.3), causing the efficiency to be below 100% all the way up to the very high value of $P_{\mathrm{T}}^{\mathrm{recoil}} \approx 800$ GeV.

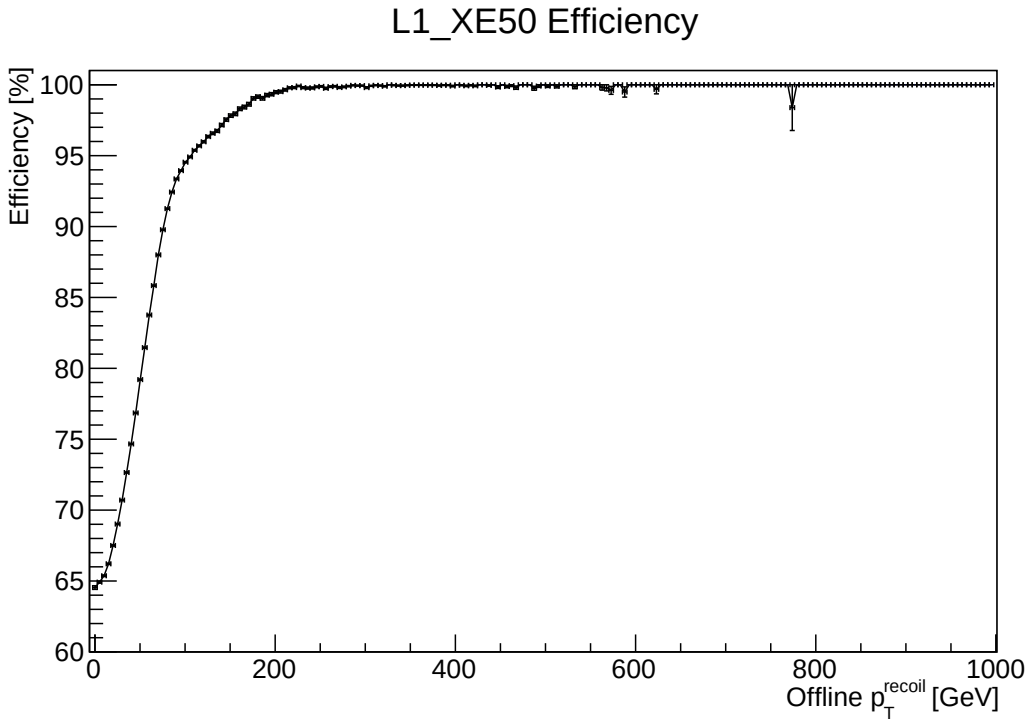

Figure 5.2: L1_XE50 turn-on curve with monojet cuts. By $P_{\mathrm{T}}^{\mathrm{recoil}} = 250$ GeV, L1_XE50 is $\approx 100\%$ efficient, however there are still a small number of events missed by L1_XE50. Up to ≈ 300 GeV these missed events are possibly just an inefficiency in L1_XE50 at low $P_{\mathrm{T}}^{\mathrm{recoil}}$. However, it can be seen there are still a small number of events missed beyond 600 GeV, even as high as 775 GeV, where L1_XE50 should be completely efficient.

There are four known properties of the L1_XE50 trigger in Run 2 that could cause high offline $P_{\mathrm{T}}^{\mathrm{recoil}}$ events to be missed:

- Jet calibration
- Jet definition
- Pile-up corrections
- Jet overflow

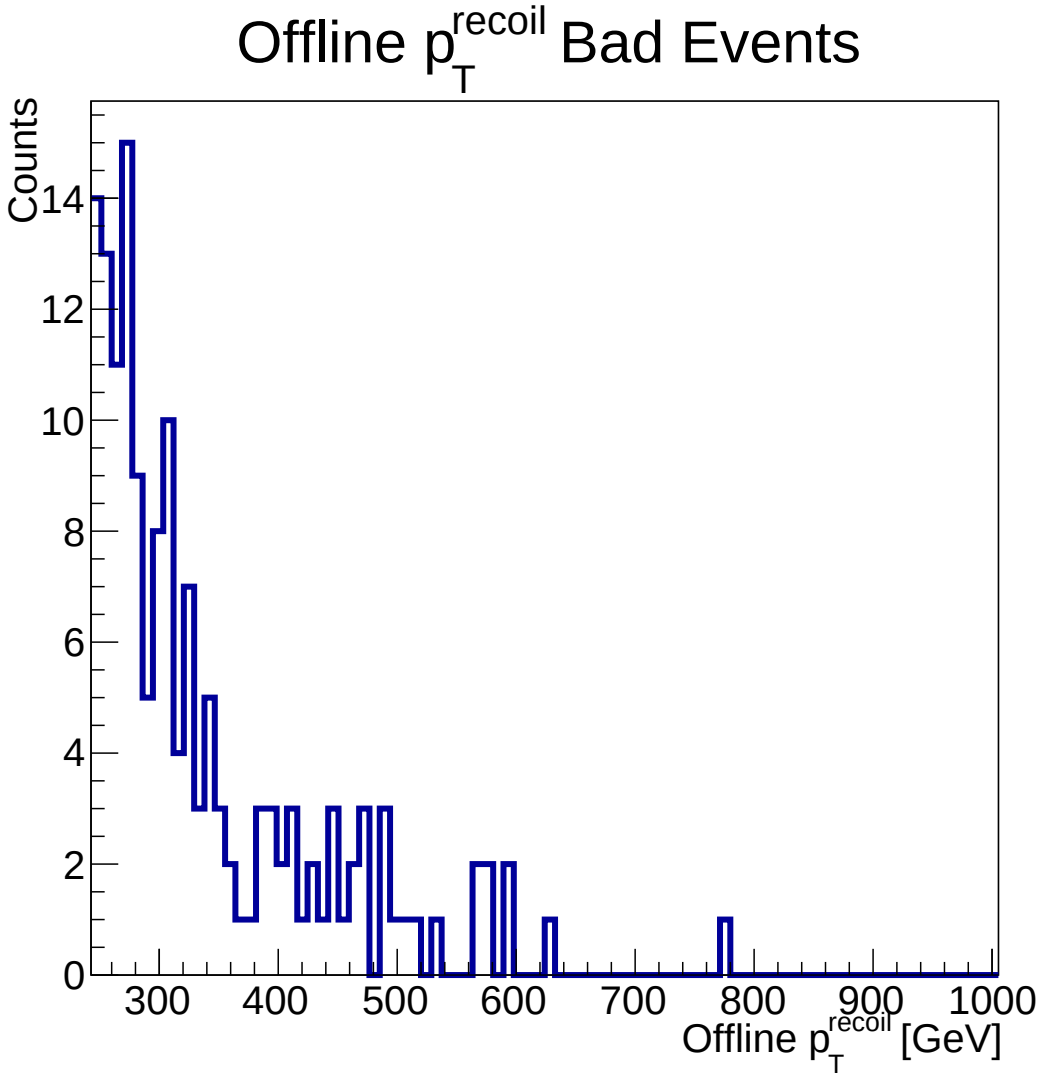

Figure 5.3: $P_{\mathrm{T}}^{\mathrm{recoil}} > 250$ GeV events with monojet cuts that do not trigger L1_XE50.

5.1.1 Jet calibration

L1 calorimeter triggers have a slightly different momentum calibration for jets than used offline. Hence some events with multiple jets where offline the jets do not balance, do balance at L1 due to the different calibrations.

5.1.2 Jet definition

L1 calorimeter triggers use a slightly different definition of a jet than the offline algorithm does. A high p_T muon can emit a photon via Bremsstrahlung causing a particle shower. Offline, this shower is treated as belonging to the muon and not as a jet. However, at L1 this particle shower appears like any other jet and is treated in the same way.

5.1.3 Pile-up corrections

As the rate of proton-proton interactions in ATLAS is high there are often multiple interactions that happen effectively simulatenously within a single bunch crossing, known as pile-up. Offline energy reconstruction around $|\eta| = 3.0$ has a problem with the pile-up correction, resulting in an excess of pile-up jets, as shown in Figure 5.4 [68].

5.1.4 Jet overflow

New hardware was introduced to the calorimeter in Run 2. It was found that the firmware for this new hardware has a problem with overflowing jets. The L1 calorimeter trigger can only measure a jet up to a total energy of 1023 GeV. In addition, the L1 calorimeter is split up into many different towers that each measure a fraction of the jet's total energy, each of which saturates at 255 GeV.

This results in the energy of all jets above 1023 GeV being indistinguishable to L1 calorimeter triggers, and also some jets of a slightly lower energy that saturate a single trigger tower. This can result in measuring a low L1 $P_{\mathrm{T}}^{\mathrm{recoil}}$ for events with a large offline $P_{\mathrm{T}}^{\mathrm{recoil}}$, as illustrated in Figure 5.5, showing two jets that saturate towers back to back. This results in the measured energy of each jet in the direction the jet is travelling being set to 1023 GeV for both jets. This means that the measured

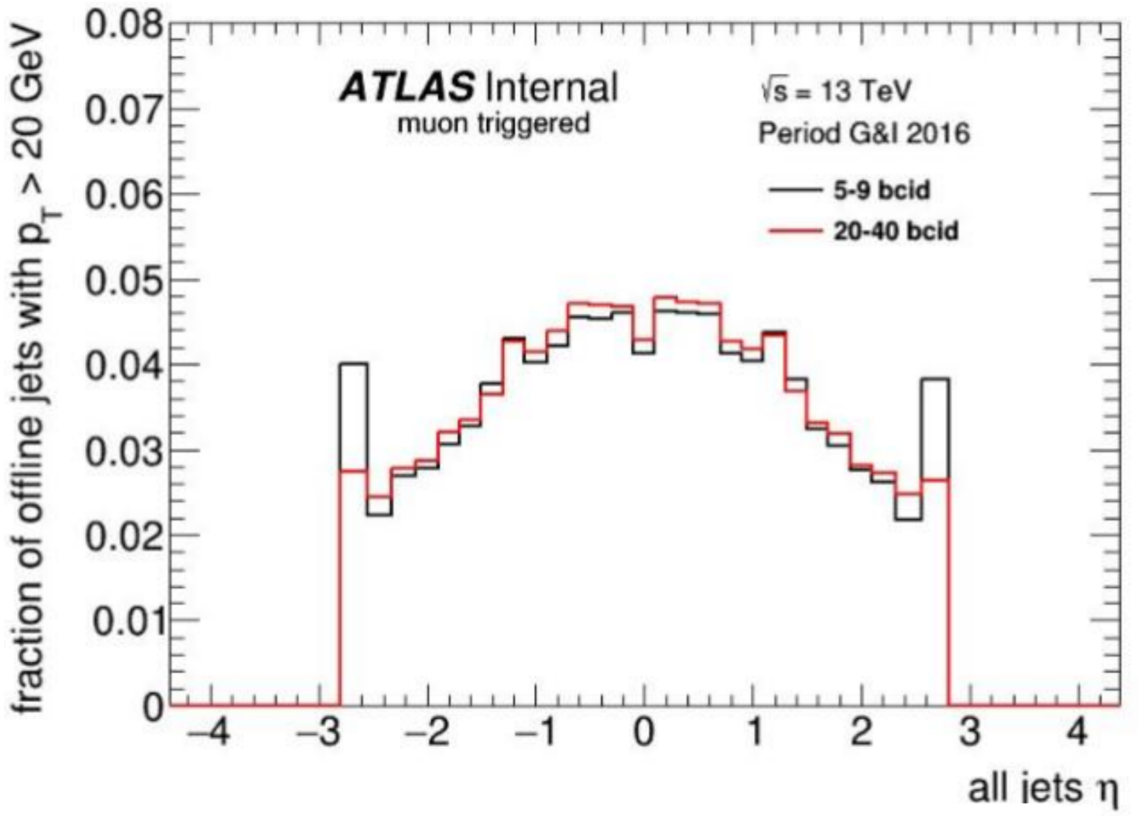

Figure 5.4: Excess of pile-up jets at high $|\eta|$. [68]

online $P_{\mathrm{T}}^{\mathrm{recoil}}$ will be 0 in the direction the jets are travelling, with all $P_{\mathrm{T}}^{\mathrm{recoil}}$ coming from the small contributions of the jets that are not approximately parallel with the dominant portion of the jet, causing a low overall online $P_{\mathrm{T}}^{\mathrm{recoil}}$.

However, in the extreme case, one of the jets could just be a single tightly confined 255 GeV jet that saturates a single trigger tower, and the other jet could be a very high energy $>$ 1023 GeV jet. This would mean that their true $P_{\mathrm{T}}^{\mathrm{recoil}}$ would be very large, however due to both jets overflowing they could not be distinguished from two jets that balance. This specific extreme case is a rarity; however it is not uncommon to encounter less extreme cases, for instance a jet of 800 GeV that saturates a single trigger tower.

There is a clear way to deal with these events, if we have L1 send a signal (the Overflow_T flag) to indicate that the jets overflowed and hence L1 cannot accurately measure the event's $P_{\mathrm{T}}^{\mathrm{recoil}}$. This allows the event to pass the L1 trigger and then be

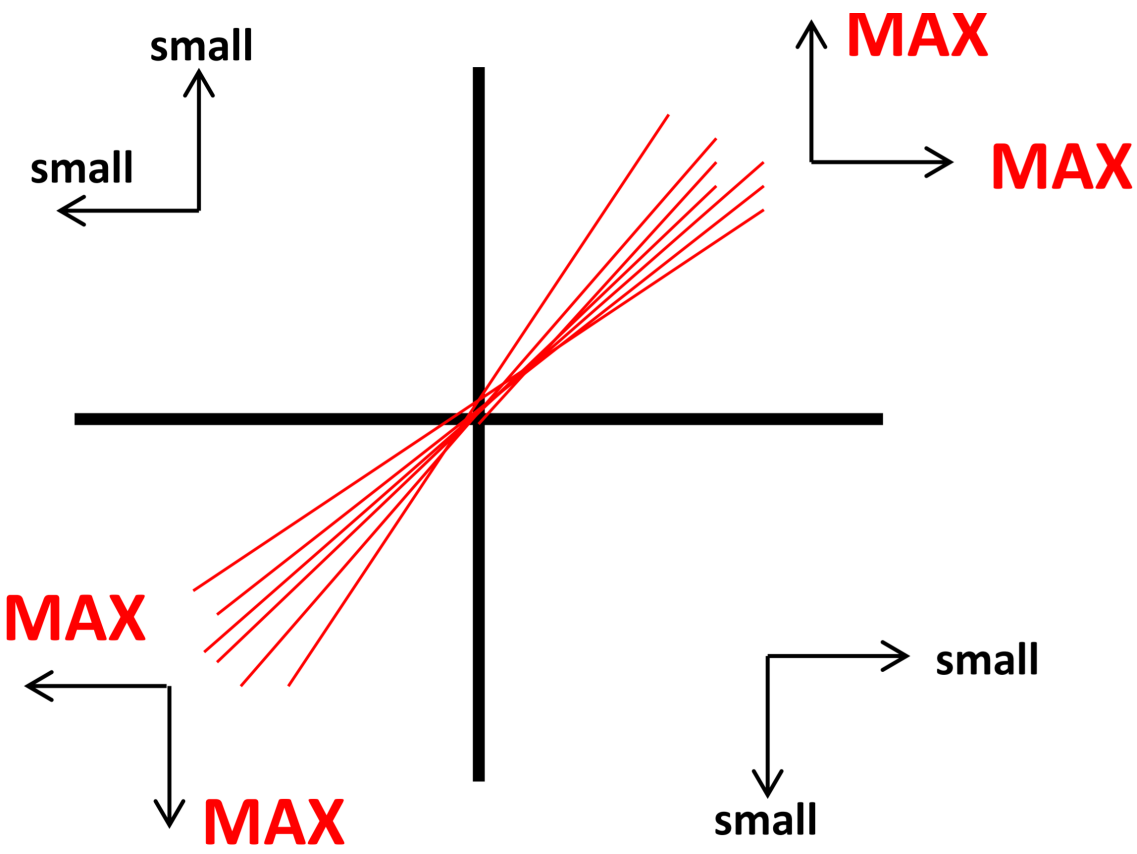

Figure 5.5: Overflowing Jets. Two back to back jets that each saturate either a single trigger tower with more than 255 GeV, or saturate the total energy measured per jet with more than 1023 GeV. Both jets' momentum in the direction of the jet will then be indistinguishable to L1 and hence the measured $P_{\mathrm{T}}^{\mathrm{recoil}} = 0$ GeV in the direction of either jet, even if one jet is much more energetic than the other and hence should have a large $P_{\mathrm{T}}^{\mathrm{recoil}}$. The $P_{\mathrm{T}}^{\mathrm{recoil}}$ measured by L1 will then just be a small $P_{\mathrm{T}}^{\mathrm{recoil}}$ resulting from off-axis portions of the jet or other particles.

dealt with by the HLT trigger which can accurately measure these jets that saturate L1. This is how L1 is supposed to work, however the firmware problem with the new hardware resulted in the overflow flag not being checked by HLT (however the flag is still saved).

To determine whether this overflow problem was a dominant cause of high $P_{\mathrm{T}}^{\mathrm{recoil}}$ events being lost in the monojet analysis, it was realised that this problem should cause a distinctive shape in the distribution of efficiency in L1 $P_{\mathrm{T}}^{\mathrm{recoil}}$ for collisions that pass L1_J400 but fail L1_XE50, where L1_J400 is a L1 trigger designed to trigger on events with jets that have more than 400 GeV P_{T}.

If the overflow flag being ignored is a dominant cause of events not triggering L1_XE50, we expect in L1_J400 NOT L1_XE50 (lost events):

- A peak in lost events at low online $P_{\mathrm{T}}^{\mathrm{recoil}}$ for overflowing jets, where we essentially lose all online $P_{\mathrm{T}}^{\mathrm{recoil}}$ due to trigger saturation, but which should still trigger L1_J400 as jets energetic enough to overflow should be energetic enough to trigger L1_J400 (So L1_J400 triggers but L1_XE50 does not).
- A decrease in lost events is expected as $P_{\mathrm{T}}^{\mathrm{recoil}}$ increases due to less overflow events reaching higher online $P_{\mathrm{T}}^{\mathrm{recoil}}$ from the small component of the jets not approximately parallel to the overflow direction.
- An increase in lost events is expected as $P_{\mathrm{T}}^{\mathrm{recoil}}$ increases further due to more events with L1_J400 triggering at higher online $P_{\mathrm{T}}^{\mathrm{recoil}}$, as larger P_{T} jets in an event tend to result in larger $P_{\mathrm{T}}^{\mathrm{recoil}}$.

If however the overflow flag being lost is a minor component of lost events, the first two points will not be true as these are only caused by the overflow flag being lost, and hence there should just be a monotonic increase. Figure 5.6 shows the measured efficiency distribution in online $P_{\mathrm{T}}^{\mathrm{recoil}}$ for events that pass L1_J400 NOT L1_XE50. The efficiency in this is strongly related to the proportion of lost events in L1_XE50. As can be seen, it follows the predicted distribution for the overflow flag not being used being a dominant cause of these events not triggering L1_XE50.

It was therefore decided to attempt to extract the $P_{\mathrm{T}}^{\mathrm{recoil}}$ Overflow_T flag and trigger on L1_XE50 OR Overflow_T flag. Figure 5.2 & Figure 5.3 were reproduced with this new trigger, shown in Figure 5.7 and Figure 5.8.

As can be seen, the turn-on curve is cleaned up at high $P_{\mathrm{T}}^{\mathrm{recoil}}$. Four events still remain with offline $P_{\mathrm{T}}^{\mathrm{recoil}} > 250$ GeV that do not trigger, however these all have $P_{\mathrm{T}}^{\mathrm{recoil}} < 280$ GeV and appear to be a genuine inefficiency of the L1_XE50 trigger at low $P_{\mathrm{T}}^{\mathrm{recoil}}$. Therefore, of the 136 $P_{\mathrm{T}}^{\mathrm{recoil}} > 250$ GeV events that are lost, 132 can be retained via redefining L1_XE50→ L1_XE50 OR Overflow_T flag.

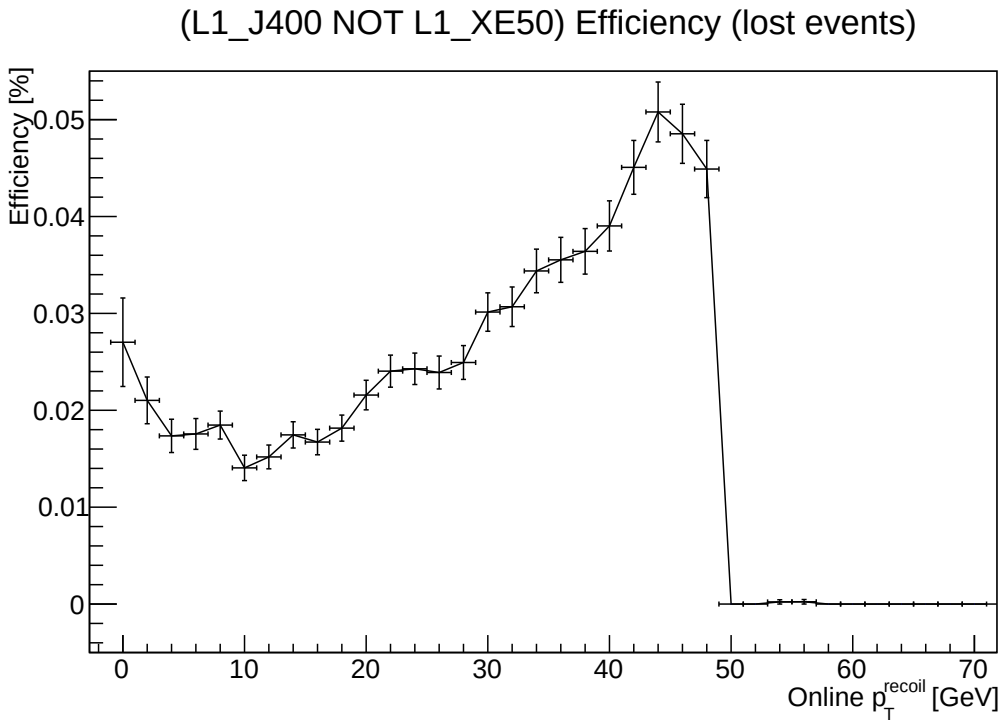

Figure 5.6: Online $P_{\mathrm{T}}^{\mathrm{recoil}}$ efficiency of (L1_J400 NOT L1_XE50) distribution indicates Overflow flag problem being dominant.

Another method to retain these lost events was found; instead of combining with the Overflow_T flag, combining with the L1_J400 trigger, as an overflowing jet is very likely to be a high energy jet that will trigger L1_J400. It was found this was marginally more effective. Of the 4 events that were still lost when including the overflow flag, the 2 most energetic were recovered by using the trigger L1_XE50 OR L1_J400 instead.

However, since not all collisions that set the Overflow_T flag or pass L1_J400 are recorded (a HLT trigger must be passed as well), there is a small irretrievable loss of statistics compared to if the trigger was working correctly, hence the trigger has been fixed for future runs.

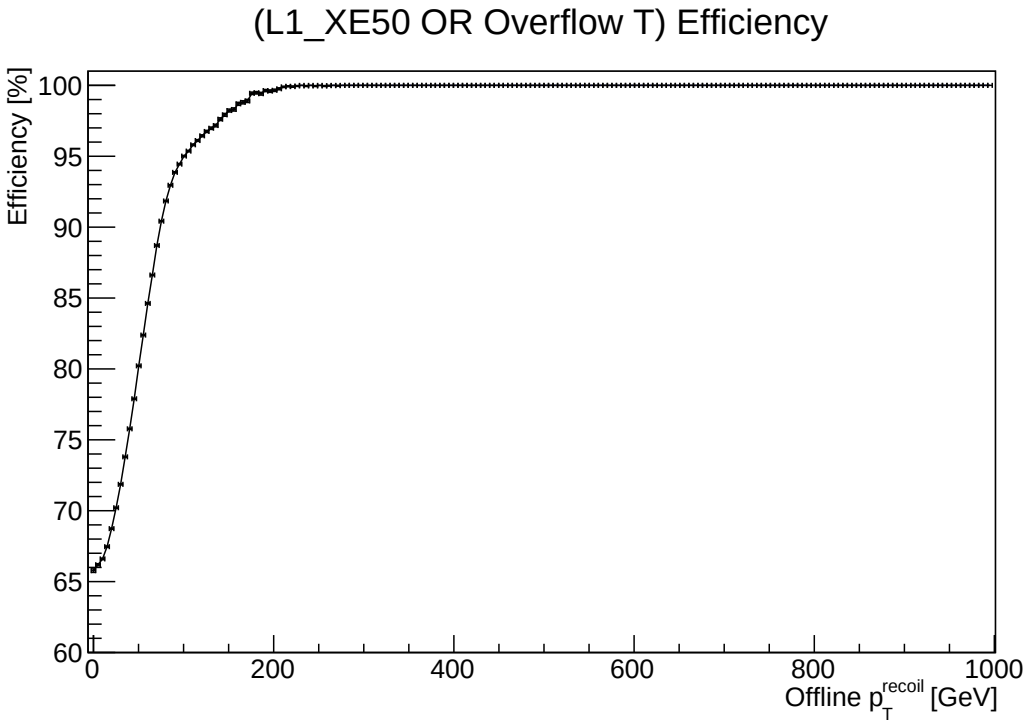

Figure 5.7: (L1_XE50 OR Overflow_T flag) turn-on curve with monojet cuts. High $P_{\mathrm{T}}^{\mathrm{recoil}}$ events that fail to pass L1_XE50 trigger the Overflow_T flag, causing the efficiency to reach 100%.

5.1.5 Prescale precision

An unexpected property was noticed from Figure 5.6. It can be seen that there is a sharp cut-off at L1 $P_{\mathrm{T}}^{\mathrm{recoil}} = 50$ GeV as expected, since events with L1 $P_{\mathrm{T}}^{\mathrm{recoil}} > 50$ GeV pass L1_XE50 by definition. However it can be seen in Figure 5.9 that the efficiency in this region is not 0, indicating events exist with L1 $P_{\mathrm{T}}^{\mathrm{recoil}} > 50$ GeV that do not pass L1_XE50, which by definition should not be possible. To investigate further the same plot was made for higher L1 $P_{\mathrm{T}}^{\mathrm{recoil}}$, as shown in Figure 5.10.

Across all of the ($\gtrsim 500 \cdot 10^6$) events that pass basic monojet cleaning cuts in the good run list (runs without known significant problems) of the monojet data sample, it was found only 15 had this issue, corresponding to a proportion of $3\text{x}10^{-8}$. These events were distributed uniformly across multiple different runs, with no obvious features in common.

Due to the large volume of data recorded by ATLAS, certain triggers in ATLAS are

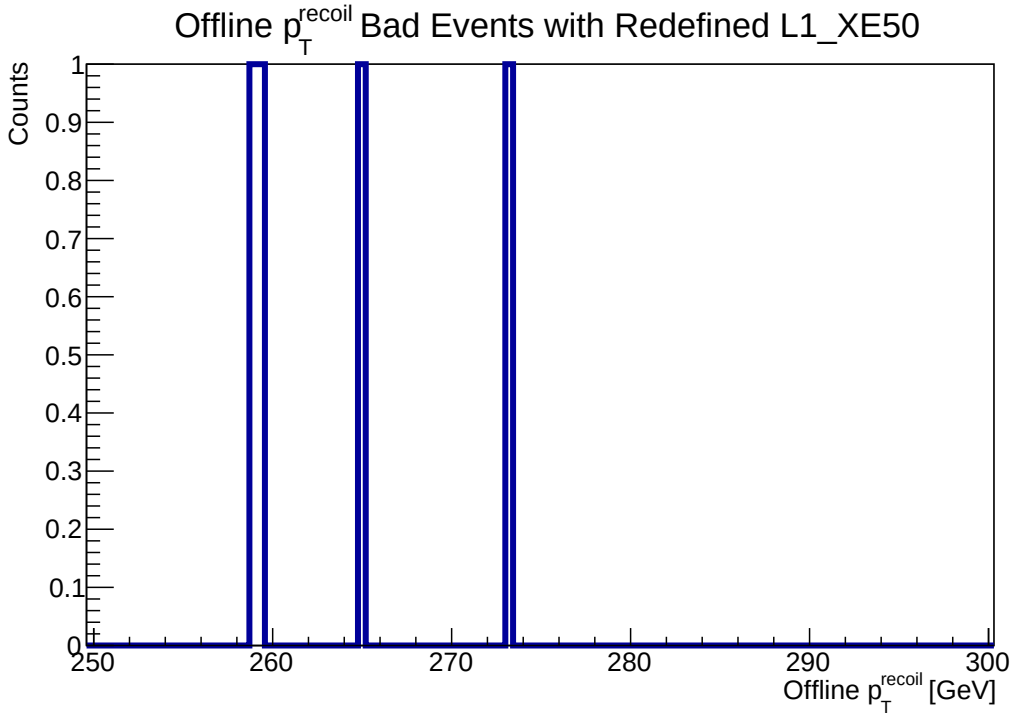

Figure 5.8: $P_{\mathrm{T}}^{\mathrm{recoil}} > 250$ GeV events with monojet cuts that do not trigger L1_XE50 OR Overflow_T flag. A much smaller number of events are missed than just triggering L1_XE50, and the events that are missed are all below $P_{\mathrm{T}}^{\mathrm{recoil}} = 300$GeV, indicating this is just a genuine inefficiency in L1_XE50.

prescaled. This means only a certain proportion of events that have the properties to pass the trigger are actually passed by the trigger. However, one of the reasons L1_XE50 was chosen is because it is not prescaled.

However, after checking these events, L1 reports them all as passing L1_XE50 before prescaling, and then failing L1_XE50 after prescale, indicating that they are prescaled. Not only should L1_XE50 not be prescaled, but no triggers are prescaled by such a small amount.

It was found that this issue does not arise from L1_XE50 in particular, or even just calorimeter triggers, but all triggers. The Central Trigger Processor (CTP) stores integers as string representations of floating point numbers with 24-bit precision and does not ensure unity is preserved. This resulted in a floating point rounding error, resulting in 1 (unprescaled) being represented by $1 - \left(\frac{1}{2}\right)^{24} = 0.999{,}999{,}94$, consistent with the measured value of 1-3x10^{-8} = 0.999,999,97. The CTP has now

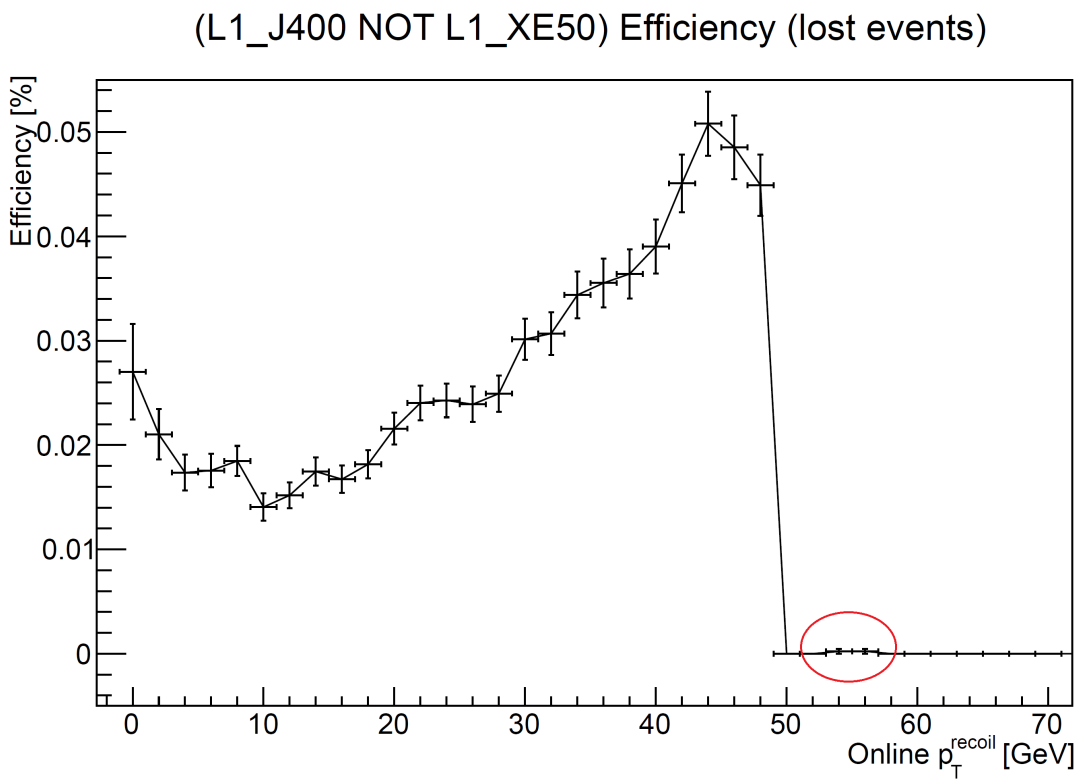

Figure 5.9: L1 $P_{\mathrm{T}}^{\mathrm{recoil}}$ efficiency distribution, showing it is not 0 past $P_{\mathrm{T}}^{\mathrm{recoil}} = 50$ GeV, which should not be possible by definition, as L1_XE50 is defined such that it triggers on every event with online $P_{\mathrm{T}}^{\mathrm{recoil}} > 50$ GeV.

been updated to treat unprescaled triggers correctly. However, lost data from before is irretrievable and hence to more accurately report results, all 'unprescaled' triggers before 2017 should be treated as prescaled by $1 - \left(\frac{1}{2}\right)^{24}$.

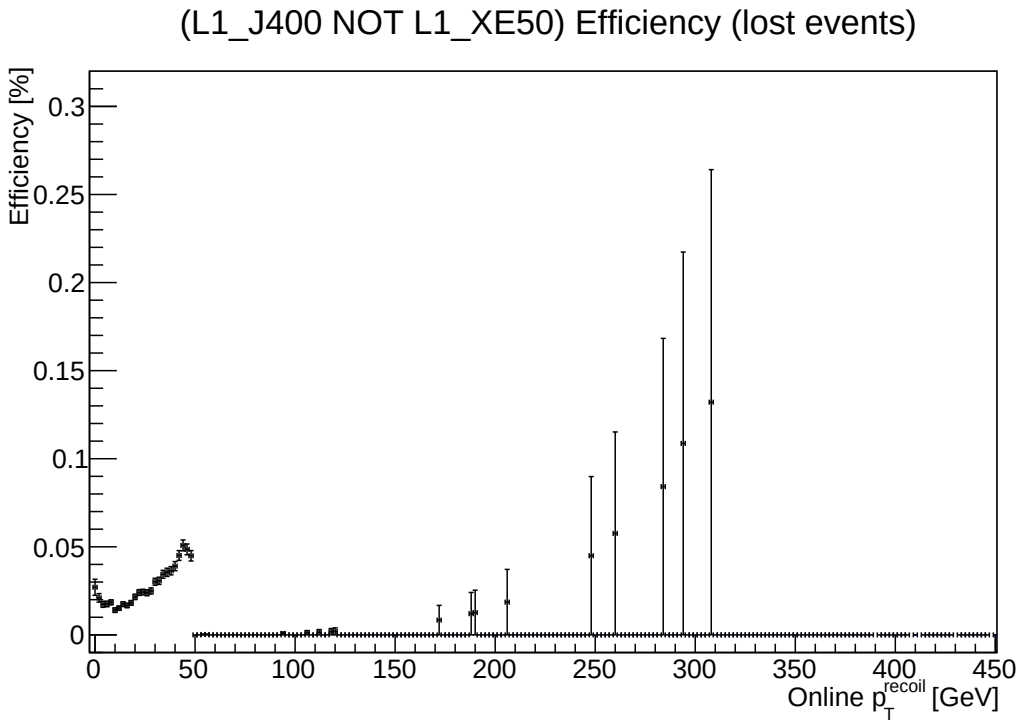

Figure 5.10: L1 $P_{\mathrm{T}}^{\mathrm{recoil}}$ efficiency distribution, same as Figure 5.9 but with a higher limit on L1 $P_{\mathrm{T}}^{\mathrm{recoil}}$, showing that the missed events continue to large values of L1 $P_{\mathrm{T}}^{\mathrm{recoil}}$.

5.2 HLT $P_{\mathrm{T}}^{\mathrm{recoil}}$ trigger scale factors for lowering $P_{\mathrm{T}}^{\mathrm{recoil}}$ threshold

In the previous analysis version the $P_{\mathrm{T}}^{\mathrm{recoil}}$ threshold for all control regions and the signal region of the monojet analysis was > 250 GeV, where all HLT triggers are 100% efficient. However, lowering the $P_{\mathrm{T}}^{\mathrm{recoil}}$ threshold to 200 GeV requires evaluating $P_{\mathrm{T}}^{\mathrm{recoil}}$ trigger scale factors potentially for a systematic uncertainty, as for the higher HLT $P_{\mathrm{T}}^{\mathrm{recoil}}$ triggers, which are used in higher luminosity runs, 200 GeV is very close to the start of the plateau of the turn-on curve.

The trigger efficiencies are determined using the full 13 TeV ATLAS Run 2 dataset, which has varying pileup conditions, and MC samples that match these. Due to the varying pileup conditions, to prevent trigger saturation while ensuring sufficient statistics are stored, the lowest unprescaled $P_{\mathrm{T}}^{\mathrm{recoil}}$ trigger varies throughout Run 2,

increasing the $P_{\mathrm{T}}^{\mathrm{recoil}}$ required to trigger the lowest unprescaled $P_{\mathrm{T}}^{\mathrm{recoil}}$ trigger as the pileup increases.

To determine the efficiency of the $P_{\mathrm{T}}^{\mathrm{recoil}}$ triggers, events are selected using a muon trigger with an almost identical signal selection to the SR, however requiring one or more muons to be reconstructed to ensure orthogonality to the SR.

The $P_{\mathrm{T}}^{\mathrm{recoil}}$ trigger efficiency is defined as

$$\frac{\#\text{Events passed selection AND triggered}}{\#\text{Events passed selection}} \tag{5.1}$$

The muon trigger used to select events was `mu26_ivarmedium`, except for data measured in 2015 which was selected with `mu26_imedium`, as the `mu26_ivarmedium` trigger was not in the 2015 trigger menu.

The following unprescaled $P_{\mathrm{T}}^{\mathrm{recoil}}$ triggers were used, which were found to be fully efficient in data at:

- 2015, `HLT_xe70_mht` fully efficient at 150GeV
- 2016, period A to D3: `HLT_xe90_mht_L1XE50` fully efficient at 160GeV
- 2016, period A to D3: `HLT_xe100_mht_L1XE50` fully efficient at 170GeV (*)
- 2016, period D4 to end: `HLT_xe110_mht_L1XE50` fully efficient at 170GeV
- 2017, period A to D5: `HLT_xe110_pufit_L1XE55` fully efficient at 180GeV
- 2017, period D6 to end: `HLT_xe110_pufit_L1XE50` fully efficient at 180GeV
- 2018, period A1 to J: `HLT_xe110_pufit_xe70_L1XE50` fully efficient at 180GeV
- 2018, period K to end: `HLT_xe110_pufit_xe65_L1XE50` fully efficient at 180GeV

(*) `HLT_xe100_mht_L1XE50` ran unprescaled during D4-end other than at the start of some high-luminosity runs. Efficiency was measured in period A to D3 where it

is unprescaled in all runs.

The efficiencies for the various $P_{\mathrm{T}}^{\mathrm{recoil}}$ triggers in 2015 and 2016 are shown in Figure 5.11 and for 2017 and 2018 in Figure 5.12. The scale factors are defined as the ratio of the trigger efficiencies in data and MC. These ratios are then fitted with an error function in the range $100 < P_{\mathrm{T}}^{\mathrm{recoil}} < 220$ GeV:

$$f\left(P_{\mathrm{T}}^{\mathrm{recoil}}\right) = \frac{1}{2}\left(1 + Erf\left(\frac{P_{\mathrm{T}}^{\mathrm{recoil}} - p_0}{\sqrt{2}p_1}\right)\right). \tag{5.2}$$

Since the values for the $P_{\mathrm{T}}^{\mathrm{recoil}}$ -bins used in the analysis are compatible with 1, no scale factors are applied and no additional systematic uncertainty is included in the fit.

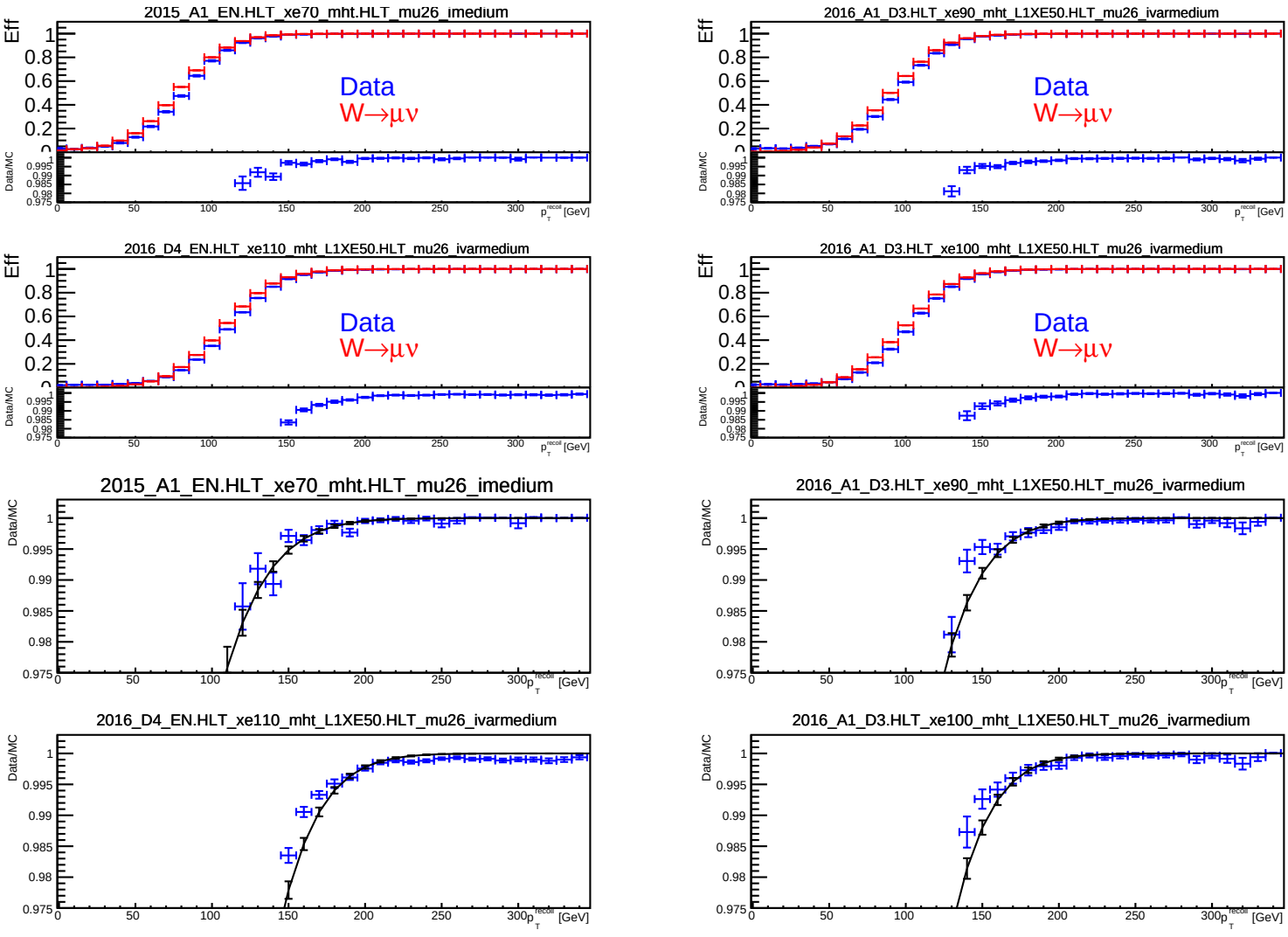

Figure 5.11: Unprescaled $P_{\mathrm{T}}^{\mathrm{recoil}}$ scale factors and HLT trigger efficiencies for data and $W(\mu\nu)+$jets MC in 2015 and 2016.

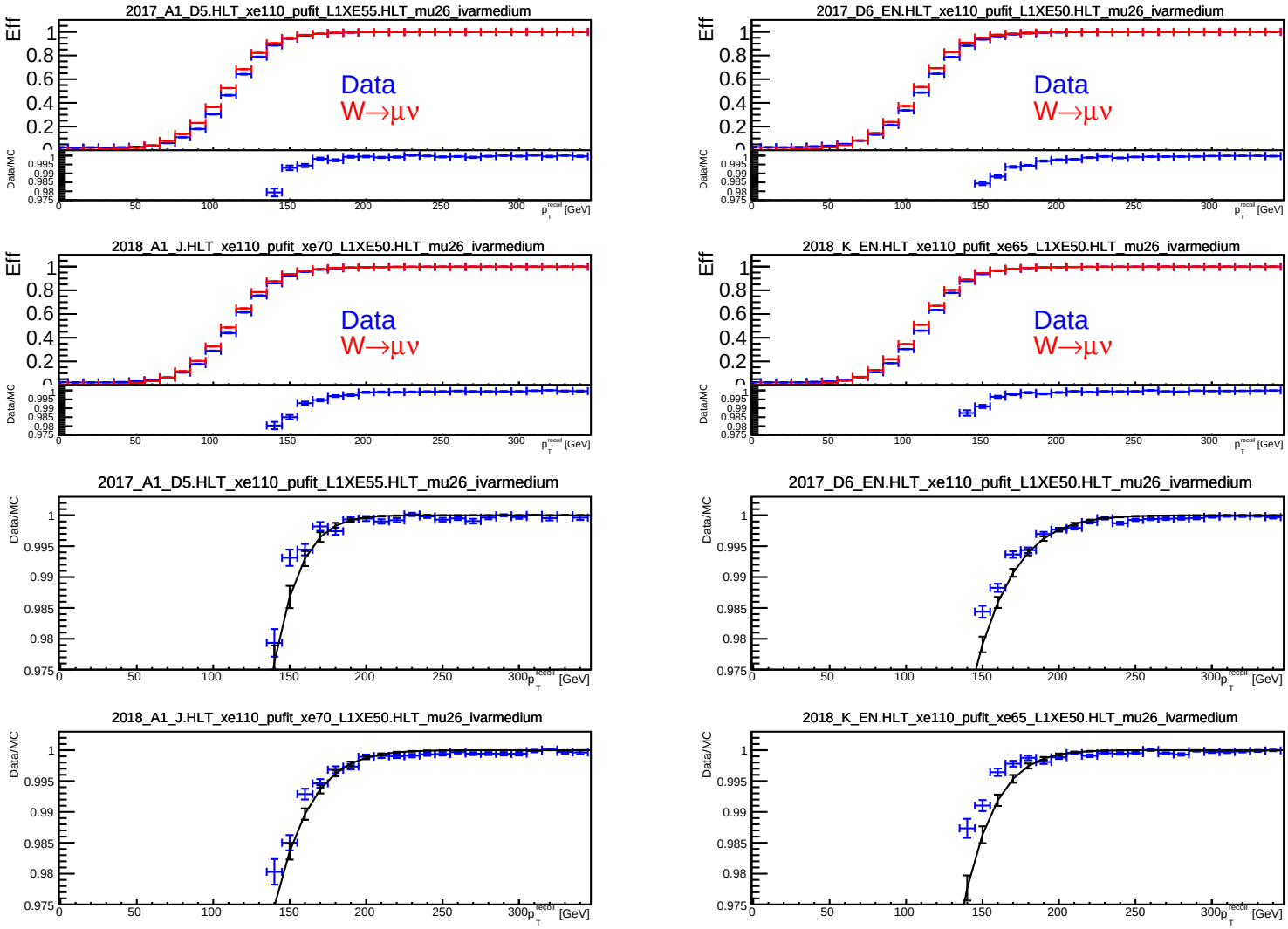

Figure 5.12: Unprescaled $P_{\mathrm{T}}^{\mathrm{recoil}}$ scale factors and HLT trigger efficiencies for data and $W(\mu\nu)+\mathrm{jets}$ MC in 2017 and 2018.

CHAPTER 6

Monojet Analysis Results

Along with the details of the analysis and the data taking described in the previous chapters, systematic uncertainties are required to be calculated to quantify agreement or disagreement with the Standard Model, which is described in this chapter. Following this, the results for a selection of models and model-independent results are shown.

6.1 Systematic uncertainties

To distinguish beyond Standard Model physics from Standard Model physics, it is important to predict accurately and precisely both what we expect the Standard Model background distribution to be, and what we expect our beyond Standard Model signal distributions to be. To do this, it is important to understand the systematic uncertainties both for our Standard Model backgrounds and the beyond Standard Model signals.

6.1.1 Systematic smoothing

The monojet analysis is affected strongly by the shape of the disribution of systematic uncertainties as a function of $P_{\mathrm{T}}^{\mathrm{recoil}}$. Because of this, fluctuations due to limited MC statistics, which are non-physical, can have large effects on the overall results. To prevent this the systematic uncertainty distributions are smoothed algorithmically. Two procedures for this are used, both based upon rebinning. For the systematic uncertainties "JET_Flavor_Composition" and "JET_Flavor_Response" the parabolic rebinning procedure is used, whereas for all other systematic uncertainties the monotonic rebinning procedure is used.

The monotonic rebinning procedure rebins the systematic uncertainty as a function of $P_{\mathrm{T}}^{\mathrm{recoil}}$ until a binning is found where the distribution has no local extrema. Then, starting from the upper edge in $P_{\mathrm{T}}^{\mathrm{recoil}}$, the bins are merged until the statistical uncertainty in every bin is lower than 5%. The parabolic procedure is similar, but allows local extrema as they are expected for these systematic uncertainties.

Examples of systematic uncertainty variations which show the performance of the algorithm are shown in Figure 6.1 for three experimental systematic processes, showing both the UP and DOWN systematic variation. A comparison of the smoothed and non-smoothed experimental systematic uncertainty variations used as input to the fitting machinery has also been studied [69].

6.1.2 Systematic pruning

To ensure fit stability, systematic uncertainties with very small effects are pruned. This pruning is performed in three steps; if a systematic uncertainty passes all three steps it is not pruned, otherwise it is.

- Integrated $P_{\mathrm{T}}^{\mathrm{recoil}}$ distribution of a specific background in a specific region must be greater than 0.2% of the total background in the region.
- Systematic uncertainty variation of a specific background in a specific region must be at least 0.2% (up or down) in one bin.
- Systematic uncertainty variation times the yield of a specific background in a specific region must be at least 0.2% of the total background in at least one bin (up or down).

6.1.3 Experimental systematics

The following nuisance parameters, listed in Table 6.1, are used to model in the $P_{\mathrm{T}}^{\mathrm{recoil}}$ fit the impact of experimental systematic uncertainties on expected background and signal event yields in different $P_{\mathrm{T}}^{\mathrm{recoil}}$ bins; the different nuisance parameters are treated as binwise correlated systematic uncertainties over the regions used for the corresponding fits.

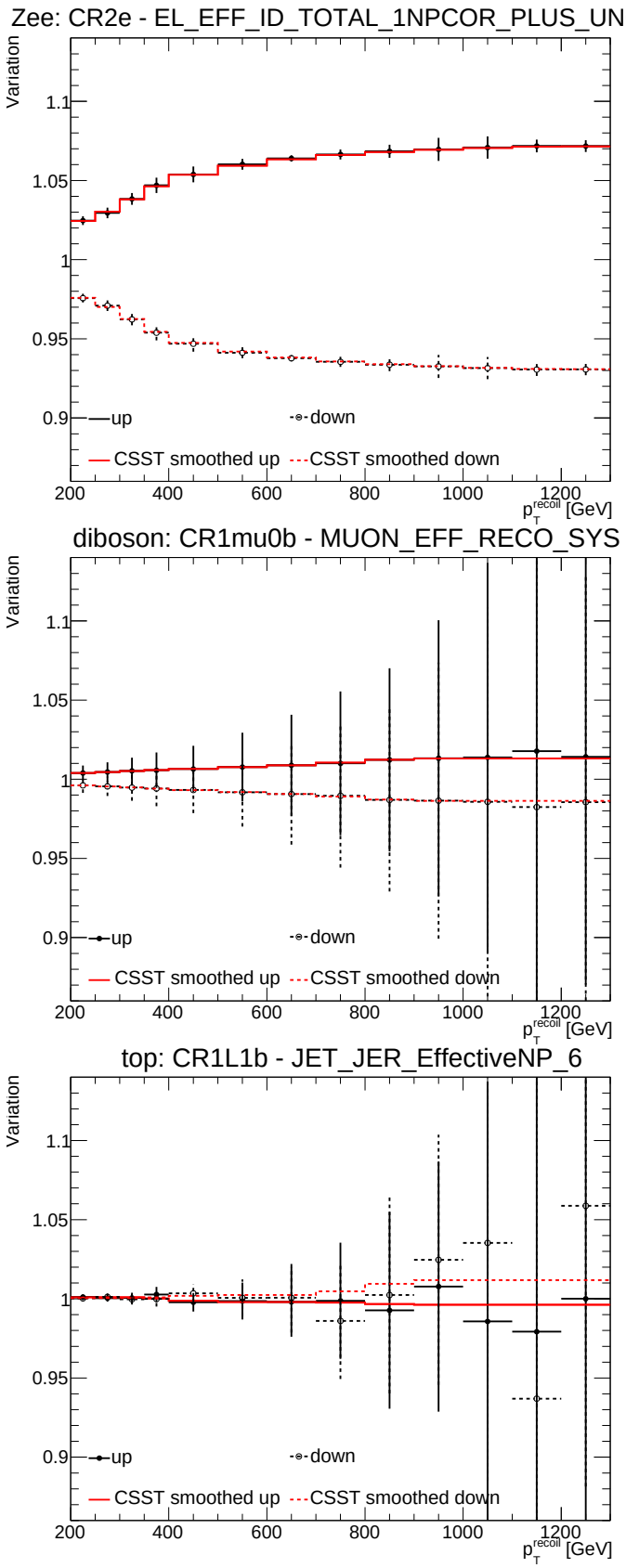

Figure 6.1: Example experimental systematic uncertainty variations of processes with limited MC statistics without (black) and with (red) smoothing applied. From top to bottom, the uncertainty on the: electron identification efficiency scale factors in `CR2e`, muon reconstruction efficiency in `CR1mu0b`, jet energy resolution in `CR1l1b`.

Systematic uncertainty	Short description
Luminosity	uncertainty on the total integrated luminosity (1.7% [70])
Electrons	
EL_EFF_Trigger_TOTAL_1NPCOR_PLUS_UNCOR EL_EFF_TriggerEff_TOTAL_1NPCOR_PLUS_UNCOR	trigger efficiency uncertainty
EL_EFF_Reco_TOTAL_1NPCOR_PLUS_UNCOR	reconstruction efficiency uncertainty
EL_EFF_ID_TOTAL_1NPCOR_PLUS_UNCOR	ID efficiency uncertainty
EL_EFF_Iso_TOTAL_1NPCOR_PLUS_UNCOR	isolation efficiency uncertainty
EG_SCALE_ALL	energy scale uncertainty
EG_RESOLUTION_ALL	energy resolution uncertainty
Photons	
PH_EFF_ID_Uncertainty	ID efficiency uncertainty
PH_EFF_ISO_Uncertainty	isolation efficiency uncertainty
Muons	
MUON_EFF_RECO_STAT MUON_EFF_RECO_SYS	reconstruction uncertainty for $p_{\mathrm{T}} > 15$ GeV
MUON_EFF_RECO_STAT_LOWPT MUON_EFF_RECO_SYS _LOWPT	reconstruction and ID efficiency uncertainty for $p_{\mathrm{T}} < 15$ GeV
MUON_ISO_STAT MUON_ISO_SYS	isolation efficiency uncertainty
MUON_TTVA_STAT MUON_TTVA_SYS	track-to-vertex association efficiency uncertainty
MUONS_SCALE	energy scale uncertainty
MUONS_SAGITTA_RHO	variations in the momentum scale (charge dependent)
MUONS_SAGITTA_RESBIAS	variations in the momentum scale (charge dependent) – symmetrised
MUONS_ID	energy resolution uncertainty from inner detector
MUONS_MS	energy resolution uncertainty from muon system
Taus	
TAUS_TRUEHADTAU_EFF_RECO_HIGHPT	reconstruction uncertainty for 3-prong taus with p_{T} 100 GeV
TAUS_TRUEHADTAU_EFF_RECO_TOTAL	reconstruction uncertainty for taus with p_{T} 20 GeV
TAUS_TRUEHADTAU_EFF_JETID_1PRONGSTATSYSTUNCORR2025	ID uncertainty for 1-prong taus with $p_{\mathrm{T}}\epsilon[20, 25]$ GeV
TAUS_TRUEHADTAU_EFF_JETID_1PRONGSTATSYSTUNCORR2530	ID uncertainty for 1-prong taus with $p_{\mathrm{T}}\epsilon[25, 30]$ GeV
TAUS_TRUEHADTAU_EFF_JETID_1PRONGSTATSYSTUNCORR3040	ID uncertainty for 1-prong taus with $p_{\mathrm{T}}\epsilon[30, 40]$ GeV
TAUS_TRUEHADTAU_EFF_JETID_1PRONGSTATSYSTUNCORRGE40	ID uncertainty for 1-prong taus with $p_{\mathrm{T}} > 40$ GeV
TAUS_TRUEHADTAU_EFF_JETID_3PRONGSTATSYSTUNCORR2030	ID uncertainty for 3-prong taus with $p_{\mathrm{T}}\epsilon[20, 30]$ GeV
TAUS_TRUEHADTAU_EFF_JETID_3PRONGSTATSYSTUNCORRGE30	ID uncertainty for 3-prong taus with p_{T} 30 GeV
TAUS_TRUEHADTAU_EFF_JETID_HIGHPT	ID uncertainty for taus with p_{T} 100 GeV
TAUS_TRUEHADTAU_EFF_JETID_SYST	ID uncertainty for taus
TAUS_TRUEHADTAU_SME_TES_DETECTOR	Tau Energy Scale coming from detector effects
TAUS_TRUEHADTAU_SME_TES_INSITU	Tau Energy Scale coming from in-situ corrections
TAUS_TRUEHADTAU_SME_TES_MODEL	Tau Energy Scale coming from the MC-modelling uncertainty

Systematic uncertainty	Short description
Small-R Jets	
The Category Reduction scheme is used to perform combinations in the future	
JET_GroupedNP	energy scale uncertainty split into 30 components
JET_JER	energy resolution uncertainty split into 13 components
JET_EtaIntercalibration	calibrate the scale of FRW jets wrt central jets, split into 5 components
JET_Flavor_Composition	Flavour-related uncertainties
JET_Flavor_Responce	Flavour-related uncertainties
JET_BJES	Flavour-related uncertainties
JET_Pileup	Pileup uncertainties (depend on pT, eta, NPV, and mu)
JET_PunchThrough_MC16	Punch-through uncertainty
JET_SingleParticle_HighPt	"Absolute in situ" propagation of single particle and test beam uncertainties
JvtEfficiency	JVT efficiency uncertainty
FT_EFF_EIGEN_B FT_EFF_EIGEN_C FT_EFF_EIGEN_Light	3 components for b-jets, 4 for c-jets and 5 for light jets
FT_EFF_EIGEN_extrapolation	b-tagging efficiency uncertainty on the extrapolation on high p_{T} -jets
FT_EFF_EIGEN_extrapolation_from_charm	b-tagging efficiency uncertainty on τ-jets
$P_{\mathrm{T}}^{\mathrm{recoil}}$ **-Trigger and** $P_{\mathrm{T}}^{\mathrm{recoil}}$ **-Terms**	
MET_SoftTrk_ResoPerp	track-based soft term related to transversal resolution uncertainty
MET_SoftTrk_ResoPara	track-based soft term related to longitudinal resolution uncertainty
MET_SoftTrk_Scale	track-based soft term related to longitudinal scale uncertainty
Pile-up	
PRW_DATASF	uncertainty on data scale factors used for computation pileup reweighting

Table 6.1: Qualitative summary of the experimental systematic uncertainties considered in this analysis. The impact of each systematic uncertainty varies across the $P_{\mathrm{T}}^{\mathrm{recoil}}$ distribution in the signal region, with the total systematic uncertainty being larger at high $P_{\mathrm{T}}^{\mathrm{recoil}}$. The dominant experimental systematic uncertainties in the low $P_{\mathrm{T}}^{\mathrm{recoil}}$ region are MUON_EFF_RECO_SYS, EL_EFF_ID_TOTAL_1NPCOR_PLUS_UNCOR, PRW_DATASF, MET_SoftTrk_Scale, EG_SCALE_ALL, at a percent uncertainty within the 200-250 GeV $P_{\mathrm{T}}^{\mathrm{recoil}}$ bin of $\pm$ (0.61,0.58), (0.59,0.56), (0.40,0.47), (0.42,0.52), (0.37,0.45) % respectively. The dominant experimental systematic uncertainties in the high $P_{\mathrm{T}}^{\mathrm{recoil}}$ region are EL_EFF_ID_TOTAL_1NPCOR_PLUS_UNCOR, MUON_EFF_RECO_SYS, EG_SCALE_ALL, MUON_SAGITTA_RESBIAS, FT_EFF_EIGEN_extrapolation, at a percent uncertainty within the 1100-1200 GeV $P_{\mathrm{T}}^{\mathrm{recoil}}$ bin of $\pm$ (2.04,1.85), (1.99,1.80), (0.53,0.54), (0.52,0.53), (0.51,0.49)% respectively.

6.1.4 Background systematic uncertainties

6.1.4.1 Matching uncertainties on W + jets, Z + jets backgrounds

As the monojet signal is dominated by jets, it is important that our simulation of jets is accurate, to correctly describe our background. However, there is no known theoretically sound method to simulate jets in all regimes. Fortunately, as discussed in Section 2.4, there are two methods that complement each other well: matrix-element generators of jets, which describe jets far from the soft-collinear limits well (the soft-collinear limit being jets resulting from low energy emissions at small angles), and parton shower generators, which describe jets close to the soft-collinear limits well. Hence, with a technique combining these two methods, jets can be reliably simulated in all regimes.

To combine these methods it is important to ensure there is no double counting. For instance, in a region that is fairly, but not very, close to the soft-collinear limit, both parton shower and matrix element generators may describe the event well, but the events generated by both methods cannot be taken together as this will overcount the number of events in this region.

It may be thought that the best way to combine these methods is fairly straightforward; just choose an area of phase space described by the parton shower method and reject all events in this area generated by the matrix element method, then describe the rest of phase space by the matrix element method and reject all events in this area generated by the parton shower method. However, while this is a valid algorithm, it introduces a large discontinuity in the transition between methods and causes a large dependence on the fairly arbitrary choice of where the transition boundary is, hence adding a large uncertainty.

There are therefore multiple different algorithms aimed at combining these methods. The algorithm used in this analysis is the Catani, Krauss, Kuhn, Webber (CKKW) matching scheme [71], which instead of accepting or rejecting events from each

method, reweights them depending on the area of phase space in which they are, dependent on the CKKW matrix-element-matching scale. This still has the problem that this scale is fairly arbitrary, however it prevents any large discontinuity and hence results in a smaller dependence on this value, and so a smaller uncertainty.

Uncertainties due to the choice of the CKKW matrix-element-matching scale were studied using the parameterisation of reference [72], which was derived using $V+jets$ samples generated with Sherpa 2.1 by varying the matching scale from its nominal value of 20 GeV, to 15 GeV and 30 GeV. Up and down variations of the $p_{\mathrm{T}}^{\mathrm{recoil}}$ distribution are obtained using event-by-event reweighting, based on the number of truth jets, as defined in Section 3 of reference [72] and depending on the vector boson p_{T} (PTV) slice of the generated samples. The uncertainty can then be applied to the event yields.

A mapping is shown in Table 6.2 between the samples used in this analysis and the samples used to calculate the CKKW reweighting in reference [72] which is used to perform the event-by-event reweighting. This is required as the samples used to calculate the CKKW reweighting are 'sliced' (split up into independent samples) in different ranges of vector boson p_{T} than the samples used in this analysis, which are also sliced in different (but similar) variables to vector boson p_{T} .

CKKW PTV Samples [GeV]	MAXHTPTV Samples [GeV]	PTV Samples [GeV]
0-70	0-70	none
70-140	70-140	70-100, 100-140
140-280	140-280	140-280
280-500	280-500	280-500
500-700	500-1000	500-1000
700-1000	none	none
1000-2000	1000-13,000	1000-13,000
2000-13,000	none	none

Table 6.2: Mapping from the CKKW parameterisation samples to the samples used. Systematic variated samples were generated filtered in PTV, shown in the left column. However, a different filtering scheme was used for background samples used, both in MAXHTPTV and PTV. A mapping is used to apply the systematics calculated from the systematic variated samples onto the background samples used. Other possible mappings were tested (such as averaging the 500-700 and 700-1000 systematic sample to be used in the 500-1000 background sample), however no significant differences for 'reasonable' mappings were found.

To avoid counting effects due to the fact that the CKKW reweighting procedure was obtained with an older version of Sherpa than that used in this analysis, the relative uncertainty on the yield in each bin of $p_{\mathrm{T}}^{\mathrm{recoil}}$ in the SR is computed by comparing the ratios of the yields of each process in the signal and control regions, obtained with the up and down variations described above. This relative uncertainty is evaluated for all W + jets and Z + jets background uncertainties in the SR and all the CRs.

The reweighting prescriptions are based on 2-dimensional weight maps as functions of the truth jet multiplicity and the vector boson p_{T} . After following this prescription, a large difference is observed between the $Z(\nu\nu)$ + jets and $Z(ee)$ + jets (and $W(e\nu)$ + jets) processes, while they are expected to be very similar due to their kinematics being almost identical. This difference is due to statistical fluctuations of weight values in the 0-truth-jet bin of the $Z(\nu\nu)$ + jets map. It is fixed by applying the weights coming from the 1-truth-jet bin to the few events with 0 truth jets that are selected in this analysis, which is approximately valid as neighbouring bins should be approximately equal.

The relative uncertainty as a function of $P_{\mathrm{T}}^{\mathrm{recoil}}$ is shown in Figure 6.2 for $Z(\nu\nu)$+jets in the SR, $Z(ee)$ + jets in CR2e and $W(e\nu)$ + jets in CR1e0b. The residual steps are an artifact due to the mapping of the different sliced samples, as shown in Table 6.2.

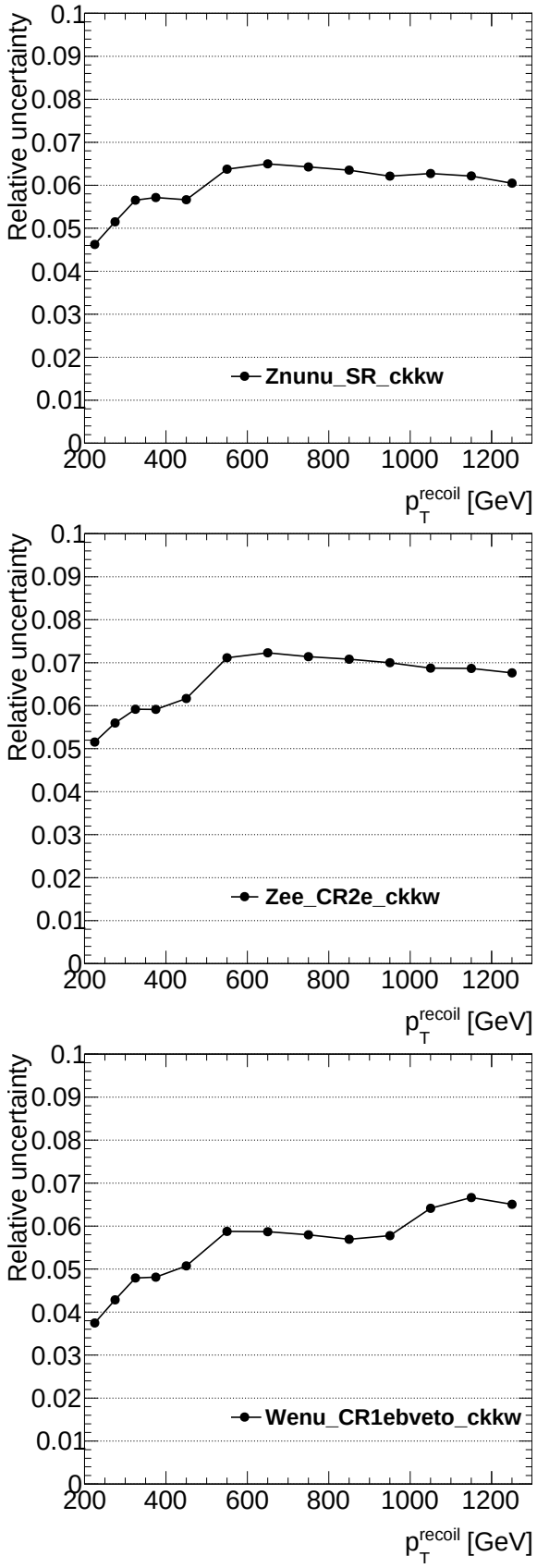

Figure 6.2: CKKW relative systematic uncertainty over the full $p_{\mathrm{T}}^{\mathrm{recoil}}$ range for $Z(\nu\nu)+\mathrm{jets}$ in the SR, $Z(ee)+\mathrm{jets}$ in `CR2e` and $W(e\nu)+\mathrm{jets}$ in `CR1e0b`.

In order to check the robustness of the systematic uncertainty estimation and of the residual differences between the processes (expected to be negligible in our phase space), the CKKW variations were also propagated by retrieving the nominal weight values from the 2-dimensional maps, plus or minus their statistical uncertainty and comparing these variations to the uncertainty calculated. It was found that this was not consistent with our estimate of the CKKW uncertainty.

This inconsistency, combined with the known use of outdated Sherpa samples, lack of MC statistics in some regions, unphysical steps in the distribution and noticing unphysical impacts of the CKKW merging cut (where variations around 20 GeV affect the high PTV region above 100 GeV), led to the decision that the current prescription for estimating CKKW systematic uncertainties, while sufficient in the previous monojet and other analyses, is not sufficient with the higher precision reached by the current monojet analysis. Hence the impact of the CKKW systematic uncertainty on the fit was investigated and it was found that it is possible not to include the CKKW systematic uncertainty with only a negligible impact on the fit. Hence, for the current monojet analysis it was decided not to include the CKKW systematic uncertainty, however work is ongoing to improve the CKKW estimation for the next iteration.

6.1.4.2 Top systematic uncertainties

Normalization and modelling uncertainties on the top-quark production processes ($t\bar{t}$, single-t) are considered.

The variations given by different matrix-element generators, parton shower generators and two other models of shower radiation with different factorization and renormalization scale are taken into account. The choice of renormalization and factorization scales affects the signal cross section. To prevent ultraviolet divergences, a momentum cutoff is applied in the calculation called the renormalization scale. However, as this cutoff is arbitrary, the physics should not depend upon it. Simi-

larly, to prevent infrared divergences, the factorization scale is applied, which is also arbitrary and hence physics should not depend upon it.

These uncertainties are evaluated by using dedicated $t\bar{t}$ MC samples in the lepton+jets channel, listed in Table 6.3, and dedicated single-t samples in the Wt-inclusive-channel, listed in Table 6.4.[1]. The initial- and final-state radiation scale uncertainties are evaluated for $t\bar{t}$ only and applied to both $t\bar{t}$ and single-t samples (the effect of the radiation scale on the single-t process is found to be consistent with $t\bar{t}$).

Each systematic uncertainty is assumed to be uncorrelated and, with the exception of the radiation uncertainties, they are symmetrised in the UP and DOWN variations. In order to avoid being significantly affected by statistical fluctuations, all the control regions and signal region are merged into one, since similar $p_{\mathrm{T}}^{\mathrm{recoil}}$ shapes are observed. The systematic variations are then fitted with a linear fit, as shown in Figure 6.3, and summed in quadrature to get 4 variations, $t\bar{t}$ UP, $t\bar{t}$ DOWN, single-t UP, single-t DOWN, as shown in Figure 6.4. Finally the $t\bar{t}$ and single-t uncertainties ($\sigma_{t\bar{t}}$,σ_t) are summed in quadrature, and weighted by the proportion of single top to total top background (f_t), which is shown in Figure 6.5, according to

$$\sigma_{top}^{i} = \sqrt{(f_t^i * \sigma_t^i)^2 + ((1 - f_t^i) * \sigma_{t\bar{t}}^i)^2},$$

where i is the bin index. The total top systematic uncertainty is shown in green in Figure 6.6.

Since the top cross section normalisation is estimated through the top normalisation factor, as discussed in Section 4.7.1, only the shape of the systematic uncertainties is included in the fit. The choice of using this approach or of using the total uncertainty band does not impact the final results. The shape and normalisation components of the systematic uncertainty are decoupled, so that their sum in quadrature reproduces

[1] $t\bar{t}$ represents the most important contribution to the top background in the signal region at low $p_{\mathrm{T}}^{\mathrm{recoil}}$ ($\sim$ 80%), however the upper $p_{\mathrm{T}}^{\mathrm{recoil}}$ bins have a larger fraction of single-t ($\sim$ 70% at $p_{\mathrm{T}}^{\mathrm{recoil}}$ >1000 GeV). The proportion of $t\bar{t}$ to single-t is shown in Figure 6.5.

Type of variation
Nominal Powheg+PYTHIA8
Hard Scatter Generation and matching
Fragmentation/Hadronization
Higher radiation hdamp = $3m_{top}$, scale=0.5
Lower radiation scale=2.0
Final state radiation scale

Table 6.3: $t\bar{t}$ MC sample list used to evaluate the top systematic uncertainties, and the type of variation with respect to the nominal sample used in the analysis. Systematic uncertainties are evaluated by internal weights in the nominal sample, as prescribed in reference [73].

Type of variation
Nominal Powheg+PYTHIA8
Hard Scatter Generation and matching
Fragmentation/Hadronization
Single Top Interference

Table 6.4: single-t MC sample list used to evaluate the top systematic uncertainties, and the type of variation with respect to the nominal sample used in the analysis. Systematic uncertainties are evaluated by internal weights in the nominal sample, as prescribed in reference [73].

the total uncertainty

$$\Delta_{shape} = \sqrt{\Delta^2_{total} - \Delta^2_{norm}}.$$

The two decoupled components and the total systematic uncertainty band are shown in Figure 6.7.

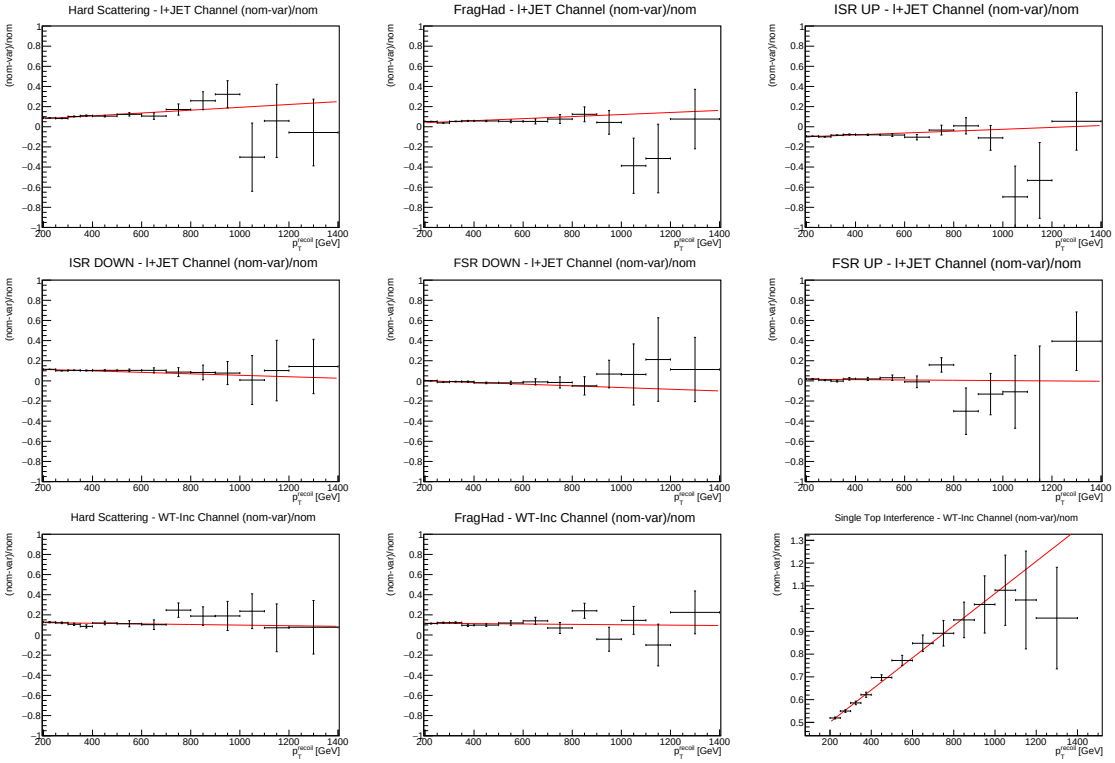

Figure 6.3: Individual systematic uncertainties fitted with a linear fit for both $t\bar{t}$ and single-t systematics. Shown for the l+jet channel for $t\bar{t}$ and for the Wt-inclusive channel for single-t, the dominant channels of $t\bar{t}$ and single-t respectively in the monojet analysis. Hard Scattering is the uncertainty associated with the scattering between partons, FragHad is the uncertainty associated with hadronization of the final state particles, ISR/FSR is uncertainty in initial/final state radiation. Single top interference is the uncertainty in the single-t case associated with production of a $t\bar{t}$ pair.

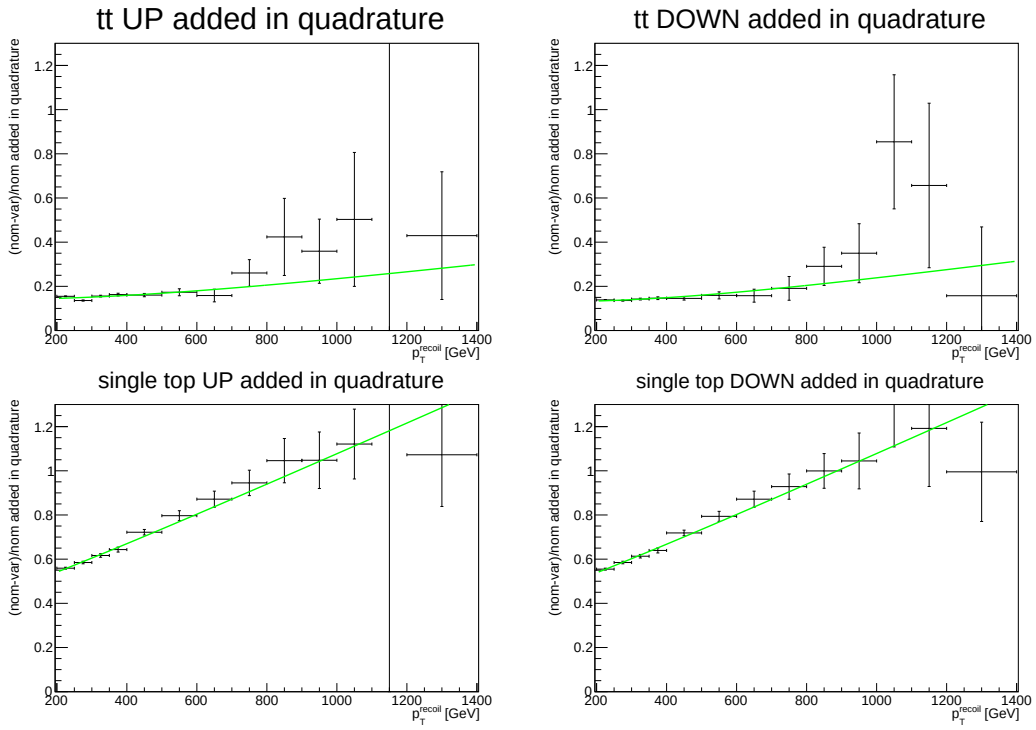

Figure 6.4: All $t\bar{t}$ systematic uncertainties summed in quadrature, in both UP and DOWN variations, and all single-t systematic uncertainties summed in quadrature, in both UP and DOWN variations. Absolute values of the variations are shown in the plots.

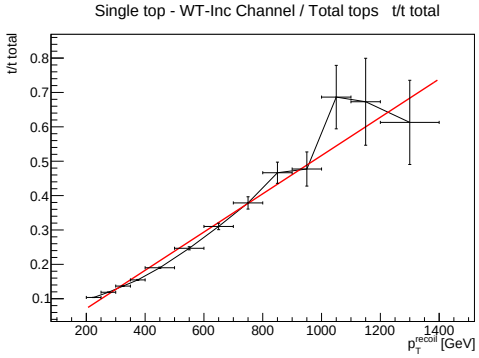

Figure 6.5: Proportion of Wt events in the background compared to all top events in the background.

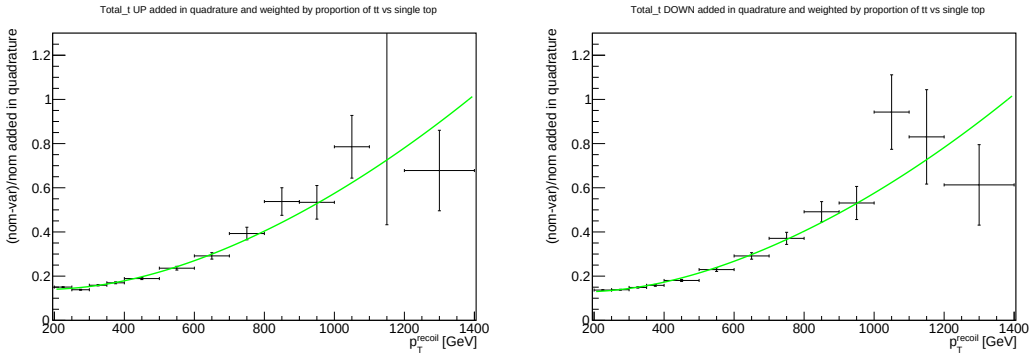

Figure 6.6: $t\bar{t}$ and single-t total UP and DOWN variation after weighting by proportion of $t\bar{t}$ and single-t events.

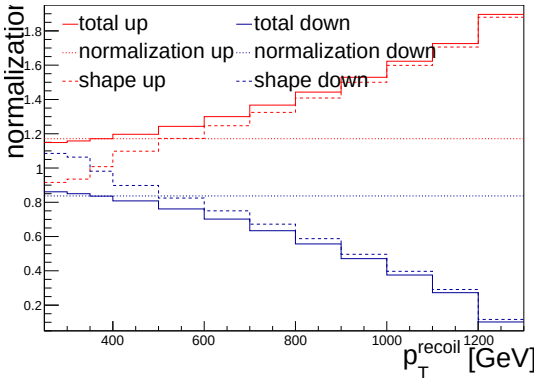

Figure 6.7: Total top systematic uncertainty and its normalisation and shape decoupled components. As mentioned in 4.7 the $t\bar{t}$ and single-t backgrounds are only relevant at low to medium $P_{\mathrm{T}}^{\mathrm{recoil}}$ and hence the very large normalization at high $P_{\mathrm{T}}^{\mathrm{recoil}}$ has negligible effect.

6.1.4.3 Background Systematic Summary

The total contribution of the dominant systematic uncertainties in each $P_{\mathrm{T}}^{\mathrm{recoil}}$ bin after the fit is performed is shown in Table 6.5, shown with systematic uncertainties grouped together into relevant categories by summing in quadrature the single components.

Source (%)	200-250	250-300	300-350	350-400	400-500	500-600	600-700	700-800	800-900	900-1000	1000-1100	1100-1200	1200-∞
Multijet	1.05	0.73	0.36	0.28	0.06	0.02	0.01	0.0	0.01	0.0	0.0	0.0	0.0
Non-collision bkg	0.2	0.1	0.08	0.06	0.05	0.05	0.08	0.0	0.0	0.0	0.0	0.0	0.0
Muons	0.62	0.7	0.8	0.89	1.03	1.19	1.36	1.54	1.71	1.85	1.96	2.06	2.24
Electrons	0.74	0.79	0.86	0.94	1.06	1.22	1.4	1.58	1.76	1.91	2.01	2.12	2.32
Jets	0.32	0.34	0.37	0.38	0.43	0.51	0.57	0.62	0.72	0.83	0.86	1.0	1.44
$P_{\mathrm{T}}^{\mathrm{recoil}}$	0.61	0.55	0.49	0.44	0.38	0.33	0.31	0.3	0.29	0.27	0.24	0.23	0.29
V+jet theoretical	0.36	0.4	0.47	0.57	0.67	0.8	0.96	1.12	1.3	1.44	1.53	1.7	1.98
$t\bar{t}$ theo.	0.22	0.2	0.18	0.17	0.19	0.23	0.26	0.29	0.32	0.4	0.45	0.56	0.73
Single Top theo.	0.21	0.2	0.17	0.18	0.19	0.23	0.24	0.2	0.21	0.13	0.09	0.19	0.42
Diboson	0.05	0.06	0.06	0.06	0.06	0.04	0.02	0.04	0.04	0.05	0.05	0.09	0.18
VBF V + jets theoretical	0.02	0.02	0.03	0.05	0.08	0.12	0.16	0.13	0.09	0.11	0.36	0.7	1.36
MC stat. uncertainty	0.0	0.0	0.0	0.0	0.0	0.0	0.53	0.55	0.85	0.93	1.11	1.67	1.68

Table 6.5: The most relevant post-fit systematic uncertainty impacts, grouping the systematic components by type and summed in quadrature.

6.1.5 Signal systematic uncertainties

6.1.5.1 Theoretical uncertainties on axial-vector and pseudoscalar WIMP models

There are 3 main theoretical systematic uncertainties for the DMA/DMP models, these being the scale, PDF (Parton Density Function) and ISR/FSR+MPI (Multi Parton Interaction) modelling uncertainties.

The scale uncertainty is dependent on how the choice of renormalization and factorization scales affects the signal cross section, the same as discussed in Section 6.1.4.2. The PDF uncertainty is dependent upon how the choice of proton PDF set (measurements of the momentum distributions of the partons that make up the proton) affects the signal.

The ISR/FSR+MPI uncertainty is dependent upon many different factors, summarized in Table 6.6.

The scale uncertainty is estimated by calculating the acceptance in each $p_{\mathrm{T}}^{\mathrm{recoil}}$ bin for 6 variations of the renormalization and factorization scale factors, [μ_R,μ_F] = [0.5,0.5], [0.5,2.0], [1.0,0.5], [1.0,1.0], [1.0,2.0], [2.0,0.5], [2.0,2.0]. The relative scale uncertainty for each variation was then calculated as $\frac{A-A_0}{A_0}$, where A_0 is the value for μ_R=μ_F=1.0. The UP variation is then taken to be the largest positive variation, and the DOWN variation the most negative variation. The scale variations of all the signal samples are summarised in Figure 6.8. For the axial-vector mediator case it ranges from 0.1% to 6.5% and increases as a function of $p_{\mathrm{T}}^{\mathrm{recoil}}$, except for two samples with a much higher uncertainty than all the others: $m_\chi = 1$ GeV, $m_{Z_A} = 10, 50$ GeV, with uncertainties that range from 8% to 20% and 4% to 12% respectively. Generally both higher dark matter particle mass and higher mediator mass result in a lower scale uncertainty for all $p_{\mathrm{T}}^{\mathrm{recoil}}$ ranges (with a larger effect at high $p_{\mathrm{T}}^{\mathrm{recoil}}$), though the mediator mass appears to have a larger effect overall. In the pseudoscalar mediator scenario, the scale uncertainty ranges between 0.4% and 21%, increasing as a function of $p_{\mathrm{T}}^{\mathrm{recoil}}$. Higher mediator mass results in lower scale

Param	+ variation	- variation
VAR1: MPI+CR (UE activity and incl jet shapes)		
BeamRemnants:reconnectRange	1.73	1.69
MultipartonInteractions:alphaSvalue	0.131	0.121
VAR2: ISR/FSR (jet shapes and substructure)		
SpaceShower:pT0Ref	1.60	1.50
SpaceShower:pTdampFudge	1.04	1.08
TimeShower:alphaSvalue	0.139	0.111
VAR3a: ISR/FSR ($t\bar{t}$ gap)		
MultipartonInteractions:alphaSvalue	0.125	0.127
SpaceShower:pT0Ref	1.67	1.51
SpaceShower:pTdampFudge	1.36	0.93
SpaceShower:pTmaxFudge	0.98	0.88
TimeShower:alphaSvalue	0.136	0.124
VAR3b: ISR/FSR (jet 3/2 ratio)		
SpaceShower:alphaSvalue	0.129	0.126
SpaceShower:pTdampFudge	1.04	1.07
SpaceShower:pTmaxFudge	1.00	0.83
TimeShower:alphaSvalue	0.114	0.138
VAR3c: ISR ($t\bar{t}$ gap, dijet decorrelation and Z-boson p_{T})		
SpaceShower:alphaSvalue	0.140	0.115

Table 6.6: Parameters considered in the ISR/FSR+MPI systematic uncertainty with distributions most sensitive to that variation indicated [74]. For the monojet analysis, the most sensitive variations are VAR2 and VAR3c. The values listed are the value the relevant parameter is for that variation, with the unvaried parameter being somewhere between the + and - variation.

uncertainty for all $p_{\mathrm{T}}^{\mathrm{recoil}}$ values.

The PDF uncertainty is estimated by calculating the acceptance in each $p_{\mathrm{T}}^{\mathrm{recoil}}$ bin for 100 different PDF sets via internal event weights in the nominal sample. The PDF uncertainty is then evaluated as the standard deviation of the distribution of these acceptances (δA^{pdf}) divided by the acceptance for a nominal PDF set, $\frac{\delta A^{pdf}}{A_0}$. The PDF uncertainties for all the signal samples are summarised in Figure 6.9. Statistical fluctuations are smoothed by performing a linear fit. For the axial-vector mediator scenario the uncertainty ranges from 0.1% to about 10%, increasing as a function of $p_{\mathrm{T}}^{\mathrm{recoil}}$. There is not any significant dependence on either the mediator mass or the dark matter particle mass. In the case of pseudoscalar mediators, PDF uncertainties range between 0.2% and 20%, increasing as a function of $p_{\mathrm{T}}^{\mathrm{recoil}}$. Higher

dark matter particle mass results in lower PDF uncertainty for all $p_{\mathrm{T}}^{\mathrm{recoil}}$ ranges.

The ISR/FSR+MPI modelling uncertainty is estimated from 5 pairs of different variation samples corresponding to `VAR1, VAR2, VAR3a, VAR3b, VAR3c`. All five variation pairs are conservatively summed in quadrature to get full coverage of the tune uncertainties. In the axial-vector scenario the estimated impact is about 3%, whereas in the pseudoscalar scenario it is about 6%.

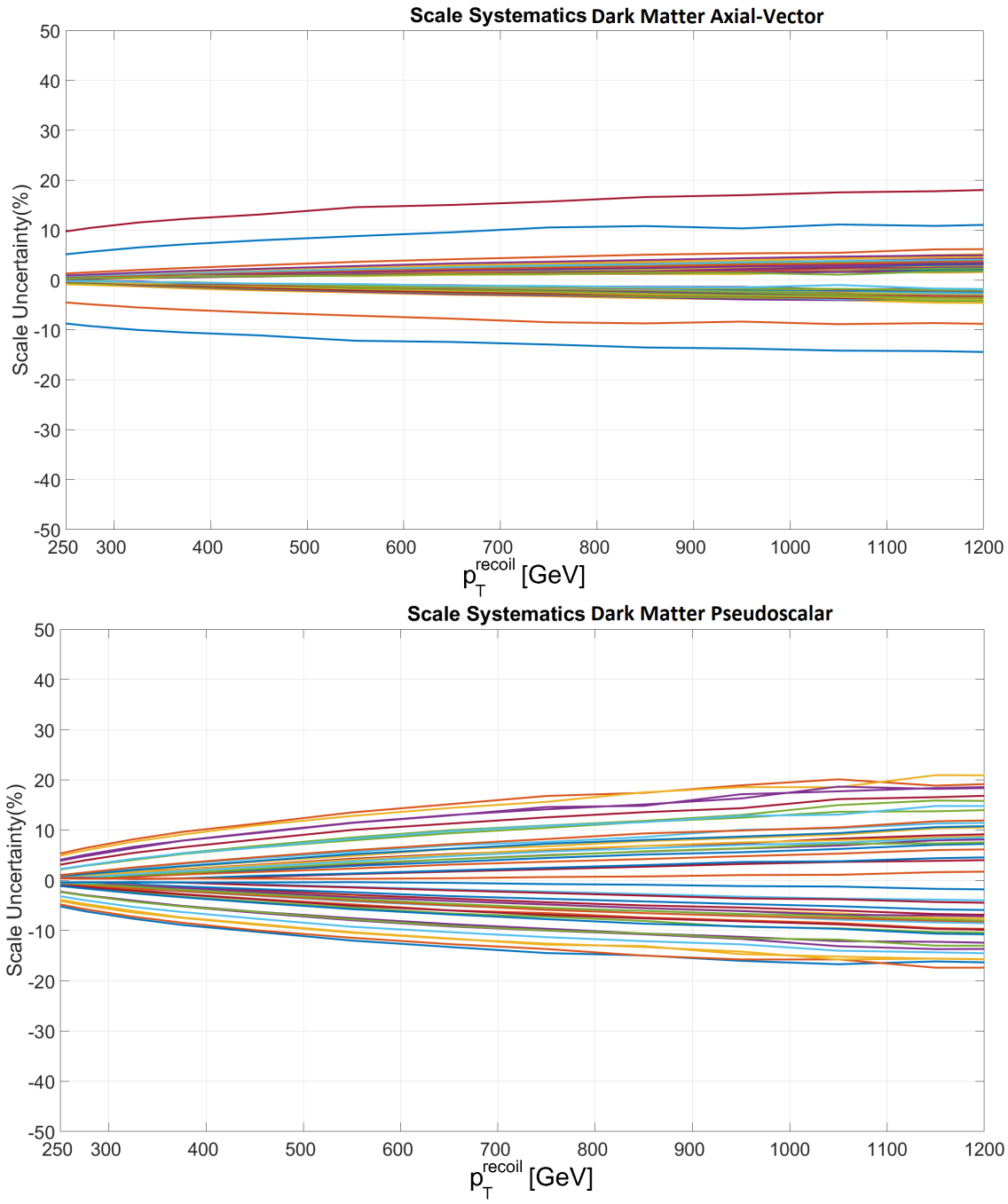

Figure 6.8: Scale uncertainties for axial-vector and pseudoscalar WIMPs for all samples. The different lines are different samples. The two outliers in the top plot are samples much further from the expected limit than the other samples which are used for validating the extrapolation procedure. Which sample each line represents is omitted, as all that is important is the overall spread of the uncertainty.

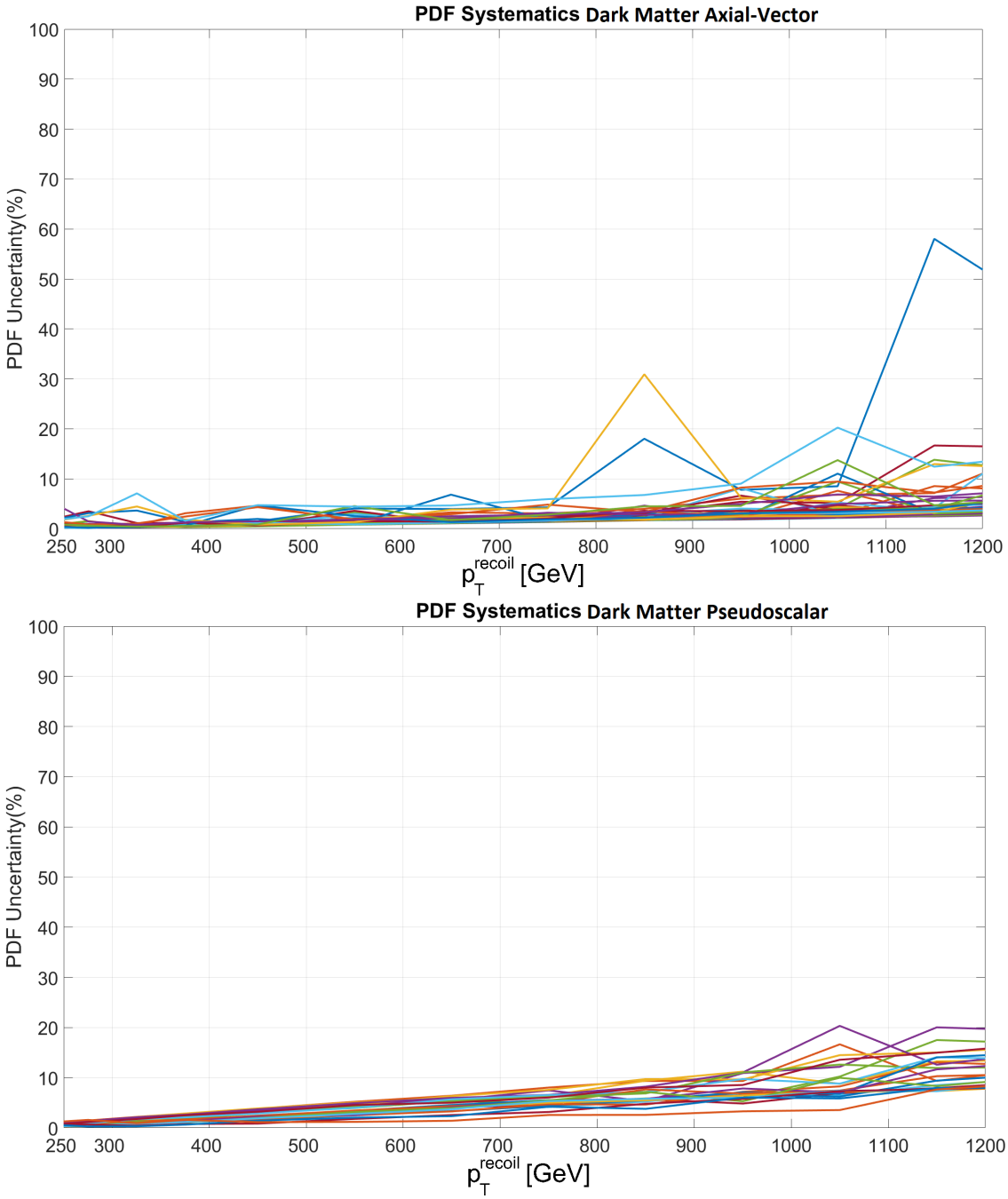

Figure 6.9: PDF uncertainties for axial-vector and pseudoscalar WIMPs for all samples. The different lines are different samples. Which sample each line represents is omitted, as all that is important is the overall spread of the uncertainty. The few large fluctuations in the top plot are purely due to low statistics in the high $P_{\mathrm{T}}^{\mathrm{recoil}}$ region for these particular samples.

6.1.5.2 Theoretical uncertainties on Horndeski dark energy model

There are 3 main theoretical systematic uncertainties for the dark energy models, these being the scale uncertainty and the PDF uncertainty as described in the previous section, and also the α_S uncertainty from the strong coupling constant.

For simulation of the dark energy model and calculation of the uncertainties, a nominal sample is used with the Wilson coefficients $\mathcal{O}_i = 0$ except for $\mathcal{O}_2 = 1$ and the mass scale of the theory, M_2, set to $M_2 = 1000$ GeV. Varying the mass scale in the simulation scales only the cross section and does not affect the kinematics, a property which has been verified by comparing to other mass scale samples (e.g. $M_2 = 2000$ GeV).

The scale and PDF uncertainties are estimated in the same way as detailed in the previous section.

The α_S uncertainty is estimated by comparing the nominal sample to a separate Dark Energy sample, which was generated with a different PDF set with a different value of α_S, which is summarised along with the scale and PDF uncertainties in Table 6.7.

The PDF and α_S uncertainties are combined according to the PDF4LHC prescription [75].

The scale variation, estimated as a function of $p_{\mathrm{T}}^{\mathrm{recoil}}$, ranges between 0.1% and 3.5% (in agreement with the previous estimation used in Ref. [21]). The PDF uncertainties are reduced, thanks mainly to the larger statistics of the shifted samples compared to the previous analysis, and range between 1% and 16%. The α_s uncertainty, estimated as a function of $p_{\mathrm{T}}^{\mathrm{recoil}}$, ranges between 0.1% and 4.9%.

$P_{\mathrm{T}}^{\mathrm{recoil}}$ [GeV]	Scale(min,max)	$\frac{\delta A^{pdf}}{A_0}$	$\frac{\delta A^{\alpha_S}}{A_0}$	Total
(200-250)	(−0.2,0.2)	1.5	−1.7	2.3
(250-300)	(−0.1,0.1)	0.4	−0.7	0.8
(300-350)	(−0.5,0.5)	1.1	−1.1	1.6
(350-400)	(−0.4,0.3)	1.8	−0.1	1.9
(400-500)	(−0.8,0.8)	2.4	−1.3	2.8
(500-600)	(−1.0,1.0)	4.0	−0.9	4.2
(600-700)	(−1.3,1.3)	5.3	−0.5	5.5
(700-800)	(−1.8,1.9)	6.3	−1.1	6.6
(800-900)	(−1.7,1.8)	7.6	0.5	7.8
(900-1000)	(−2.2,2.3)	8.6	−1.6	9.0
(1000-1100)	(−2.3,2.4)	9.6	−4.9	11.0
(1100-1200)	(−2.9,3.1)	10.7	4.3	11.8
(1200+)	(−3.3,3.6)	16.1	0.2	16.4

Table 6.7: Scale, PDF and α_S systematic uncertainties for the C2 Horndeski dark energy model per $P_{\mathrm{T}}^{\mathrm{recoil}}$ bin.

6.1.6 Results

6.1.6.1 Post-fit signal region results

After performing the fit, Figures 6.10-6.13 are obtained, showing good agreement between the Standard Model and measurement in the $P_{\mathrm{T}}^{\mathrm{recoil}}$ distribution, which is what is used in the subsequent sections to produce limits. While the other distributions also show fairly good agreement with the Standard Model, there is a non-negligible tension particularly in the leading jet p_{T} distribution. However, this tension is (at least largely) not due to a disagreement between measurement and Standard Model prediction, but is instead due to a known mismodelling in Sherpa. This mismodelling is removed in the $P_{\mathrm{T}}^{\mathrm{recoil}}$ distribution when performing the fit, however it remains in the other distributions. Since the limits are based solely upon the $P_{\mathrm{T}}^{\mathrm{recoil}}$ distribution, this does not cause a problem.

Overlaid on these are example signals at signal points close to the exclusion limits for Dark Energy (DE) and axial-vector WIMPs ($m(\chi, Z_A)$).

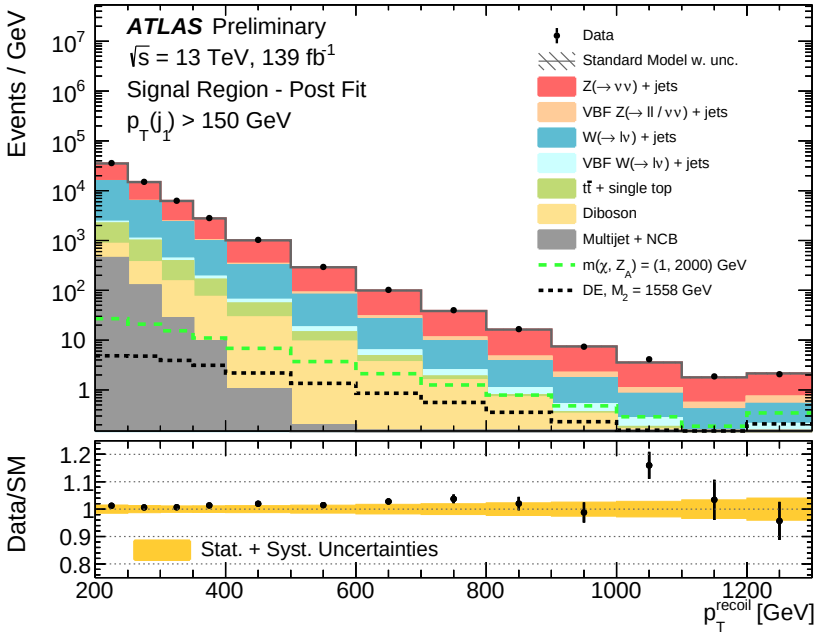

Figure 6.10: SR $P_{\mathrm{T}}^{\mathrm{recoil}}$ distribution after fit based on the full Run 2 dataset, with two example signal distributions overlaid. The error bands in the ratios include both the statistical and systematic uncertainties in the background predictions. Across the full range the largest deviation between data and Standard Model is in the $P_{\mathrm{T}}^{\mathrm{recoil}}$ = 1000 - 1100 GeV bin having a value of (data-SM)/σ=2.2. [10]

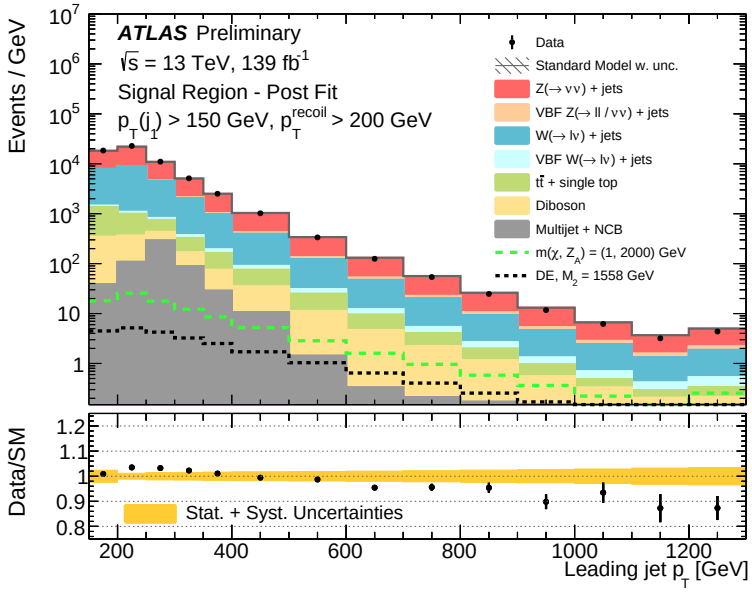

Figure 6.11: SR leading jet p_{T} distribution after fit based on the full Run 2 dataset, with two example signal distributions overlaid. The error bands in the ratios include both the statistical and systematic uncertainties in the background predictions. The deviation from unity is due to a known mismodelling in Sherpa, however this does not affect our results which are dependent on the $P_{\mathrm{T}}^{\mathrm{recoil}}$ distribution.

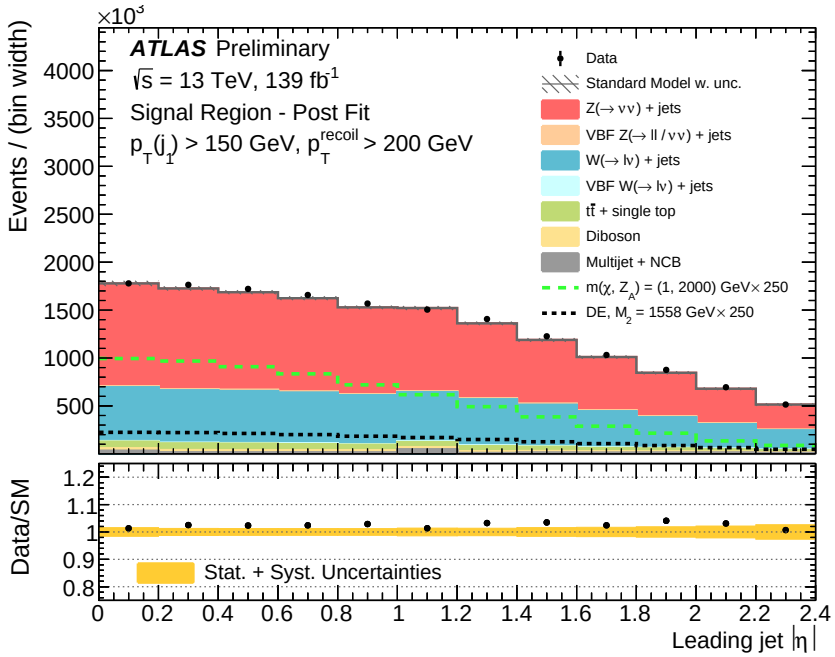

Figure 6.12: SR leading jet $|\eta|$ distribution after fit based on the full Run 2 dataset, with two example signal distributions overlaid. The error bands in the ratios include both the statistical and systematic uncertainties in the background predictions.

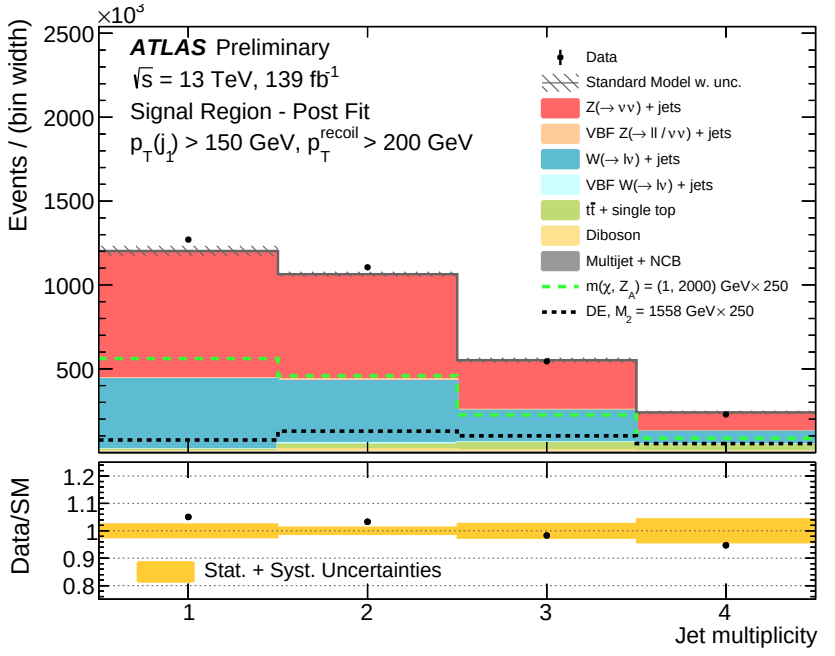

Figure 6.13: SR number of jets distribution after fit based on the full Run 2 dataset, with two example signal distributions overlaid. The error bands in the ratios include both the statistical and systematic uncertainties in the background predictions.

To obtain the limits at 95% confidence level (and 90% confidence level for comparison to direct detection experiments), the background yields are used, combined with the considered signal model, fitted as described in Section 4.7.1 to calculate the likelihood, which is used to derive the confidence intervals. For the model-independent result, as mentioned in Section 4.7.1, inclusive $P_{\mathrm{T}}^{\mathrm{recoil}}$ bins are used to remove shape dependence, while for the model-dependent cases exclusive $P_{\mathrm{T}}^{\mathrm{recoil}}$ bins are used.

6.1.6.2 Model-independent results

In this section the model-independent limits on the visible cross section are derived using the inclusive $p_{\mathrm{T}}^{\mathrm{recoil}}$ signal regions with the global fit performed over the full $p_{\mathrm{T}}^{\mathrm{recoil}}$ range. The limits on the number of signal events and on the visible cross section are shown in Figure 6.14 and Figure 6.15 respectively.

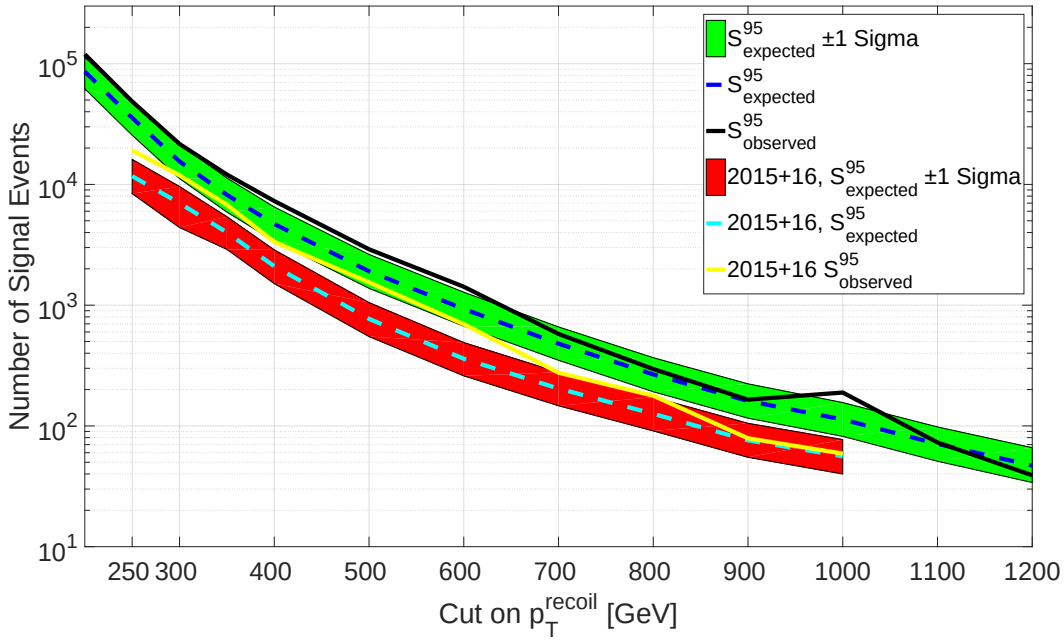

Figure 6.14: Observed and expected 95% confidence level upper limits on the number of signal events, for the inclusive selections. The red curve shows the previous version of the monojet analysis, while the green is the current. These curves are not normalized by luminosity, hence while even though the more recent analysis has a small relative uncertainty on the number of signal events the absolute uncertainty is larger due to the larger integrated luminosity. Figure 6.15 instead shows the visible cross-section limit, which is effectivley normalized by luminosity.

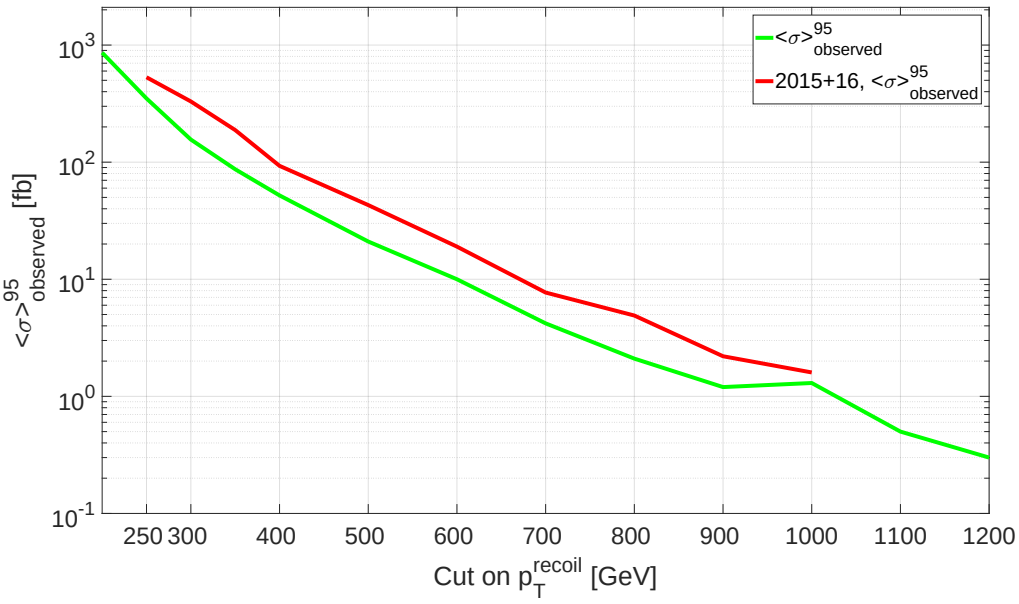

Figure 6.15: Observed 95% confidence level upper limit on the visible cross section, defined as the product of cross section, acceptance and efficiency, $\langle\sigma\rangle^{95}_{obs}$, for the inclusive selections. The red curve shows the previous version of the monojet analysis, while the green is the current.

6.1.6.3 Dark matter WIMP interpretation

As in the previous analysis [76], since the acceptance of the $P_{\mathrm{T}}^{\mathrm{recoil}}$ distribution does not change as a function of the mass of the WIMP (m_χ) at fixed mediator mass ($m_{Z_A}$and m_{ZP} for axial-vector and pseudoscalar mediators respectively) in the on-shell regime ($m_{Z_A/Z_P} > 2m_\chi$) (see also Ref. [18]), the limits for the WIMP models discussed in Section 2.3.1 are calculated with a grid over the (m_χ,m_{Z_A/Z_P}) plane on full RECO level samples which are then rescaled by the cross sections generated by a large number of TRUTH level samples, using an interpolation procedure to cover the full 2D plane.

Figure 6.16 shows the observed and expected contours (limits set) at 95% confidence level in the m_{Z_A}, m_χ plane for an axial-vector mediator with $g_q = 0.25$ and $g_\chi = 1.0$, chosen to be consistent with other analyses, different couplings can be achieved from this exclusion plot via a rescaling procedure. The region below the curve is excluded. The region for which the tested models predict a dark matter relic density higher

than the one measured by the Planck [77] and WMAP [78] collaborations, namely $\Omega h^2 > 0.12$, is computed using MadDM [79, 80]. The observed (expected) limits extend up to m_{Z_A} ≥2060(2175) GeV for dark matter particle mass candidates of $m_\chi = 1$ GeV extending the previous reach by about 500(400) GeV. The contours obtained in the previous versions of the analysis based on 3 fb^{-1}and 36 fb^{-1}are in Ref. [76, 81].

Figure 6.17 shows the observed and expected contours at 95% confidence level in the m_{Z_P}, m_χ plane for a pseudo-scalar mediator with $g_q = g_\chi = 1.0$. The region below the curve is excluded. Also in this context, the region for which the tested models predict a dark matter relic density higher than the one measured by the WMAP collaboration, namely $\Omega h^2 > 0.12$, is shown. For the first time in ATLAS this channel is sensitive to such a signature and the observed (expected) limits extend up to about $m_{Z_P} \geq 368(404)$ GeV for dark matter particle mass candidates of $m_\chi = 1$ GeV.

6.1.6.4 Dark energy interpretation

Figure 6.18 shows the observed and expected contours at 95% confidence level in the σ, M_2 plane for the disformal coupling of the Horndeski dark energy model, discussed in Section 2.3.2, investigated with $m_\phi = 0.1$ GeV and $C_{i\neq 2} = 0$, $C_2 = 1$. As m_ϕ is light compared to collider scales, the mass scale (M) has no effect on the kinematics of the interaction, and purely scales the cross section $\propto M^{-8}$. The cross section as a function of mass is then predicted by extrapolating the cross section from a sample generated at $M_2 = 1000$ GeV. This is validated by using another generated point with $M_2 = 2000$ GeV.

The limit set on the mass scale is then the intersection of the predicted cross section with the observed(expected) limit at $\sigma \leq 0.0433(0.0366)$ fb, $M_2 \geq 1558(1591)$ GeV, shown in Figure 6.18. These results represent a significant improvement of about 400(300) GeV in M_2 over the limits obtained using only the 2015+2016 data [21].

However, as mentioned in Section 2.3.2.1, the mass limits can be affected slightly by the truncation procedure used to ensure effective field theory validity. The truncation procedure was applied only to the results using the 2015+2016 data [21]. From this it is clear that the truncation procedure does not noticeably affect the limits, other than at the lowest limit we can set on g_*, for which we do not expect any significant improvement with the increased statistics. In addition, due to the way the truncation procedure is performed by reweighting events that satisfy $Q_{tr} > g_* M$, with the larger limits on M with increased statistics, the truncation procedure will have even less effect, hence the truncation procedure was not applied over the full dataset.

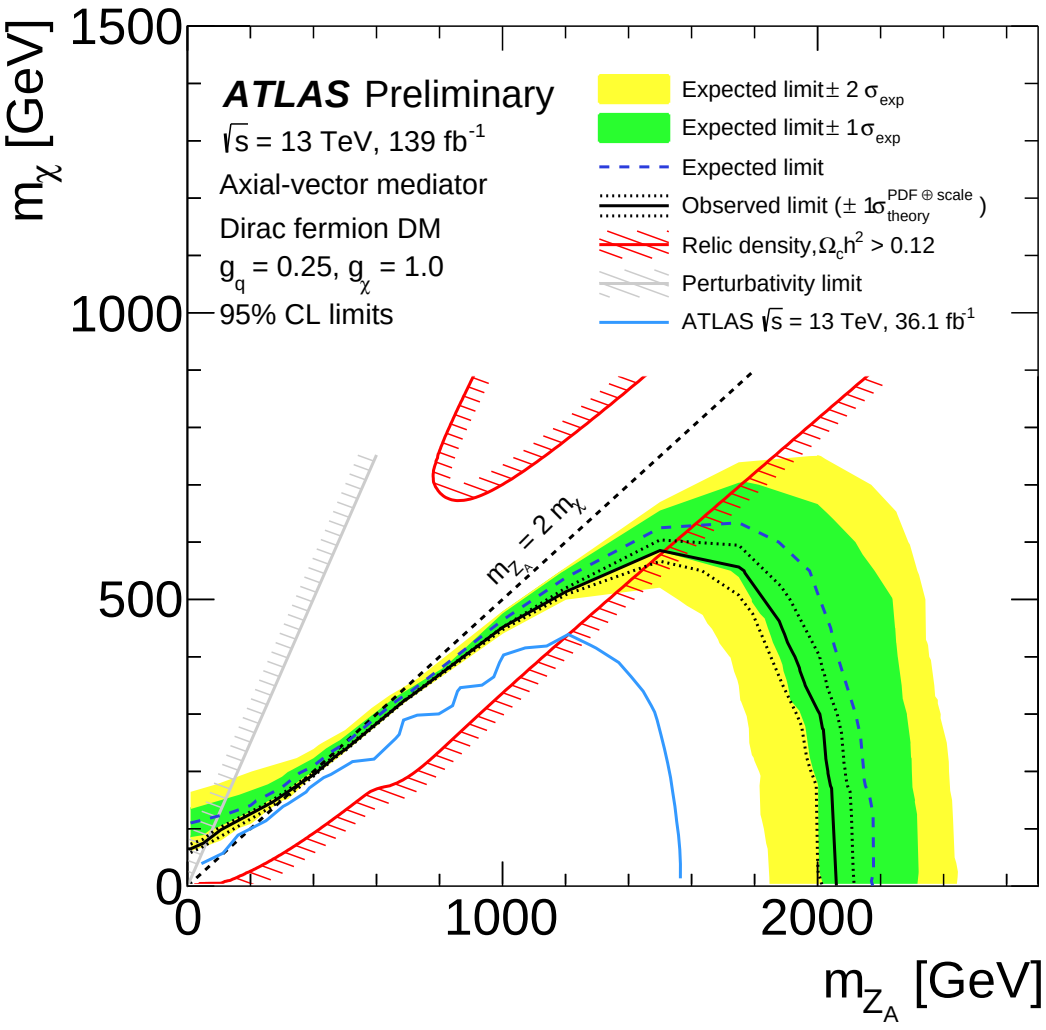

Figure 6.16: Expected (dashed line) and observed (solid line) exclusions at 95% confidence level on the axial–vector mediator models, with couplings $g_q = 0.25, g_\chi = 1.0$, chosen to be consistent with other analyses, different couplings can be achieved from this exclusion plot via a rescaling procedure, and minimal mediator width, as a function of the assumed mediator and dark matter particle masses. The regions within the drawn contours are excluded. The area on the right of the dashed black line in the on-shell part of the plane (above the line in the off-shell part) corresponds to predicted values of the relic density abundance inconsistent with the WMAP measurements (i.e. $\Omega h^2 > 0.12$). The region excluded due to perturbativity, defined by $m_\chi > \sqrt{\pi/2}\, m_{Z_A}$, is indicated by the grey hatched area. The dotted line indicates the kinematic limit for on-shell production $m_{Z_A} = 2 \times m_\chi$. Figure and caption from [10].

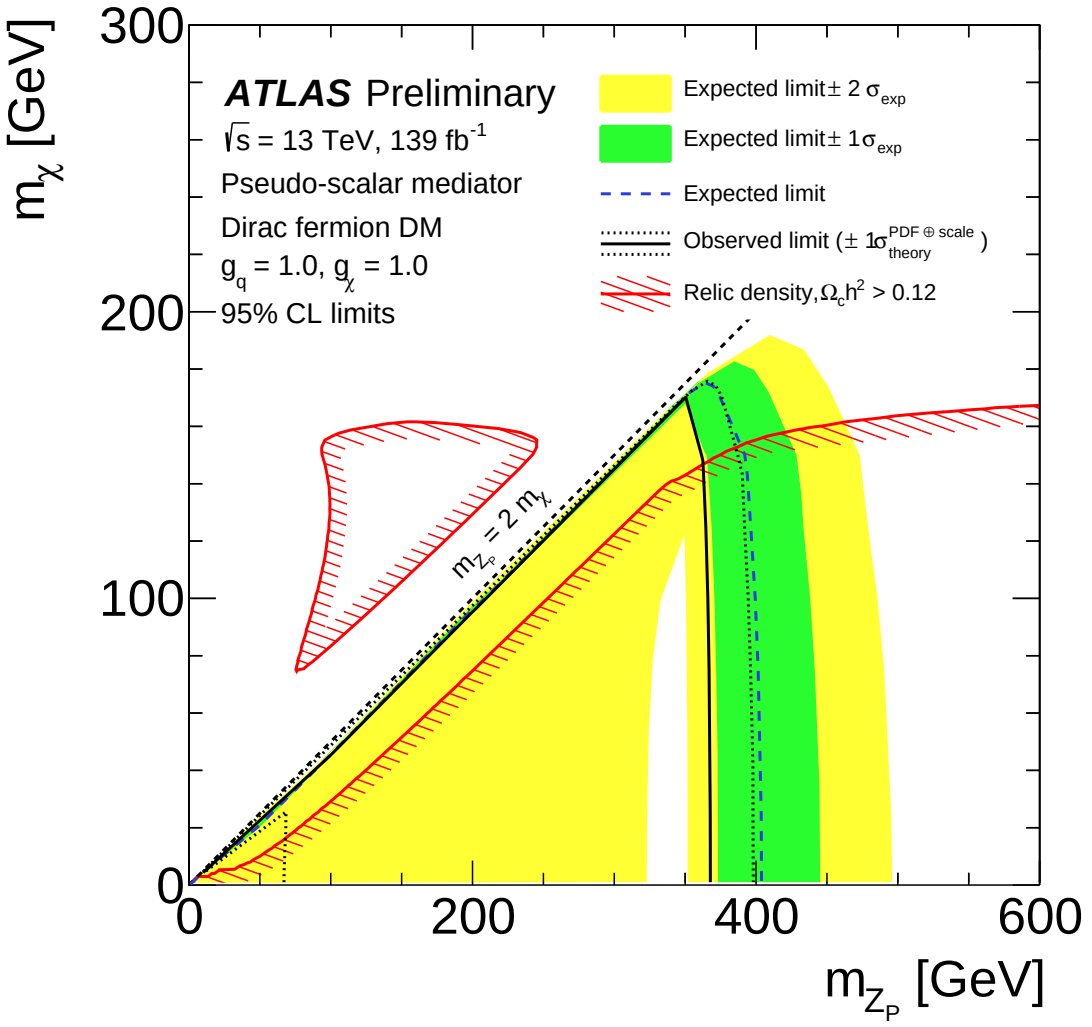

Figure 6.17: Expected (dashed line) and observed (solid line) exclusions at 95% confidence level on the pseudo-scalar mediator models with $g_q = g_\chi = 1.0$, chosen to be consistent with other analyses, different couplings can be achieved from this exclusion plot via a rescaling procedure, and minimal mediator width, as a function of the assumed mediator and dark matter particle masses. The area on the right of the continuous red line in the on-shell part of the plane (above the line in the off-shell part) corresponds to predicted values of the relic density abundance inconsistent with the WMAP measurements (i.e. $\Omega h^2 > 0.12$). Figure and caption from [10].

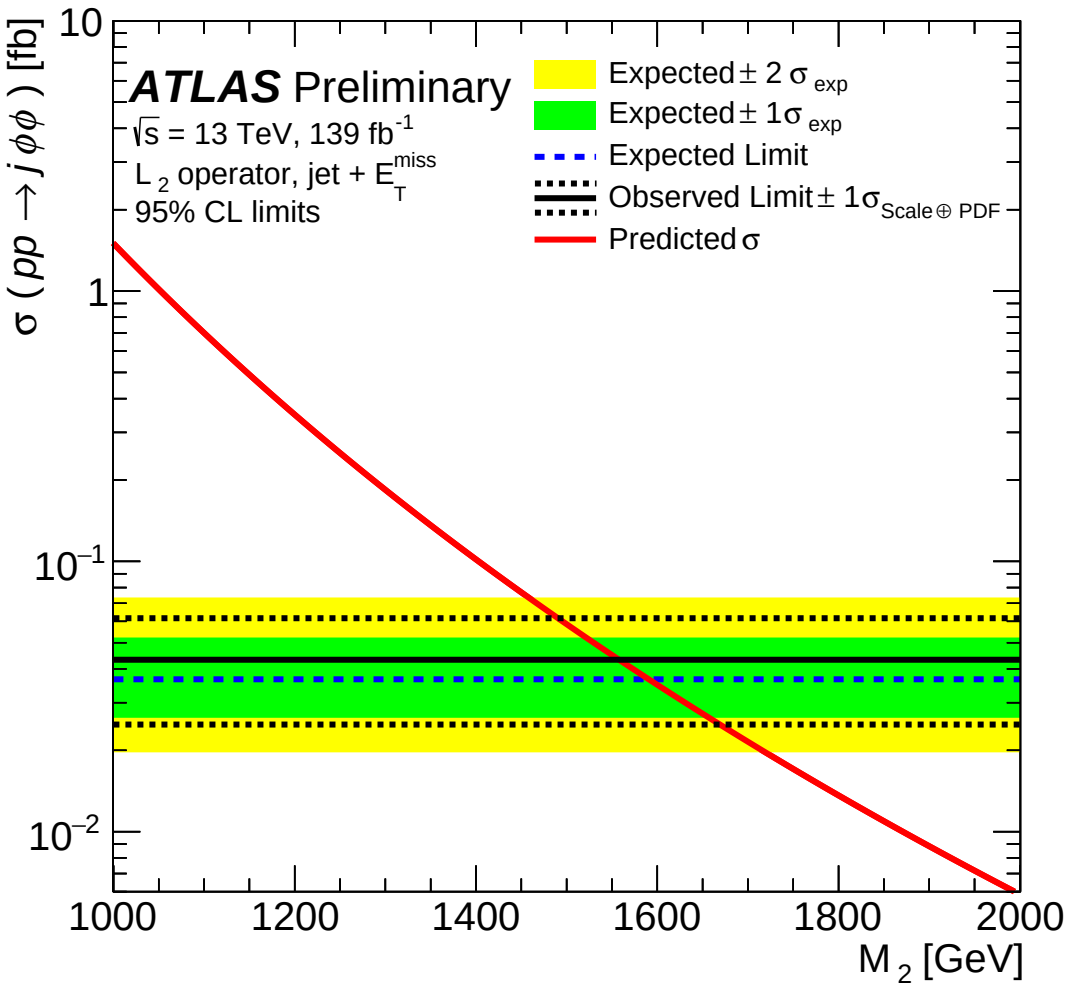

Figure 6.18: Observed (solid line) and expected (dashed line) exclusions at 95% confidence level on the Horndeski dark energy model for the mass of the scalar field $m_\phi = 0.1$ GeV and Wilson coefficients $C_{i\neq 2} = 0$, $C_2 = 1$. The cross-section limit is flat across the mass scale, M_2, range as the kinematics are entirely independent of M_2, instead M_2 purely scales the cross-section $\propto M^{-8}$. The parameters and model were explained further in Section 2.3.2. A suppression scale for the disformal coupling below 1558(1591) GeV is excluded [10].

6.2 Summary

Many improvements have been made to the monojet analysis. In particular the lowering of the $P_{\mathrm{T}}^{\mathrm{recoil}}$ and leading jet p_{T} thresholds allow probing of a wider range of signals than was previously possible by increasing sensitivity to more soft signals. Due to the monojet's place in the wider field as a channel for model independent and diverse searches this represents a significant improvement to the overall aims of the experiment.

In addition new models have been probed, and to higher precision. The Horndeski dark energy signal probed in this analysis, which is the first time any dark energy signal has been probed in a particle collider, hopefully represents a step forward towards more diverse probes and the beginning of a new field in collider-based searches for dark energy. As well as showing that dark energy searches with a collider are a possibility, strong constraints have been set on the Horndeski dark energy signal, setting limits an order of magnitude higher than other non-collider-based searches at high couplings.

Shown in Figure 6.19 and Figure 6.20 are the limits set on the axial-vector mediator WIMP discussed earlier, overlaid with the current leading direct detection results for this WIMP model [82–84], showing that the monojet analysis continues to set WIMP limits that can probe areas of phase space direct detection cannot, and hence combining the two techniques allows a more thorough search of the available phase space. The exclusion limit for the monojet case in these figures is arrived at by a rescaling procedure that takes the exclusion limits in the (m_{χ}, m_{Z_A/Z_P}) plane (shown in Figures 6.16 and 6.17) and rescales them to the (σ_{SD},m_{χ}) plane where σ_{SD} is the spin-dependent cross-section and differs for protons and neutrons. This rescaling procedure is outlined in [85]. This is only performed for the axial-vector case, as for the pseudo-scalar case velocity-dependent terms on the cross-section suppress the sensitivity of direct detection experiments making the limits arived at on this model by direct detection experiments negligible.

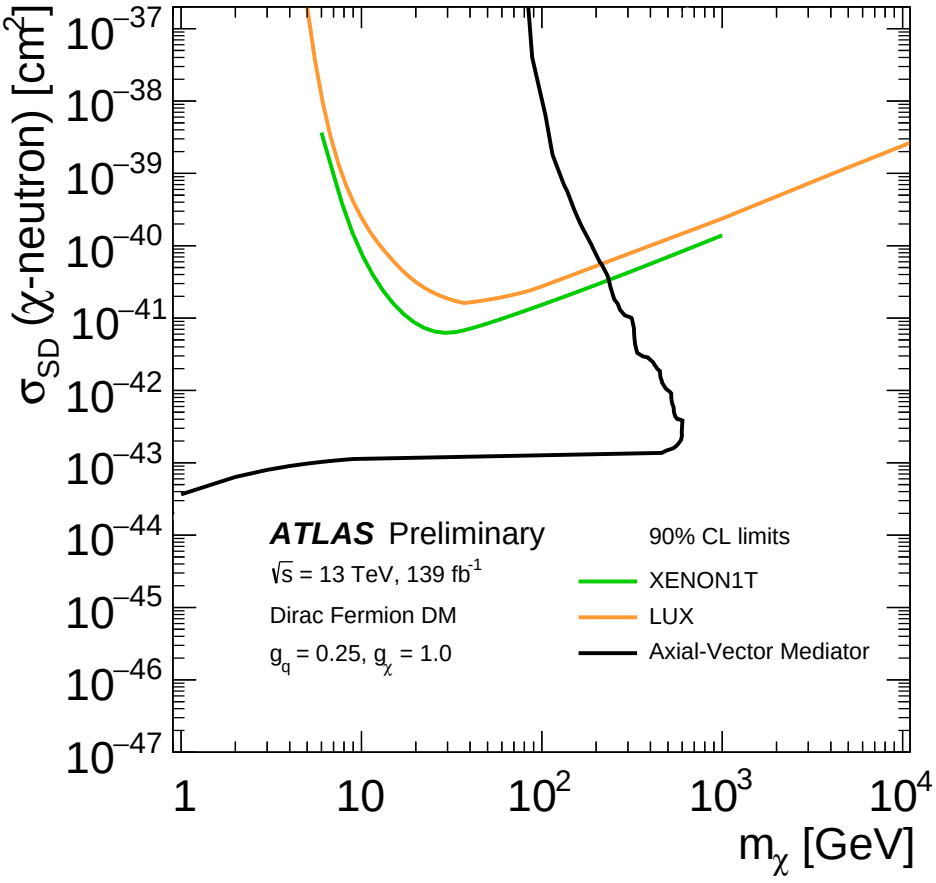

Figure 6.19: Axial-vector WIMP limits at 90% confidence level compared to neutron direct detection experiments, showing that the searches are complementary and together explore a large range of phase space. The excluded regions are above the lines. The results for direct detection are obtained by the XENON1T experiment [82] and the LUX experiment [83]. Figure from [10].

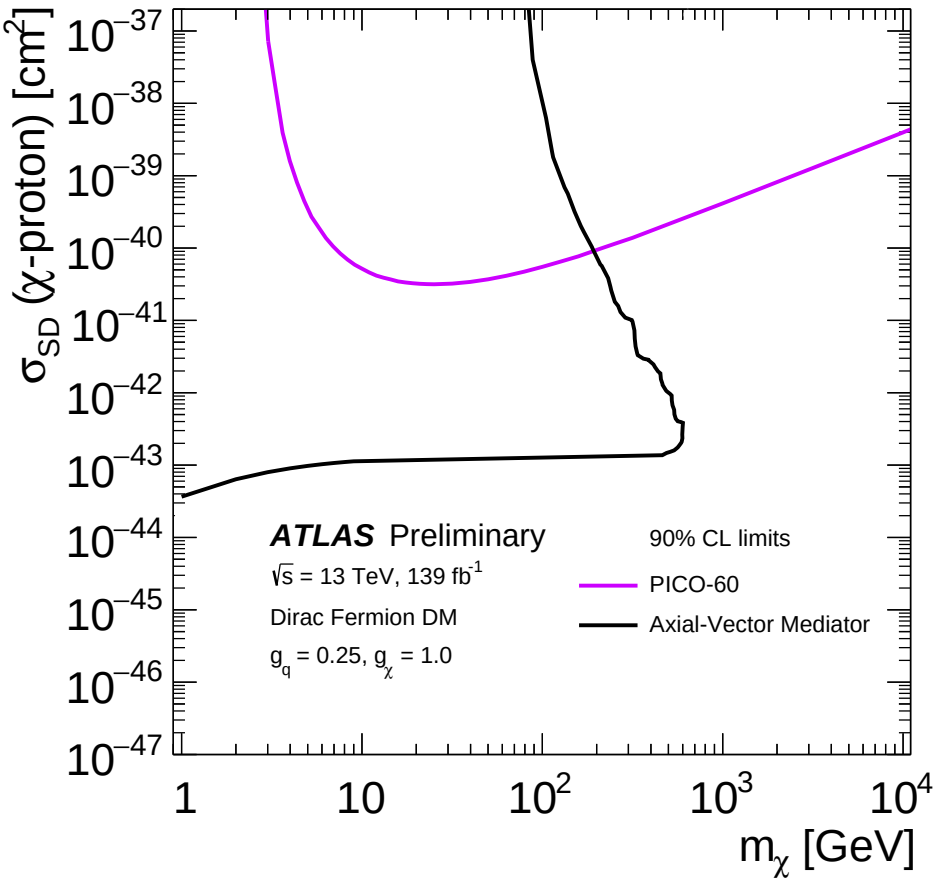

Figure 6.20: Axial-vector WIMP limits at 90% confidence level compared to proton direct detection experiments, showing that the searches are complementary and together explore a large range of phase space. The excluded regions are above the lines. The results for direct detection are obtained by the PICO-60 experiment [84]. Figure from [10].

The axial-vector WIMP limit set is less competitive than that from dijet analyses [86–90], however it is more sensitive than other $P_{\mathrm{T}}^{\mathrm{recoil}}$ + X analyses. Due to the reduced model-dependence of $P_{\mathrm{T}}^{\mathrm{recoil}}$ + X analyses compared to other techniques it is important to cover all regions of phase space in case model-dependent assumptions result in the exclusion of signals that actually exist. Leading ATLAS constraints for this model [10, 86–94] are shown in Figure 6.21 [95] and leading CMS constraints for this model [96–102] are shown in Figure 6.22 [103].

In addition, while the direct axial-vector limits set by the monojet analysis are less competitive than the dijet analyses, they can be reinterpreted, for example by cross section rescaling, in terms of other models. One example is the reinterpretation of the axial-vector limits in terms of a leptophilic vector mediator. Leading ATLAS constraints on this model [10, 87, 92, 104] are shown in Figure 6.23 [95], for which the monojet analysis is very competitive and covers a large range of phase space not covered by other analyses.

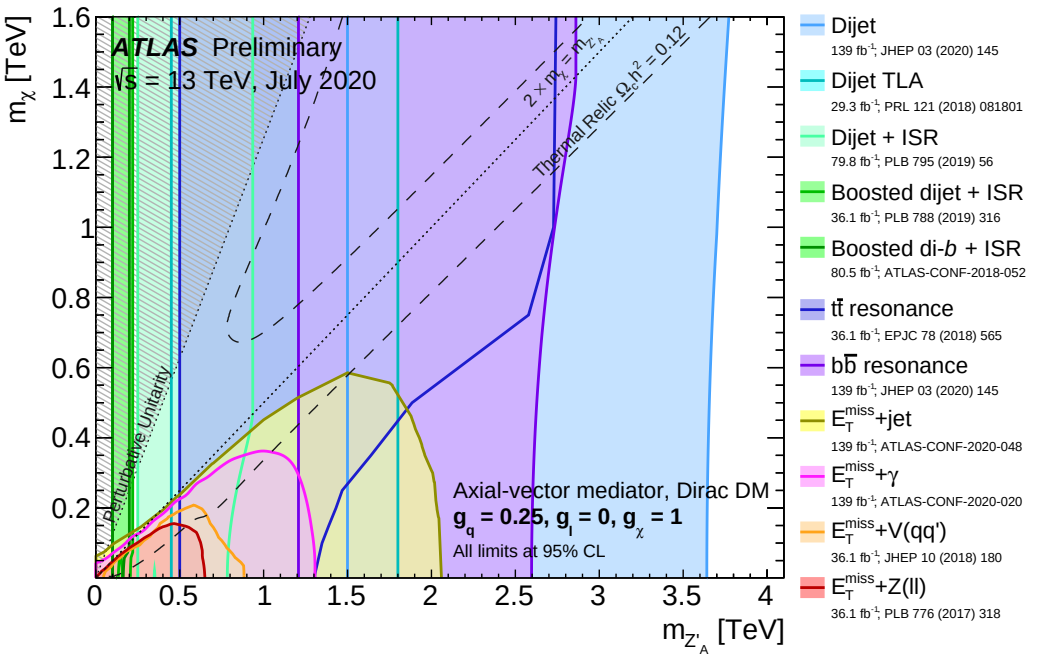

Figure 6.21: Summary of ATLAS searches for axial-vector WIMPs. Note that not all analyses have yet been performed over the full Run 2 dataset [95].

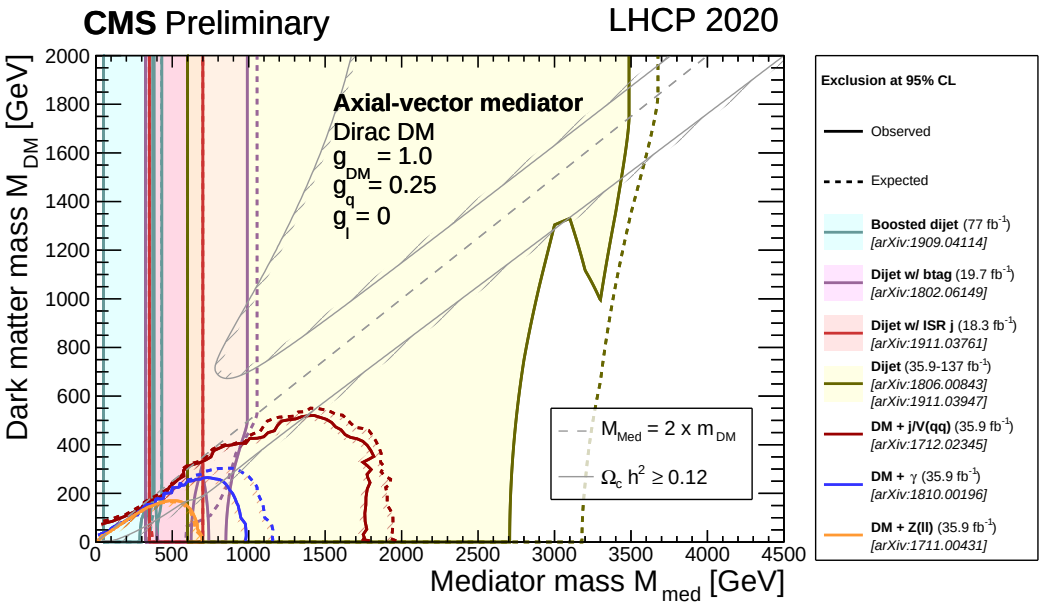

Figure 6.22: Summary of CMS searches for axial-vector WIMPs. Note that not all analyses have yet been performed over the full Run 2 dataset [103].

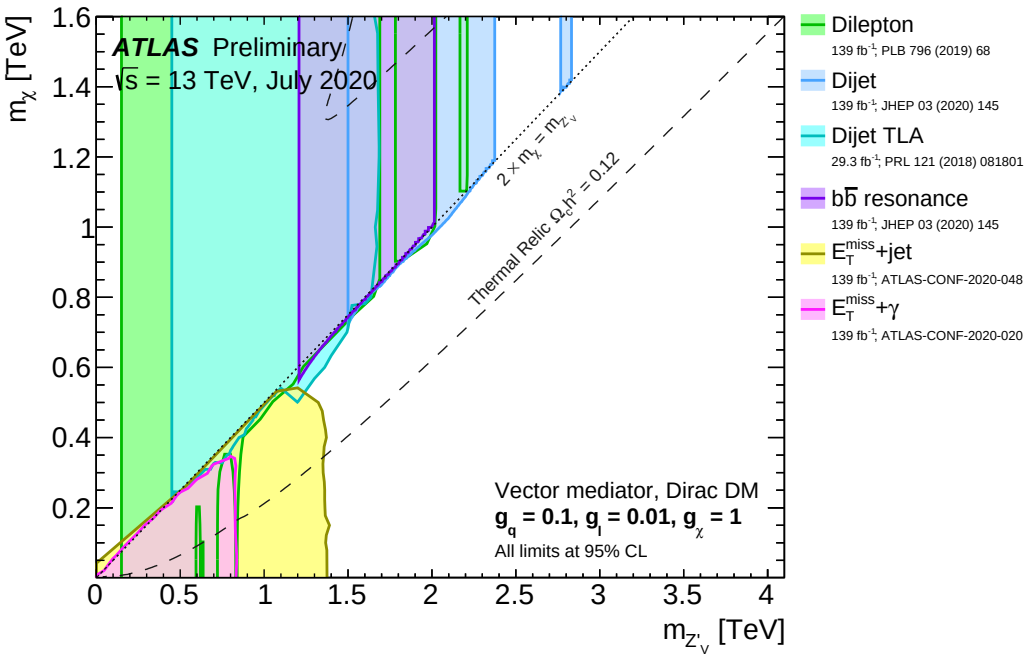

Figure 6.23: Summary of ATLAS searches for leptophilic vector WIMPs. Note that not all analyses have yet been performed over the full Run 2 dataset [95].

The pseudoscalar limit is competitive across the full mass range and is currently the strongest limit set at high values of m_{Z_A}. Leading ATLAS constraints on this model [10, 105–107] are shown in Figure 6.24 [95] and leading CMS constraints on this model [100, 102, 108] are shown in Figure 6.25 [103].

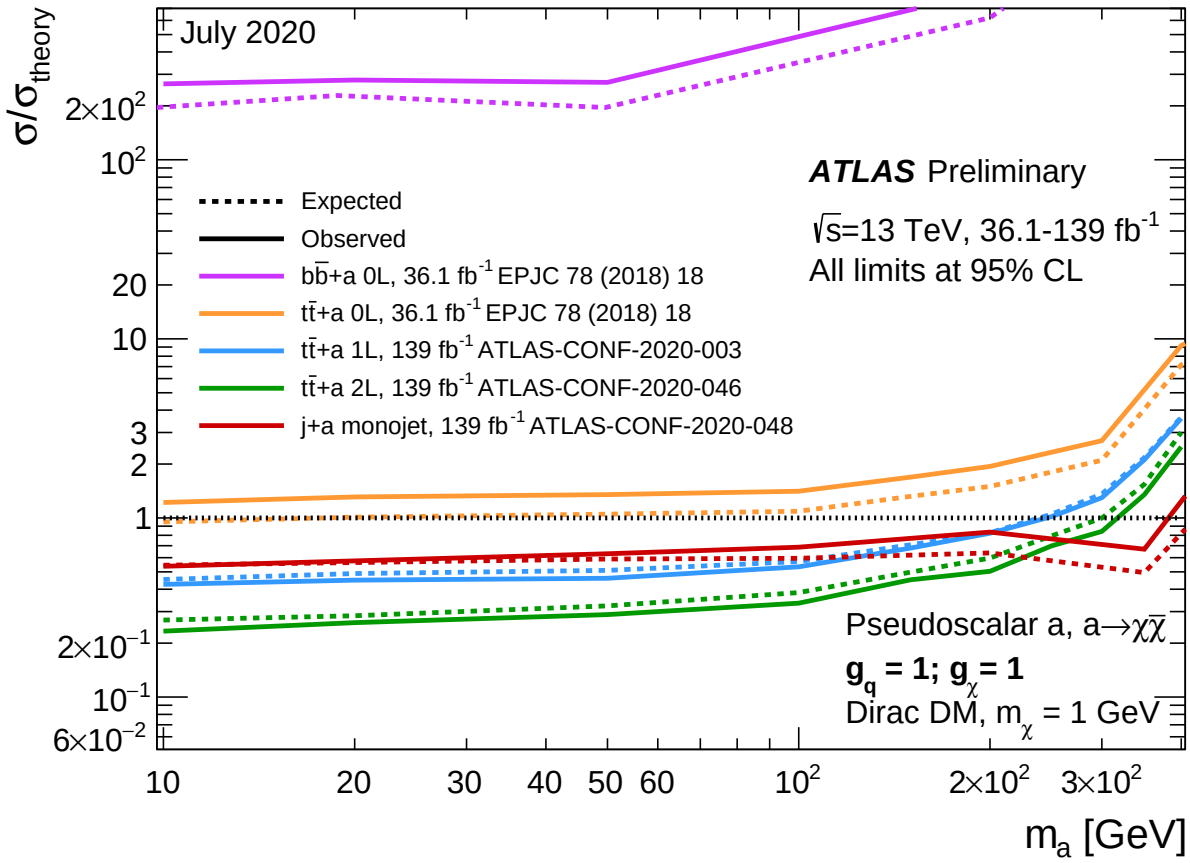

Figure 6.24: Summary of ATLAS searches for pseudoscalar WIMPs. m_a in this plot is referred to as m_{Z_P} elsewhere in this thesis. Note that not all analyses have yet been performed over the full Run 2 dataset [95].

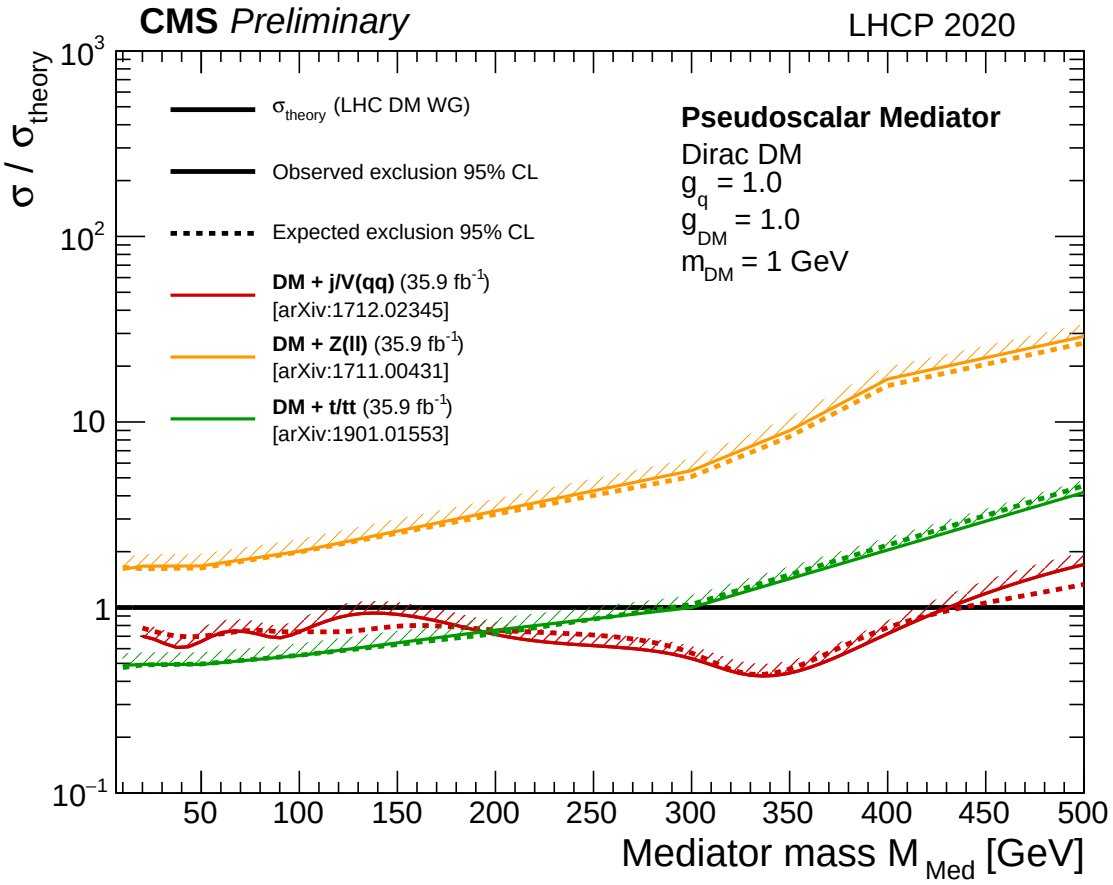

Figure 6.25: Summary of CMS searches for pseudoscalar WIMPs. Note that not all analyses have yet been performed over the full Run 2 dataset [103].

It is important to note that some of the analyses in these plots have not yet been performed with the full Run 2 dataset and instead use only 2015+2016 data, or another subset of data. In particular the large increase in sensitivity of the ATLAS monojet result compared to the CMS monojet result is mainly because of this.

The 2015+2016 results (with truncation included) for the Horndeski dark energy model discussed in Section 2.3.2 are shown for the monojet analysis in the $\mathcal{L}_2$ operator, compared to other non-collider searches [109], in Figure 6.26. For completeness the $t\bar{t}$ search in the $\mathcal{L}_1$ operator is also shown in Figure 6.27. This is the only other current collider based search for dark energy, which was developed closely alongside the monojet search for dark energy described in this thesis.

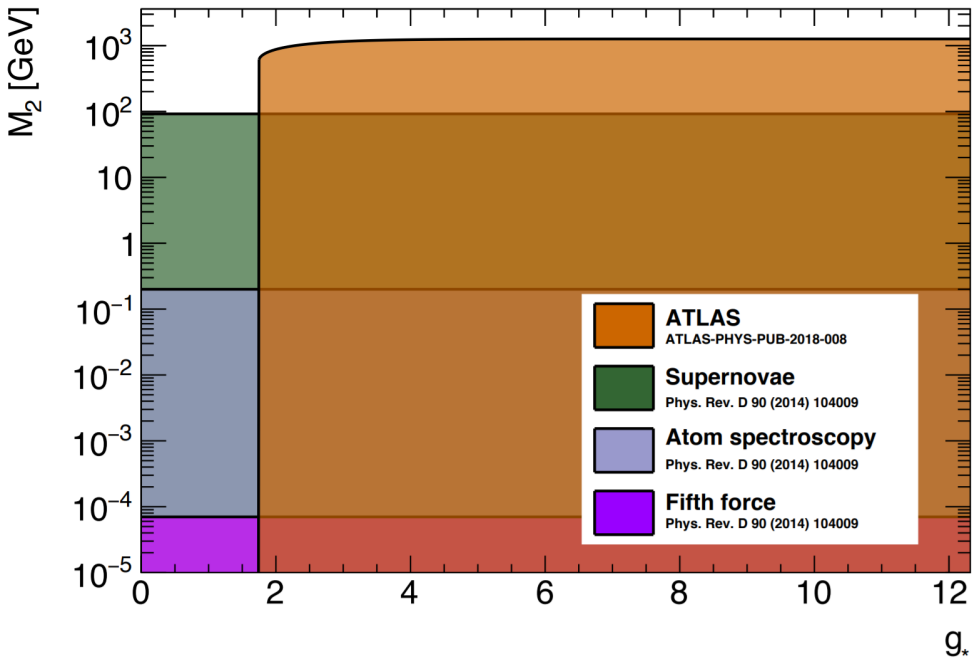

Figure 6.26: Exclusion plots from the monojet analysis for $\mathcal{L}_2$ on the g_*, M_2 plane, after rescaling to take into account the effective field theory validity criterion, compared to non-collider searches, with 2015+2016 data. The effect of including the full Run 2 data would be just to raise the flat top of the ATLAS results from 1260 GeV to 1558 GeV, with negligible effect on lowering the limit on g_*.

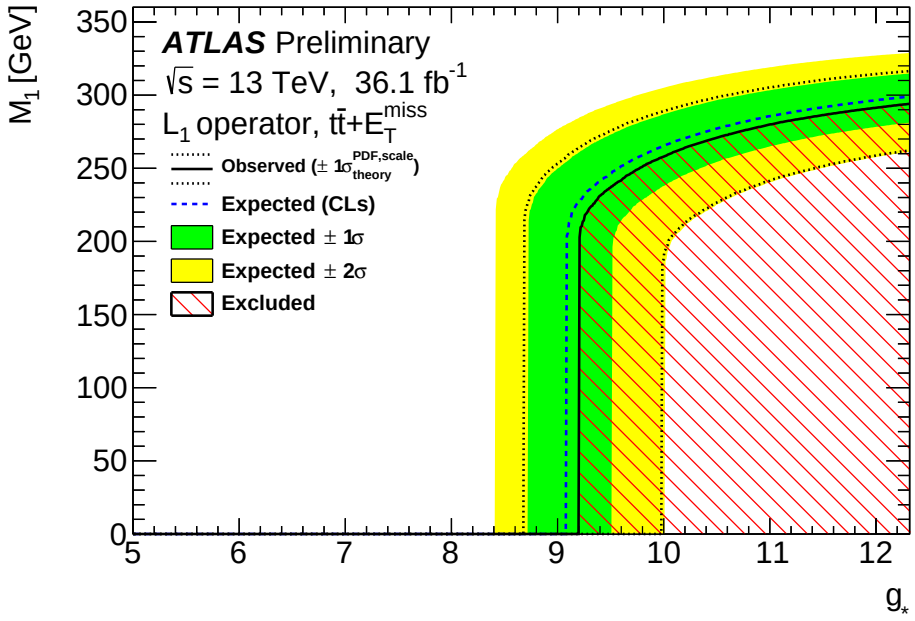

Figure 6.27: Exclusion plots from $t\bar{t}$ for $\mathcal{L}_1$ on the g_*, M plane, after rescaling to take into account the effective field theory validity criterion, with 2015+2016 data.

CHAPTER 7

MC40 Beam Monitoring Upgrade For Precise Fluence Delivery For Testing HL-LHC Components

As the components of the ATLAS inner tracker upgrade for HL-LHC will experience a high radiation dose of fluences up to 2x10^{16} MeV n_{eq}/cm^2 [110], particularly due to their proximity to the collision point, it is essential to test their radiation hardness before they are added to ATLAS. One of the parts of this process is irradiating components to high fluences in the MC40 cyclotron beamline at the University of Birmingham. The MC40 proton beamline can deliver doses in a uniform 10x10 mm^2 square beam, with a much lower current component extending 2 mm beyond the main beam region. The MC40 can deliver in minutes doses that these components will receive over their lifetime in the HL-LHC. The beam current can be adjusted from 0.1 to 1000 nA to precisely irradiate to various fluences (dose rate integrated over time), though at much lower energies than the LHC, up to a maximum kinetic energy of 36 MeV. The irradiation facility used for these studies uses protons with kinetic energy of 27 or 28 MeV. In addition, there is a low energy component of

the beam that is removed by placing a 300 μm aluminium sheet at the end of the beamline.

At the time of these studies in the MC40 beamline we irradiated at a temperature below the nominal operating temperature of $\approx -27\,^{\circ}\mathrm{C}$ to reduce annealing, changes to the material's structure due to thermal effects, in a box mounting system at the end of the beamline (Figure 7.1). The box's position can also be adjusted via a motor to allow irradiation of samples in the areas desired, the face of the box being 15 mm downstream of the vacuum window.

Figure 7.1: Setup at the MC40 Beamline, showing the coldbox (in white with an orange window) which can be moved via a motor mounted downstream of the proton beamline (which comes out of the silver coloured cylinder with a square hole). [111].

7.1 Fluence monitoring motivation

To determine the fluence to which samples have been exposed, a thin nickel foil is attached in front of the samples being irradiated, which becomes activated during the irradiation. The gamma spectrum of this nickel foil is then measured at the end of an irradiation, and the peak at 1337 keV can be used to measure the dose of protons/cm^2, which can then be used to calculate the total neutron equivalent dose to a precision of 10%. This is performed using a hyperpure germanium detector cooled by liquid nitrogen. A germanium detector is used for this purpose rather than silicon as the depletion region for germanium can be made to be of the order of cm, rather than mm as for silicon. As gamma ray photons are very penetrating this extra depth is required to ensure the entirety of the photon's energy is deposited within the detector.

However, the gamma spectrum can only be measured after the irradiation, not during, so another method is needed to ensure samples are irradiated up to the desired fluence. Currently to do this, a Faraday cup is placed in the beam before the samples are inserted to measure the dose rate. This works by the beam hitting the metal in the Faraday cup, charging the metal, which is then discharged to produce a current that can be converted into the number of protons colliding with the metal.

The Faraday cup cannot be used during irradiation to measure the fluence accurately as it is thick enough to stop the beam and hence cannot be placed in front of (upstream of) the samples. However if the samples are placed upstream of the Faraday cup, accurate measurement of fluences on the sample is not possible as the beam reaching the Faraday cup has been attenuated by the samples. This could be calibrated out if all samples were the same, however each sample irradiated is different and hence each would have to be calibrated individually.

On rare occasions the fluence predicted via this method and the measured fluence from the nickel foil have been found to differ by a significant amount. It was therefore

decided that a method that monitors the beam upstream of the sample was needed to allow a more precise fluence delivery.

7.2 Beam position monitoring motivation

It is important that the sensors receive a uniform radiation dose across their whole area. While this should be trivial with a uniform square beam, on occasion certain areas appear to receive more fluence than others. To prevent this currently rather than having the beam stationary with the sensor within it, the samples are scanned through the beam in a raster pattern. Hence any non-uniformities in the beam should be averaged out.

However, this averaging out assumes that the beam shape is constant over time. For a particular example, a time-dependent non-uniformity, where a small region of the beam was temporarily more intense than the rest of the beam, would leave a larger fluence delivered on the area of the sensor hit by the beam during this period.

It is therefore desired to be able to measure the beam shape and position of the beam at all times during the irradiation, to ensure the sensors receive a uniform dose across their surface.

7.3 Beam monitor upgrade

It was decided that a single system that could achieve both of these goals (removing any assumption of constant dose rate and real-time monitoring of the beam profile) is desired. To measure the beam-shape and dose rate during irradiation, the system must be in place at the time of the irradiation and be upstream of the samples (otherwise the samples will obstruct the beam). At the time of design the system had to satisfy the following constraints.

1. The radiation length must be equivalent to $\lessapprox$ 300 μm aluminium. This is because a 300 μm aluminium sheet is currently used to remove the low energy component of the beam, so if this system has a radiation length less than this, the aluminium sheet thickness can simply be reduced and the beam hitting the samples should be unchanged.

2. The area in the beam should be uniform or the thickness should be negligible, to prevent introducing non-uniformities into the beam.

3. The system must be $<$ 15 mm in depth due to the proximity of the box to the beamline.

4. The active area of the sensor must be $\geq$ 10x10 mm^2 as this is the size of the beam.

5. The sensor must have a linear response up to at least 400 nA, as while the beam can reach up to 1000 nA, it is uncommon for a current above 400 nA to be used.

7.3.1 Pixel monitor

To ensure the beam remains uniform, strip sensors were first investigated as, due to the uniform nature of strip sensors, they would prevent introducing non-uniformities into the beam. However, via simulations it was found the resolution of a strip sensor setup was too low. Hence, a pixel monitor was investigated instead as a pixel monitor can be made to a high resolution via a high pixel density. Unlike strip sensors, a pixel array is not uniform due to the gaps in between pixels. However, if the pixels can be made with sufficiently thin material, the non-uniformity introduced to the beam will be negligible.

A sheet of 50x50 mm^2, 12.5 μm thick copper was placed in front of the MC40 beamline, as a proof of concept of a single copper pixel, connected to an ammeter. As the beam passes through the copper, some protons collide with atoms ionising

them, with enough energy for the electrons to travel a significant distance from their parent atom. This then produces a current that is measured by the ammeter. In addition, this current is amplified by secondary electron emission which occurs when the ionised electrons have enough energy themselves to ionise more atoms. This is primarily a surface effect, as electrons emitted in the bulk will lose energy and likely be re-absorbed before reaching the ammeter, hence a thin material should be ideal for detecting this effect.

This copper sheet was irradiated in 5 runs that scanned across beam currents measured in the Faraday cup in steps of 50 nA, and the current in the copper sheet was measured. Each run had a short $\approx$ 10 minute break before the next run. These runs were:

- Run 1 and 2 were performed sequentially up in Faraday cup current from 150 nA to 400 nA,
- Run 3 and 4 were performed sequentially down in Faraday cup current from 400 nA to 50 nA,
- Run 5 was performed sequentially up in Faraday cup current from 50 nA to 400 nA, with a 5 minute break with no incident beam current between each measurement.

The reason for these different runs was to ensure the response of the copper was not affected by previous measurements/beam incident upon it. The result of this is shown in Figure 7.2 which demonstrates a linear response up to at least 400 nA, as required, showing promise that a pixel array can be made out of this material, that will introduce a negligible non-uniformity into the beamline.

A prototype 10x10 mm^2, 7x7 pixel sensor made of thicker ($\approx$ 200 μm) copper pads was obtained from colleagues in Liverpool, as shown in Figure 7.3. As the current is produced via a surface effect, the current produced via a thicker sheet should be approximately the same as the bulk only negligibly contributes. A 50 channel

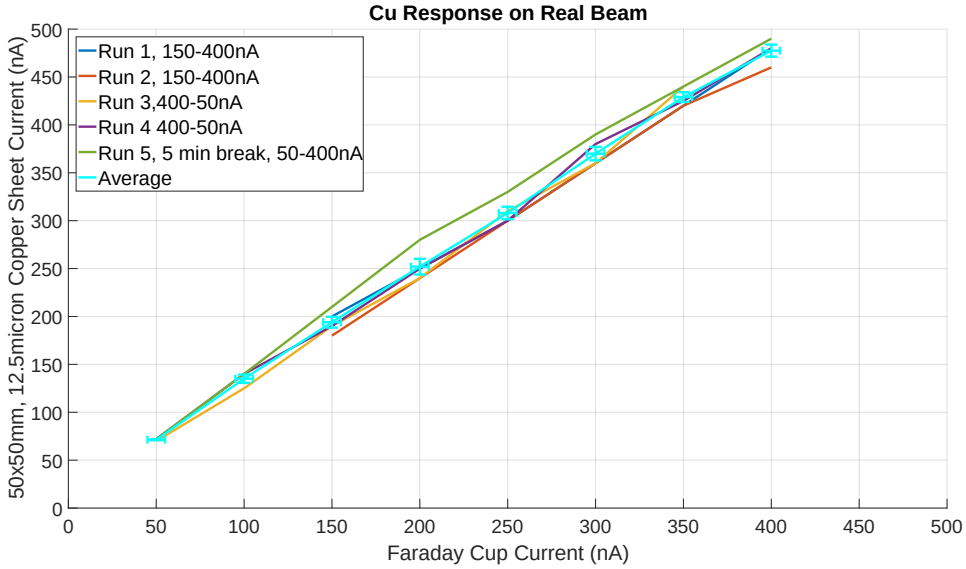

Figure 7.2: Current measured across a copper sheet placed in the MC40 proton beam at various beam currents, showing a linear response.

integrator board was also obtained, as shown in Figure 7.4, which is used to readout each copper pad similar to how the single large copper sheet is read out with an ammeter.

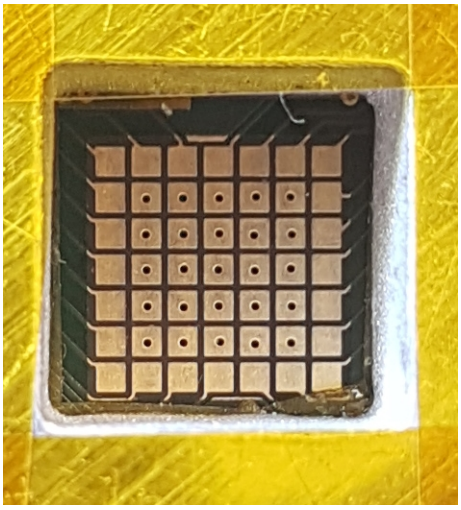

Figure 7.3: Pixel sensor attached to collimator.

This integrator board measures the charge collected on each pixel, which is then read out via a custom program on an Arduino board (a board with a microcontroller), which pipes the data to a desktop PC.

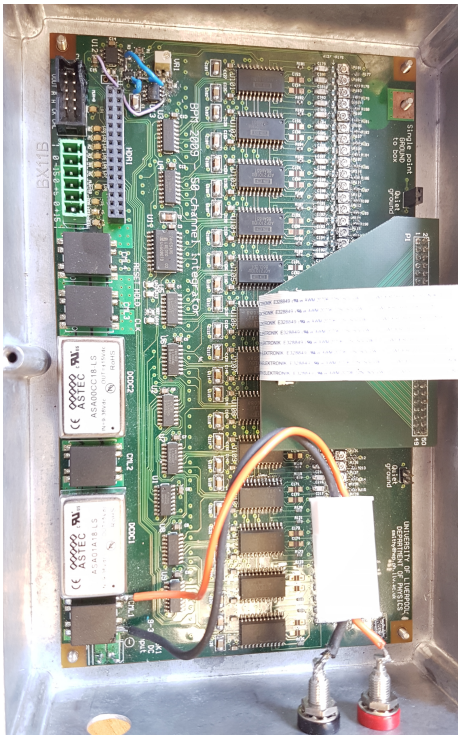

Figure 7.4: Integrator board to readout sensor.

7.3.1.1 Realtime readout

A real-time monitor was developed, so that operators can continuously monitor the cyclotron beam incident on samples. Before the beam is incident upon the sensor, the monitor takes a background reading which is subtracted from subsequent measurements.

This monitor is shown in Figure 7.5 for a simulated circular beam. As can be seen, the shape of the beam is visible in real-time as well as the beam current. A warning is emitted if this strays outside of a range which the cyclotron operator can specify.

In addition to this, graphs display various beam properties over time, either as instantaneous or as a rolling average. These graphs show:

- Beam centre position
- Beam current

- Derivative of beam current
- Integral of beam current (fluence/charge)

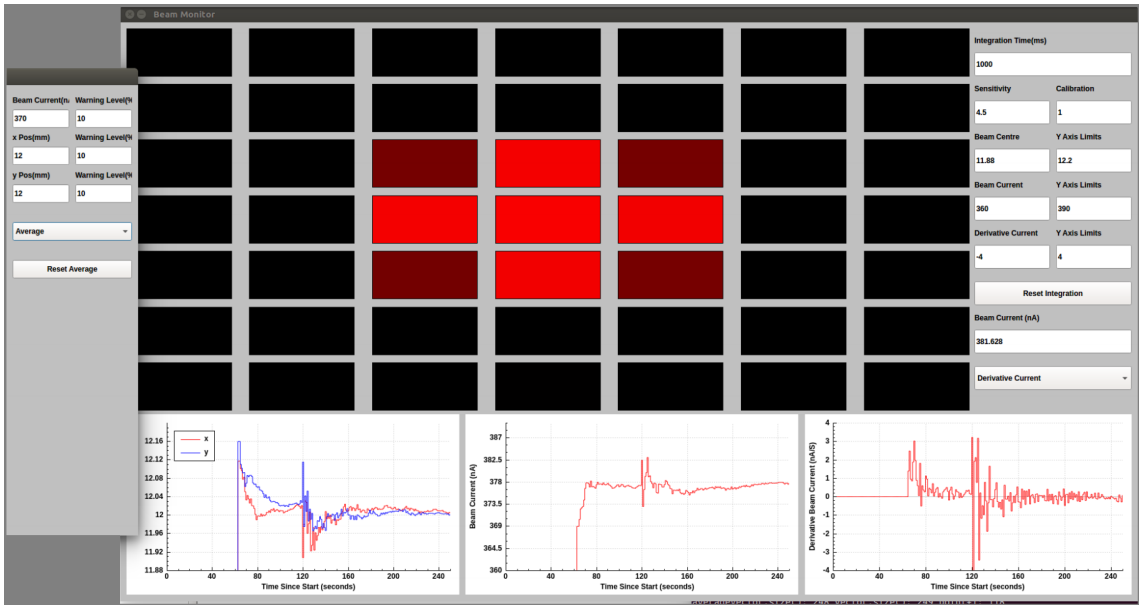

Figure 7.5: Beam monitor realtime display for simulated circular beam on a 7x7 pixel sensor; showing the position of the beam upon the sensor, as well as plots, from left to right, measuring the position of the centre of the beam (via an average weighted by current), total beam current and derivative of beam current.

7.3.1.2 Testing

Some preliminary tests were run on the MC40 beam. The sensor was also purposefully misaligned with the beam, to test whether the visual monitor would be able to notice this in real-time.

Firstly, a run was performed with a nominally high current, then a short period where the beam was turned off from about 580 s to 750 s, followed by a nominally low current, then another short period where the beam was off from about 1600 s to 1750 s, followed by a nominally high current, Figure 7.6. From this, two effects were immediately obvious, which show why the assumption currently made of the beam being a constant current over time sometimes gives slightly inaccurate fluence predictions.

Firstly, there are many short periods of time where the beam current drops to zero, due to radiofrequency cavity drops in the cyclotron. This will result in the average dose rate being lower than any instantaneously measured dose rate. Secondly, it can be seen that the current drifts over time.

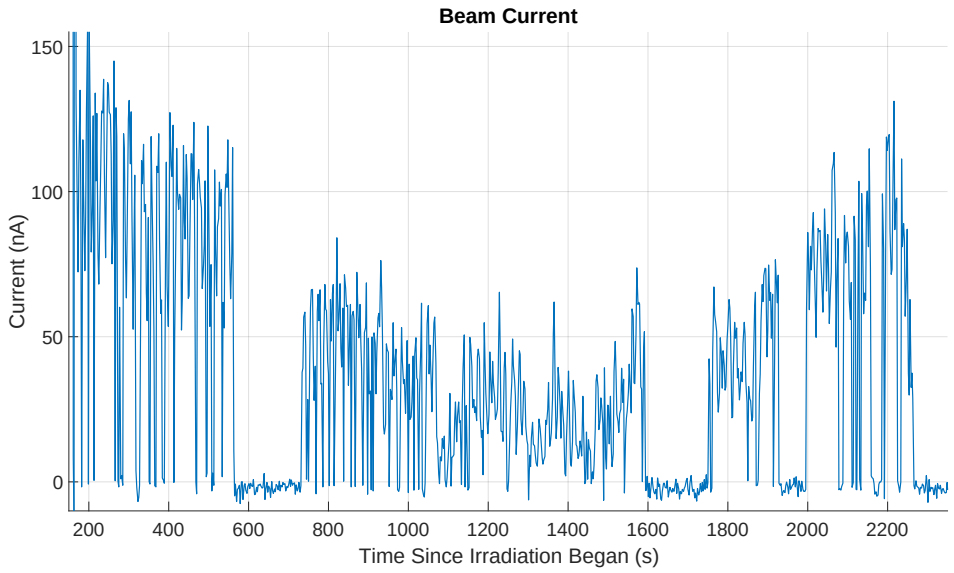

Figure 7.6: Beam current measured via copper pixel sensor over long run.

Another preliminary test with the MC40 beam was then performed with this setup on a nominally low and high current.

The integrated current for these two runs is shown in Figure 7.7. It can be seen that the sensor manages to determine accurately which of the two currents is higher, however it can also be seen in the low current case, that at $\approx$ 80 s the gradient increases. This indicates that the instantaneous current has increased.

At the end of the test it was observed that the sensor that was aligned with the beam had burnt slightly, which appears to be only aesthetic damage though more testing needs to be performed to determine the long-term properties of the sensor. However, this gives a very clear way of determining whether or not the real-time pixel monitor managed to show the beam shape incident upon it accurately. The burnt sensor is shown in Figure 7.8 and the pixel monitor with the burnt pixels outlined in green in Figure 7.9. Qualitatively it is clear that the pixel monitor

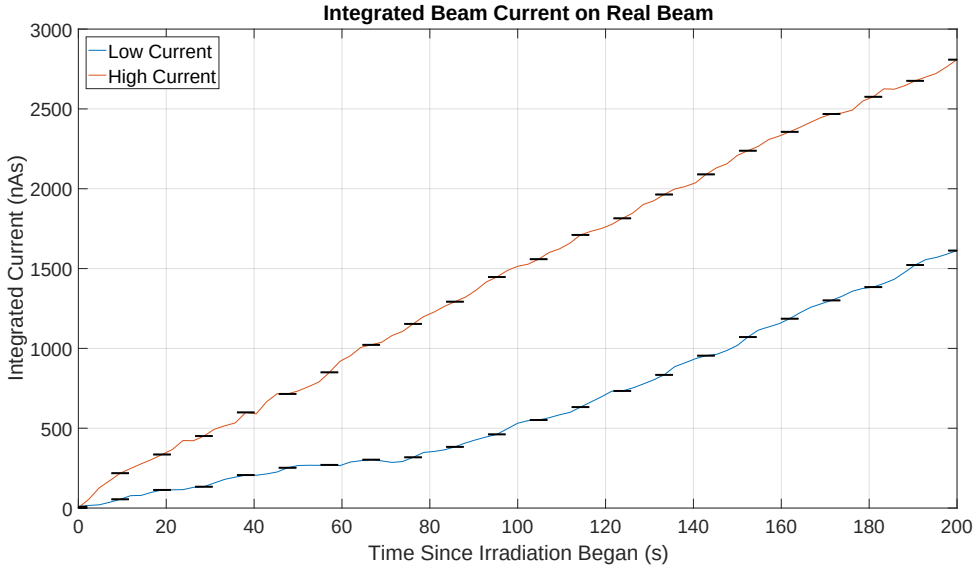

Figure 7.7: Measured integrated current.

managed to accurately display the position of the beam. Due to the beam having a lower current component that extends out from the centre of the beam, the pixel sensor also measures a smaller current nearby where there are no burn marks.

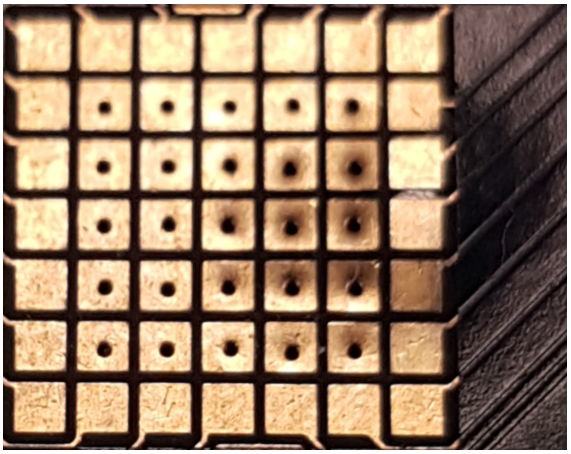

Figure 7.8: Copper pixel sensor burn marks due to the MC40 proton beam.

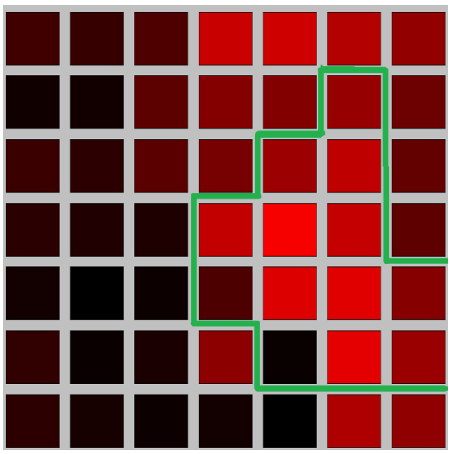

Figure 7.9: Copper pixel sensor monitor with burnt pixels outlined.

7.3.2 Ionisation chamber

A problem with the pixel sensor, however, is that there are small inactive regions in the gaps between the pixels. If a non-uniformity in the beam arose that made a portion of the beam more or less intense in just one of these inactive regions, this monitor would have no way of detecting it. Hence a parallel plate ionisation chamber, made of 2 copper sheets separated by 2 mm, and a copper guard ring, which has no position monitoring but can measure the full fluence of the beam, has been designed to be used in conjunction with the pixel sensor, as shown in Figure 7.10 and Figure 7.11. As the beam passes through the ionisation chamber, it will ionise the air within it. There is a thin sheet of copper at the top and bottom of the ionisation chamber, with a voltage across them, acting as a cathode and anode, hence producing an electric field between them. Electrons drift towards the anodes and ions towards the cathode of the ionisation chamber, thus inducing an electric current, which is measured using an arduino board from the potential drop across a resistor of known resistance. A diagram of the setup is shown in Figure 7.12. The final ionisation chamber has been adjusted slightly to have the copper ring surrounding the cathode with a layer of insulation between them, rather than being in a separate layer from it.

A copper ring kept at the same potential as the cathode is also used to help shape the electric field lines, ensuring they remain straight, and to reduce leakage current. This is required because the ionisation chamber will have to measure very small currents, such that current from outside the ionisation chamber that leaks through even a good insulator will contribute significant noise. With the guard ring, the charge from the leakage current will be collected upon it and then, as it is at the same potential as the cathode, there is no driving potential to induce charge leakage to the copper sheet.

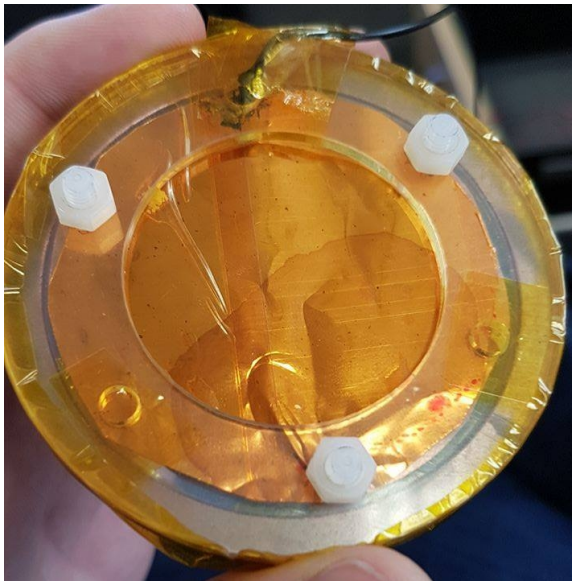

Figure 7.10: Ionisation chamber top down.

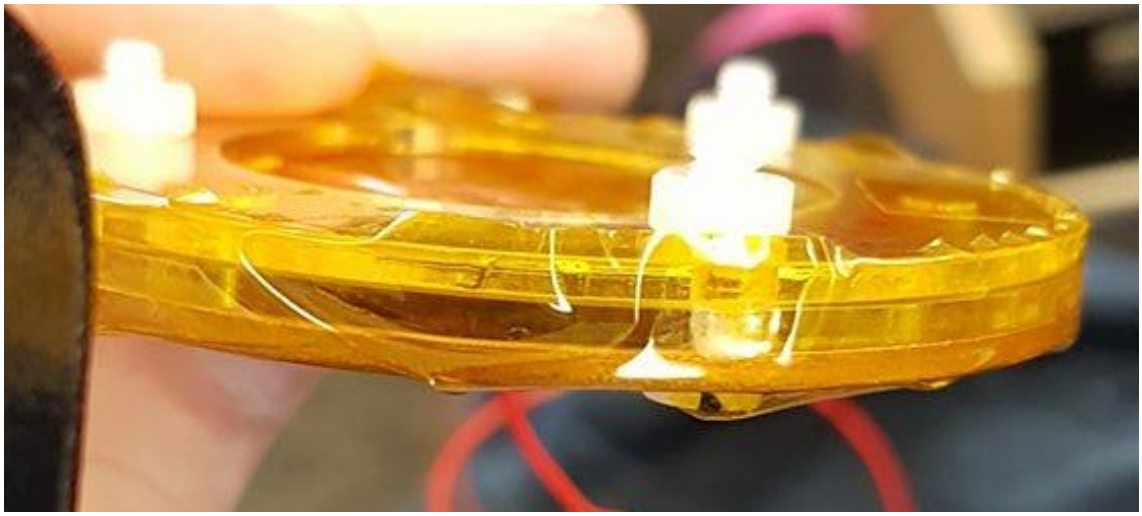

Figure 7.11: Ionisation chamber side on.

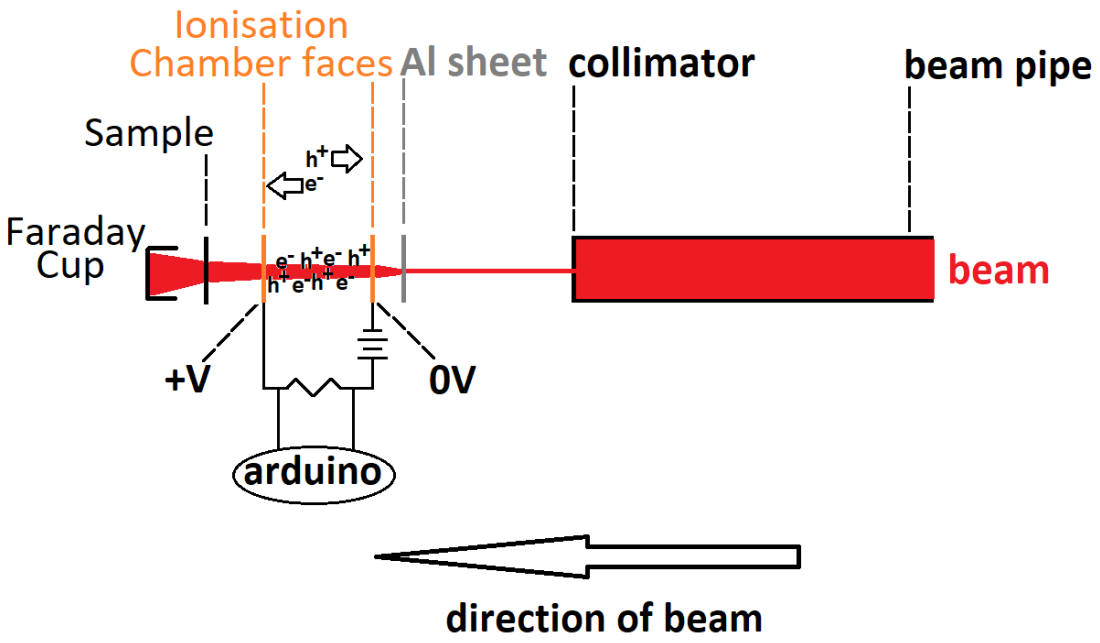

Figure 7.12: Diagram showing ionisation chamber setup in the MC40 beam room. The beam travels from right to left, passing through a collimator to reduce the beamsize to a uniform square. The beam then passes through an aluminium sheet that removes a low energy component of the beam, and introduces a (negligible) divergence to the beam. The beam then passes through the front face of the ionisation chamber, and within the ionisation chamber ionises the air producing electrons (e^-) and ions (h^+) which travel in opposite directions thanks to a voltage across the ionisation chamber, causing a current to flow. The current is read out by an arduino board measuring a potential difference over a resistor in series with the ionisation chamber. The beam then passes through the sample, which diverges and absorbs the beam by a non-negligible amount, and finally passes into a Faraday cup.

7.3.2.1 Testing on strontium-90 source

Before testing on beam, the ionisation chamber was tested with a strontium-90 β source to determine whether a signal was measurable. From this it is clear that the strontium-90 source can be distinguished from background at all voltages across the plates from 0 to 1000 V, and the current rises more rapidly as voltage is increased when the strontium-90 source is applied. The results with no source, source and with no source subtracted from source are shown in Figure 7.13.

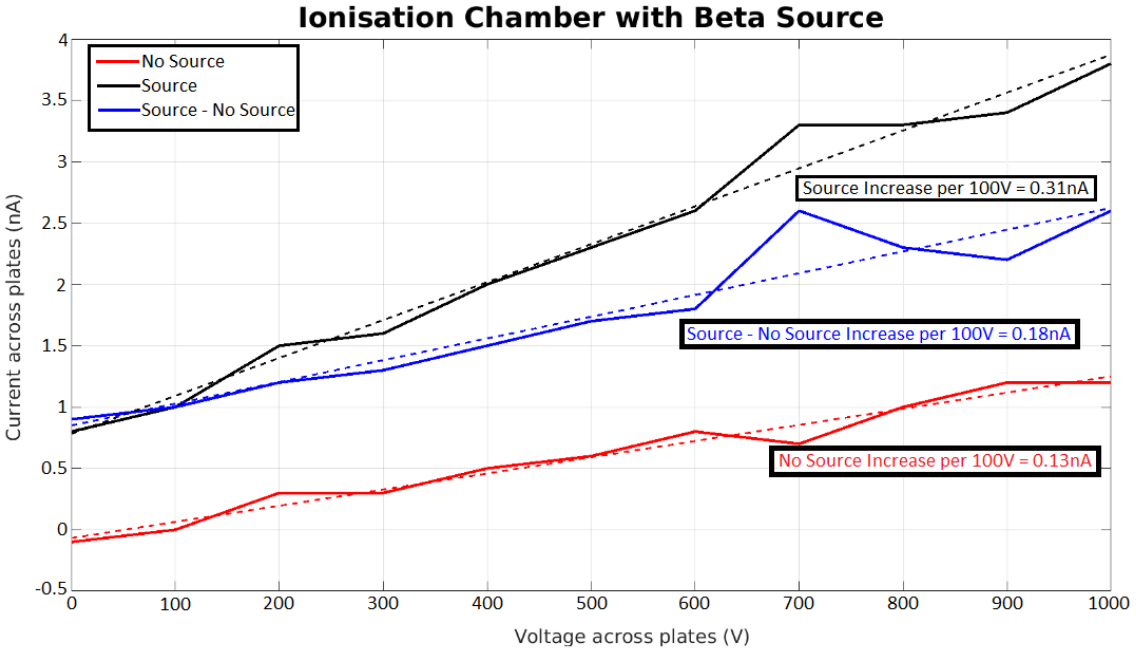

Figure 7.13: Ionisation chamber test with strontium-90.

7.3.2.2 Testing on MC40 28 MeV proton beam

A typical proton energy at the MC40 cyclotron is 28 MeV. In air a proton of this energy has a stopping power of $\frac{dE}{dx} = 1.773$ MeVm^{2}kg^{-1} [112].

For air at 20 °C $\rho = 1.2047$ kgm^{-3} [113], hence a 28 MeV proton will deposit 2.1360 MeVm^{-1} into the air. E = 33.97 eV is required to produce an electron/ion pair in air [114]. Hence $\approx$ 63 electron/ion pairs are produced per mm. Therefore for every nA of beam current, with the 2 mm gap between the plates we expect to see 126 nA across the ionisation chamber.

The ionisation chamber was tested on the beam by comparing against a Faraday cup that is already used at the MC40 to measure the beam current; the results are shown in Figure 7.14. It can be seen that the measured current is much below what was predicted. Although this is the case, there is still a clear increase in measured current as the beam current increases, with a higher gradient the larger the voltage across the plates.

It appears that the higher voltages are linear over a shorter range, however normalizing the curves such that at each voltage the maximum measured current is one is shown in Figure 7.15. From this it is clear the shape is the same for the different voltages but appears less linear due to the larger values at high voltages. This indicates what was already known to be the case, which is that at low beam currents the Faraday cup is non-linear. Hence the nonlinearity in these plots appears to be due to the ionisation chamber outperforming the current beam fluence measuring system at low currents.

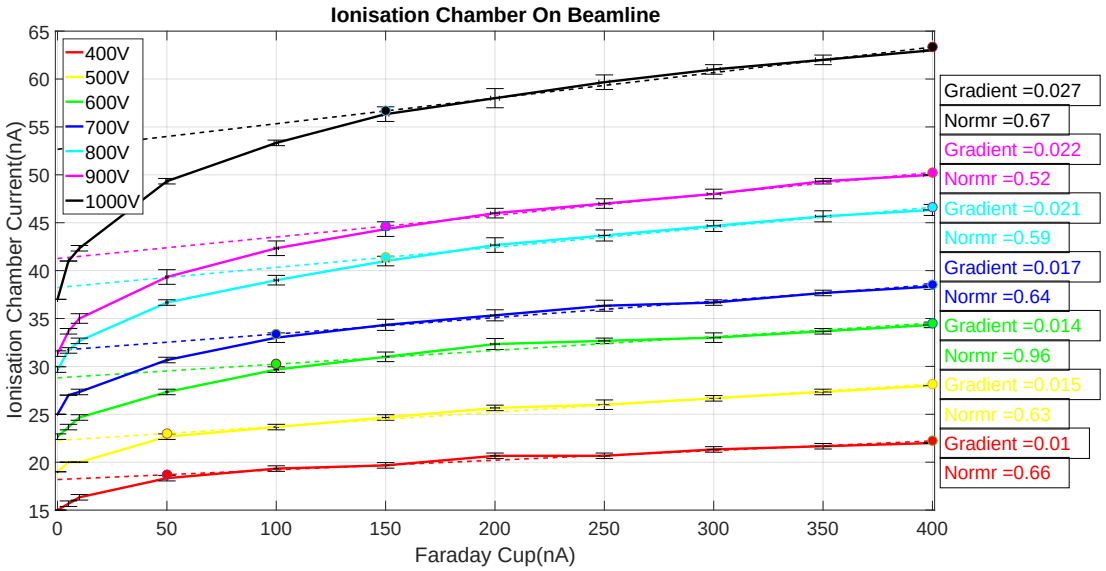

Figure 7.14: Ionisation chamber test on 28 MeV proton beam, showing that the current measured in the ionisation chamber increases as beam current increases, and increases more rapidly as the voltage across the ionisation chamber is increased, as expected.

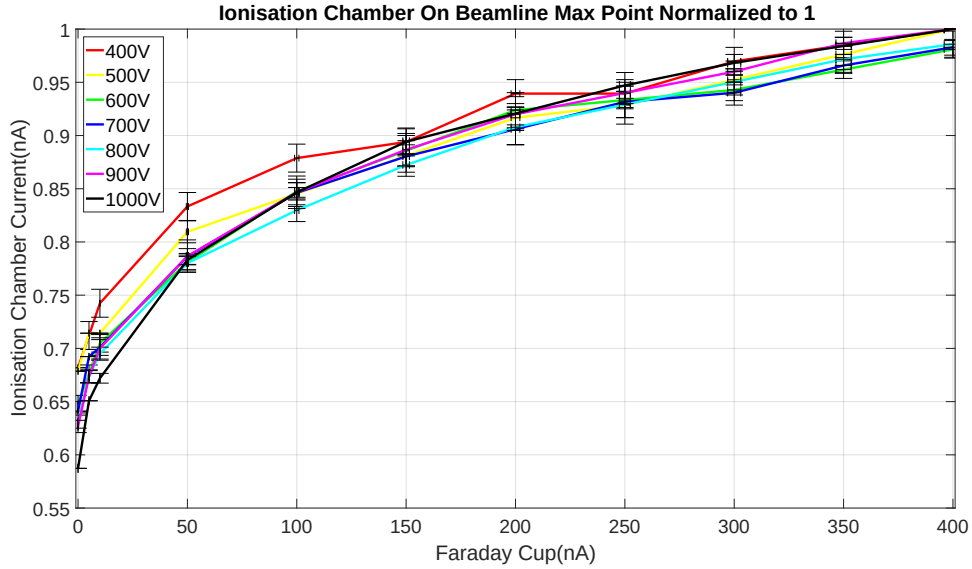

Figure 7.15: Ionisation chamber test on 28 MeV proton beam normalized, showing that the shape of the current measured in the ionisation chamber versus current measured in the Faraday cup is constant regardless of voltage across the ionisation chamber.

Due to the unexpectedly low current measured, the electrical connections of the ionisation chamber were re-soldered in case the current was low due to a poor connection. A preliminary measurement indicates that this has fixed the issue. A beam current of 420 nA was measured on the Faraday cup while 50 μA were measured on the ionisation chamber, 95% of the prediction of 53 μA.

7.3.2.3 Testing on MC40 28 MeV proton beam Vs nickel foil

To determine whether the nonlinearity measured in Figure 7.14 is in fact due to nonlinearities in the Faraday cup, the total fluence was measured for different beam currents deposited on nickel foils attached to the ionisation chamber measured via gamma spectroscopy as mentioned in Subsection 7.1. This total fluence can then be converted into an average beam current as the duration of irradiation and the beam area are known.

The average current is also measured across the ionisation chamber, which is con-

verted into a measurement of the beam current via the 126 scaling factor derived in Section 7.3.2.2.

The beam current measured via the ionisation chamber is plotted against the beam current measured via the nickel foil in Figure 7.16. A linear fit is performed for this comparison, as well as a band of uncertainty assuming a 1.8 mm and 2.2 mm gap due to imprecision in the machining of the ionisation chamber.

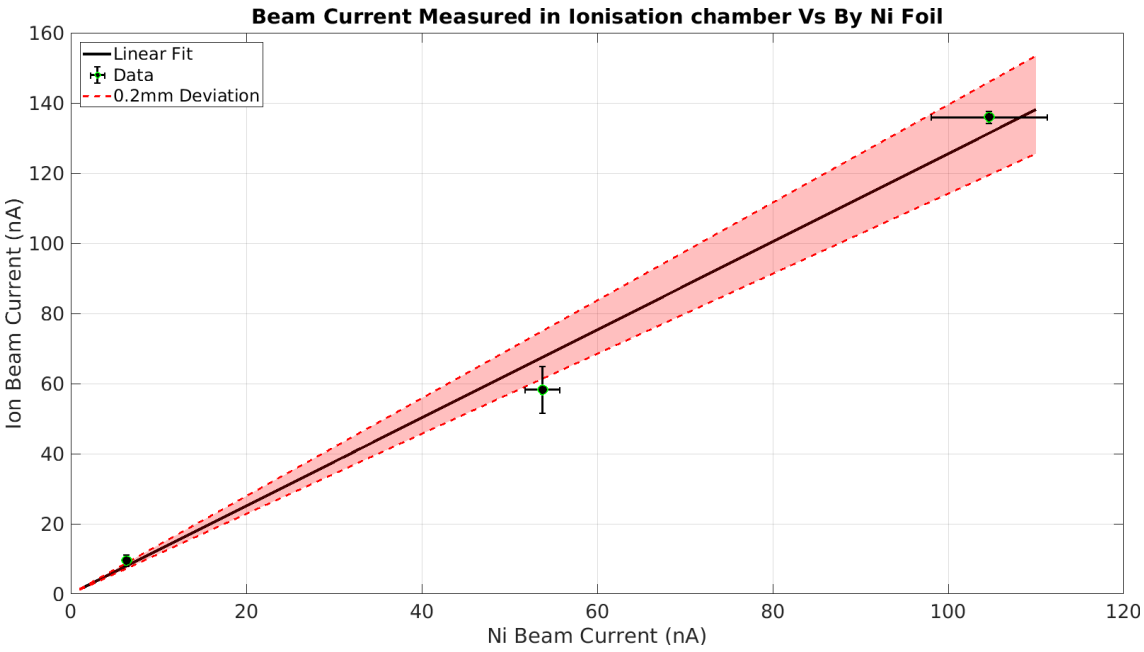

Figure 7.16: Beam current measured via ionisation chamber vs via nickel foil, including a 0.2 mm deviation in the ionisation chamber gap width.

From this it can be seen that at low currents a linear fit correctly describes the data, showing that the nonlinearity is due to the Faraday cup and not the ionisation chamber. This demonstrates that the ionisation chamber can measure fluence more precisely at low currents than the present beam monitoring system.

However, further measurements were performed up to 400 nA and it was found that the response was not linear over the whole range. This was originally believed to be due to the air volume within the ionisation chamber being too small, saturating the device. However, further study by others demonstrated that this is due to the electron-ion recombination; as the beam current increases enough electron-ion

pairs are produced that over the length of the ionisation chamber a non-negligible proportion recombine, hence a much smaller ionisation chamber would need to be produced to be linear up to 400 nA [115].

7.4 Beam monitoring outlook

A system that can accurately measure the beam position in real-time was developed. While a system that can measure the beam current upstream of samples up to 400 nA has not been produced, the necessity for this has been demonstrated with an initial prototype. It has been shown that the reason for differences between expected dose and measured dose with nickel foil that is sometimes apparent is due to instabilities in the beam, mainly drifts in beam current and radiofrequency cavity drops. Hence, it is essential to continue this work and develop a finalised system that can measure the beam current upstream of samples up to 400 nA, and this work is ongoing.

In addition, software and hardware for readout has been developed, which can be easily modified to be used with future monitoring systems.

CHAPTER 8

Conclusion

The monojet analysis reach has been improved, in particular now having much higher sensitivity to soft signals due to lowering of $P_{\mathrm{T}}^{\mathrm{recoil}}$ and leading jet p_{T} thresholds. For some soft signals investigated, the gain in sensitivity on the cross-section from this is as much as 25%. With the monojet analysis now moving into the precision regime, with a background uncertainty as low as the percent level, improvements to the range of signals that can be searched for by the monojet analysis helps the field as a whole to investigate as much of the beyond the Standard Model landscape as possible.

Many models have been probed, in particular the first ever collider-based probe of a dark energy model has been performed, the monojet analysis setting an observed(expected) limit on the mass scale of $M_2 \geq 1558(1591)$ GeV at the 95% confidence level for the disformal coupling of this model at high couplings, an order of magnitude higher than any non-collider based experiments and an improvement of 400(300) GeV over using only the 2015+2016 data. This shows the ability of colliders

to contribute well to this field, and hopefully paves the way for more collider-based probes of dark energy.

In addition, thanks to the improved sensitivity to soft signals, a strong limit on a pseudoscalar WIMP candidate has been set at $m_{Z_P} \geq 368(404)$ GeV for dark matter particle mass candidates of $m_\chi = 1$ GeV, the first time the monojet analysis is sensitive to this channel. The axial-vector WIMP candidate limit has been improved by about 500(400) GeV to $m_{Z_A} \geq 2060(2175)$ GeV for dark matter particle mass candidates of $m_\chi = 1$ GeV.

The LHC will be shortly upgraded to the HL-LHC, which will further increase the reach of the monojet analysis (and most other analyses). Shown in Figure 8.1 are approximate predictions of the 3σ and 5σ discovery contours that will be set by the monojet analysis on the axial-vector WIMP model with 3000 fb^{-1} of pp collision data (approximately the amount of data HL-LHC will deliver over its lifetime) at $\sqrt{s} = 13$ TeV. HL-LHC is planned to run at $\sqrt{s} = 14$ TeV, which will lead to a further small increase in the limits set for this model.

Towards achieving this improvement in the reach of analyses, preliminary results of development of a realtime beam monitor for the University of Birmingham MC40 cyclotron have been presented, for eventual use in delivering precise fluence to components destined for the inner detector of ATLAS, allowing precise radiation hardness studies to be performed to ensure they can survive the harsh conditions that will be involved in the HL-LHC.

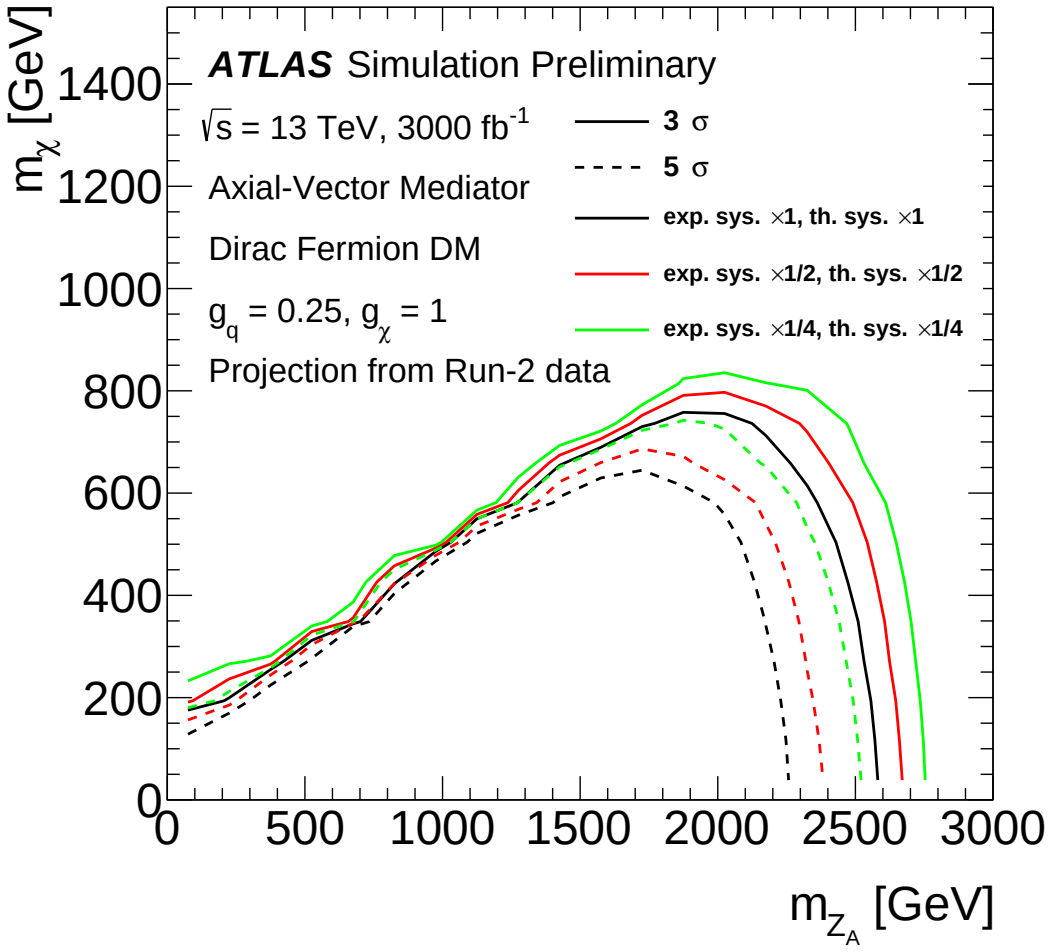

Figure 8.1: Expected 3σ (solid) and 5σ (dashed) discovery contours on the ($m(\chi, Z_A)$) mass plane for the axial-vector model, for a luminosity of 3000 fb^{-1}. Three contours are shown, corresponding to the three different systematic uncertainty scenarios, in comparison to the previous monojet analysis systematics [76]: standard (black), reduced by a factor 2 (red) and 4 (green) [116]. The current monojet limits for this model were shown in Figure 6.16

REFERENCES

[1] V. Trimble, "Existence and nature of dark matter in the universe," *Annual Review of Astronomy and Astrophysics*, 1987. https://www.annualreviews.org/doi/10.1146/annurev.aa.25.090187.002233.

[2] G. Bertone, D. Hooper and J. Silk, "Particle dark matter: evidence, candidates and constraints," *Physics Reports*, 2005. https://www.sciencedirect.com/science/article/abs/pii/S0370157304003515?via%3Dihub arXiv: hep-ph/0404175 [hep-ph].

[3] J. L. Feng, "Dark matter candidates from particle physics and methods of detection," *Annual Review of Astronomy and Astrophysics*, vol. 48, 2010. https://www.annualreviews.org/doi/10.1146/annurev-astro-082708-101659.

[4] D. Clowe et al., "A direct empirical proof of the existence of dark matter," *The Astrophysical Journal Letters*, vol. 648, 2006. https://iopscience.iop.org/article/10.1086/508162.

[5] A. G. Riess et al., "Observational evidence from supernovae for an accelerating universe and a cosmological constant," *The Astronomical Journal*, vol. 116, 1998. https://iopscience.iop.org/article/10.1086/300499.

[6] S. Perlmutter et al., "Measurements of omega and lambda from 42 high-redshift supernovae," *The Astrophysical Journal*, vol. 517, 1999. https://iopscience.iop.org/article/10.1086/307221.

[7] Planck Collaboration, "Planck 2015 results," *Astronomy & Astrophysics*, vol. 594, 2016. https://www.aanda.org/articles/aa/abs/2016/10/aa25830-15/aa25830-15.html.

[8] S. Alam et al., "The eleventh and twelfth data releases of the sloan digital sky survey: final data from sdss-iii," *The Astrophysical Journal Supplement Series*, vol. 219, 2015. https://iopscience.iop.org/article/10.1088/0067-0049/219/1/12.

[9] J. Lindon on behalf of the ATLAS Collaboration, "Searches for dark matter and dark energy produced in association with a jet with the ATLAS detector," *Proceedings of Science*, vol. 159, 2019. https://doi.org/10.22323/1.367.0159.

[10] ATLAS Collaboration, "Search for new phenomena in events with jets and missing transverse momentum in p p collisions at $\sqrt{s} = 13$ TeV with the ATLAS detector," *ICHEP2020*, 2020. http://cdsweb.cern.ch/record/2728058.

[11] D. Hanneke, S. Fogwell Hoogerheide, and G. Gabrielse, "Cavity control of a single-electron quantum cyclotron: Measuring the electron magnetic moment," *Physical Review A*, vol. 83, 2011. https://journals.aps.org/pra/abstract/10.1103/PhysRevA.83.052122.

[12] ATLAS Collaboration, "Observation of a new particle in the search for the Standard Model Higgs boson with the ATLAS detector at the LHC," *Physics Letters B*, vol. 716, 2012. https://www.sciencedirect.com/science/article/pii/S037026931200857X.

[13] S. Chatrchyan et al, "Observation of a new boson at a mass of 125 GeV with the CMS experiment at the LHC," *Physics Letters B*, vol. 716, 2012. https://www.sciencedirect.com/science/article/pii/S0370269312008581?via%3Dihub#!

[14] J. Baez, "Renormalizability," *UC Riverside Department of Mathematics*, 2006. http://math.ucr.edu/home/baez/renormalizability.html.

[15] V. Kaplunovsky, "QFT Dimensional Analysis," 2015. http://bolvan.ph.utexas.edu/~vadim/Classes/2015f/diman.pdf.

[16] MissMJ (wikimedia pseudoname), "Standard Model of Elementary Particles," *wikimedia*, 2020. https://commons.wikimedia.org/wiki/File:Standard_Model_of_Elementary_Particles.svg.

[17] S. Höche, "Introduction to parton-shower event generators," *arXiv*, 2014. https://arxiv.org/abs/1411.4085.

[18] D. Abercrombie *et al.*, "Dark Matter Benchmark Models for Early LHC Run-2 Searches: Report of the ATLAS/CMS Dark Matter Forum," 2015.

[19] G. Busoni *et al.*, "Recommendations on presenting LHC searches for missing transverse energy signals using simplified *s*-channel models of dark matter," 2016.

[20] M. Papucci, A. Vichi, and K. M. Zurek, "Monojet versus the rest of the world I: t-channel models," *JHEP*, vol. 11, p. 024, 2014.

[21] ATLAS Collaboration, "Search for scalar dark energy in $t\bar{t}+E_T^{\text{miss}}$ and mono-jet final states with the ATLAS detector," Tech. Rep. ATL-PHYS-PUB-2018-008, CERN, Geneva, Jun 2018. https://cds.cern.ch/record/2627837.

[22] P. A. R. Ade *et al.*, "Planck 2015 results. XIII. Cosmological parameters," *Astron. Astrophys.*, vol. 594, p. A13, 2016.

[23] D. H. Weinberg, M. J. Mortonson, D. J. Eisenstein, C. Hirata, A. G. Riess, and E. Rozo, "Observational Probes of Cosmic Acceleration," *Phys. Rept.*, vol. 530, pp. 87–255, 2013.

[24] D. Weinberg, D. Bard, K. Dawson, O. Dore, J. Frieman, K. Gebhardt, M. Levi, and J. Rhodes, "Facilities for Dark Energy Investigations," 2013.

[25] A. Joyce, L. Lombriser, and F. Schmidt, "Dark Energy Versus Modified Gravity," *Ann. Rev. Nucl. Part. Sci.*, vol. 66, pp. 95–122, 2016.

[26] T. Clifton, P. G. Ferreira, A. Padilla, and C. Skordis, "Modified Gravity and Cosmology," *Phys. Rept.*, vol. 513, pp. 1–189, 2012.

[27] M. Kunz and D. Sapone, "Dark Energy versus Modified Gravity," *Phys. Rev. Lett.*, vol. 98, p. 121301, 2007.

[28] M. Kunz, "The dark degeneracy: On the number and nature of dark components," *Phys. Rev.*, vol. D80, p. 123001, 2009.

[29] P. Brax, C. Burrage, C. Englert, and M. Spannowsky, "LHC Signatures Of Scalar Dark Energy," *Phys. Rev.*, vol. D94, no. 8, p. 084054, 2016.

[30] G. W. Horndeski, "Second-order scalar-tensor field equations in a four-dimensional space," *Int. J. Theor. Phys.*, vol. 10, pp. 363–384, 1974.

[31] P. Brax, "What makes the Universe accelerate? A review on what dark energy could be and how to test it," *Reports on Progress in Physics*, vol. 81, 2017. https://iopscience.iop.org/article/10.1088/1361-6633/aa8e64.

[32] Giorgio Busoni, Andrea De Simone, Enrico Morgante, Antonio Riotto, "On the Validity of the Effective Field Theory for Dark Matter Searches at the LHC," *Physics Letters B*, vol. 728, 2014. https://doi.org/10.1016/j.physletb.2013.11.069.

[33] ATLAS/CMS Dark Matter Forum, "Dark Matter benchmark models for early LHC Run-2 Searches: Report of the ATLAS/CMS Dark Matter Forum," *Physics of the Dark Universe*, vol. 27, 2020. doi.org/10.1016/j.dark.2019.100371.

[34] ATLAS Collaboration, "Constraints on mediator-based dark matter and scalar dark energy models using $\sqrt{s} = 13$ TeV pp collision data collected by the ATLAS detector.," *Journal of High Energy Physics*, vol. 142, 2019. https://link.springer.com/article/10.1007/JHEP05(2019)142.

[35] J. Alwall et al, "The automated computation of tree-level and next-to-leading order differential cross sections, and their matching to parton shower simulations," *Journal of High Energy Physics*, vol. 79, 2014. https://doi.org/10.1007/JHEP07(2014)079.

[36] E. Bothmann et al, "Event Generation with Sherpa 2.2," *SciPost Phys.*, vol. 7, 2019. https://doi.org/10.21468/SciPostPhys.7.3.034.

[37] T. Sjöstrand, S. Mrenna and P. Skands, "A Brief Introduction to PYTHIA 8.1," *Comput. Phys. Comm.*, vol. 178, 2008. https://doig.org/10.1016/j.cpc.2008.01.036.

[38] C. Oleari, "The POWHEG-BOX," *Nucl.Phys.Proc.Suppl.*, vol. 205, 2010. https://doig.org/10.1016/j.nuclphysbps.2010.08.016.

[39] S.Agostinelli et al, "GEANT4 — a simulation toolkit," *Nucl. Instr. Methods Phys. Res. A*, vol. 506, 2003. https://www.sciencedirect.com/science/article/pii/S0168900203013688.

[40] ATLAS Collaboration, "The ATLAS Simulation Infrastructure," *The European Physical Journal C*, vol. 70, 2010. https://link.springer.com/article/10.1140%2Fepjc%2Fs10052-010-1429-9.

[41] L. Evans and P. Bryant, "LHC Machine," *Journal of Instrumentation*, 2008. https://iopscience.iop.org/article/10.1088/1748-0221/3/08/S08001/pdf.

[42] STFC, "CERN Accelerator Complex," , 2016. https://stfc.ukri.org/research/particle-physics-and-particle-astrophysics/large-hadron-collider/cern-accelerator-complex/.

[43] 0. Bruning, P. Collier, P. Lebrun, S. Myers, R. Ostojic, J. Poole and P. Proudlock, "LHC Design Report," , vol. 1, 2004. https://cds.cern.ch/record/782076/files/CERN-2004-003-V1-ft.pdf.

[44] ATLAS Collaboration, "Luminosity Public Results Run2," , 2019. https://twiki.cern.ch/twiki/bin/view/AtlasPublic/LuminosityPublicResultsRun2#Luminosity_summary_plots_for_201.

[45] ATLAS Collaboration, "The ATLAS Experiment at the CERN Large Hadron Collider," *JINST*, vol. 3, 2008. http://iopscience.iop.org/article/10.1088/1748-0221/3/08/S08003/meta.

[46] ATLAS Collaboration, "XYZ Right handed coordinate system with z in beam direction," .

[47] ATLAS Collaboration, "Expected performance of the ATLAS experiment - detector, trigger and physics," *CERN-OPEN-2008-020*, 2008. https://cds.cern.ch/record/1125884/files/CERN-OPEN-2008-020.pdf.

[48] ATLAS Collaboration, "ATLAS Insertable B-Layer Technical Design Report," *ATLAS TDR*, 2010. https://cds.cern.ch/record/1291633/files/ATLAS-TDR-019.pdf.

[49] Matteo Cacciari, Gavin P Salam and Gregory Soyez, "The anti-kt jet clustering algorithm," *Journal of High Energy Physics*, vol. 2008, 2008. https://doi.org/10.1088%2F1126-6708%2F2008%2F04%2F063.

[50] ATLAS Collaboration, "Topological cell clustering in the ATLAS calorimeters and its performance in LHC Run 1," *The European Physical Journal C*, vol. 77, 2017. https://link.springer.com/article/10.1140/epjc/s10052-017-5004-5.

[51] M. Nedden on behalf of the ATLAS Collaboration, "The Run-2 ATLAS Trigger System: Design, Performance and Plan," *Topical Seminar on Innovative Particle and Radiation Detectors*, vol. 14, 2016. https://cds.cern.ch/record/2238679.

[52] ATLAS Monojet Group, "Search for new physics in final states with an energetic jet and missing transverse momentum using *pp* collision data collected in Run-2 by ATLAS experiment at LHC," *ATLAS Internal*, 2020. https://cds.cern.ch/record/2308078/files/ATL-COM-PHYS-2018-224.pdf.

[53] ATLAS Collaboration, "Tagging and suppression of pileup jets with the ATLAS detector." ATLAS-CONF-2014-018, 2014.

[54] ATLAS Collaboration, "Selection of jets produced in 13 TeV proton-proton collisions with the ATLAS detector," Tech. Rep. ATLAS-CONF-2015-029, CERN, Geneva, Jul 2015. https://cds.cern.ch/record/2037702.

[55] ATLAS Collaboration, "Measurements of b-jet tagging efficiency with the ATLAS detector using $t\bar{t}$ events at $\sqrt{s} = 13$ TeV," *arXiv*, vol. 089, 2018. https://link.springer.com/article/10.1007%2FJHEP08%282018%29089.

[56] ATLAS Collaboration, "Photon identification efficiency measurements with the ATLAS detector using LHC Run 1 data," Tech. Rep. ATL-COM-PHYS-2014-949, CERN, Geneva, Aug 2014. https://cds.cern.ch/record/1747242.

[57] ATLAS Collaboration, "Improved electron reconstruction in ATLAS using the Gaussian Sum Filter-based model for bremsstrahlung." ATLAS-CONF-2012-047, 2012.

[58] ATLAS Collaboration, "Electron and Photon Selection and Identification for Run2." TWiki, https://twiki.cern.ch/twiki/bin/viewauth/AtlasProtected/EGammaIdentificationRun2.

[59] ATLAS Collaboration, "Electron identification measurements in ATLAS using $\sqrt{s} = 13$ TeV data with 50 ns bunch spacing," *CDS*, 2015. http://cds.cern.ch/record/2048202.

[60] E. Moyse, "ATLAS Muon Combined Reconstruction in Run 2," tech. rep., CERN, Geneva, May 2016. https://twiki.cern.ch/twiki/bin/view/AtlasProtected/MuonsCollection.

[61] ATLAS Collaboration, "Muon reconstruction performance of the ATLAS detector in proton–proton collision data at $\sqrt{s}$=13 TeV," 2016.

[62] ATLAS Collaboration, "Measurement of the tau lepton reconstruction and identification performance in the ATLAS experiment using *pp* collisions at $\sqrt{s}$ = 13 TeV," *CDS*, 2017. https://cds.cern.ch/record/2261772.

[63] ATLAS Collaboration, "Measurement of the photon identification efficiencies with the ATLAS detector using LHC Run 2 data collected in 2015 and 2016," *Eur. Phys. J.*, vol. C79, no. 3, p. 205, 2019.

[64] ATLAS Collaboration, "Performance of Missing Transverse Momentum Reconstruction in ATLAS studied in Proton–Proton Collisions recorded in 2012 at $\sqrt{s} = 8$ TeV." ATLAS-CONF-2013-082, 2013.

[65] ATLAS Collaboration, "Recommendations of the Physics Objects and Analysis Harmonisation Study Groups 2014," Tech. Rep. ATL-PHYS-INT-2014-018, CERN, Geneva, Jul 2014. https://cds.cern.ch/record/1743654.

[66] ATLAS Collaboration, "Search for new physics in final states with jets and missing transverse momentum using *pp* collision data collected in 2015 and 2016 by ATLAS," Tech. Rep. ATL-COM-PHYS-2016-1487, CERN, Geneva, Oct 2016. https://cds.cern.ch/record/2225958.

[67] K. Cranmer, G. Lewis, L. Moneta, A. Shibata, and W. Verkerke, "HistFactory: A tool for creating statistical models for use with RooFit and RooStats," Tech. Rep. CERN-OPEN-2012-016, New York U., New York, Jan 2012. https://cds.cern.ch/record/1456844.

[68] J. Burr, "New understanding of L1Calo MET performance vs offline," *ATLAS Internal*, 2016.

[69] G. Gustavino, "List of systematic uncertainties used in the MET+jet analysis based on the full Run-2 dataset," *ATL-COM-PHYS-2019-1305*, 2019. https://cds.cern.ch/record/2693169.

[70] ATLAS Collaboration, "Luminosity determination in *pp* collisions at $\sqrt{s} = 13$ TeV using the ATLAS detector at the LHC," tech. rep., 2019.

[71] S. Hoeche et al., "Matching Parton Showers and Matrix Elements," *Proceedings of the "HERA and the LHC" workshop, CERN/DESY 2004/2005*, 2006. https://arxiv.org/abs/hep-ph/0602031.

[72] J. Anders and M. D'Onofrio, "V+Jets theoretical uncertainties estimation via a parameterisation method," Tech. Rep. ATL-COM-PHYS-2016-044, CERN, Geneva, Aug 2016. https://cds.cern.ch/record/2125718.

[73] ATLAS Collaboration, "Top Focus Group," 2019. https://twiki.cern.ch/twiki/bin/viewauth/AtlasProtected/TopFocusGroup.

[74] ATLAS collaboration, "ATLAS Pythia 8 tunes to 7 TeV data," *CDS*, 2014. https://cds.cern.ch/record/1966419.

[75] J. Butterworth *et al.*, "PDF4LHC recommendations for LHC Run II," *J. Phys.*, vol. G43, p. 023001, 2016.

[76] ATLAS Collaboration, "Search for dark matter and other new phenomena in events with an energetic jet and large missing transverse momentum using the ATLAS detector," *JHEP*, vol. 01, p. 126, 2018. https://doi.org/10.1007/JHEP01(2018)126.

[77] Y. Akrami *et al.*, "Planck 2018 results. I. Overview and the cosmological legacy of Planck," 2018.

[78] G. Hinshaw *et al.*, "Nine-Year Wilkinson Microwave Anisotropy Probe (WMAP) Observations: Cosmological Parameter Results," *Astrophys. J. Suppl.*, vol. 208, p. 19, 2013.

[79] A. Albert *et al.*, "Recommendations of the LHC Dark Matter Working Group: Comparing LHC searches for dark matter mediators in visible and invisible decay channels and calculations of the thermal relic density," *Phys. Dark Univ.*, vol. 26, p. 100377, 2019.

[80] M. Backovic, A. Martini, K. Kong, O. Mattelaer, and G. Mohlabeng, "MadDM: New dark matter tool in the LHC era," *AIP Conf. Proc.*, vol. 1743, no. 1, p. 060001, 2016.

[81] ATLAS Collaboration, "Search for new phenomena in final states with an energetic jet and large missing transverse momentum in pp collisions at $\sqrt{s} =$ 13 TeV using the ATLAS detector," *Phys. Rev.*, vol. D94, no. 3, p. 032005, 2016.

[82] XENON Collaboration, "Constraining the Spin-Dependent WIMP-Nucleon Cross Sections with XENON1T.," *Physical Review Letters*, vol. 122, 2019. https://doi.org/10.1103/PhysRevLett.122.141301.

[83] LUX Collaboration, "Limits on Spin-Dependent WIMP-Nucleon Cross Section Obtained from the Complete LUX Exposure.," *Physical Review Letters*, vol. 118, 2017. https://doi.org/10.1103/PhysRevLett.118.251302.

[84] PICO Collaboration, "Dark Matter Search Results from the Complete Exposure of the PICO-60 C_3F_8 Bubble Chamber.," *Physical Review D*, vol. 100, 2019. https://doi.org/10.1103/PhysRevD.100.022001.

[85] A. Boveia *et al.*, "Recommendations on presenting LHC searches for missing transverse energy signals using simplified s-channel models of dark matter," *Physics of the Dark Universe*, vol. 27, 2020. https://www.sciencedirect.com/science/article/pii/S2212686419301633.

[86] ATLAS Collaboration, "Search for new resonances in mass distributions of jet pairs using 139 fb^1 of *pp* collisions at $(\sqrt{s}) = 13$ TeV with the ATLAS detector," *Journal of High Energy Physics*, vol. 145, 2020. https://doi.org/10.1007/JHEP03(2020)145.

[87] ATLAS Collaboration, "Search for Low-Mass Dijet Resonances Using Trigger-Level Jets with the ATLAS Detector in *pp* Collisions at $\sqrt{s} = 13$ TeV," *Physical Review Letters*, vol. 121, 2018. https://doi.org/10.1103/PhysRevLett.121.081801.

[88] ATLAS Collaboration, "Search for low-mass resonances decaying into two jets and produced in association with a photon using *pp* collisions at $\sqrt{s} = 13$ TeV with the ATLAS detector," *Physics Letters B*, vol. 795, 2019. https://doi.org/10.1016/j.physletb.2019.03.067.

[89] ATLAS Collaboration, "Search for light resonances decaying to boosted quark pairs and produced in association with a photon or a jet in proton–proton collisions at $\sqrt{s} = 13$ TeV with the ATLAS detector," *Physics Letters B*, vol. 788, 2019. https://doi.org/10.1016/j.physletb.2018.09.062.

[90] ATLAS Collaboration, "Search for boosted resonances decaying to two b-quarks and produced in association with a jet at $\sqrt{s} = 13$ TeV with the ATLAS detector," *Higgs Couplings 2018*, 2018. https://cds.cern.ch/record/2649081.

[91] ATLAS Collaboration, "Search for heavy particles decaying into top-quark pairs using lepton-plus-jets events in proton–proton collisions at $\sqrt{s} = 13$ TeV with the ATLAS detector," *European Physical Journal C*, vol. 565, 2018. https://doi.org/10.1140/epjc/s10052-018-5995-6.

[92] ATLAS Collaboration, "Search for dark matter in association with an energetic photon in *pp* collisions at $\sqrt{s} = 13$ TeV with the ATLAS detector," *ICHEP2020*, 2020. https://cds.cern.ch/record/2720250.

[93] ATLAS Collaboration, "Search for dark matter in events with a hadronically decaying vector boson and missing transverse momentum in *pp* collisions at $\sqrt{s} = 13$ TeV with the ATLAS detector," *Journal of High Energy Physics*, vol. 180, 2018. https://cds.cern.ch/record/2720250.

[94] ATLAS Collaboration, "Search for an invisibly decaying Higgs boson or dark matter candidates produced in association with a Z boson in *pp* collisions at $\sqrt{s} = 13$TeV with the ATLAS detector," *Physics Letters B*, vol. 776, 2018. https://doi.org/10.1016/j.physletb.2017.11.049.

[95] ATLAS Collaboration, "Dark matter summary plots for s-channel mediators," *CDS*, 2020. http://cdsweb.cern.ch/record/2725266.

[96] CMS Collaboration, "Search for low mass vector resonances decaying into quark-antiquark pairs in proton-proton collisions at $\sqrt{s} = 13$ TeV," *Physical Review D*, vol. 100, 2019. https://doi.org/10.1103/PhysRevD.100.112007.

[97] CMS Collaboration, "Search for narrow resonances in the b-tagged dijet mass spectrum in proton-proton collisions at $\sqrt{s} = 8$ TeV," *Physical Review Leters*, vol. 120, 2018. https://doi.org/10.1103/PhysRevLett.120.201801.

[98] CMS Collaboration, "Search for dijet resonances using events with three jets in proton-proton collisions at $\sqrt{s} = 13$ TeV," *Physics Letters B*, vol. 805, 2020. https://doi.org/10.1016/j.physletb.2020.135448.

[99] CMS Collaboration, "Search for narrow and broad dijet resonances in proton-proton collisions at $\sqrt{s} = 13$ TeV and constraints on dark matter mediators and other new particles," *Journal of High Energy Physics*, vol. 130, 2018. https://doi.org/10.1007/JHEP08(2018)130.

[100] CMS Collaboration, "Search for new physics in final states with an energetic jet or a hadronically decaying W or Z boson and transverse momentum imbalance at $\sqrt{s} = 13$ TeV," *Physical Review D*, vol. 97, 2018. https://doi.org/10.1103/PhysRevD.97.092005.

[101] CMS Collaboration, "Search for new physics in final states with a single photon and missing transverse momentum in proton-proton collisions at $\sqrt{s} = 13$ TeV," *Journal of High Energy Physics*, vol. 74, 2019. https://doi.org/10.1007/JHEP02(2019)074.

[102] CMS Collaboration, "Search for new physics in events with a leptonically decaying Z boson and a large transverse momentum imbalance in proton–proton collisions at $\sqrt{s} = 13$ TeV," *European Physical Journal C*, vol. 78, 2019. https://doi.org/10.1140/epjc/s10052-018-5740-1.

[103] V. Sharma on behalf of the CMS Collaboration, "Searches for Dark Matter in CMS," *LHCP2020*, 2020. https://indico.cern.ch/event/856696/contributions/3742221/.

[104] ATLAS Collaboration, "Search for high-mass dilepton resonances using 139 fb^1 of pp collision data collected at $\sqrt{s} = 13$ TeV with the ATLAS detector," *Physics Letters B*, vol. 796, 2019. https://doi.org/10.1016/j.physletb.2019.07.016.

[105] ATLAS Collaboration, "Search for dark matter produced in association with bottom or top quarks in $\sqrt{s} = 13$ TeV pp collisions with the ATLAS detector," *European Physical Journal C*, vol. 78, 2018. https://doi.org/10.1140/epjc/s10052-017-5486-1.

[106] ATLAS Collaboration, "Search for new phenomena with top quark pairs in final states with one lepton, jets, and missing transverse momentum in pp collisions at $\sqrt{s} = 13$ TeV with the ATLAS detector," *CDS*, 2020. https://cds.cern.ch/record/2711489.

[107] ATLAS Collaboration, "Search for new phenomena in events with two opposite-charge leptons, jets and missing transverse momentum in pp collisions at $\sqrt{s} = 13$ TeV with the ATLAS detector," *ICHEP2020*, 2020. https://cds.cern.ch/record/2728056.

[108] CMS Collaboration, "Search for dark matter produced in association with a single top quark or a top quark pair in proton-proton collisions at $\sqrt{s} = 13$ TeV," *Journal of High Energy Physics*, vol. 141, 2019. https://doi.org/10.1007/JHEP03(2019)141.

[109] P. Brax and C. Burrage, "Constraining disformally coupled scalar fields," *Physial Review D*, vol. 90, 2014. https://doi.org/10.1103/PhysRevD.90.104009.

[110] ATLAS Collaboration, "ATLAS ITK Upgrade Project," *HKUST Jockey Club Institute For Advanced Study Program on High Energy Physics 2018*, 2018. https://cds.cern.ch/record/2302625/.

[111] D. Briglin, "Irradiation and testing of silicon strip sensors for the ATLAS ITk upgrade," *Midterm Report*, 2017.

[112] M.J. Berger et al, "Stopping-power and range tables for electrons, protons, and helium ions," *NIST*, 2005. https://www.nist.gov/pml/stopping-power-range-tables-electrons-protons-and-helium-ions.

[113] F. Jones, "The Air Density Equation and the Transfer of the Mass Unit," *JOURNAL OF RESEARCH of the National Bureau of Standards*, vol. 83, 1978. http://nvlpubs.nist.gov/nistpubs/jres/83/jresv83n5p419_A1b.pdf.

[114] E. Podgorsak, "Radiation Oncology Physics: A Handbook for Teachers and Students," , 2005. http://www-pub.iaea.org/mtcd/publications/pdf/pub1196_web.pdf.

[115] N. Attree, "Optimisation of current monitoring and beam quality at the high intensity irradiation line at the MC40 irradiation facility," *Master's Thesis*, 2020.

[116] ATLAS Collaboration, "Extrapolation of E_T^{miss} + jet search results to an integrated luminosity of 300 fb[1] and 3000 fb[1]," *CDS*, vol. 43, 2018. http://cdsweb.cern.ch/record/2650050.

[117] A. Martínez on behalf of the ATLAS Collaboration, "The ATLAS Run-2 Trigger Menu for Higher Luminosities: Design, Performance and Operational Aspects," *EPJ Web of Conferences*, vol. 182, 2018. https://doi.org/10.1051/epjconf/201818202083.

APPENDIX A

Trigger Naming Scheme

A.1 $P_{\mathrm{T}}^{\mathrm{recoil}}$ triggers

HLT_xe90_mht_L1XE50 means an HLT trigger that has a trigger threshold of $P_{\mathrm{T}}^{\mathrm{recoil}}$ (xe) > 90 GeV, using the "mht" algorithm, combined with a L1 trigger with a trigger threshold of $P_{\mathrm{T}}^{\mathrm{recoil}}$ (XE) > 50 GeV. There are 3 different $P_{\mathrm{T}}^{\mathrm{recoil}}$ calculation strategies used by HLT: "cell", "mht", "pufit". The monojet analysis considers only mht and pufit. In the mht algorithm, $P_{\mathrm{T}}^{\mathrm{recoil}}$ is calculated as the negative of the transverse momentum vector sum of all jets reconstructed by the anti-k_t jet finding algorithm from calorimeter topological clusters. These jets have a procedure called pileup subtraction applied to them, a calibration which reduces the effect of pileup, and Jet Energy Scale (JES) calibration, which adjusts the energy and momentum of a jet as a function of its p_T and $|\eta|$ to account for detector effects. In the pufit algorithm, $P_{\mathrm{T}}^{\mathrm{recoil}}$ is calculated as the negative value of the transverse momentum vector sum of all calorimeter topological clusters corrected for pileup. The pileup correction is done by grouping the clusters into coarser "towers", which are then marked as being due to pileup if their $P_{\mathrm{T}}^{\mathrm{recoil}}$ falls below a pileup-dependent threshold. A fit to below-threshold towers is performed, taking into account their resolutions, making the assumption that the contribution of the pileup to $P_{\mathrm{T}}^{\mathrm{recoil}}$ is zero [117].

A.2 Electron triggers

HLT_e24_lhmedium_L1EM20VH means an HLT trigger with a threshold of an electron p_{T} (e) > 24 GeV, identified as an electron with medium certainty (lhmedium; possible certainties from least to most certain are: loose, medium, tight, very tight), with an L1 trigger with a threshold of 20 GeV deposited in the electromagnetic calorimeter and no energy deposited in the hadronic calorimeter (VH). In addition, ivarloose is a requirement that the electron is isolated from other particles within a cone around the electron track, and nod0 indicates no transverse impact parameter cuts are applied.